

Mechanisms of cone dysfunction in inherited retinal degenerations

Mark M Hassall

Merton College

Thesis submitted for a DPhil in Clinical Neuroscience

Supervised by

Prof. Robert MacLaren & Mr. Sher Aslam





DEDICATION

For my world, Maddie

ABSTRACT

This thesis examines the mechanisms of cone dysfunction in two different inherited retinal diseases: Achromatopsia and Retinitis Pigmentosa (RP). The first, minor, component of the thesis explored and characterised the loss of cone function in a novel mouse model of achromatopsia (*cpfl10*). The second, major, component of the thesis explored the loss of cone function in a mouse model of RP. I hypothesised that the cone function lost in RP could be restored using AAV vectors to over-express down regulated cone genes. This thesis subsequently developed and tested two AAV vectors delivering *CRX* and *OPN1LW* genes to photoreceptors in RP mice.

Achromatopsia is a congenital condition characterised by absent or diminished cone function due to mutations of a single gene, typically those involved in the cone phototransduction cascade. This thesis provides a detailed phenotype of a novel *cpfl10* mouse model of Achromatopsia that arose spontaneously in a local mouse colony. The causative (NM_013927)c.692G>A; p.(R231H) missense mutation in *Cngb3* was also identified and explored.

Retinitis pigmentosa (RP) is an inherited retinal degeneration in which secondary loss of cones follows the initial death of genetically abnormal rod photoreceptors. Strategies to prolong cone photosensitivity or survival would offer an important treatment. Such universal interventions could be effective regardless of which genetic mutation is underlying primary rod death.

The molecular mechanisms by which cone photoreceptors lose photosensitivity in RP are poorly understood. I examined the gene expression profile of the cone phototransduction cascade in the $Rho^{-/-}$ mouse model of RP and correlated these changes to declining retinal function. The cone opsins were

substantially down-regulated, as was the photoreceptor transcription factor *Crx*.

I hypothesised that the cone function lost in RP could be restored using AAV vectors to over-express these down regulated cone genes. Using an AAV gene therapy vectors, I delivered the human homologs *CRX* and *OPN1LW* to the retinas of the same $Rho^{-/-}$ mouse model. Both vectors successfully transduced photoreceptors and RPE cells across three different doses. Transduced retinas did not show any improvement in cone function or survival.

Whilst the observed down-regulation of cone genes correlates with cone function loss, it appears that both down-regulation and dysfunction arise from an unknown common cause. Ongoing research into mechanisms of metabolic starvation, oxidative stress and trophic factors in cone cell death offer promise for a common intervention to rescue cone photoreceptors.

DECLARATION

I declare that this thesis is my own original work. Where I have consulted or quoted the work of others, this is clearly attributed. No part of this thesis has previously been submitted for a degree or any other qualification at this University or any other institution.

Mark Hassall University of Oxford 2017

ACKNOWLEDGEMENTS

I thank my supervisor, Robert MacLaren, for his advice and leadership over the last three years. I am grateful for his weekly advice on my data, questions and problems — and for his steady hand and broader perspective during difficulty. His tireless dedication to an impressive translational and clinical Ophthalmology research program has been a powerful example of an impactful career. I particularly appreciate his efforts to develop a spirit of teamwork and belonging in the lab through regular group journal clubs, dinners and *fugu*.

I thank my co-supervisor, Sher Aslam, for his support and counsel. I've enjoyed the chance to decompress over a coffee and discuss my interim results with him in detail; his style of questioning often guided me to a solution.

I thank my colleagues at the Nuffield Laboratory of Ophthalmology, particularly the concerted experience and guidance of the post-docs by my bench side every μL of the way: Alun Barnard, the doyen of functional testing and precise scientific writing; Michelle McClements, the authority on cloning and a paradigm of well-planned science; Maria Patricio, a generous contributor to the inclusive lab atmosphere and resource sharing; Cristina Martinez, an exemplar of relentless hard-work; Tina Storm, a munificent guide on proteins and antibodies; and Marco Bellini, the silent workhorse of lab logistics and good humoured about the considerable recent South African sporting drought.

I also thank the other students who have been in the laboratory during my time: Dominik Fisher, who taught me my first subretinal injection; Dany Dauletbekov, who helped me perform my first IHC; Doron Hickey, who showed me FACS sorting; Shaun Wood, whose persistence in patch-clamping encouraged me in my own work; Harry Orlans, a great cycle-buddy for Paris and

Washington and whose strong work-ethic inspired me to re-double my efforts in second year; Sophia Bellingrath, a great friend and support; Caroline Peddle, the gate-keeper of motivational stickers and always good-humoured in the face of frustrations; Laurel Chandler, a conscientious worker and a great colleague to take to visit a secret military base; as well as Lewis Fry and Imran Yusuf for their fun company in the lab.

I am thankful to the Rhodes Trust for awarding me a scholarship and empowering me to undertake this opportunity. In particular, Mary Eaton, Charles Conn, and Bob and Dawn Wyllie have all been a great personal support to me throughout my time in Oxford. Thank you also to the Merton College travel grants and the NDCN graduate support fund. I am also grateful to Dan Lunn at the department of statistics for our regular sessions throughout my third year, I learned a huge amount about statistics and data analysis.

Finally, I sincerely thank my friends and family for being a source of inspiration. My parents, who instilled in me a love of learning, encouraged me to chase after hard ambitions and have always been a steadfast support. Thank you to Maddie, who moved halfway around the world so I could pursue a dream, motivated me every day, and who made these years more fun and worthwhile than I could have imagined.

List of Publications

Original manuscripts contributing to DPhil thesis

Hassall MM, Barnard AR, MacLaren RE. Gene Therapy for Color Blindness. Yale J Biol Med. 2017 Dec;90(4):543–51.

The final published version of this published manuscript can be found in Appendix A.

Conference abstracts during DPhil

From the work generated in this thesis, 10 conference abstracts were presented as a verbal presentation or a poster. The full text of each abstract can be found in full in Appendix A.

1. *Submitted Nov 2017* **Hassall M M**, McClements M, Barnard A R, Aslam S A MacLaren R E. E-abstract. Loss of cone photosensitivity in RP is not caused by down-regulation of genes in the phototransduction cascade. ARVO conference 2018

2. **Hassall M M**, Barnard A R, Charbel Issa P, Aslam S A MacLaren R E. An improved mouse model of complete achromatopsia for development of Cngb3 gene therapies. EuRetina conference 2017

3. Barnard AR, **Hassall M M**, Charbel-Issa P, Aslam S A MacLaren RE. A missense change in Cngb3 causes achromatopsia in a naturally occurring mouse model. Oxford Ophthalmological Congress, UK, June 2017

4. **Hassall M M**, McClements ME, Barnard AR, Aslam SA and MacLaren RE. Gene therapy for cone photoreceptor rescue in a mouse model of retinitis pigmentosa, Oxford Ophthalmological Congress, UK, June 2017 (Presentation)

5. **Hassall M M**, A new mouse model of achromatopsia that more closely resembles the human condition, Oxford-Bristol-Cardiff-Southampton Ophthalmology meeting, Southampton, UK, June 2017

6. **Hassall M M**, McClements ME, Barnard AR, Aslam SA and MacLaren RE. Crx and Cone Opsins are candidates for gene therapy in a mouse model of Retinitis Pigmentosa, ARVO, Baltimore, USA, May 2017

7. Barnard A R, **Hassall M M**, Charbel-Issa P and MacLaren RE. A spontaneously occurring mouse model of complete achromatopsia due to a missense mutation in Cngb3. ARVO, Baltimore, USA

8. **Hassall M M**, Barnard AR, Charbel-Issa P and MacLaren RE. An improved mouse model of achromatopsia for pre-clinical development of gene therapies. FLOREtina conference, Italy, 2017

9. **Hassall M M**, Barnard A, Charbel-Issa P and MacLaren R, The 129S6/SvEvTac mouse strain exhibits achromatopsia and abnormal cone morphology unrelated to Cnga3, Oxford Ophthalmological Congress, UK, 2016.

10. **Hassall M M**, Barnard A, Charbel-Issa P and MacLaren R. Identification of a potential new mouse model of achromatopsia through spontaneous occurrence of cone pathway function loss, ARVO, 2016 International conference, Seattle WA, USA.

CONTENTS

Page

Dedication **i**

Abstract **ii**

Declaration **iv**

Acknowledgements **v**

List of Publications **vii**

Contents **xxi**

List of Figures **xxiv**

List of Tables **xxvi**

Abbreviations **xxxii**

1 Introduction **1**

1.1 The Retina 1

1.1.1 Photoreceptors 1

1.1.2 The phototransduction cascade 2

1.1.2.1 Opsins 5

1.1.2.2 Cyclic nucleotide-gated channels 5

1.1.3 Transcription factors in cone photoreceptors 6

1.1.3.1 Orthodenticle transcription factor 6

1.1.3.2 Cone-rod homeobox transcription factor 6

1.2 Achromatopsia 8
1.2.1 Pre-clinical rescue of animal models 11
1.2.2 The human retina in Achromatopsia 13
1.2.3 Gene therapy clinical trials for Achromatopsia 14
1.2.4 The future for Achromatopsia therapies 17
1.3 Retinitis Pigmentosa 18
1.3.1 Cone photoreceptor death 19
1.3.1.1 Trophic factors 20
1.3.1.2 Oxidative stress 20
1.3.1.3 Degeneration of cone outer segments and opsin mislocalisation 21
1.3.2 Evidence of inactive cone cells 23
1.4 Retinal gene therapy 23
1.4.1 Previous experiments exploring ectopic opsin expression . 24
1.4.1.1 Halorhodopsin 24
1.4.1.2 Rhodopsin 25
1.4.1.3 Melanopsin 25
1.5 Summary, hypothesis and objectives 26

2 Materials & methods 28

2.1 Animals 28
2.1.1 Overview 28
2.1.1.1 Cone photoreceptors in mouse models 28
2.1.1.2 pR6.5.Lacz reporter line 29
2.1.2 B6$^{TgOPN1LW\text{-}EGFP}$ mouse strain 30
2.1.3 C57Bl/6 mouse strain 30
2.1.4 Cone Photoreceptor Function Loss mouse strain 30
2.1.5 129S6 SvEvTac strain 31
2.1.6 Triple knock-out mouse strain 31
2.1.7 Nrl-L-EGFP mouse strain 31

2.1.8 Rho$^{-/-}$ mouse strain 32
2.1.8.1 RP phenotype 32
2.1.8.2 Cross-breeding Rho$^{-/-}$ with GFP lines 32
2.2 *In Vivo* procedures 32
2.2.1 Anaesthesia and mydriatics 33
2.2.2 Subretinal injections 33
2.2.2.1 Preparation 33
2.2.2.2 Delivery of vector 34
2.2.2.3 Cleaning injection equipment 35
2.2.3 Confocal scanning laser ophthalmoscopy 36
2.2.3.1 Phenotyping mice using SLO 36
2.2.3.2 Correlation of PCR and SLO 36
2.2.4 Optical coherence tomography 37
2.2.5 Optomotor response 39
2.2.6 Electroretinography 40
2.2.6.1 Creation of electrodes 41
2.2.6.2 Testing protocol 41
2.3 Molecular techniques 41
2.3.1 Extraction of DNA from tissue 42
2.3.1.1 Low fidelity genomic DNA from ear clips 42
2.3.1.2 High fidelity genomic DNA from tails 42
2.3.2 Polymerase chain reaction 42
2.3.2.1 Splice PCR by overlap extension 43
2.3.2.2 Genotyping using PCR 44
2.3.3 Electrophoresis and gel extraction 44
2.3.4 Spectrophotometry 45
2.3.5 Dideoxynucleic acid sequencing of sequence 45
2.3.6 Extraction of RNA from dissociated retinal cells 45
2.3.6.1 Dissociation of retinal cells 45
2.3.6.2 Fluorescence-activated cell sorting 46

2.3.7 Extraction of RNA whole retinal tissue 46
2.3.7.1 Harvesting of whole mouse retinal tissue 46
2.3.7.2 mRNA extraction from tissue 46
2.3.7.3 RNA reverse transcription to cDNA 47
2.3.8 Quantitative PCR 47
2.3.8.1 Primer design 47
2.3.8.2 Sanger sequencing of cGFP transgene 48
2.3.8.3 qPCR plates 49
2.3.9 Extraction of protein from tissue 49
2.3.10 Western blot 49
2.3.10.1 Bicinchoninic acid assay 50
2.3.10.2 Image analysis of WB 51
2.4 Cloning of vector plasmids 51
2.4.1 Design of plasmids 51
2.4.2 Genetic components 51
2.4.2.1 Plasmid backbone 51
2.4.2.2 Transgenes 52
2.4.3 Introduction of restriction sites into amplicons 53
2.4.4 Restriction digest and ligation 53
2.4.5 Ligation of digested DNA fragments 53
2.4.6 Amplification in bacteria 53
2.5 Production of AAV 54
2.5.0.1 RepCap AAV8^{Y733F} plasmid 54
2.5.0.2 Helper plasmid 55
2.5.1 Plasmid transfection of HEK293T cell line 55
2.5.2 Harvesting and lysing transfected HEK293T cells 56
2.5.3 Isolation of the AAV particles using Iodixanol gradient . . . 57
2.5.4 Virus purification and concentration 59
2.5.5 Virus titring 59
2.5.5.1 Calculation of titre 60

2.5.6 Virus capsid quality control using SDS-PAGE 60
2.6 Cell culture 62
2.6.1 Subculturing cell lines 62
2.6.2 *In Vitro* plasmid transfection 62
2.6.3 *In Vitro* AAV transduction 63
2.7 Histological analysis 63
2.7.1 Embedding and cryo-sections 63
2.7.2 Immunohistochemistry 64
2.7.2.1 Overview 64
2.7.2.2 Protocol 64
2.7.3 Immunocytochemistry 65
2.7.4 Microscopy 65
2.7.4.1 Confocal laser microscopy 66
2.7.4.2 Evos LED microscopy 67
2.7.5 Image analysis 67
2.7.5.1 Confocal microscope images of ICC/IHC 67
2.7.5.2 Evos images 67
2.7.5.3 cSLO images 68
2.7.5.4 OCT images 68
2.8 Statistical analysis 68
2.8.1 Analysis of non-repeated measures and non-complex datasets 69
2.8.2 Hierarchical modelling of complex repeated measures datasets 70
2.8.3 Fitting functions to ERG response curves 71
2.8.4 Interpreting P-values 72

3 Cone Photoreceptor Function Loss mutation 73
3.1 Introduction 73
3.2 Aims & objectives 77

3.3 Materials & methods 77
3.3.1 Animals 77
3.3.2 *In vivo* procedures 78
3.3.3 Molecular techniques 78
3.3.3.1 Re-sequencing and genotyping 78
3.3.3.2 Retinal gene qPCR 79
3.3.4 Immunohistochemistry 79
3.3.5 *In silico* modelling of Cngb3 79
3.4 Results 80
3.4.1 Origin and phenotype of the mouse *cpfl10* mutant 80
3.4.2 Inheritance pattern 80
3.4.3 Retinal phenotype 81
3.4.4 Effect of the cpfl10 mutation on mRNA expression 85
3.4.5 Mutation analysis 87
3.4.6 Effect of the cpfl10 mutation on protein expression 93
3.5 Discussion 98
3.6 Conclusion 102

4 Cone cell qPCR 103

4.1 Introduction 103
4.1.1 RNA quantification technologies 104
4.1.1.1 Microarray 105
4.1.1.2 RNA-seq 105
4.1.1.3 qPCR 106
4.1.2 Selection of qPCR test genes 106
4.1.2.1 Crx isoforms 1 and 2 107
4.1.3 Correlating gene expression analysis to phenotype 107
4.2 Aims & objectives 108
4.3 Materials & methods 109
4.3.0.1 Animals 109

4.3.0.2 *In vivo* procedures . . . 109
4.3.0.3 FACS . . . 110
4.3.0.4 IHC . . . 110
4.3.1 qPCR . . . 110
4.3.1.1 Sampling error . . . 110
4.3.1.2 RNA integrity and quantification . . . 111
4.3.1.3 Appropriate reference genes . . . 112
4.3.1.4 Primer efficiency . . . 113
4.3.1.5 qPCR technical methods . . . 113
4.3.1.6 Statistical analysis of qPCR . . . 114
4.4 Results . . . 114
4.4.1 *In Vivo* OCT measurements . . . 114
4.4.2 Validation of *In vivo* cSLO manual counts . . . 115
4.4.2.1 Results of cSLO manual counts . . . 117
4.4.3 *In vivo* cone function . . . 119
4.4.3.1 Cone electrophysiological function . . . 119
4.4.3.2 Cone optomotor response function . . . 121
4.4.4 Cone sampling bias caused by GFP . . . 122
4.4.4.1 Proportion of cones expressing GFP on IHC . . . 122
4.4.4.2 Proportion of GFP cones isolated using FACS . . . 123
4.4.5 Sequencing the $B6^{TgOPN1LW\text{-}EGFP}$ transgene . . . 124
4.4.6 Optimisation of cone qPCR primer pairs . . . 124
4.4.7 mRNA isolation from retinal sample . . . 126
4.4.8 qPCR test plates . . . 127
4.4.8.1 Negative controls . . . 127
4.4.8.2 Positive controls . . . 128
4.4.8.3 Reliability of the *Actb* reference gene . . . 128
4.4.8.4 *Rho* transcript expression . . . 131
4.4.9 Hierarchical model of the cone qPCR data . . . 133
4.4.9.1 Fitting the model . . . 133

4.4.9.2 Results of the polynomial model 135
4.4.10 Correlation of *Crx* and *Rho* changes 139
4.5 Discussion 140
4.5.1 Validation of the OCT for rod measurements 140
4.5.2 Validation of SLO manual counting technique 140
4.5.2.1 Cone function outcome measures 141
4.5.3 Suitability of *Actb* as a single qPCR reference gene 142
4.5.4 Nonsense-mediated decay of mutant Rhodopsin mRNA . . 143
4.5.5 GFP as an internal control 143
4.5.6 Gene expression peak from 2 to 6 weeks 144
4.5.7 Expression of Crx 145
4.5.8 Expression of Opsin genes 146
4.6 Conclusion 147

5 Creation and validation of AAV vectors 148
5.1 Introduction 148
5.1.1 Delivery mechanism 149
5.1.2 Choice of viral vector 149
5.1.3 Rationale for transgene selection 151
5.1.3.1 Human genes function in mice 151
5.1.3.2 CRX 151
5.1.3.3 OPN1LW 151
5.1.4 Rationale for promoter selection 152
5.1.5 Rationale for including intron-exon and WPRE elements . . 153
5.1.6 Rationale for capsid serotype AAV^{Y733F} 154
5.2 Aims & objectives 154
5.3 Materials & methods 157
5.3.1 Genetic components 157
5.3.1.1 Human CRX gene 157
5.3.1.2 Human OPN1LW gene 157

5.3.1.3 Plasmid backbone 157
5.3.2 Molecular techniques 157
5.3.2.1 PCR and Agarose gels 157
5.3.2.2 Restriction digests and ligation 158
5.3.2.3 XL-10 cell transformation and amplification 158
5.3.3 AAV production 158
5.3.4 Cell culture and histological analysis 158
5.3.4.1 HEK293T cell transfection with plasmid 158
5.3.4.2 ICC protocol 159
5.3.4.3 HEK293T cell transduction with AAV 159
5.3.4.4 Western Blot 159
5.4 Results 160
5.4.1 Design of AAV plasmids 160
5.4.2 Cloning the AAV.CAG.OPN1LW.WPRE.pA plasmid 162
5.4.3 Cloning the AAV.CAG.CRX.WPRE.pA plasmid 164
5.4.4 Validation of plasmid promoter 166
5.4.5 AAV8^{Y733F} production 167
5.4.6 AAV quality control 168
5.4.6.1 qPCR titring of AAV concentration 168
5.4.6.2 SDS-PAGE of AAV capsid 169
5.4.6.3 Western Blot optimisation on cell lysate 171
5.4.7 Differentiating between species *in Vivo* with qPCR and IHC 173
5.5 Discussion 176
5.6 Conclusion 178

6 Pilot study of AAV 179
6.1 Introduction 179
6.2 Aims & objectives 180
6.3 Materials & methods 181
6.3.1 Mouse model 181

6.3.2 Study design . . . 181
6.3.3 Route of delivery . . . 183
6.3.3.1 Subretinal injections . . . 183
6.3.4 Dose and volume selection . . . 184
6.3.5 Randomisation . . . 184
6.3.6 Outcome measures . . . 185
6.3.6.1 Electroretinography . . . 185
6.3.6.2 OCT and cSLO . . . 185
6.3.6.3 Immunohistochemistry . . . 186
6.3.6.4 Statistical analysis . . . 186
6.4 Results . . . 186
6.4.1 Surgical outcome criteria . . . 186
6.4.2 Effect on ERG function . . . 189
6.4.2.1 Mesopic and scotopic function . . . 189
6.4.2.2 Photopic function . . . 190
6.4.3 Retinal architecture on OCT . . . 193
6.4.3.1 Effect of sham injections . . . 193
6.4.3.2 Effect of AAV.CRX treatment . . . 194
6.4.3.3 Effect of AAV.OPN treatment . . . 194
6.4.4 Macroscopic appearance of the retina *in vivo* on cSLO . . . 196
6.4.4.1 GFP signal on BAF . . . 196
6.4.4.2 Pigmentary pattern on ICGA . . . 198
6.4.5 Transgene expression on IHC . . . 200
6.5 Discussion . . . 204
6.5.1 Surgery . . . 204
6.5.2 Transgene expression . . . 205
6.5.3 Evidence of AAV mediated damage . . . 207
6.5.4 Exploring the IRAF changes in the full trial . . . 209
6.5.5 Future dose selection . . . 209
6.5.6 Effect of a different mouse model . . . 210

6.5.7 Rationale for proceeding to full trial 210
6.6 Conclusion 211

7 Full study of AAV efficacy 212
7.1 Introduction 212
7.2 Aim & objectives 213
7.3 Materials & methods 215
7.3.1 Animals 215
7.3.2 Subretinal injections 215
7.3.2.1 Rationale for dose range 215
7.3.2.2 Randomisation and blinding 216
7.3.3 Adjusting for the $B6^{TgOPN1LW\text{-}EGFP}$ allele 217
7.3.4 Power calculations and sample sizes 218
7.3.5 Study design 218
7.3.6 *In vivo* functional testing 221
7.3.6.1 OCT and cSLO 221
7.3.6.2 ERG 221
7.3.6.3 OMR 221
7.3.7 Molecular techniques 221
7.3.7.1 Retinal samples and cDNA 221
7.3.7.2 qPCR 221
7.3.7.3 IHC 222
7.3.8 Statistical analysis 222
7.3.8.1 Hierarchical non-linear modelling of the ERG IRC 222
7.4 Results 223
7.4.1 Surgical success and details of excluded mice 223
7.4.2 Retinal architecture measured with OCT 226
7.4.3 Cone photoreceptor survival measured *in vivo* with cSLO BAF 230

7.4.4 Pigmentary changes in treated retinas measured *in vivo* with cSLO IRAF 232
7.4.5 Retinal function measured with ERG 234
7.4.6 Effect on mesopic and scotopic ERG function 234
7.4.7 Effect on photopic ERG function 241
7.4.8 Effect on OMR function in photopic conditions 247
7.4.9 Transgene mRNA expression in the retinal transcriptome . 249
7.4.9.1 Cone opsin mRNA 249
7.4.9.2 CRX and Crx mRNA 250
7.4.10 Transgene protein expression on retinal histology 251
7.4.10.1 CRX expression in RPE cells 251
7.4.11 CRX expression in the neurosensory retina 252
7.4.12 OPN1LW expression in the neurosensory retina 257
7.5 Discussion 262
7.5.1 Surgical success 262
7.5.1.1 Randomisation and heterogenous treatment groups 262
7.5.2 Functional and structural toxicity 263
7.5.2.1 Crx-mediated differentiation to photoreceptors . . 263
7.5.3 Conclusions 264

8 Conclusion 265

8.1 Overview 265
8.2 *Cpfl10* mouse model 267
8.3 $B6^{TgOPN1LW\text{-}EGFP}$ model techniques and limitations 268
8.4 $Rho^{-/-}$ mouse rhodopsin transcript 269
8.5 Cone phototransduction cascade gene expression analysis 271
8.6 AAV over-expression of CRX 272
8.7 AAV over-expression of OPN1LW 273
8.7.1 Compared to previous human opsin work 273
8.7.2 Compared to previous halorhodopsin work 275

8.8 Proximate and ultimate causes of cone dysfunction and death . . . 275
8.8.1 Ultimate cause: rod death 276
8.8.2 Proximate causes 277
8.8.2.1 Proximate cause: Trophic factors 277
8.8.2.2 Proximate cause: Oxidative stress 279
8.8.2.3 Proximate cause: Metabolic starvation 280
8.9 Concluding remarks 283

A Manuscripts and abstracts **285**

B Reagents **312**

C Kits **314**

D Hardware **315**

E Software **317**

F Antibodies & stains **318**

G Solutions **320**

H Cone photoreceptor qPCR primers **321**

List of References **323**

List of Figures

1.1 Phototransduction 4

2.1 Subretinal injections 35
2.2 Functional testing 38
2.3 OMR testing 40
2.4 Iodixanol gradients 58
2.5 AAV protein capsid SDS-PAGE 61
2.6 Sigmoidal curve function 72

3.1 Outcross bleeding plan 81
3.2 cpfl10 ERG phenotype-genotype correlation 83
3.3 Retinal phenotype 84
3.4 Mutation effect on mRNA 86
3.5 cpfl10 genotyping 88
3.6 cpfl10 expressivity 90
3.7 Arginine conservation across species 92
3.8 Cngb3 IHC with antibody orb156415 94
3.9 Cngb3 IHC with antibody CPBT-31596RH 96
3.10 Cngb3 IHC with antibody ABIN5715 97
3.11 Cngb3 IHC on cpfl10 mice 98

4.1 OCT phenotype 115
4.2 SLO phenotype 118
4.3 ERG phenotype over time 120
4.4 Cone function 122

4.5 GFP expression on IHC . . . 123
4.6 FACS pilot study . . . 124
4.7 qPCR test primer melt curves . . . 126
4.8 qPCR quality control . . . 130
4.9 Rhodopsin transcript . . . 132
4.10 Polynomial model diagnostic tests . . . 134
4.11 Cone qPCR results . . . 137
4.12 Correlation of Crx and Rho . . . 139

5.1 Cloning strategies . . . 161
5.2 OPN1LW cloning . . . 163
5.3 CRX cloning . . . 165
5.4 Validation of plasmid promoters . . . 167
5.5 AAV quality control . . . 170
5.6 Western Blot optimisation . . . 172
5.7 Differentiating species by qPCR . . . 174
5.8 Differentiating species by IHC . . . 175

6.1 Pilot study design . . . 182
6.2 Surgical outcomes . . . 187
6.3 Pilot study ERG results . . . 192
6.4 Pilot study OCT . . . 196
6.5 Pilot study cSLO . . . 199
6.6 CRX IHC . . . 201
6.7 OPN1LW IHC . . . 203

7.1 Design of the study . . . 220
7.2 Surgical outcomes . . . 225
7.3 Effect of AAV on retinal structure . . . 229
7.4 Representative cSLO for AAV.OPN mice . . . 231
7.5 Representative cSLO for AAV.CRX mice . . . 233
7.6 Particle counts of cSLO BAF images . . . 234

7.7 Pigmentary changes on cSLO IRAF 235
7.8 Mesopic ERG function at 3 weeks 237
7.9 Mesopic ERG function at 9 weeks 240
7.10 Photopic ERG function at 3 weeks 243
7.11 Photopic ERG function at 9 weeks 246
7.12 OMR function in photopic conditions 248
7.13 Gene expression in injected eyes 250
7.14 Transgenic CRX expression in RPE 252
7.15 Transgenic CRX expression at PNW10 254
7.16 Endogenous CRX expression at PNW10 255
7.17 Transgenic CRX expression at PNW14 256
7.18 Transgenic OPN1LW expression at PNW10 258
7.19 Endogenous cone opsin expression at PNW10 259
7.20 Transgenic OPN1LW expression at PNW15 261

List of Tables

1.1 Summary of the human opsins 5
1.2 Achromatopsia genes 10
1.3 Achromatopsia gene therapy trials 16

2.1 ERG protocol 41
2.2 Rho genotyping primers 43
2.3 AAV transfections 56
2.4 Iodixanol gradients 58
2.5 Titering primers 60

3.1 Summary of the cpfl mouse mutations 76

4.1 Cone cell qPCR primers 125
4.2 Negative control wells 128
4.3 Statistical details of cone cell qPCR 138

5.1 Optimised ICC antibodies 166
5.2 AAV plasmid transfections 168
5.3 AAV titres 169
5.4 Non-homologous interspecies primers 173

6.1 Surgical exclusion criteria 188

7.1 Baseline ERG characteristics across treatment groups 242

B.1 List of reagents 313

C.1 List of all commercial kits 314

D.1 List of hardware 316

E.1 List of software 317

F.1 List of blocking serums 318
F.2 List of primary antibodies 318
F.3 List of all secondary antibodies 319
F.4 List of recombinant proteins 319

G.1 List of prepared solutions 320

H.1 qPCR primer pairs and optimisation 322

ABBREVIATIONS

AAV	Adeno-associated virus.
Ad	Adenoviral.
AF	autofluorescence.
ARVO	Association for Research in Vision and Ophthalmology.
B-actin	beta actin.
B-ME	B-mercaptoethanol.
BAF	blue laser autofluorescence.
BCA	bicinchoninic acid.
BDNF	brain derived neurotrophic factor.
BSA	bovine serum albumin.
BSG1	Basigin-1.
C57Bl/6	C57 Black 6 mouse line.
CBA	chicken β-actin.
CDS	coding DNA sequence.
cGMP	cyclic GMP.
ChIP	Chromatin immunoprecipitation.
CNG	cyclic nucleotide-gated.
Cnga3	cyclic nucleotide gated channel alpha-3.

CNTF	ciliary neurotrophic factor.
cpfl	cone photoreceptor function loss.
CRISPR	clustered regularly interspaced palindromic repeats.
Crx	Cone-rod homeobox gene.
cSLO	confocal scanning laser ophthalmoscopy.
cv	coefficient of variation.
DAPI	4',6-diamidino-2-phenylindole.
DIC	differential interference contrast.
dLGN	dorsal lateral geniculate nucleus.
DMEM	Dulbecco's modified Eagle's medium.
DMSO	Dimethyl sulfoxide.
dsDNA	double-stranded DNA.
DSMO	dimethyl sulfoxide.
ECL	enhanced chemiluminescence.
eNpHR	enhanced halorhodopsin.
ERG	electroretinography.
ERG	electroretinography.
EYFP	enhanced yellow fluorescent protein reporter protein.
FACS	fluorescence-activated cell sorting.
FBS	foetal bovine serum.
Gapdh	glyeraldehyde-3-phosphate dehydrogenase.

gDNA	genomic DNA.
GFP	green fluorescent protein.
GMP	good manufacturing protocols.
Gnat1	guanine nucleotide-binding protein subunit alpha transducin-1.
GPCR	G-protein coupled receptor.
HEK29T	human embryonic kidney 293T.
ICC	immunocytochemistry.
ICGA	Indocyanine green angiography.
IHC	immunohistochemistry.
IRC	irradiance response curve.
IRES	internal ribosome entry site.
LED	light emitting diode.
MACS	magnetic assisted cell sorting.
MB-H2O	molecular biology H2O.
MOI	multiplicity of infection.
mRNA	messenger RNA.
NADPH	nicotinamide adenine dinucleotide phosphate.
NFE2L2	nuclear factor (erythroid-derived)-like 2.
NGF	nerve growth factor.
NHP	non-human primate.

NMD	nonsense mediated decay.
NpHR	halorhodopsin.
Nr2e3	nuclear receptor subfamily 2 group E member 3.
Nrl	neural retina leucine zipper gene.
Nxnl1	nucleoredoxin-like-1.
OCT	optical coherence tomography.
OKN	optokinetic nystagmus.
OMR	optomotor response.
OPN1LW	long wavelength sensitive cone opsin.
Opn4	melanopsin.
ORF	open reading frame.
Otx	orthodenticle transcription factor.
PBS	phosphate buffered solution.
PCR	polymerase chain reaction.
PDE	phosphodiesterase.
PEI	polyethylenimine.
PFA	paraformaldehyde.
PI	propidium iodide.
PND	postnatal day.
pRGC	photosensitive retinal ganglion cells.
RdCVF	rod derived cone viability factor.
REML	restricted maximum likelihood.
rER	rough endoplasmic reticulum.

RFLP	Restriction fragment length polymorphism.
Rho	rhodopsin.
$Rho^{-/-}$	Rhodopsin knockout.
RIPA	radio-immunoprecipitation assay buffer.
RNases	ribonucleases.
Rorβ2	retinoid-related orphan receptor β2.
RP	retinitis pigmentosa.
RPE	retinal pigment epithelium.
RPKM	reads per kilobase transcript per million mapped reads.
rRNA	ribosomal RNA.
Rxry	retinoid X receptor (gamma).
SDS	sodium dodecyl sulfate.
SDS-PAGE	sodium dodecyl sulfate polyacrylamide gel electrophoresis.
SEM	scanning electron microscopy.
siRNA	small interfering RNA.
SLO	scanning laser ophthalmoscope.
Tbp	TATA-binding protein.
TKO	"triple knock-out".
Trβ2	Thyroid-hormone receptor β2.
Trx	thioredoxin.
TrxR	thioredoxin reductase.
WB	Western Blot.

WPRE	Woodchuck hepatitis virus post-transcriptional regulatory element.

1

INTRODUCTION

1.1 The Retina

This introduction will focus on cone photoreceptors, which are located in the retina of the eye. The retina is a layered photosensitive structure inside the eye that enables the perception of light. The cornea and crystalline lens focus light onto the retina, thereby exciting light-sensitive opsin proteins in the photoreceptor cells of the outer layer. This initiates the chemical phototransduction cascade and the propagation of an electrochemical signal to the brain. The inner retina derives nutrients and oxygen from the retinal vasculature. The retinal pigment epithelium (RPE) supports the metabolism of the photoreceptors in the outer retina.

1.1.1 Photoreceptors

Photoreceptors are cells that convert visible light into chemical signals. There are three types of photoreceptors: rods, cones and photosensitive retinal ganglion cells (pRGC). Rods and cones allow the conscious sensation of vision and mediate tectal visual reflexes; pRGC largely contribute to circadian rhythm regulation. Rods are distributed throughout most of the retina and enable both low-light and peripheral vision. Cones, however, are concentrated at the central foveal region in humans where they enable high acuity vision and colour

perception. In mice, there is a smaller population of cone photoreceptors and no centrally concentrated foveal region [1].

The outer nuclear layer contains the cell bodies of rods and cones. The outer limiting membrane delineates the cell body from the inner and outer segments of the photoreceptor. The inner segment contains mitochondria as well as rough endoplasmic reticulum (rER) for light-sensitive opsin protein assembly. The inner and outer segments are linked by a thin connecting cilium. The cilium traffics opsin proteins to the membrane discs of the outer segment, where they couple with the chromophore, 11-cis retinal. The outer segments of photoreceptors interdigitate with the RPE and the RPE replenishes 11-cis retinal; as well as delivering nutrients and clearing metabolites.

1.1.2 The phototransduction cascade

In the dark, the photoreceptor maintains a resting state of depolarisation at approximately -40mV. This *dark current* is maintained by two separate currents that contribute to the membrane potential. Primarily, a steady state of potassium efflux through non-gated K^+ channels. A second, smaller, influx of Na^+ continues through cGMP-gated channels and is maintained by an excess of cGMP at rest in scotopic conditions. The resulting negative membrane potential opens voltage-gated Ca^{2+} channels. Subsequent glutamate release causes inhibitory downstream signalling; glutamate depolarises *off* bipolar cells and hyperpolarises *on* bipolar cells. Photoreceptor projections to the outer plexiform layer allow synaptic signalling to the bipolar cells.

In the light, the photoreceptor is hyperpolarised to -60mV. As outlined in Figure 1.1, when a photon of light strikes the 11-cis retinal chromophore, it undergoes photoisomerisation to all-*trans* retinal. This causes a conformational change in the coupled opsin protein. Opsin is a G-protein coupled receptor (GPCR) and the change activates transducin protein, which in turn activates phosphodiesterase (PDE). PDE breaks down intracellular cyclic GMP (cGMP), triggering the cGMP-gated Na^+ channels to close. The unopposed outflow of K^+

causes hyperpolarisation of the cell to-60mV and closure of voltage-gated Ca^{2+} channels. The resulting drop in calcium-mediated glutamate release excites the *on* bipolar cells and hyperpolarises *off* bipolar cells. Down-stream bipolar signalling is integrated in ganglion cells and relayed to the central visual pathways of the brain. Finally, the phototransduction cascade is deactivated in photoreceptors by enzymes that halt the activity of PDE and replenish cGMP levels.

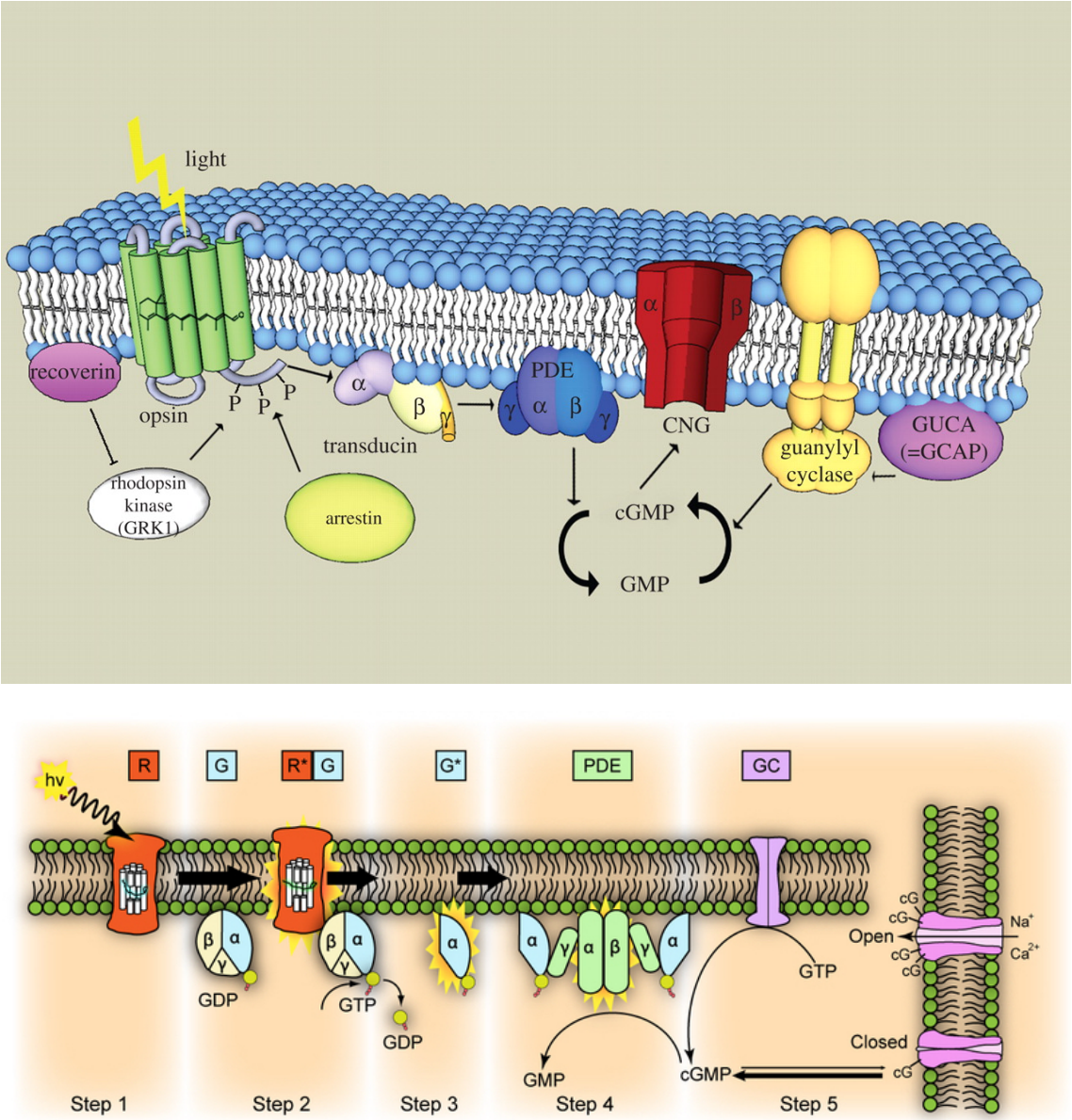


Figure 1.1 | Phototransduction

Top: Enzymes of the rod phototransduction cascade. *(L to R):* Light strikes membrane-bound opsin and induces a conformational change that sequentially activates the transducin and phosphodiesterase (PDE) enzymes. Degradation of cGMP substrate by PDE closes cGMP-gated channels (CNG) and cellular hyperpolarisation. The steps of cone phototransduction are similar to these well-characterised steps in rods.
Adapted from Larhammer et al, 2009 [2]

Bottom: Steps of phototransduction. 1) Excitation of chromophore by a photon on light causing photoisomeration and conformation change of opsin protein. 2) Opsin catalyses activation of transducin enzyme. 3) Transducin activates phophodiesterase (PDE) enzyme. 4) PDE hydrolyses cGMP. 5) Reduced levels of cGMP causes closure of Na^+ channels
Available under common licence. Jason J. Corneveaux

1.1.2.1 Opsins

Opsins are a class of proteins found in multiple cell types; a smaller subset of opsins are found exclusively in photoreceptors. Table 1.1 show five of the relevant retinal subtypes: rhodopsin, melanopsin and the short, medium and long-wavelength cone opsins. Their structure consists of seven transmembrane domains, a binding site for the chromophore 11-cis retinal and a catalyst site for transduction activation.

The outer segment of rod photoreceptors contains rhodopsin. It consists of covalently bound scotopic rhodopsin protein and the 11-cis retinal chromophore. Rhodopsin is exquisitely sensitive to light and enables vision in low-light environments via the rod pathway. The cone opsins are each expressed in a subpopulation of cone photoreceptors. The three different spectral sensitivities permit diverse colour perception. Cone opsins need greater photon excitation and have poor sensitivity in low light settings [3].

Table 1.1 | Summary of five of the human opsins.

Gene	Name	λ max	Colour	Chromsome	Exons	CDS length (bp)	Translation (aa)
OPN1LW	L-cone (red-cone) opsin	557 nm	yellow	Xq28	6	1095	364
OPN1MW	M-cone (green-cone) opsin	527 nm	green	Xq28	6	1095	364
OPN1SW	S-cone (blue-cone) opsin	420 nm	violet	7q32.1	5	1047	348
OPN2 (RHO)	Rhodopsin	505 nm	blue-green	3q22.1	5	1047	348
OPN4	Melanopsin	480 nm	NA	10q23.2	11	1437	478

1.1.2.2 Cyclic nucleotide-gated channels

cyclic nucleotide-gated (CNG) channels are located in the outer segments of photoreceptors. Photoreceptor Na^+ influx occurs through CNG channels and maintains resting state depolarisation by opposing K^+ efflux [4]. cGMP binding modulates CNG channel activity. The channels have a complex heterotetramer structure comprised of alpha and beta subunits [5]. The subunit amino acid sequences vary between photoreceptor class, but always assemble in a 3:1 ratio of alpha to beta subunits [6, 4]. As outlined, PDE mediated hydrolysis of cGMP results in closure of the CNG channels during phototransduction.

1.1.3 Transcription factors in cone photoreceptors

1.1.3.1 Orthodenticle transcription factor

There are two subtypes of the orthodenticle transcription factor (Otx) transcription factor; Otx1 and Otx2, which both exert an effect on downstream factors such as Cone-rod homeobox gene (Crx). Homozygous Otx2 mutations in mice are lethal due to failed development of the rostral brain [7].

1.1.3.2 Cone-rod homeobox transcription factor

Crx (also known as LCA7, CORD2, OTX3, CRD2) is an Otx-like homeodomain nuclear transcription factor. The human *CRX* maps to 19q13.3, within the *CORD2* locus [8]. It is related to the *Otx1* and *Otx2* homeodomain genes, but has diverged to specifically modulate photoreceptor and pineal gland development [8]. It is expressed in both cone and rod photoreceptors. Crx is also expressed in the inner nuclear layer of the retina in mammals [9, 10]. Crx is the earliest expressed photoreceptor marker in the developing retina and is turned on at E12.5 in the mouse, coinciding with rising *Otx2* expression [10]. In humans, it is turned on between approximately 9.5 and 10.5 weeks [10]. Temporal and spatial *Otx2* expression during later embryogenesis also helps define the photoreceptor layer by restricting the region of Crx signalling [7, 11].

Mutations in human *CRX* causes Leber congenital amaurosis type III and cone-rod dystrophy 2 [12, 11]. Heterozygous *CRX* mutations are inherited in an autosomal dominant pattern and may act through a dominant negative mechanism [12, 11].

In mice, *Crx* modulates photoreceptor gene expression through a number of pathways. *Crx* binds directly to promoters of specific photoreceptor genes [8, 11]. The homeodomain feature of the CRX tertiary protein structure binds the DNA sequences containing the TAAGCT or TAATCC sequences [7]. These sequences are present in the upstream promoter sequences of the genes of the phototransduction cascade[11].

Interaction with other transcription factors is also necessary in order to modulate gene expression. In rods, *Nrl* and *Nr2e3* interact with Crx [7]. In cones, retinoid-related orphan receptor β2 (Rorβ2) interacts with Crx to modulate S-opsin expression [7] and Thyroid-hormone receptor β2 (Trβ2) synergistically modulates M-ospin expression [7]. It appears that Trβ2 actively differentiates a subset of developing cones into M-cones and photoreceptor functions have been shown to be diminished in patients with Thyroid hormone deficiency [13].

Crx positively auto-regulates expression by binding to its own 5'-UTR and promoter. There are two Crx-binding sites in the promoter region of Crx [14]. Reduced Crx expression in Crx knockout mice results in reduced Crx-promoter driven *LacZ* reporter expression [11, 8]. $Crx^{-/-}$ mice have 31% of wt *LacZ* expression whereas $Crx^{+/-}$ mice have 57% of wt *LacZ* mice [11]. Thus, any decline in Crx expression in a disease state may initiate a negative spiral of further Crx down-regulation.

Furthermore, Crx binds to promoter sequences of other inter-related transcription factors. Chromatin immunoprecipitation (ChIP)-qPCR assays on $Crx^{-/-}$ mice shows Crx binds and positively regulates NeuroD1, neural retina leucine zipper gene (Nrl) and other factors [14, 7]. Crx negatively regulates Trβ2 and retinoid X receptor (gamma) (Rxry) by binding to their promoters. Finally, after being activated by Otx2 binding to the Crx promoter, Crx itself binds to the promoter of Otx2 to feedback regulate itself [7]. Crx knock-out mice show early deficits in cone photoreceptor differentiation and maturation [15]. Induced pluripotent stem cells (iPSC) derived from human corneal or iris cell types can be re-differentiated into photoreceptor type cells by exogenous expression of *CRX* in culture [16, 17].

CRX is important in the mature human adult retina, although it has been characterised in less detail than during retinal development. Adult patients with inherited *CRX* mutations typically show under-developed photoreceptor outer segments and subsequent photoreceptor degeneration [8], although this is likely

a consequence of insufficient *CRX* activity during embryogenesis, rather than adulthood insufficiency.

CRX RNA is expressed in both the INL and ONL of adult human retinas on *in situ* hybridisation [10] and this finding has been replicated elsewhere [8]. This is strong evidence that a sustained baseline of CRX expression is required for normal adult photoreceptor and retinal function. This is consistent with *in situ* hybridisation and IHC findings in adult wild type mice (p80), showing both ONL and INL expression of *Crx* [10]. No experiments have yet used conditional-knockout *Crx* mice to test the effects of *Crx* insufficiency in adult mice after normal photoreceptor development.

Hennig et al [7] provide a detailed review of CRX and the associated gene network regulating photoreceptors.

1.2 Achromatopsia

Achromatopsia is a rare (1 in 30 000) congenital visual impairment defined by diminished or absent cone photoreceptor function [18]. Patients have severely reduced visual acuity ($\approx$ 20/200), nystagmus and photophobia [19, 18]. Causative autosomal recessive mutations affect genes of the cone phototransduction cascade; *CNGA3* [20], *CNGB3* [21], *GNAT2* [22, 23], *PDE6H* [24], *PDE6C* [25] or *ATF6* [26] (Table 1.2). Nevertheless, there is still a subset of patients with no identified mutations [27]. Patients typically show complete cone function loss, as shown by absent cone-isolating electroretinogram (ERG) recordings. An incomplete phenotype occurs more rarely, but is not clearly correlated to the underlying mutation [19]. Achromatopsia affects all three classes of colour vision. As such, it is distinguishable from blue cone monochromatism and red-green colour-blindness, in which there remains a subpopulation of functional cones [18].

Since CNGA3 was the first gene identified in 1998 [20], five other autosomal genes have been reported. The exonic sequences of all the genes causing

achromatopsia are under 2500bp, making them all small enough to package in an Adeno-associated virus (AAV) gene therapy vector. This work has already begun and is detailed elsewhere [28].

A notable population of achromatopsia patients lives on the South Pacific island of Pingelap [29]. A genetic bottleneck following Typhoon Lengkeki in 1775 created a founder effect and over 10% of the island population had complete achromatopsia. The story is notably popularised in The Island of the Colourblind by Neurologist Oliver Sacks. The causative CNGB3 mutation was first genotyped in 2000 [30].

Table 1.2 | Achromatopsia genes.

Gene	Gene ID	Nucleotide ID	Full name	Location	Size (kB)	Exons	CDS length (bp)	First reported	Prevalence [27]	Prevalence [19]
CNGB3	54714	NM_019098.4	cyclic nucleotide gated channel beta 3	8q21.3	170	19	2430	[21]	47%	87%
CNGA3	1261	NM_001298.2	cyclic nucleotide gated channel alpha 3	2q11.2	53	9	2085	[20]	23%	5%
GNAT2	2780	NM_005272.3	G protein subunit alpha transducin 2	1p13.3	16.6	9	1065	[22] [23]	2%	0%
PDE6C	5146	NM_006204.3	phosphodiesterase 6C	10q23.33	69	22	2577	[25]	Unknown	Untested
PDE6H	5149	NM_006205.2	phosphodiesterase 6H	12p12.3	9.6	4	252	[24]	Unknown	Unknown
ATF6	22926	NM_007348.3	activating transcription factor 6	1q23.3	197.8	17	2013	[26]	Unknown	Unknown

1.2.1 Pre-clinical rescue of animal models

The first successful rescue of an animal model of achromatopsia was reported in 2007. Murine Gnat2 coding DNA sequence (CDS) was expressed in the Gnat^{cpfl3} mouse model of achromatopsia. The transgene was packaged in AAV5 under control of a fragment of human red cone opsin gene promoter that expresses in L/M-cones but not S-cones [31]. The vector was delivered by subretinal injection at a 10^{10} titre. Restoration of cone function was demonstrated on ERG and in a optomotor response (OMR) test . This work showed proof of principle for gene therapy to restore electroretinography (ERG) function in achromatopsia caused by a missense mutation.

Two canine models of Cngb3 achromatopsia (missense in exon 6 or full deletion of Cngb3) were rescued using an AAV5 vector expressing human CNGB3 [32]. The transgene was expressed with the same fragment of human red-green opsin promoter. The vector was delivered by trans-vitreal subretinal injection at a 10^{12} titre. Treatment improved both photopic electrophysiological response and functional vision in a photopic maze task. This study was the first to rescue a larger cone-enriched model of achromatopsia and confirmed that a human CDS could rescue an animal model. Animals receiving treatment after a year of age gained little benefit, raising questions about the therapeutic age range for delivery the vector.

The *cpfl5* mouse model of achromatopsia results from a missense mutation in exon 5 of the Cnga3 gene [33]. The first gene therapy rescue of this Cnga3 mouse model gave a modest improvement in scotopic ERG and showed improved complex visually-mediated water maze behaviour [34]. This study showed that restored cone signalling was integrated into higher cortical function, not just tectal-mediated optomotor responses. This model of Cnga3 achromatopsia also had a slow cone degeneration; a phenotype that is not typical in human patients. AAV rescue largely prevented cone degeneration and the transgene normalised disrupted cone opsin trafficking.

This Cnga3 knockout mouse model was rescued using mouse *Cnga3* CDS under control of a 0.5kB mouse short wavelength opsin promoter [34]. 10^9 genome particles packaged in mutant AAV5^{Y719F} capsid was injected into the subretinal space of 2 week old mice. A modest cone ERG rescue was observed, approximately 40-50%. The full magnitude of the ERG rescue may have been masked because the mouse blue opsin promoter only expresses in S-cones and only a subset of L-cones. To explore this question further, the same research group subsequently rescued the same Cnga3 mouse model using a ubiquitous chicken β-actin (CBA) promoter [35]. This modified *Cnga3* vector restored cone ERG response to 80% of wild type just three weeks after treatment. This difference in promoter efficacy in restoring normal electrophysiology to all subpopulations of cones may be a significant factor in the human trials currently underway.

Carvalho et al ([36]) were the first to explore the therapeutic age window for gene therapy in achromatopsia. A mouse model caused by a premature stop codon was rescued with human *CNGB3* transgene packaged in an AAV8 capsid. The use of a Cone Arrestin fragment promoter resulted in universal expression in all cone subpopulations, an important improvement on earlier studies. The subretinal vector rescued retinal function, as tested by ERG, at a range of ages. Yet the poor visual reflexes in mice treated at later ages suggests an optimal therapeutic window at a younger age. The limited benefit at later ages may be amblyopia related or a result of slow retinal degeneration in this model.

Two serendipitous discoveries of day blindness in unrelated Awassi sheep flocks in Israel yielded two new large-animal cone-rich models of Cnga3 achromatopsia. Both models — a premature stop codon [37] and a missense mutation [38] — were rescued using the same human PR2.1-CNGA3 vector described by Komaromy et al [32]. As expected, photopic ERG was restored. Treated animals were also able to use the restored cone function to navigate a maze in photopic conditions. Interestingly, AAV-delivered mouse CDS also provided the same size rescue effect.

All of the above studies delivered the vector by subretinal injection. The outer retina is difficult to efficiently target from intravitreal injections and the risk of off-target transduction of inner retinal cells is increased in an intravitreal approach.

These animal studies have explored if developed visual pathways of adults benefit from gene therapy. Yet, evidence for the plasticity of the mammalian cone visual pathways exists elsewhere. Two related papers explore cone opsin gene therapy in naive visual systems. Human L-opsin gene therapy produces trichromatic vision in Old World dichromatic adult primates. Multifocal-ERG and modified Cambridge Colour test show new spectral sensitivity in treated monkeys [39]. Secondly, a vector containing rat M-opsin restored M-cone ERG function in a rat model of congenital S-cone monochromatism [40]. Thus, naive visual systems can integrate and interpret novel cone spectral sensitivity. Although, in humans, the potential for integration and its relationship to older age at treatment is unknown.

1.2.2 The human retina in Achromatopsia

Achromatopsia fundi may often only be identified by an abnormal foveal reflex, yet cone structure and density — as measured with adaptive-optics SLO — may vary by genotype. Studies of *CNGB3* and *CNGA3* patients show variable foveal appearance on OCT and cone density [41, 42]. Notably, patients with Gnat2 have almost normal cone density [43, 41]. Thus, the causative mutation and cone count may limit the magnitude of any treatment effect.

Approximately half of adult *CNGB3* patients have some degree of foveal hypoplasia [19, 44, 42]. Foveal cone density is less than normal adults, yet cone inner segments remain intact. The cone mosaic pattern is often irregular. Cones can also have abnormal reflectance patterns [19]. However, cone density has not been shown to decline with age and is likely a static feature throughout life [42]. This metric is likely not an important influence or barrier to selecting patient age in a trial.

All these studies on cone mosaics rely on manual quantification of cones by

an unreported number of human observers, raising questions about their reliability. Inter-observer variability has been observed during manual counts of cones in adaptive-optics SLO images [45]. Inter-observer variability [46, 47] and test-retest variability [48] are well-known pitfalls in scientific techniques that should be reported and considered. These cone mosaic studies fail to check for, and adjust, any such sources of variability. The observed differences between groups may not be a true phenomenon and further study is required.

In one study, adult patients with congenital achromatopsia viewed photopic and scotopic visual stimuli; fMRI recorded the cortical retinotopic representations of foveal function [49]. The study controlled for the effects of achromatopsia nystagmus on vision. Normal controls demonstrated a region of V1 occipital cortex dedicated to the cone-specific fovea. In achromatopsia patients, this same rod-free foveolar representation in the visual cortex was activated by rod-isolating visual tests. Rod visual pathways had monopolised the unused cortical space normally dedicated to cones. Thus, absence of cone visual input during childhood development remodels and re-allocates retinofugal pathways.

A separate study showed that female carriers of blue cone monochromatism demonstrated reduced foveal cone counts. Yet, these same patients had a normal amount of cortical space dedicated to foveal input [50]. Potentially, gene therapy treatment rescuing just a small subpopulation of foveal cones in a child could allow normal cone-mediated visual pathway development.

1.2.3 Gene therapy clinical trials for Achromatopsia

As of June 5th, 2017, there are four registered clinical trials for gene therapy in achromatopsia (Table 1.3). All trials are using human CDS driven by cone-specific promoter fragments and packaged in an AAV capsid. Patients receive delivery of the vector by subretinal injection after vitrectomy. None of the constructs include regulatory elements that increase transgene expression such as WPRE [51] or intron/exon splice sites. All trials are phase I/II and the primary outcome measure is safety. Secondary outcomes include visual acuity, electrophysiology and colour

vision function.

The safety profile will initially be tested in adult patients. Then three of the trials have plans to include patients as young as 6 years in later groups. Thus, the trials will examine differences in cone rescue effect between age groups. If the pattern observed in the animal trials holds true, there may be a difference in benefit due to patient age at time of treatment.

Mutations in *CNGA3* and *CNGB3* account for 70% of mutations in human patients. Both are channel proteins that insert into the cell membrane. It is unclear whether the CNG-naive immune system of null mutation achromatopsia patients may react to transgene proteins expressed in the cell membrane. The modest pro-inflammatory stimulus of retinal surgery and viral capsid proteins may potentiate the effects of these transmembrane proteins. None of the clinical trials have publicly recorded plans to for routine immunosuppression in treated patients.

Table 1.3 | Achromatopsia gene therapy trials.

ClinicalTrials identifier	Gene	Vector	Promoter	Dose	Locations	Company
NCT03001310	CNGB3	AAV2/8-hCARp.hCNGB3	Human cone arrestin fragment	Unreported low dose: $\leq$ 1x10e10 vgp (n=3) Intermediate dose: $\leq$ 5x10e10 vgp (n=3) High dose: $\leq$ 1x10e11 vgp (n=3)	United Kingdom	MeiraGTx UK II Ltd
NCT02610582	CNGA3	rAAV.hCNGA3	Unreported		Tubingham, Germany	STZ eyetrial
NCT02935517	CNGA3	rAAV2tYF-PR1.7-hCNGA3 ('AGTC-402')	PR1.7 (Fragment L-Opsin pr)	Three doses, unspecified	USA, Israel	Applied Genetic Technologies Corp
NCT02599922	CNGB3	rAAV2tYF-PR1.7-hCNGB3	PR1.7 (Fragment L-Opsin pr)	Three doses, unspecified	USA	Applied Genetic Technologies Corp

There has been one other therapeutic trial registered for achromatopsia (ClinicalTrials.gov number, NCT01648452). Six CNGB3 achromatopsia patients received intraocular implants that released levels of ciliary neurotrophic factor (CNTF) [52]. CNTF provides neuroprotection to rod and cone photoreceptors in degenerative retinal disease [53]. Concurrent treatment with intravitreal CNTF in a canine model of CNGB3 achromatopsia potentiated gene therapy rescue. CNTF improved ERG rescue in older animals, overcoming a notable inability of gene therapy alone to benefit the majority of dogs over 1 year of age [54]. Limited evidence suggested that CNTF pretreatment de-differentiated the cone photoreceptors and allowed CNGB3 protein assembly in the outer segments.

In the CNTF trial, no functional improvement in cone function could be detected. There are no current plans to include CNTF pre-treatment in any of the registered human gene therapy trials. This discussion may be reignited if the early trials show difficulty in rescuing cone function in older patients.

1.2.4 The future for Achromatopsia therapies

Animal trials have demonstrated that gene therapy can restore the electrophysiological function of cones. The three most common causative mutations (Cnga3, Cngb3 and Gnat2) have all been rescued [36, 34, 31]. Often by multiple groups using different vectors.

Cone ERG b-waves have never been fully restored to wild-type levels [36, 34, 31]. Cone subtype promoters that express in a partial subpopulation of cones appear to diminish the size of ERG rescue [34]. Regardless, any restored ERG function improves functional vision in optomotor or maze testing [34].

There is little evidence that cone density or appearance declines with age. This metric is unlikely to affect the therapeutic window [42]. Nonetheless, in a mouse model showing atypical cone degeneration, Cnga3 re-expression halted cell loss and corrected opsin mis-localisation [35].

The electrophysiological treatment effect is long-lasting; over 180 days in mice [36] and over 3 years in sheep [55]. The effect is maximal in younger animals

and more modest in older mice and dogs [32, 36]; making age an important consideration in study design. CNTF potentiates cone rescue in animals and is an example of the adjuvant therapies that may be needed to successfully treat older patients [56, 57].

Beyond electrophysiological rescue, what is the ability of cone photoreceptors to re-integrate into occipital cortical circuitry? Particularly outside the critical early years of visual pathway development. Adult patients may not see a benefit. Optimally, treatment would occur in childhood (under 6 years). Thus, allowing functional cones to direct retinofugal pathway development. In such young patients there could be extra technical challenges to the injection surgery.

Finally, what is the risk in a patient who is otherwise functioning day-to-day? Surgery and the potential immune response to gene therapy do carry risks. The current human trials and subsequent larger studies will need to prove the functional utility of any visual rescue.

1.3 Retinitis Pigmentosa

Inherited retinal diseases (IRD) are a family of diseases that generally refer to degenerative conditions that affect the outer retina. Mutation of a vital gene may also result in impaired light sensitivity or altered cellular metabolism. By definition, progressive loss of visual function occurs as the cells die [58, 12, 59].

Retinitis pigmentosa (RP) is an incurable IRD that affects approximately 1 in 4,000 people [59]. It arises from genetic mutations in rod photoreceptors. It is a rod-cone dystrophy, beginning with rod degeneration and the loss of night vision and peripheral vision [58, 12]. Rod death results in characteristic scattered pigmentary changes in the retina. The cone photoreceptors then undergo secondary degeneration. This secondary cell loss occurs despite the cones being genetically normal and is more debilitating because cones are responsible for central acuity and daytime vision, which is important for humans [60, 61, 62,

63].

RP can occur as a result of a sporadic mutation or from a variety of inheritance patterns. There are over 70 disease genes associated with retinitis pigmentosa (RP) and over 200 different affected genes are known to cause retinal degenerations RetNet [64]. Many thousands of different substitution, deletion, insertion and other mutations have been reported in human cases of RP.

The first genetic therapies for inherited retinal diseases are being trialled. Multiple clinical trials have demonstrated the safety of AAV vector in delivering gene therapy for inherited fundus dystrophies [65][66][67]. In our lab, pre-clinical retinal gene therapy for autosomal-dominant and X-linked RP have both been promising and phase 1 trials for the latter have begun. Also, at least five models of electronic retinal prosthesis are also being investigated in trials for end-stage RP [68]. There have been promising early results for both treatment modalities, yet this lengthy pre-clinical development and clinical trial process would need to be repeated for each disease gene. There does not currently exist a universal intervention to protect cone cells after the death of rod photoreceptors [63].

This heterogeneity of RP genotypes limits the ability of a single intervention to prevent all forms of rod cell death. Developing individualised gene or clustered regularly interspaced palindromic repeats (CRISPR) therapies to each disease gene and known mutation would be an expensive and lengthy process. As such, a common intervention to restore cone cell function and prevent cone cell apoptosis would be valuable. Such a broad treatment could be more widely applied than a narrow therapy targeting only a single mutant variant of RP. Although it would not address the loss of rod photoreceptors, it could potentially maintain central visual acuity and patient visual function.

1.3.1 Cone photoreceptor death

Degeneration of cone cell photoreceptors occurs via apoptosis in both human and mouse models of RP [69]. The mechanisms underpinning this apoptosis are

not completely understood. There are many prevailing theories, but recent studies have strongly implicated oxidative stress [70, 71, 72]. A second prominent hypothesis involves the loss of rod derived cone viability factor (RdCVF), which is a trophic protein thought to be required for cone survival [73, 74, 75]. Alternatively-spliced RdCVF may have antioxidant activity [75]. Authors have also suggested mechanisms of inappropriate microglial activation [76] or toxic agent release by dying cone cells [77].

1.3.1.1 Trophic factors

CNTF is a polypeptide hormone that promotes neuron outgrowth and synthesis of neurotransmitter in certain populations of neurons [78]. Early gene therapy work with Adenoviral (Ad) vectors demonstrated prolonged photoreceptor survival following intravitreal injection of a CNTF expressing Ad vector [79]. Treatment with exogenous CNTF has been shown to stimulate the regrowth of cone outer segments in the S334ter-3 transgenic rat model of RP [80, 81]. An ERG rescue effect was also observed. Similarly, intravitreal injections of an AAV vector expressing CNTF in the $Rho^{-/-}$ transgenic mouse model of RP provides rescue [53]. Rescue of cone ERG function and histological cone cell counts of cone photoreceptors occurred well beyond the normal time-point of cell death [53].

A single study has shown *CNTF* levels are up-regulated during the early stages of the rd1 and $Rho^{-/-}$ mouse models [82]. However, whilst exogenous CNTF supplementation is beneficial to cones, declining endogenous CNTF levels have not yet been demonstrated to correlate to the natural history of RP cone cell death.

1.3.1.2 Oxidative stress

RdCVF is a trophic factor expressed only in rods, not cones [83]. The thioredoxine RdCVFL is an alternative long splice of *Nxnl1* gene and plays an important role in redox functions. It is expressed in both cone and rod photoreceptors [83]. Both

splice forms are encoded by the *Nxnl1 (Txnl6)* gene.

Intravitreal injections of RdCVF protein rescues cone photoreceptors in the P23H rat model of RP [74]. The photopic B-wave and histological cone cell counts are both significantly improved at 6 months [74]. Similarly, over-expression of RdCVF by AAV.RdCVF injections rescues cone function and survival [84].

AAV-mediated nuclear factor (erythroid-derived)-like 2 (NFE2L2) expression in retinal cells prolongs cone photoreceptor survival in *rd1* mice [85]. This is consistent with broader work showing NFE2L2 over-expression rescues neurons [86]. *NFE2L2* is a transcription factor involved in regulating phase II detoxification and antioxidant enzymes [87]. The complex of genes involved in the antioxidant response — heme oxygenase-1 (HO-1), NAD[P] H:quinone oxidoreductase-1 (NQO1), superoxide dismutase (SOD) etc — contain an antioxidant response element (ARE) motif in the upstream promoter region [88]. *NFE2L2* binds to this ARE nucleotide sequence to activate this collection of genes involved in the antioxidant response [87].

1.3.1.3 Degeneration of cone outer segments and opsin mislocalisation

During cone photoreceptor death, cone outer segments shorten and cone opsin expression is down-regulated. Some or all of the remaining opsin proteins are mis-localised away from the shortened outer segments.

Outer and inner segments of cone cells degenerate early in rd1 mice and this finding has been replicated in limited studies of human retinas with RP. Opsin protein continues to be expressed in cone cell photoreceptors during degeneration in rd1 mice and RP humans [89, 90]. However, there is reduced expression of cone opsin during cone cell degeneration in multiple models of rod-cone dystrophies [62].

Opsins are mis-localised in both carriers and affected patients with RP X-linked mutations [91]. The opsins are instead located in the inner segments, cell bodies and plexiform layer. Cone opsin mislocalisation has also been shown

in mouse models of non-RPGR RP [62]; mis-localisation normally precedes cone photoreceptor cell death. In some models, although opsin is still present in the outer segment, it is also ectopically redistributed to the membranes of the remaining cell bodies, axons and cone pedicles [90].

Opsin mis-localisation is reversible in an $RPE65^{-/-}$ mouse model of retinal degeneration [92]. $RPE65^{-/-}$ $Rho^{-/-}$ double-knockout mice show no rod function and negligible cone electrophysiological function in the absence of normal chromophore. The mice also demonstrate malformed outer segments and mislocalised cone opsins [92]. In these mice, intraperitoneal injections of chromophore restore normal levels of cone response on ERG. Similarly, immunohistochemistry (IHC) analysis shows that cone opsins are correctly localised to the outer segments again. These findings of corrected opsin localisation and cone outer segment rescue were replicated in a different model of RPE65 mutation [93]. However, because rhodopsin appears to preferentially bind chromophore before cone opsins, both experiments relied upon $Rho^{-/-}$ cross-breeding to remove the natural presence of rhodopsin.

Similarly, cone photoreceptor rescue by administration of insulin to RP mice correlates with correct localisation of cone opsins to the outer segments once more [62]. The evidence suggests therefore that cone opsin mislocalisation might simply reflect a more general sign of cone stress, rather than being related to any specific gene defect.

It has been shown that inadequate aerobic glycolysis and consequent glucose metabolite insufficiency contribute to loss of cone photoreceptor outer segments [94]. Also, cone photoreceptor death correlates with down regulation of the Insulin-mTOR pathway modulating glucose metabolism [62]. The exact cause of outer and inner segment degeneration is unknown, but it is temporally related to mis-localisation or switching-off of opsins. We hypothesise that down-regulation of cone opsin expression is an early step that leads to outer segment loss by subsequent mechanisms.

1.3.2 Evidence of inactive cone cells

Inactive cone cells refers to cone photoreceptors that have down-regulated photosensitivity mechanisms. Despite no longer contributing to visual function, these cells may be reactivated. This potential for reactivation is most clearly demonstrated by halorhodopsin retinal gene therapy restoring visual responses [95]. Halorhodopsin is a bacterial photosensitive membrane channel. In a mouse model of rod-cone dystrophy, AAV vector gene therapy successfully transduced cone cells with Halo-rhodopsin, resulting in restoration of visual response.

LCA mouse models have also shown that down regulation of cone opsin mRNA, cone opsin mislocalisation and loss of the outer segment of photoreceptors may be reversed if the underlying pathology is treated [92]. Therefore, gene therapy to normalise the level of cone opsin expression could potentially a) restore visual function in cone cells and b) could interrupt apoptotic mechanisms.

1.4 Retinal gene therapy

Gene therapy is a therapeutic intervention for genetic disease involving the delivery of DNA into affected cells to act as a treatment [96]. The retina is an optimal target for gene therapy due to three features. The retina has easy surgical access for intravitreal and subretinal injections of therapy [97]. The blood-retina barrier creates partial immune privilege that reduces immune damage to injected vectors [98]. Visual testing and direct imaging of the target site allow convenient measurement clinical outcomes [99, 100]. Additionally, the variety of mutations underlying IRDs offer great scope for genetic targets.

1.4.1 Previous experiments exploring ectopic opsin expression

1.4.1.1 Halorhodopsin

Halorhodopsin NpHR is a light-activated chloride pump found in *Natronomonas pharaonis* bacteria. It can function in mammalian cells without the need for external cofactors; NpHR utilises the readily-available chromophore, all-*trans* retinal [101]. The pump operates on a millisecond timescale and can hyper-polarise cells with good temporal resolution. This feature could be applied therapeutically to diseased photoreceptors to supplement or replace the normal phototransduction cascade that causes photoreceptor hyperpolarisation.

The genetic sequence of halorhodopsin had been enhanced (eNpHR) to avoid intracellular aggregations or toxicity at high expression levels in mammalian cells [101]. The enhanced halorhodopsin (eNpHR) sequence was fused with enhanced yellow fluorescent protein reporter protein (EYFP) and placed under the control of one of three cell-specific promoters: human rhodopsin, human red-opsin or mouse cone arrestin. Cell-specific promoters avoid eNpHR expression in downstream non-photoreceptor retinal cells that could impair the flow of visual information. Busskamp et al [95] treated two mouse models of RP with these AAV vectors expressing eNpHR; the vectors activated cone retinal pathway and mediated visually-guided behaviour.

The two mouse models treated were a *Cnga3*$^{-/-}$ and *Rho*$^{-/-}$ double-knockout mouse (slow RD model) and the *Pde6b*^{rd1} (rd1) single-knockout mouse (fast RD model) [95]. Both models showed persistent expression of eNpHR and the fused EYFP reporter protein in cones up to eight months after treatment.

eNpHR-reactivated cone photoreceptors showed restoration of photocurrents during two-photon patch clamping of *ex vivo* retinal sections [95]. Light-evoked excitatory currents were also observed in ganglion cells, showing functional connections. Furthermore, eNpHR treated eyes performed better in OMR and light-dark box tests. Notably, eNpHR induces cone photosensitivity at longer

wavelengths (λ of 580nm) and requires a much higher intensity of light [95]; a potential barrier to human translation, alongside the obvious bacterial origin of the gene.

Busskamp et al [95] confirm that inactive cone photoreceptors exist in RP mice; they also show evidence for their existence in humans with RP. The paper demonstrates that these cones can be reactivated with photosensitive opsins. There may be a potential role for over-expression of endogenous mammalian opsin proteins in restoring photosensitivity.

1.4.1.2 Rhodopsin

Ectopic expression of human rhodopsin in mouse retinas has been shown to restore vision [102]. Unlike the halorhodopsin work, this paper is an example of optogenetic therapy; Rhodopsin was deliberately expressed outside native photoreceptors. The *Pde6b*^{rd1} mouse model was used and mice were treated with intravitreal AAV.RHO at PNW8-10, long after the photoreceptors were completely lost.

There was convincing widespread expression of Rhodopsin in the inner retina [102]. *Ex vivo* retina testing showed restoration of light response. dorsal lateral geniculate nucleus (dLGN) electrode testing showed integrated central signalling in response to visual stimuli. Furthermore, there was some evidence to suggest that ectopic rhodopsin expression mediated visually-guided behaviour.

Cehajic-Kapetanovic et al [102] give a clear demonstration of human opsin generating visual impulses in mice. The paper shows visual impulses, but the spatial resolution and complexity of this vision require further exploration. It is less likely that this ganglion-targeting approach could achieve good visual acuity because it bypasses the extensive signal processing circuitry of a normal retina.

1.4.1.3 Melanopsin

Melanopsin optogenetic therapy has been shown to restore functional vision in *Pde6b*^{rd1} mice [103]. Subretinal delivery of AAV2/8^{Y733F}.CBA.OPN4.IRES.DsRed

vector resulted in sustained melanopsin expression throughout the inner retina and inner plexiform layer; with correct melanopsin localisation to the membrane. Functional melanopsin was confirmed with multi-electrode array recordings on *ex vivo* retinal explants. Also, the pupil light reflex and light-avoidance tests were improved in treated eyes. Functional gains were sustained as long as 13 months. Melanopsin may be less immunogenic than eNpHR for vision restoration because it is an native protein.

1.5 Summary, hypothesis and objectives

The multi-stage retinal phototransduction cascade is well characterised in normal physiological conditions. The majority of historical work has focussed on rods because they constitute the majority of photoreceptors and are easier to identify and study [104, 105, 106, 107, 108]. More recent work has explored the differences in cone phototransduction [109, 110].

Recent work in animal models has explored cone phototransduction dysfunction in isolated cone pathologies such as achromatopsia [111, 112, 113, 114, 33, 115, 116, 117, 118, 119, 31, 25, 120]. However, the dysfunction of cone electrophysiology in complex rod-cone retinal diseases like RP is less well understood. Most of the molecular characterisation of cone photoreceptors in RP has focussed on mechanisms of cell death [62, 94].

The core hypothesis of this thesis is that, in RP, the loss of photosensitivity in cone photoreceptors occurs much earlier than cone cell death and is driven by down-regulation of select cone phototransduction genes. Furthermore, this loss of cone photosensitivity can be reversed by supplementing the cone photoreceptor transcriptome by exogenous over-expression of select cone phototransduction genes.

This thesis aims to:

- Characterise the cone phototransduction dysfunction in a novel mouse model of isolated cone blindness (*cpfl10*) that closely simulates human

achromatopsia. Thereby contributing to the evolving understanding of mammalian cone phototransduction (Chapter 3).

- Characterise the cone phototransduction dysfunction in an existing Rhodopsin knockout mouse model of Retinitis Pigmentosa (*Rho*$^{-/-}$). This will be achieved by measuring the magnitude and timing of changes in cone phototransduction gene expression levels. Then correlating these changes in gene expression to the changes in the structural and functional phenotype (Chapter 4).

- Identify one or more candidate cone genes for therapeutic over-expression in *Rho*$^{-/-}$ mice (Chapter 4).

- Develop and validate AAV gene therapy vectors containing the chosen candidate cone genes for therapeutic over-expression (Chapter 5).

- Optimise the techniques for subretinal AAV delivery and *Rho*$^{-/-}$ mouse functional testing in a small pilot study (Chapter 6).

- Determine whether either of the AAV gene therapy vectors improves or prolongs cone photosensitivity in *Rho*$^{-/-}$ mice (Chapter 7).

2

MATERIALS & METHODS

2.1 Animals

2.1.1 Overview

All animal experiments adhered to the Association for Research in Vision and Ophthalmology (ARVO) Statement for the Use of Animals in Ophthalmic and Vision Research and the UK Home Office guidelines. All animals were kept in a 12h light (<100lux)/12h dark cycle, with food and water available *ad libitum*. Pups were weaned from breeding cages at postnatal day (PND) 21. Adult mice were defined as at least six weeks old (PND42). Breeding pairs and triplicates were optimally matched between PND42 and PND56.

2.1.1.1 Cone photoreceptors in mouse models

In rodents, photoreceptors are approximately three-quarters of all neurons [1]. Cone photoreceptors comprise 3% of the mouse photoreceptor population as counted in whole retinal mounts using differential interference contrast (DIC) microscopy [121]. In humans, cones represent 5% of the total retinal cell population [122]. Mice do not possess the cone-rich fovea in the human retina; cones are sparsely distributed across the whole retina. Mice are dichromats and

express only short-wavelength (S-) and medium-wavelength (M-) cone opsins. Mouse S-opsin spectral sensitivity λ-max is 359nm and mouse M-opsin spectral sensitivity λ-max is 511nm [123].

Trichromacy was a later development in the old world primate lineage [124]. The medium-wavelength cone opsin gene on the X-chromosome was duplicated to create a tandem head-to-tail copy number variant. The duplicate opsin sequence subsequently developed an alternative spectral sensitivity through point mutations.

Cone photoreceptor subtypes in mice vary by vertical retinal topography, but there is no nasal-temporal variation. Most cones express both S-opsin and M-opsin [125]; a substantial difference from human cones which only possess one of three mutually-exclusive single spectral sensitivities. In mice, the dorsal retina contains a sub-population of cones that express only M-opsin. The levels of M-opsin mRNA and protein tapers from the dorsal to ventral retina [125]. However, S-opsin mRNA and protein is relatively constant throughout the retina, yet terminates abruptly in the far dorsal retina. The addition of two cone spectral sensitivities increases the range of detectable light and improves contrast in different lighting environments; the mouse spectral sensitivity is optimised for a nocturnal and low-light environment [125].

These substantial differences in cone subtypes, their distribution and function are limitations in using a mouse model to study human cone diseases. However, the short mouse life-cycle, small size, easy functional testing and rapid degeneration timeline in RP models are benefits. Furthermore, in mice, there are a number of techniques for identifying cone photoreceptors and for monitoring these cells *in vivo*.

2.1.1.2 pR6.5.Lacz reporter line

Transgenic expression of a β-Galactosidase reporter under control of 6.5kB red-green promoter fragment allows post-mortem X-Gal staining of cones [126]. The LacZ reporter is fully expressed in both cone types. β-galactosidase reporter is

considered a stronger reporter than fluorescent proteins and highlights a greater cone count on IHC than intrinsic GFP signals. LacZ reporter cannot be used to monitor cone survival *in vivo* and was not utilised in this thesis.

2.1.2 B6$^{TgOPN1LW\text{-}EGFP}$ mouse strain

C57BL/6J$^{TgOPN1LW\text{-}EGFP85933Hue}$ mice express enhanced green fluorescent protein (GFP) only in the cone photoreceptors and are herein known as B6$^{TgOPN1LW\text{-}EGFP}$ mice. The existing mouse model was obtained from another research group [127]. The transgene comprises 6.8 kb of human genomic DNA containing the 5' regulatory sequence of the human opsin 1 long-wave-sensitive gene joined to the coding sequence for enhanced green fluorescent protein followed by a *Myc* epitope tag and an intron and polyadenylation signal from SV40. Transgenic mice exhibit green fluorescence specifically of cone cells of the visual retina. In this transgenic line, EGFP-expressing cells reproducibly constitute a small proportion of cone cells in the ventral retina and the majority of dorsal retinal cone cells [127]. The fluorescent signal in these mice is sufficient for fluorescence-activated cell sorting (FACS) and can also be monitored *in vivo* using scanning laser ophthalmoscope (SLO).

These mice suffer an unintended cone dystrophy due to the insertion locus of the GFP transgene potentially disrupting a gene implicated in human North Carolina macula dystrophy [128].

2.1.3 C57Bl/6 mouse strain

The C57 Black 6 mouse line (C57Bl/6) inbred mouse strain was obtained commercially from the Jackson Laboratory. Age at delivery was typically PND35 to PND56.

2.1.4 Cone Photoreceptor Function Loss mouse strain

A local colony of inbred mice (129S6/SvEvTac origin), that had been bred in isolation for over a decade, were found to have completely absent light-adapted

ERG responses. The original breeding pair was delivered from *DNAX USA* in 1997. We investigated the inheritance and genetic basis of this phenotype of cone photoreceptor function loss (cpfl). This strain is herein referred to as CPFL.

2.1.5 129S6 SvEvTac strain

A colony 129S6/SvEvTac origin without retinal disease, used as closely-related wild type controls in experiments of the CPFL mouse colony.

2.1.6 Triple knock-out mouse strain

$Cnga3^{tm1Biel}Opn4^{tm1Yau}Gnat1^{tm1Clma}$ mice are herein known as "triple knock-out" (TKO) mice. They have no retinal light sensitivity due to targeted disruption of the cone, rod and melanopsin visual pathways [129]. The existing mouse model was a kind gift from Prof Rob Lucas at the University of Manchester. The cyclic nucleotide gated channel alpha-3 (Cnga3) gene was disrupted by replacement of exon 7 with a neomycin resistance cassette. The endogenous melanopsin (Opn4) locus was disrupted by the insertion of a cassette containing tau-lacZ and floxed PGK-neo immediately downstream of the endogenous start codon. The guanine nucleotide-binding protein subunit alpha transducin-1 (Gnat1) gene was disrupted by a neomycin resistance cassette replacing a genomic fragment containing exons 4 and 5 and parts of exons 3 and 6. Although it is appreciated that some residual rod function may remain despite absence of Gnat1 [130].

2.1.7 Nrl-L-EGFP mouse strain

$B6^{Tg(Nrl\text{-}EGFP\ 1Asw}$ mice express enhanced GFP only in the rod photoreceptors [131] and are herein known as Nrl-L-EGFP mice as described in the original article. The existing mouse model was obtained from another research group. A 2.5 kb upstream segment of the mouse Nrl gene (from -2408 to +115; GenBank AY526079) that includes four sequence regions that are conserved between mouse and human drives expression of EGFP . This line contains three copies of the EGFP gene.

2.1.8 Rho$^{-/-}$ mouse strain

Rho^{tm1Phm} mice (herein known as Rhodopsin knockout (Rho$^{-/-}$) mice) have target disruption of the Rhodopsin gene, resulting in rod degeneration [132]. A neomycin cassette under the control of a polymerase II promoter was inserted at codon 135 in exon 2. RT-PCR analysis of total RNA derived from ocular tissue showed an absence of downstream transcript in homozygous mutant mice. A lack of encoded protein was determined in homozygous mutant mice via immunohistochemical staining of retinal sections [132].

2.1.8.1 RP phenotype

ERG in the Rho$^{-/-}$ mouse is stable until P52 (7.5 weeks) [62]. Then, a rapid decline in cone photoreceptor function occurs over 4-5 weeks [62, 133]. *In vivo* SLO imaging of fluorescent retinal cells shows stable GFP expression until the complete loss of ERG function . Degeneration of cone cell fluorescence occurred for the next 6 weeks after the loss of cone cell ERG. By week 17, there are almost no cone cells visible on SLO [62, 133]. Total loss of GFP expression occurs at approximately 17 weeks. Histology confirms reduced count of fluorescent cone cells at both 11 and 17 weeks. Another paper lists that the major phase of cone cell death in the Rho$^{-/-}$ model is between PW17 and PW45 [62]. Although, cones have been identified up to PW80.

2.1.8.2 Cross-breeding Rho$^{-/-}$ with GFP lines

The Rho$^{-/-}$ mice were cross-bred in turn with Nrl-L-EGFP and B6$^{TgOPN1LW\text{-}EGFP+/-}$ mice. As detailed in chapter 4 and chapter 6, these new transgenic lines demonstrated rod degeneration and also expressed reporter protein in either the rod photoreceptors or a subpopulation of cone photoreceptors.

2.2 *In Vivo* procedures

2.2.1 Anaesthesia and mydriatics

Mice were anaesthetised by a single intraperitoneal injection containing a mixture of 0.8mL of Vetalar (100mg/ml Ketamine Hydrochloride, Boehringer Ingelheim) and 0.5mL Rompun (20mg/ml Xylazine, Bayer) suspended in 8.6mL of 0.9% normal saline. Using a 29-gauge needle and syringe, an intraperitoneal injection was delivered whilst holding the mouse scruffed and supine. The mouse was administered 0.1mL of this induction mixture per 10 grams of body weight (for a dose of 80mg/kg Ketamine and 10mg/kg Xylazine).

For longer procedures, such as ERG, anaesthetised mice were administered a further 0.1mL of anaesthetic mixture by subcutaneous injection.

Pupil dilatation was achieved with tropicamide (Mydriaticum 1%; Bausch & Lomb, Kingston-on-Thames, UK) and phenylephrine (phenylephrine hydrochloride 2.5%; Bausch & Lomb) eye drops.

To reverse the effects of anaesthesia after a procedure, mice were injected with a mixture of 0.4 mL of Antisedan (5mg/ml Atipamezole, Zoetis) suspended in 9.6mL of 0.9% normal saline. The mouse was subcutaneously administered 0.1mL per 10 grams of mouse body weight (for a dose of 2mg/kg Atipamezole), thereby reversing the effects of the Xylazine - but not Ketamine - by competitive antagonism.

2.2.2 Subretinal injections

2.2.2.1 Preparation

The AAV viral vector was defrosted from the -80°C freezer on the day of the surgery and diluted in sterile PBS to the appropriate titre. The mouse was weighed, anaesthetised and the pupils were dilated as described in section 2.2.1. Proxymetacaine hydrochloride 0.5% (Bausch & Lomb) eye drops were also applied for topical anaesthesia. The mouse was positioned in a customised foam mould to insulate body temperature and facilitate surgical access.

The globe was stabilised by grasping the superior rectus muscle with toothed

titanium forceps (WPI). A syringe-mounted 33G needle (TSK laboratory, The Hague, Netherlands) was used to pierce the inferonasal peripheral cornea to create a self-sealing anterior chamber paracentesis. This decompression of the eye facilitated the later subretinal injection of AAV vector without reflux.

2.2.2.2 Delivery of vector

A 6mm circular glass coverslip (VWR International, East Grinstead, UK) was positioned on a viscous coupling gel (Viscotears liquid gel, 0.2mg/g polyacrylic acid; Alcon Laboratories Ltd, Camberley, UK) covering the cornea. This covering prevented cataract formation, but also altered the refraction of the eye; the fundus was then visualised using an operating microscope (Leica Biosystems; Figure 2.1.

A Nanofil 10μL syringe (Precision instruments) was assembled with the Nanofil 35G beveled needle (WPI) and flushed with sterile phosphate buffered solution (PBS) to check the seal. 1.5μL of PBS sham or AAV vector at the chosen titre was then drawn up into the syringe. The globe was again stabilised by grasping the superior rectus with forceps. The injection needle was advanced through the superior sclera, choroid and RPE to reach the subretinal space. Once the full bevel of the needle was visible in the subretinal space, the needle was held steady and the forceps were discarded. The syringe plunger was depressed to deliver the vector and create a hemiretinal detachment. The needle was then retracted and antibiotic eye drops (Chloramphenicol 0.5%; Bausch & Lomb) placed on the cornea; the eye was then covered in viscotears to prevent eye desiccation during recovery.

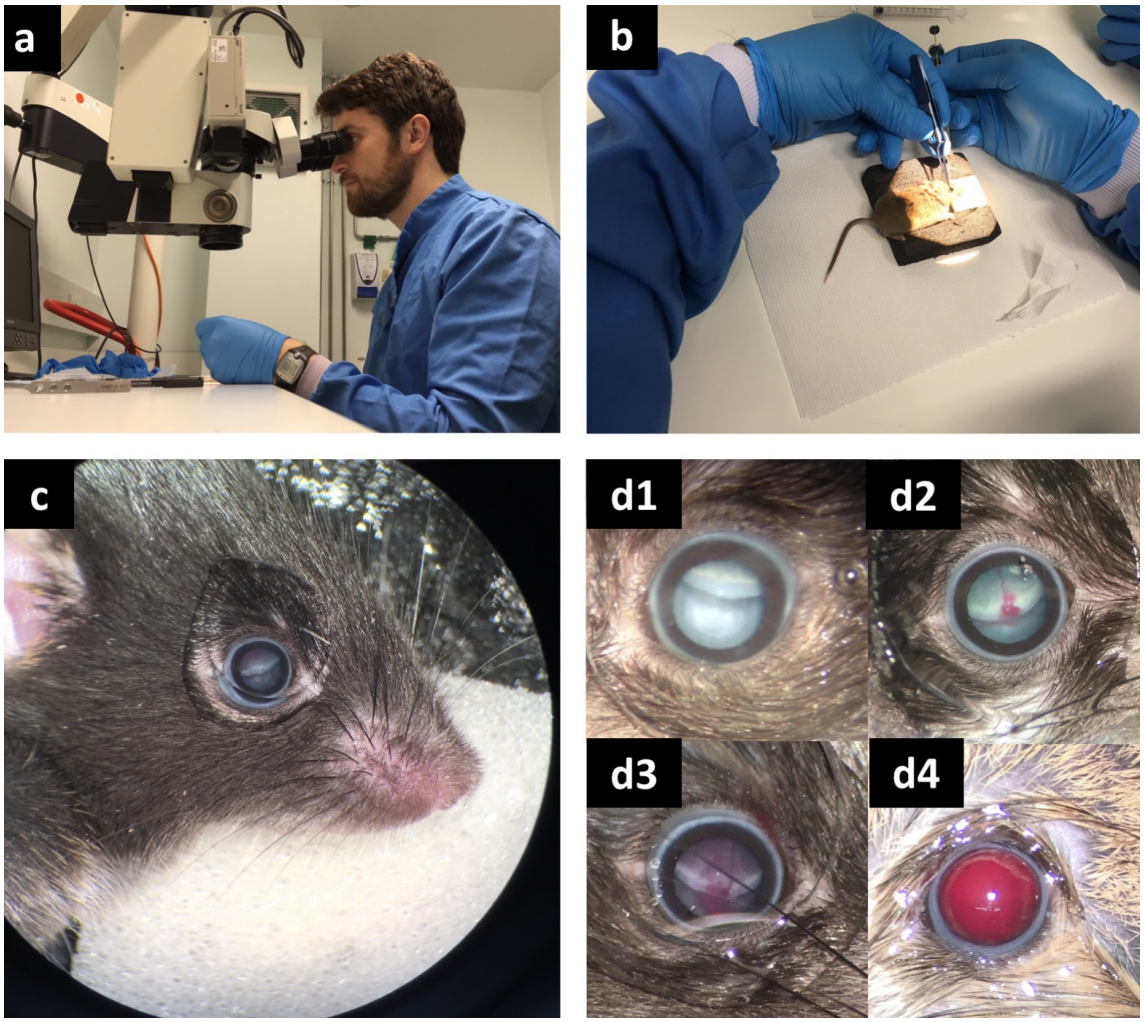


Figure 2.1 | Subretinal injections. **a,** An operating microscopy was used for magnification during surgery on the anaesthetised mouse **(b)**. **c,** The glass cover slip and viscous coupling gel allowed a clear view of the retina . An optimal injection produced a bleb of subretinal fluid without bleeding **(d1)**, although a small amount of epiretinal haemorrhage **(d2)** was permitted. Large subretinal haemorrhages **(d3)** or large vitreous or anterior chamber haemorrhages **(d4)** were excluded.

2.2.2.3 Cleaning injection equipment

To ensure cleanliness and prevent proteinaceous obstruction of the injection system, syringes and needles were cleaned after every subretinal injection. The syringe and needle were flushed with water; then flushed and incubated with diluted enzymatic cleaner (Medichem international Ltd). The syringes and needles were flushed and soaked in diluted disinfectant (Medichem international Ltd); then washed in water and air dried before assembly.

2.2.3 Confocal scanning laser ophthalmoscopy

The mouse was weighed, anaesthetised and the pupils were dilated as described in section 2.2.1. The effects of subretinal AAV injections in mice were observed using the 488nm autofluorescence (AF), 790nm Indocyanine green angiography (ICGA) , and 820nm reflectance modes of a Spectralis HRA confocal scanning laser ophthalmoscopy (cSLO) (Heidelberg Engineering, Heidelberg, Germany). Viscous coupling gel and customised afocal 3.2mm contact lenses (Cantor+Nissel) prevented corneal desiccation and standardised imaging optics. In studies comparing treated and untreated eyes, the same afocal contact lens was swapped between eyes to standardise quantitative comparisons.

All quantitative images were unnormalised and recorded with a standard technique. In reflectance mode, the image was first centered on the optic nerve head. The dioptric focus was used to localise the photoreceptor layer, as represented by the highest reflectivity. The AF and 790nm modes were used to image the photoreceptor layer. For standardised quantitative comparison, images were captured at 60% 70%, 80%, 90% and 100% detector sensitivity.

2.2.3.1 Phenotyping mice using SLO

$B6^{TgOPN1LW\text{-}EGFP+/-}$ and $Rho^{-/-\ B6TgOPN1LW\text{-}EGFP+/-}$ mice were phenotyped for GFP expression using a SLO (Heidelberg). Pupils were dilated with Tropicamide 1% and Phenylephrine 2.5% twenty minutes before examination. Mice were conscious and immobilised by scruffing during SLO. The retinal anatomy was visualised and fluorescent cells identified.

2.2.3.2 Correlation of PCR and SLO

GFP status identified on polymerase chain reaction (PCR) genotyping fully correlates with SLO phenotyping in a sample of 70 mice. Future litters of mice were only checked using PCR genotyping (subsection 2.3.2).

2.2.4 Optical coherence tomography

Optical coherence tomography captures three-dimensional images of the retina using low-coherence interferometry of infrared light. The mouse was weighed, anaesthetised and the pupils were dilated as described in section 2.2.1. optical coherence tomography (OCT) was imaged concurrently with cSLO as the Spectralis HRA cSLO (Heidelberg Engineering) performed both imaging modalities. Viscous coupling gel and customised afocal 3.2mm contact lenses (Cantor & Nissel) prevented corneal desiccation and standardised imaging optics. As described in section 2.2.3, the image was centered on the optic nerve head. All images were collected using automatic real time (ART) averaging. The section density, orientation and ART of scan patterns were customised to include a high-definition linear scan, a radial scan and a high-density grid volumetric scan (see table 2.2.4). The 30°lens was then used to collect a second high-density grid volumetric scan; images captured on the 30°lens were segmented and analysed by commercial software.

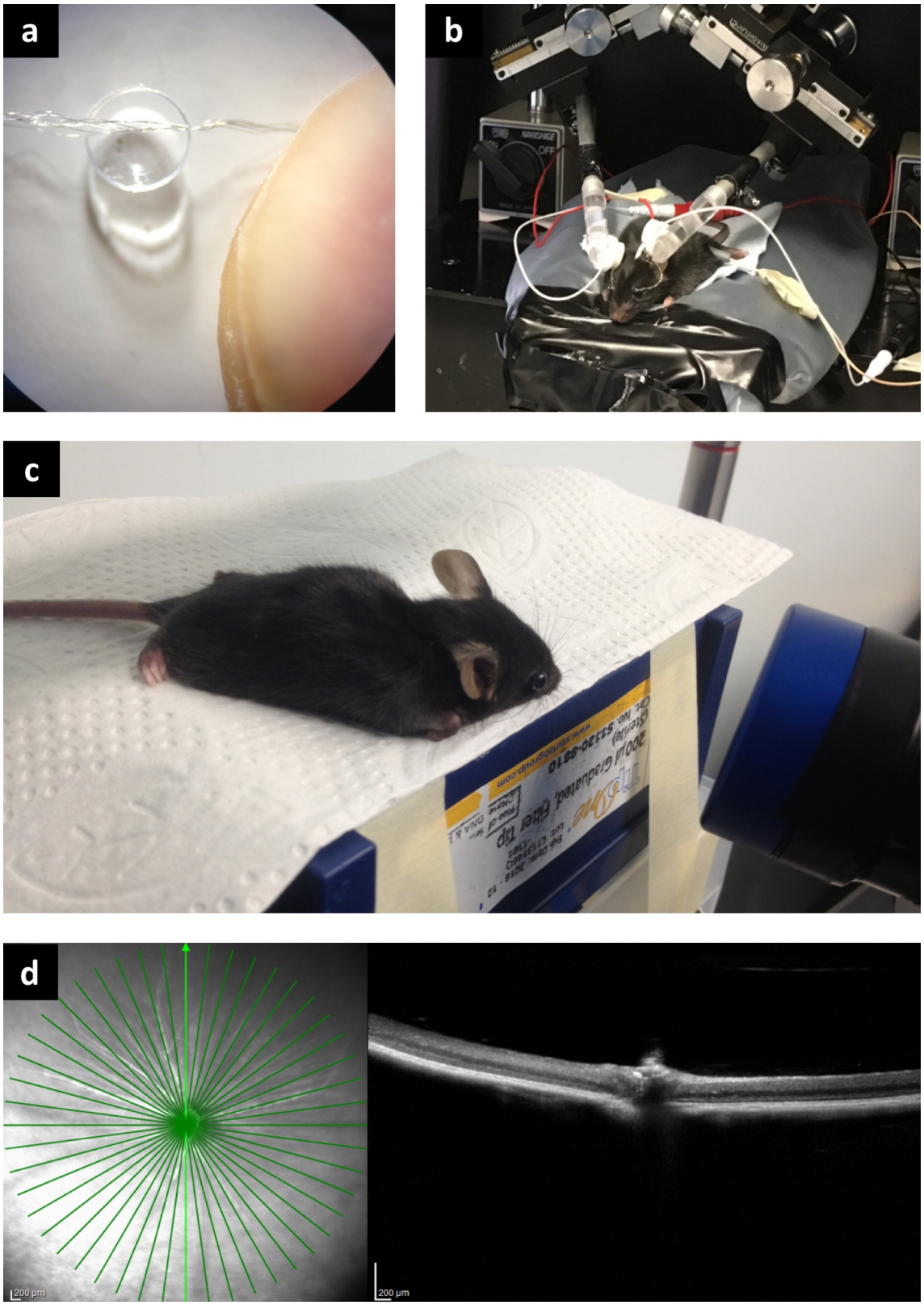


Figure 2.2 | Functional testing. **a,** ERG electrode-lens units were freshly created before each ERG test **(b)**. **c,** During cSLO or OCT testing, anaesthetised mice prepared with contact lenses were positioned in front of the cSLO/OCT lens (blue lens visible in right of image). **d,** *En face* cSLO and cross-sectional OCT images were captured.

2.2.5 Optomotor response

A custom optomotor system was produced, consisting of a rotating cylinder that allowed rotation speed to be specified. The cylinder was lined with a square-wave grating pattern of vertical black and white stripes. In response to this moving repetitive stimulus pattern, mice display smooth pursuit eye movements in the direction of rotation, followed by rapid saccadic movement in the opposite direction. This eye movement is known as optokinetic nystagmus (OKN). optokinetic nystagmus (OKN) can be measured using other testing set-ups not detailed here. The OMR head movement follows a similar pattern as OKN; a smooth head pursuit of the rotating grating, following by a rapid return to neutral position. This OMR movement can be quantified and used as a measure of visual function.OMR head movement follows the same pattern and can be used as a measure of visual detection.

The drum was cleaned with 70% ethanol between mice. The initial spatial frequency of the grating pattern was 0.1 cycles per degree. To isolate cone responses, mice were light-adapted and placed on an elevated platform in the cylinder under an overhead bright white light ($\sim$ 1000 lumens). The animal was allowed 1 minute to explore its stationary surroundings before testing commenced.

Each experimental technical replicate consisted of 1 minute of rotation in each direction, divided into 30 second alternating periods. Technical replicates were repeated 3 times for each animal. An overhead digital video camera recorded the response of the animal to the stimulus. OMR was quantified during later video playback by a single assessor blinded to treatment. The average OMR derived from all three technical replicates.

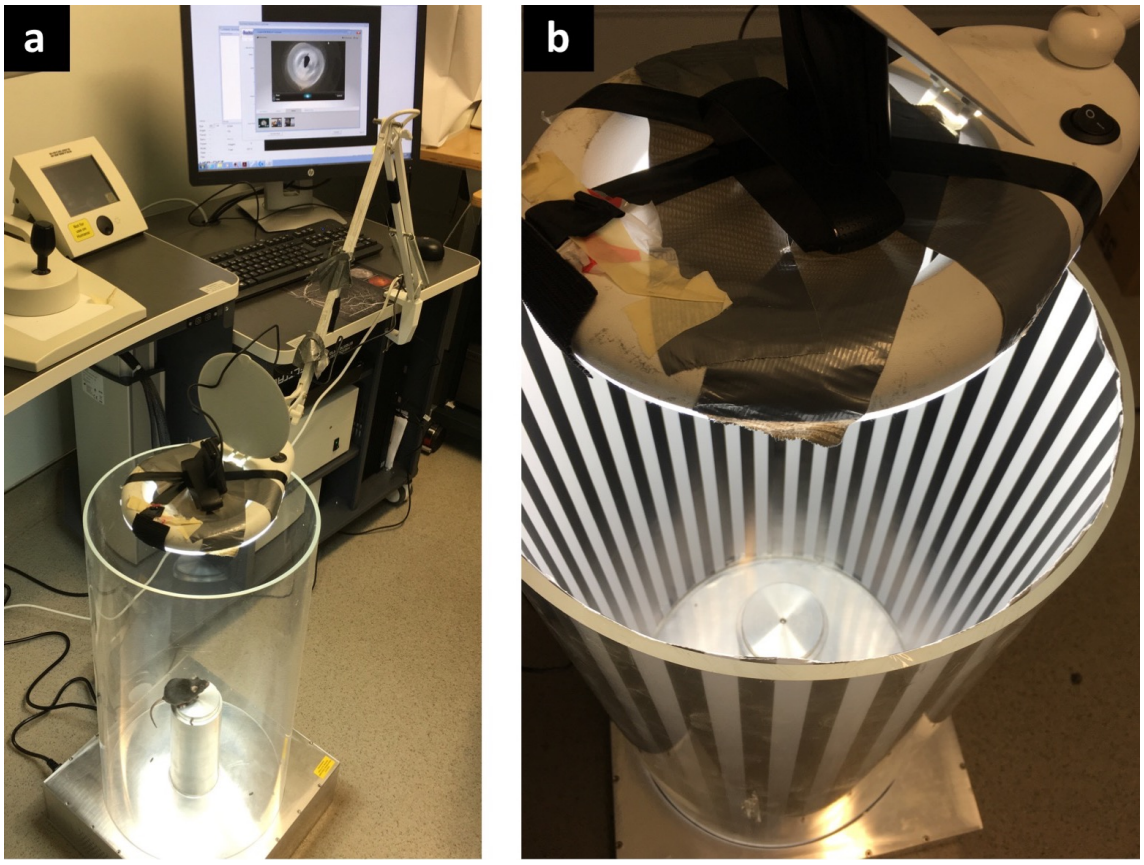


Figure 2.3 | OMR testing. a, Mice were positioned on an elevated test platform inside of rotating perspex drum lined with a spatial frequency grating. **b,** An overhead camera captured head-tracking behaviour and was scored by an observer.

2.2.6 Electroretinography

Electroretinography (ERG) records the electrical response of the retina generated by photoreceptors, inner retinal cells and ganglion cells in response to light stimulus. Full field ERG does not isolate specific regions of the retina, but is technically simpler and quicker to perform.

The mouse was weighed, anaesthetised and the pupils were dilated as described in section 2.2.1. The mouse was positioned on a body-temperature heat mat. Subcutaneous ground and reference electrodes were placed in the flank and scalp. Lens-electrodes were positioned on the cornea using coupling media (Hypromellose 1%; Alcon) and the mouse was positioned at the a testing light source (Colordome Electroretinography machine; Diagnosys LLC).

Table 2.1 | ERG protocol.

Step	Background (cd.m.s)	Type	Frequency	Intensity (cd.m.s)	ISI (secs)	Sweeps
–	*Overnight dark adaptation at 0cd.m*					
1	0	Single	0.5	0.0001	4	9
2	0	Single	0.5	10	30	4
3	0	Continuous	5	0.01	0.5	30
4	0	Continuous	7	0.01	0.5	30
5	0	Continuous	20	0.01	0.5	30
6	0	Continuous	5	10	0.5	30
7	0	Continuous	7	10	0.5	30
8	0	Continuous	20	10	0.5	30
–	*10 minutes light adaptation at 30cd.m*					
9	30	Single	0.5	0.3	1	20
10	30	Single	0.5	1	1	20
11	30	Single	0.5	3	1	20
12	30	Single	0.5	10	1	20
13	30	Single	0.5	25	1	20
14	30	Continuous	5	10	0.5	30
15	30	Continuous	7	10	0.5	30
16	30	Continuous	20	10	0.5	30

ISI: Inter-stimulus interval

2.2.6.1 Creation of electrodes

Custom electrode-lens constructs were produced the day before each ERG test (see Figure 2.2. A custom pair of flat-closing pliers soldered with a 3mm metallic ball bearing hemisphere produced optically-clear contact lenses from a sheet of Aclar embedding (Honeywell international). Two equatorial radial incisions were made using Vannas scissors (Surgitrac) and the wires of a DTL plus corneal electrode (Diagnosys LLC) threaded into the lens.

2.2.6.2 Testing protocol

Testing protocols for ERG can be customised to isolate and explore different aspects of cone and rod function across a wide dynamic range of stimulus. In this protocol (Table 2.1), mice were dark-adapted overnight. The testing began with a scotopic phase that isolated rod and mixed rod-cone response. Then, after a 10 minute light adaption step, testing examined isolated cone function.

2.3 Molecular techniques

2.3.1 Extraction of DNA from tissue

2.3.1.1 Low fidelity genomic DNA from ear clips

Mouse ear clips were added to 50nM NaOH and then heated to 96°C for an hour to dissolve the tissue. The mixture was then vortexed and, after centrifugation, was neutralised with 1M HCl. The aliquoted supernatant was then diluted fivefold with molecular biology H2O (MB-H2O) before PCR based genotyping.

2.3.1.2 High fidelity genomic DNA from tails

Higher purity genomic DNA (gDNA) was extracted from mouse tails using a commercial DNA mini kit (QIAamp DNA mini kit, Qiagen). Whole tail samples were collected from euthanised mice using scissors cleaned with ethanol. Tails were frozen at -20°C until use. 20-25g of defrosted tail tissue was cut and weighed, mixed with buffer and incubated overnight with proteinase K (QIAamp DNA mini kit, Qiagen). The enzyme was then heat inactivated and the lysed sample mixed with ethanol. The mixture was transferred into a silicon spin column, avoiding particulate contamination. The sample was centrifuged, washed with buffer and then eluted in MB-H2O. Spectrophotometry (Nanodrop, Thermo scientific) determined purity and concentration before storage at -20°C.

2.3.2 Polymerase chain reaction

PCR is a versatile technique for exponentially copying and manipulating DNA. A heat resistant bacterial polymerase enzyme uses nucleotide triphosphate substrate to repeatedly copy a short genetic sequence; termed *amplicon*.

Custom oligonucleotide primer pairs are designed *in silico* for the target sequence. To assist in cloning, restriction sites can be added to either end of the sequence. Approximately 10μM concentrations of each forward and reverse primer are combined with the DNA template (e.g. plasmid) and commercial enzyme master mix (Nonagon) in MB-H2O.

A commercial thermocycler (BioRad) heat activates the polymerase enzyme

Table 2.2 | Rho$^{-/-}$ genotyping primers.

Forward primers		Reverse primers		
Name	**Nucleotide sequence (3'-5')**	**Name**	**Nucleotide sequence (3'-5')**	**Amplicon**
Ex2RHO FW	AGGTTAGAGCTGGAGGACTG	Ex2RHO RC	TAAGACTGATTGGACCATTC	394bp
		Pol2neo	TTCAAGCCCAAGCTTCGCG	139bp
GFP FW	CAATTAAGAGATCAGGTAGTGT	GFP RC	AGTTCACCTTGATGCCGTTCTT	641bp

for 3-5 minutes. Then, the mixture undergoes 30 or more cycles of custom heating and cooling phases. Each cycle begins with a denaturing phase, when reagents are heated to 95°C to break bonds between DNA strands. During the annealing phase, the mixture is then cooled to between 50-65°C, depending upon primer property. This allows primers to bind the denatured DNA. The elongation phase then allows the polymerase enzyme to copy the target DNA amplicon. The elongation phase varies in duration depending upon the base pair length of the amplicon. Sequential cycles of these phases results in a base-2 exponential increase in target sequence.

2.3.2.1 Splice PCR by overlap extension

PCR can also combine two DNA fragments. Combinations of promoter, transgene or regulatory elements can be spliced together. The resulting spliced sequence can be ligated into a plasmid backbone in a single reaction. This approach overcomes the need to create new restriction sites in the plasmid for each element between introduced.

Primers for both template amplicons are designed *in silico*. An overlap region of approximately 30 base pairs is created for the two adjacent ends of each template. The overlap region should have a similar melt temperature to the terminal primers. This is an important consideration for the annealing temperature in the final splice PCR reaction.

The two template amplicons are then amplified using normal PCR and purified as described in 2.3.3. The concentration of each is determined by spectrophotometry (2.3.4). The equimolar ratio of template amplicons determines starting concentrations in the splice reaction. Both templates are

combined with the terminal primers and enzyme with substrate (PCR master mix, Nonagon). A thermocycler (T100 Thermal cycler, BioRad) is then again used to amplify the target sequence; adjusting the annealing temperature as explained earlier.

2.3.2.2 Genotyping using PCR

To confirm GFP status, diluted gDNA was added to a master-mix before PCR testing. The mix contained 2xImmomix Red, MB-H2O and the GFP forward and reverse primers (Table 2.2). The final solution underwent thermal cycling of 10 min at 95°C; 30 cycles of 10 sec at 95°C (denaturing phase), 30 sec at 55°C (annealing phase) and 30 sec at 72°C (elongation phase); followed by 10 min at 72°C (final elongation).

To confirm $Rho^{-/-}$ status, diluted gDNA was added to a master mix before PCR testing. The mix contained 2xImmomix Red, MB-H2O and the forward and reverse primers (Table 2.2) for the wild-type Rho gene. A further forward primer was added to detect mutant Rho allele (knock-out). The final solution underwent thermal cycling of 10 min at 95°C; 30 cycles of 10 sec at 95°C (denaturing phase), 30 sec at 58°C (annealing phase) and 30 sec at 72°C (elongation phase); followed by 10 min at 72°C (final elongation).

Agarose gel electrophoresis was used to identify amplicons in the PCR product. Amplicon size was measured against a standardised ladder to confirm the presence of GFP (641bp). Mutant Rhodopsin allele ($Rho^{-/-}$) produced a 394bp product, whilst the wild-type rhodopsin amplicon was 139bp.

2.3.3 Electrophoresis and gel extraction

The digested transgene insert and pAAV.CAG.GFP.WPRE.ITR plasmid were compared against a commercial DNA ladder on 1% Agarose gel to confirm digestion (Figure 5.3). The insert and vector gel bands were excised and extracted using a column-based commercial kit (Qiagen) before re-suspension.

2.3.4 Spectrophotometry

DNA concentration was determined by spectrophotometry using NanoDrop spectrophotometer (Thermo Scientific). The ratio of absorbance at 280nm/260nm was examined, with a ratio of 1.7 to 1.9 indicating acceptable purity.

2.3.5 Dideoxynucleic acid sequencing of sequence

gDNA was amplified using PCR and the target gene confirmed with agarose gel electrophoresis as detailed subsection 2.3.3. The remaining PCR product was purified using a commercial kit (PCR purification kit, Qiagen) according to the manufacturer's instructions and eluted in MB-H2O. Spectrophotometry confirmed DNA concentration greater than 100g/μL. Forward and reverse primers were diluted to 3.2μM with MB-H2O and 3μL of each dilution was added to gDNA aliquot. Samples underwent commercial fluorescent dideoxynucleic acid sequencing and the results were analysed with Geneious v8.0 software.

2.3.6 Extraction of RNA from dissociated retinal cells

Retinal cones labelled with GFP or other fluorescent reporter proteins can be isolated by first dissociating the harvested retina and then performing fluorescence-activated cell sorting (FACS).

2.3.6.1 Dissociation of retinal cells

$B6^{TgOPN1LW\text{-}EGFP}$ mice were sacrificed by cervical dislocation and death was confirmed by decapitation. After enucleation, the neurosensory retina was dissected from the eye in room temperature 0.01M PBS. The dissected retinas were placed into Papain (Sigma-Aldrich) prepared with 0.005% DNase; Papain is a cysteine protease that efficiently and less destructively isolates cells from tissue. After incubation at 37°C for 10 minutes, cell clumps were broken apart by gentle pipetting and then pelleted by centrifugation at 300g for 5minutes. The supernatant was discarded and the cell pellet re-suspended in PBS. The cells

were mixed with propidium iodide (PI), a cell viability marker that can only bind to DNA where the cell membrane is disrupted and hence identifies dying cells.

2.3.6.2 Fluorescence-activated cell sorting

Dissociated retinal cells on ice were transported by bicycle to the Old Road campus in Headington for FACS; an experienced technician operated the machine (Beckman Coulter CyAn ADP LX). The FACS machine line was primed with PBS before loading a small pilot sample of dissociated retinal cells into the machine. The pilot results were plotted as a two-dimensional scatter of cell fluorescence. A fluorescence intensity threshold ('gate') was manually defined for sorting the remaining cells. The final binary fluorescence threshold was typically maintained at 2×10^1 units for reproducibility. After sorting, the fluorescent and non-fluorescent cells were stored in PBS on ice and transported back to the laboratory. The same day, sorted GFP positive cells were processed for mRNA as detailed in subsubsection 2.3.7.2.

2.3.7 Extraction of RNA whole retinal tissue

2.3.7.1 Harvesting of whole mouse retinal tissue

The bench space, Vannas scissors and forceps were cleaned with RNase-Zap before processing each mouse. Animals were sacrificed by cervical dislocation and death was confirmed by decapitation. Both eyes were enucleated using forceps and washed first in PBS before dissection in fresh PBS. Under an operating microscope, the cornea was punctured with a 30-gauge needle and the cornea excised using Vannas scissors. The crystalline lens was extruded and the retina was blunt dissected away from the scleral-choroidal tissue and transferred into RNAlater for storage at -80°C.

2.3.7.2 mRNA extraction from tissue

The lab bench and tools were treated with RNase Zap. The manufacturer's instructions for the RNeasy mini kit were followed (QIAgen, Manchester, UK).

Retinal tissue was removed from RNAlater and homogenised in a lysis solution of B-mercaptoethanol (B-ME) and chaotropic buffer. Passing the solution ten times each through a 25-gauge and 30-gauge needle optimised homogenisation. After centrifugation, the supernatant was treated with 70% ethanol to optimise binding. The solution was then bound to a silica-gel-membrane spin column by centrifugation. Membrane impurities were removed by centrifugation with a second buffer. DNase was added to degrade contaminant DNA, before further wash steps with buffer. The RNA was eluted in water.

2.3.7.3 RNA reverse transcription to cDNA

Eluted retinal RNA was reverse transcribed to cDNA using the Superscript III synthesis system (Life technologies, Paisley, UK). The manufacturer's instructions were used with modification. An RNase inhibitor, a disulphide-bond reducing agent and nucleoside triphosphates were suspended Mg-balanced buffer. Retinal RNA and Oligo dT primer were added to this buffer suspension. Superscript reverse transcriptase enzyme was added before incubation at 50 °C for 50 minutes. After terminating the transcription reaction, remaining RNA was enzymatically digested. cDNA was purified for PCR using the QIAquick PCR purification kit (QIAgen, Manchester, UK). As per instructions, cDNA solution was mixed with an ethanol buffer and centrifuged through a silica-gel-membrane spin column. After multiple wash steps with buffer to remove impurities, the cDNA was eluted in MB-H2O.

2.3.8 Quantitative PCR

2.3.8.1 Primer design

Oligonucleotide primers for cone cell qPCR were designed using Geneious software version 7 (http://www.geneious.com; [134]). The following eight genes are involved in the mouse cone phototransduction cascade:

- Medium-wavelength-sensitive opsin (Opn1mws)
- Short-wavelength-sensitive opsin (Opn1sws)
- Cone arrestin (Arr3)
- Cone-rod homeobox transcription factor (Crx)
- Phosphodiesterase 6h (Pde6h)
- Cyclic nucleotide gated channel alpha-3 (Cnga3)
- Cyclic nucleotide gated channel beta-3 (Cngb3)
- Guanine nucleotide binding protein a-transducing activity polypeptide (Gnat2)

The housekeeper genes beta actin (B-actin) and glyeraldehyde-3-phosphate dehydrogenase (Gapdh) were used as controls. Primers for the rhodopsin (Rho) gene were also included to allow PCR validation of mouse models. Target and control genes were imported from the NCBI Gene and Nucleotide databases. Primers were designed using Primer3 software [135] to be 18-22 nucleotides in length and have a product length of 200 base pairs (Table 4.1). Melt temperature was kept close to 60°C by maintaining a GC content of 45% - 55%. Primers were designed to span an intron to minimise genomic DNA contamination. To ensure cross-hybridisation or self-dimerisation would not occur during the qPCR experiments, primers for these genes were carefully designed with specific 3'-ends, such that polymerisation would only occur to amplify a specific product.

2.3.8.2 Sanger sequencing of cGFP transgene

gDNA was amplified using PCR and the target gene confirmed with agarose gel electrophoresis as detailed elsewhere. The remaining PCR product was purified using a commercial kit according to the manufacturer's instructions and eluted in MB-H2O. Spectrophotometry confirmed DNA concentration greater than 100ng/μL. Forward and reverse primers were diluted to 3.2μM with MB-H2O and 3μL

of each dilution was added to gDNA aliquot. Samples underwent commercial fluorescent dideoxynucleic acid sequencing (Source Bioscience) and the results were analysed with Geneious v8.0 software [134].

2.3.8.3 qPCR plates

All reactions used a commercial qPCR kit (SYBR Green PCR Master Mix; Applied Biosystems) and 2μM final concentration of each forward and reverse primers. All qPCR experiments were performed in triplicate using a commercial real-time PCR machine (BioRad, CFX Connect Optics Module). Reactions were performed with the following settings: an initial denaturation step of 95°C for 10 minutes, followed by 40 cycles of: 95°C for 30 seconds, an annealing temperature of either 55°C and extension at 72°C for 30 seconds. Standard curve analysis was performed to ensure efficiencies were close to 100%. Optimal efficiency between 90% - 105% was achieved with at one primer set per gene before performing test plates (Table H.1). Values obtained for the target genes were normalised to the geometric mean of the housekeeping gene B-actin.

2.3.9 Extraction of protein from tissue

Mice were sacrificed by cervical dislocation and retinal tissue samples were collected promptly. As described in subsubsection 2.3.7.1, the neurosensory retina was isolated and snap-frozen in dry ice, before transfer to long-term -80°C storage. Samples were later mixed with radio-immunoprecipitation assay buffer (RIPA) buffer (National Diagnostics) and disrupted with a handheld rotor. After centrifugation, the supernatant was mixed with protein loading buffer (National Diagnostics) for use in Western Blot (WB).

2.3.10 Western blot

WB identifies and allows quantification of a specific protein in a sample. Cell pellets or retina tissue were homogenised in RIPA buffer (Temecula). Prepared

samples and recombinant protein controls were loaded alongside a protein size ladder (Geneflow) into an sodium dodecyl sulfate polyacrylamide gel electrophoresis (SDS-PAGE) gel (Bio-Rad) in a Tris buffer . An electric current was passed through the buffer and the proteins diffused down the gel proportional to size.

Using a Trans-Blot turbo transfer system (Bio-Rad), the separated proteins were transferred to a Methanol treated membrane (Bio-Rad) using an electric current. The proteins on the final membrane were incubated with antibodies using either the incubator-shaker or snap i.d. (Merck-Millipore) vacuum methods. The incubator-shaker technique required longer incubation periods (Primary for 1 hour; Secondary for 2 hours). The vacuum method accelerates antibody interaction with the membrane, but is not suitable for all antibodies and proteins.

In both methods, blocking serum (Li-Cor) was first applied to the membrane. The membrane was then incubated with dilute primary antibody before repeated washes with Tris-buffered Saline (Bio-Rad). The secondary antibody was applied to the membrane under foil to preserve fluorescence. After a final wash stage, the membrane was dried and imaged on the Odyssey imaging machine (LiCor). For some primary antibodies, traditional horseradish peroxidase enhanced chemiluminescence (ECL) techniques were superior to fluorescent secondary antibody binding. The blots were incubated in horseradish peroxidase conjugated secondary antibodies diluted in Tris-buffer saline with 1% BSA for 2 hours at room temperature.

2.3.10.1 Bicinchoninic acid assay

The bicinchoninic acid (BCA) assay measures the total protein concentration of a sample by colorimetric assessment. Equal amounts of total protein can then be loaded for each sample lane in the WB. Interaction of the added BCA with peptide bonds and Copper changes the sample colour from green to purple; the change in colour is proportional to the total protein content.

bovine serum albumin (BSA) standards were prepared. 1 ml of BSA stock (2

mg/ml, dissolved in H2O) was serially diluted (5-8x) to give a range of 20-2,000 μg/ml. The BCA working reagent was prepared by mixing 50:1 BCA Reagent A (Sigma) with BCA Reagent B (Sigma). An 8:1 mixture of working reagent and protein sample replicate was pipetted into each microplate well. Water was used as blank solutions for standard curve and protein samples, respectively. The samples were incubated at 37°C for 30 minutes, adjusted to room temperature for 10 minutes and then absorbance readings collected on the 562nm plate reader (iMark, BioRad).

2.3.10.2 Image analysis of WB

The fluorescent or chemiluminescent secondary signal was measured using the Western Blot imaging machine (LiCor). Image acquisition parameters were optimised for each image to reduce background and maximise genuine signal band detection. After collection, WB images were quantitatively analysed using the inbuilt densitometry tool of the Image Studio software (LiCor). Bands of interest were manually outlined with the border selection tool. The software then performed a greyscale pixel count in the colour channel of interest, producing a total value (expressed in arbitrary units; arb. units). The total value of the band is adjusted for the background signal immediately adjacent the area of interest.

2.4 Cloning of vector plasmids

2.4.1 Design of plasmids

Plasmids and cloning strategies were designed *in silico* using Geneious software v7. Details of specific plasmid designs are available in subsection 5.4.1.

2.4.2 Genetic components

2.4.2.1 Plasmid backbone

The plasmid for cloning was a kind gift from lab colleagues Dr Maria Patricio and Dr Michelle McClements. The plasmid contained an existing expression cassette

AAV2.CAG.GFP.WPRE.pA. Also, a non-packaging backbone containing the ampicillin resistance gene necessary for selective bacterial amplification. The existing expression cassette contained the following elements:

- **AAV2:** Inverted terminal repeat. Palindromic nucleotide sequence derived from AAV serotype 2. The sequence flanks both ends of the expression cassette and is necessary for correct packaging of transgene in AAV during creation.
- **CAG:** Ubiquitous mammalian promoter. Hybrid promoter sequence combining nucleotide sequences from C) cytomegalovirus early enhancer element, the promoter, A) the first exon and the first intron of chicken beta-actin gene and G) the splice acceptor site of the rabbit beta-globin gene
- **GFP:** Green fluorescent protein. A reporter protein used in other experiments, but removed before use.
- **WPRE:** Woodchuck hepatitis virus post-transcriptional regulatory element. Non-coding sequence shown to increase transgene expression in AAV retinal gene therapy.
- **pA:** Poly-A tail. Bovine derived poly-adenine sequence to mimic normal mRNA. The poly-A tail is important for nuclear export, translation and stability of mRNA.

2.4.2.2 Transgenes

The CRX, NFE2L2 (NRF2) and CNGB3 transgenes were obtained from commercial sources as detailed in respective chapters. The OPN1LW transgene was a kind gift from Dr Michelle McClements. Murine Cngb3 was PCR amplified from reverse transcribed retinal cDNA produced in the lab.

2.4.3 Introduction of restriction sites into amplicons

The CRX open reading frame (ORF) was PCR amplified using KOD Hot Start Master Mix (Nonagon) and custom primers that incorporated selected restriction sites at either end of the amplicon. The final solution underwent thermal cycling of 2 min at 95°C; 40 cycles of 10 sec at 95°C (denaturing phase), 30 sec at 60°C (annealing phase) and 15 sec at 70°C (elongation phase).

The 900bp amplicon length was compared against a DNA ladder on 1.5% Agarose gel to confirm correct length. The gel band was excised and extracted using a column-based commercial kit (Qiagen, Cat# 28704) before re-suspension.

2.4.4 Restriction digest and ligation

The vector plasmid and CRX amplicons were digested for one hour at 37°C using commercially available endonuclease enzymes (New England Biolabs) suspended in commercial buffer (New England BioLabs). Linearised single-enzyme digested and circular undigested plasmid control experiments were performed in parallel. These plasmids were later used during bacterial transformation to confirm the efficacy and specificity of each enzyme.

2.4.5 Ligation of digested DNA fragments

The digested insert and plasmid were ligated overnight for 12 hours using T4 DNA Ligase (New England Biolabs) in 10x T4 DNA Ligase buffer (New England Biolabs).

2.4.6 Amplification in bacteria

XL10-Gold Ultracompetent Cells (Agilent Technologies) were defrosted on ice and treated with B-ME for 10 minutes. The ligated test plasmid and a positive plasmid control were added to cell suspensions. After 30 minutes the XL-10 cells were heat-shocked at 42°C for exactly 30 seconds before a further 2 minutes on ice.

Cells were then suspended in pre-warmed SOC Medium (NZY+ medium; Invitrogen) before culture in a shaker-incubator at 37°C at 225rpm for 60 minutes. After incubation, the cells were spread onto Agar-Luria Broth culture plates containing 100μg/mL Ampicillin (Sigma). The plates were then incubated for 12 hours at 37°C, resulting in colony growth from bacteria successfully transformed with ligated plasmid.

For initial screening, single colonies were sampled and placed in 4mL LB and 8μL of Ampicillin. Samples were incubated at 37°C on a shaker rotating at 225rpm for 14-16 hours overnight. 800μL of culture broth was mixed with 400μL of 50$\%$ glycerol for stock storage at -80°C. Plasmids were then isolated from the remaining culture broth using Miniprep kit (Sigma). Plasmids were sequenced for correct ligated sequence as detailed in subsection 2.3.5.

For vector production, a scraping from a single colony or glycerol stock was placed in 2L LB and 4mL of ampicillin. The broth was similarly incubated and plasmids then isolated using a Megaprep kit (Qiagen).

Briefly, the broth were centrifuged and cell pellet re-suspended and lysed. The lysate was added to a binding column and DNA absorbed onto the silica membrane. Contaminants and cell debris were washed away before eluting the DNA in molecular grade water. Quality checks included a double-stranded DNA (dsDNA) concentration above 1200ng/μL, good spectrophotometry results as detailed in subsection 2.3.4 and sequencing results (subsection 2.3.5) consistent with the plasmid template.

2.5 Production of AAV

2.5.0.1 RepCap AAV8^{Y733F} plasmid

The AAV8^{Y733F} capsid mutant was produced by Petrs-Silva et al [136] using site-directed mutagenesis. Glyercol stock of the plasmid was a kind gift from Dr Michelle McClements. An adequate concentration of plasmid was mega-prepped (1494ng/μL) and the correct nucleotide sequence confirmed by

Sanger sequencing before AAV production.

2.5.0.2 Helper plasmid

AAV is a non self-replicating virus. It depends upon the assembly proteins provided by the co-infection of Adenovirus to replicate and assemble new AAV. Traditional AAV production methods were inefficient because they relied on cell line co-infection with live Adenovirus or genetic modification of cell lines to express the necessary Adenoviral genes. More recent work has developed helper plasmids that isolate the required Adenoviral transgenes for co-transfection during AAV production *in vitro* [137].

The pAdΔ6 helper plasmid stock used in the MacLaren lab contains four Adenoviral gene fragments to assist the assembly of AAV. An NCBI BLAST search reveals a fragment of human adenovirus strain 5 sequence (NCBI# AY601635.1) and three fragments from human adenovirus strain C sequence (NCBI# KF429754.1). The plasmid was mega-prepped from glycerol stock on two occasions (1237ng/μL and 1243ng/μL) to provide sufficient quantities for AAV production.

2.5.1 Plasmid transfection of HEK293T cell line

A T75 flask was seeded for each of the two required hyperflasks. Each T75 flask was seeded with approximately 1×10^{7} HEK293T cells in 500ml Dulbecco's modified Eagle's medium (DMEM) with 4.5g/litre glucose, 10% foetal bovine serum (FBS), 5ml L-Glutamine, 200mM solution, 10^3 units/ml Penicillin-Streptomycin, 10mg streptomycin/ml (Sigma- Aldrich). The flasks was incubated at 37°C in 5% CO_2 for 72 hours until the cells were 80-90% confluent.

The media was removed, the cells washed with PBS and then re-suspended in 200mL fresh media as above. The suspended cells were then transferred into multi-layered hyperflasks (Corning). The suspension was distributed across all layers, taking care to avoid or remove air bubbles. The hyperflasks were then filled with remaining media as above and incubated at 37°C at 5% CO_2 for 72

hours.

After 72 hours, the HEK293T cells were transfected with 500μg total DNA of transgene, rep-cap and helper plasmids. The ratio of each plasmid was dependent on the total size, as calculated in Table 2.3.

Table 2.3 | AAV transfection calculations.

Plasmid	Size (kb)	Amount per transfection (μg)
pAdΔF6 (Helper)	15.4	264.6
pRepCap	7.3	125.4
pAAV.transgene	6.4	110.0
Total	29.1	500.0

The volume of all three plasmids was added to a 50mL Falcon tube and made up to a total volume of 10mL using NaCl 150mM. In a separate 50mL Falcon tube, 1.125mL of polyethylenimine (PEI) 10mM was pipetted out and made up the volume to 10mL with NaCl 150mM. The plasmid DNA and PEI were complexed by adding the 10mL of PEI drop by drop into the tube containing 10mL DNA. This mixture was then incubated at room temperature for 20 minutes. The transfection media was prepared and then 50mL set aside in a Falcon tube.

The DNA/PEI/NaCl complex was poured into the remaining volume of transfection media (500mL). 20mL of the 50mL reserved transfection media was poured into the now empty DNA/PEI/NaCl tube to collect any remaining solution. This collection was then poured into the 500mL of transfection media containing the DNA/PEI/NaCl. The hyperflask was drained and the transfection media/DNA/PEI/NaCl solution was gently added. Any bubbles were removed as before and the hyperflasks incubated at 37°C in 5% CO_2 for 72 hours.

2.5.2 Harvesting and lysing transfected HEK293T cells

Lysis buffer was prepared containing 1M Tris(hydroxymethyl)aminomethane (VWR) and 150nM NaCl (Sigma-Aldrich). Diluted in molecular biology grade water, autoclaved and pH optimised to 8.5.

The hyperflask cells were loosened and the suspension poured into a 500mL flask (Corning) and centrifuged for 10 minutes at 1200×g at 20°C (). The supernatant media was discarded and the pellet resuspended in media. The resuspension was centrifuged for a further 10 minutes at 1200×g at 20°C.

After the second centrifugation, the supernatant media was discarded and the pelleted cells resuspended with 15mL lysis buffer (Table G.1). The lysis buffer was supplemented with 500μl of protease inhibitor mix, containing 0.5ml prepared lysis buffer and 0.5 complete mini EDTA-free protease inhibitor cocktail tablet (Roche).

Four freeze-thaw cycles were carried out (-80°C freeze for one hour followed by 15min thaw in 37°C) and lysate was stored at -80°C until ready for isolation of the AAV particles.

2.5.3 Isolation of the AAV particles using Iodixanol gradient

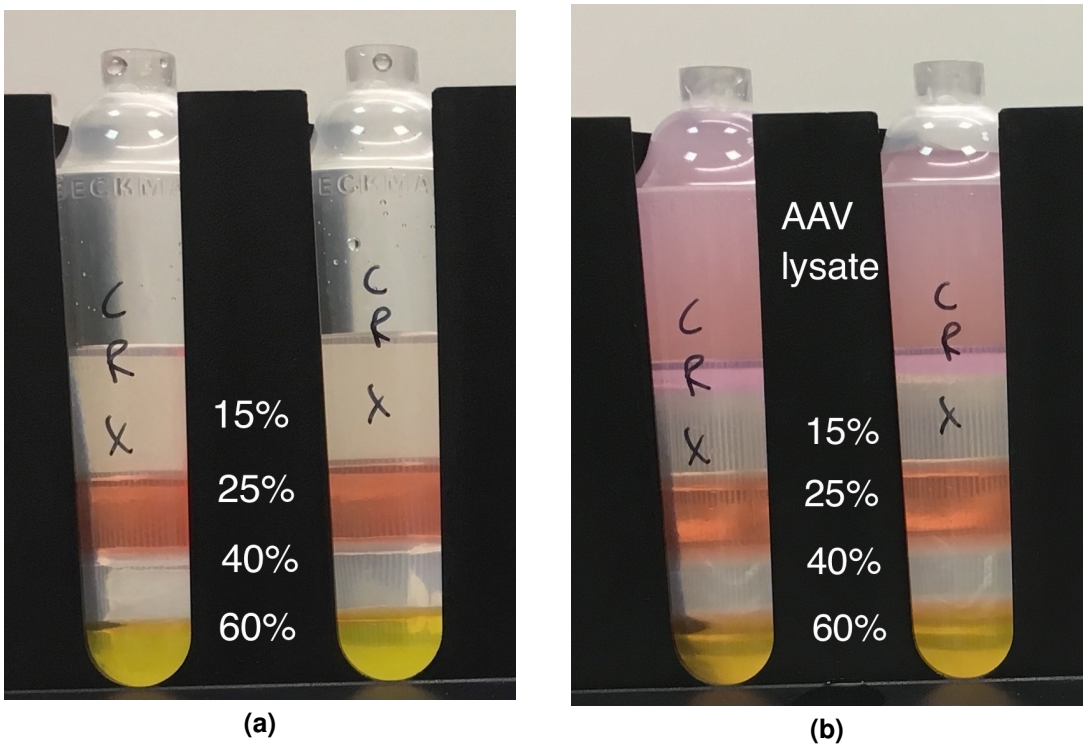
The lysate was thawed at 37°C for 15 minutes and 10μL of Benzonase (Sigma-Aldrich) was added to give a final concentration of 50U/mL. This mixture was incubated at 37°C for a further 45 minutes, with vigorous shaking every 15 minutes. The lysate was then centrifuged at 3700×g for 20 minutes at room temperature.

Four gradient fractions were prepared containing 15%, 25%, 40% and 60% Iodixanol. The final Iodixanol ratios were prepared by mixing with Iodixanol OptiPrep Density Gradient Medium (60%) (Sigma Aldrich), Phenol Red solution (Sigma Aldrich) and autoclaved 5× PBS-MK — 250ml PBS 10× (Gibco), 2.5ml 1M magnesium chloride ($MgCl_2$; Sigma Aldrich), 6.25ml 1M potassium chloride (KCl; Sigma-Aldrich) in 500ml molecular biology grade water — as per Table 2.4.

The Iodixanol fractions were loaded in layers into Quick-seal Ultra-Clear 25×89mm centrifuge tubes (Beckman) using a Pasteur pipette. In each tube, 7.2mL of 15% mixture was pipetted into the bottom of the tube, followed by careful layering of 4.8mL of 25%, 4mL of 40% and finally 4mL of 60%

Table 2.4 | Iodixanol gradients.

Fraction	Iodixanol	5M NaCl	5X PBS-MK	H2O	Phenol Red
15%	4mL (12mL)	3.2mL (9.6mL)	3.2mL (9.6mL)	5.6mL (16.8mL)	-
25%	5mL (15mL)	-	2.4mL (7.2mL)	4.6mL (13.8mL)	20μL (60μL)
40%	6.7mL (20.1mL)	-	2mL (6mL)	1.3mL (3.9mL)	-
60%	10mL (30mL)	-	-		20μL (60μL)



(a) (b)

Figure 2.4 | Iodixanol gradients. **(a)** Iodixanol gradient prepared in the centrifuge tubes. **(b)** Iodixanol gradient with cell lysate added before centrifugation

(Figure 2.4).

The cell lysate was added drop-wise to the top of the Iodixanol gradient tubes. The tube was spun in a Beckman 70Ti ultracentrifuge rotor at 59000rpm for 90 minutes at 20°C. The viral particles collected in the 40% Iodixanol fraction. (Figure 2.4).

The tube wall was pierced at the junction between 40% and 60% fractions using an 18G needle on a 5mL syringe. 2-3mL of the 40% fraction containing the virus was withdrawn with the syringe and stored overnight at 4°C.

2.5.4 Virus purification and concentration

The Amicon Ultra 100K filter was placed in an Amicon Ultra-15 tube. 5mL PBS was added and the tube centrifuged at 3000×g for 15 minutes at 20°C. The elutant was discarded. PBS was added to the collected 40% Iodixanol fraction to make a volume of 15mL and mixed by pipetting.

The volume was added to the prepared filter and centrifuged at 3000×g at 20°C until the volume in the filter was reduced to 500μL. The filter was then washed three times by adding 15mL PBS and centrifuging again at 3000×g at 20°C until the volume was reduced to 500μL. On the final centrifugation, the volume in the filter was reduced to 250μL. This contained the concentrated AAV.

The AAV concentrate was pipetted back over the filter 20 times on each side to collect any remaining AAV particles. This AAV concentrate was then aliquoted and stored at -80°C. 500μL PBS was then used to rinse the filter 20 times on each side to collect any remaining AAV particles. 40μL aliquots of this dilute AAV wash were prepared for *in vitro* work and stored at -80°C

2.5.5 Virus titring

The titring of the virus was performed to determine the concentration of viral genomes produced in the previous steps. Primers were designed for the CRX and OPN1LWS transgenes, as well as the poly-A tail in the viral genome. A dilution series (1ng, 100pg, 10pg, 1pg) of the transgene plasmid was used as a positive template control. The AAV concentrate was diluted 1:100 and 1:1000 in molecular grade water, whilst the AAV wash was diluted 1:100. Triplicate reactions were performed with 1μL of diluted virus in each well, using a melt step of 60°C.

The SYBR green nucleic acid gel stain method of qPCR reaction was used. SYBR dye (iTaq mix, Biorad) binds to amplified DNA and emits a quantifiable green fluorescence signal. A fluorescent signal threshold was set incorporating the log phase of each reaction. A comparative cycle threshold (Ct) value was

determined for each sample.

2.5.5.1 Calculation of titre

The titre of the plasmid standard curve was calculated using Equation 2.1.

$$Molecule\,count = \frac{Mass\,(g)\,of\,template \times (6.022 \times 10^{23})}{Molecular\,weight\,of\,amplicon} \quad (2.1)$$

Log_2(molecule number) was plotted against the Ct values from the plasmid dilution series to generate a standard curve. Ct values of the unknown AAV sample were then compared to the standard curve to determine the starting number. This log value was converted back to the number of molecules. The dilution factor was corrected by x100 and x1000 as appropriate. An average titre was calculated for both the transgene and poly-A primer pairs

Table 2.5 | Titring primers. Primer pairs for qPCR titring of AAV concentrate genome copies

Primer pair	Sequence Name	Sequence	%GC	Hairpin Tm	Self Dimer Tm	Tm
OPNLWS 1	OPN1LWS FW1	GGTCTCTGGCTACTTCGTGC	60	None	None	60.5
	OPN1LWS RC1	ACCAGATCCAGGAGAAGGCA	55	None	8.7	60.3
OPNIWS 2	OPN1LWS FW2	GGACCCTACACCTTCTTCGC	60	None	None	60.1
	OPN1LWS RC2	CCCGAAAAGCTGCAAGATGC	55	45.6	None	60.5
OPNLWS 3	OPN1LWS FW3	GCTATGAGGACAGCACCCAG	60	None	None	60.2
	OPN1LWS RC3	CTTGAACTTCATGGTGGCCG	55	None	None	59.5
PolyA 1	20F	CCAGCCATCTGTTGTTTGCC	55	38.7	None	60
	91R	GCCACTCCCACTGTCCTTTC				

The qPCR titre reports only the number of genome copies, without quantifying the ratio of empty to full capsids. scanning electron microscopy (SEM) can identify the number of empty capsids within an AAV sample, but was beyond the scope of this work. SEM is routinely used when producing good manufacturing protocols (GMP) grade AAV for clinical trials.

2.5.6 Virus capsid quality control using SDS-PAGE

The AAV capsid is an icosahedron formed of three protein subunits; VP1, VP2 and VP3. Correct capsid protein synthesis and AAV sample purity was tested using SDS-PAGE. A diluted sample of AAV was mixed with protein loading buffer and denatured at 95°C.

The denatured sample was loaded into a sodium dodecyl sulfate (SDS) gel in a Tris buffer alongside a protein size ladder. An electric current was passed through the buffer and the proteins diffused down the gel proportional to size. The gel was then washed and stained to identify the bands of constituent protein. Pure AAV samples produced three bands corresponding to 87, 73 and 62kDa as demonstrated in Figure 2.5.

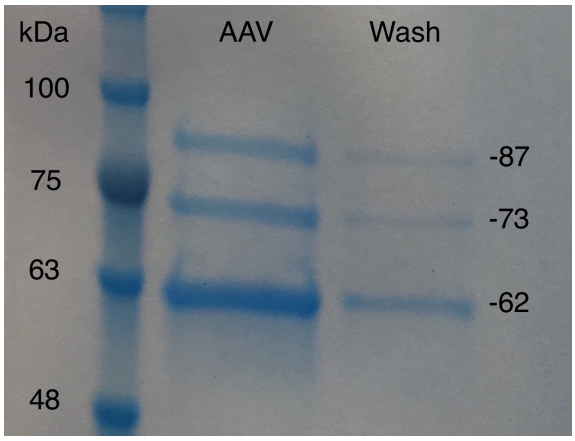


Figure 2.5 | **AAV protein capsid SDS-PAGE.** EZ Blue stained SDS gel showing electrophoretically separated protein bands of a protein reference ladder, concentrated AAV preparation and AAV wash. The three blue bands correspond to the three subunits of the AAV capsid (87, 73 and 62kDa).

2.6 Cell culture

2.6.1 Subculturing cell lines

human embryonic kidney 293T (HEK29T) cells were cultured in DMEM (Sigma), completed with penicillin-streptomycin (Sigma), L-glutamine (Sigma) and foetal bovine serum (Gibco; Appendix G). Flasks were kept at 37°C in a 5% CO_2 humidified environment (Thermo Electron). Cells were subcultured every three to five days, prior to becoming confluent.

During subculture, media was removed and the culture washed with PBS. The cells were covered with 2mL fresh PBS and left in the humidified environment for 3 minutes. The flask was removed and the cells dislodged by tapping. 8mL of complete DMEM was added and the cells fully suspended. 1mL of this resuspension was used to seed a new T75 flask with an additional 12mL of complete DMEM. The seeded flask was returned again to the 5% CO_2 humidified environment for three to five days.

2.6.2 *In Vitro* plasmid transfection

HEK293T cells at 80% confluence were diluted in DMEM and seeded into six-well plates containing circular glass cover slips (VWR). The culture wells were returned to the 5% CO_2 incubator for at least 24 hours until confluence passed 50%. For transfection, TransIT reagent (Mirus) was mixed with DMEM in a separate Eppendorf tube. 1μg of each test and control plasmid was then added to the mixture. The tubes were left at room temperature for 20 minutes whilst the DNA complexed. The DNA-TransIT-DMEM solution was pipetted over the corresponding well and mixed by rocking. The culture plates were then incubated for 48 hours. The samples were harvested once positive control GFP signal was confirmed using light microscopy (Motic) with the Retiga 2000R imagine system (Q-imaging).

For IHC samples, the cover slips were removed and placed in a 24-well plate. The samples were fixed with 4% paraformaldehyde (PFA) (16% PFA, Thermo

scientific; diluted 4-fold in PBS) before proceeding to the immunohistochemistry protocol. Western Blot samples were also isolated from the HEK293T culture by re-suspending any remaining cells in PBS. The cells were pelleted by gentle centrifugation and stored at -80°C.

2.6.3 *In Vitro* AAV transduction

HEK293T cells cultured in complete DMEM were seeded into a 6 well plate once they reached 80% confluence. The following day, one well of cells was counted with a haemocytometer to determine average cell density. The required volume of AAV was calculated by multiplying the cell density by the multiplicity of infection (MOI) ratio (e.g. 5,000 or 10,000) and dividing by the titre of the AAV batch

This final volume of AAV was mixed with 1% DMEM media and added to the respective culture wells. The reduced FBS concentration slows cell division; the non-integrated AAV transgene is not propagated in dividing cells. The cells were returned to the incubator and the 1% FBS DMEM media replaced the following day.

Three days following transduction the cells were harvested. The media was pipetted off and excess media washed away with PBS. The cells were then resuspended in PBS and gently centrifuged at 1000g for 10 minutes. The resulting pellet was resuspended in PBS, re-centrifuged, the supernatant was removed and the pellet frozen at -80°C. The cell pellet was later homogenised and prepared for WB analysis as detailed elsewhere.

2.7 Histological analysis

2.7.1 Embedding and cryo-sections

Following sacrifice and enucleation, the cornea was excised at the limbus. The zonules were blunt dissected with Vannas scissors and the lens extruded whilst avoiding retinal traction. The eyecups were then transferred to 4% (w/v) PFA for 30 minutes for initial fixation. The eyecups were then sequentially transferred to

10%, 20% and 30% sucrose. Samples were moved to the next sucrose concentration after they settled each time. Eyecups were embedded in OCT compound and stored at -80°C until sectioning. Sample blocks were later sectioned in 20μm slices at -22°C, placed onto polysine-coated glass slides (Thermo scientific) and allowed to dry overnight.

2.7.2 Immunohistochemistry

2.7.2.1 Overview

Immunohistochemistry (IHC) is the identification and localisation of proteins in tissue sections using labelled antibodies. Immunoglobulins, raised in animal species to target the antigen of interest, are applied to tissue samples. A marker - such as fluorescent dye, enzyme or radioactive element - allows antigen binding to be visualised.

Direct IHC incorporates antigen-targeting and marker-signalling on the same antibody. Indirect IHC first involves a primary unlabelled antibody, which binds the antigen. This is followed by a secondary marker-bound antibody, which reacts with the primary antibody. This allows stronger marker-signal amplification and greater variety of secondary signalling fluorescence colours. This is invaluable when using many primary antibodies on the same sample. For these reasons, only indirect IHC was used.

2.7.2.2 Protocol

Dried slide-mounted sections were demarcated on the slide with a hydrophobic Immopen (Vector Labs). Sections were incubated with 4% PFA ((Thermo scientific) for 30 minutes to achieve additional fixation. Following three 0.01M PBS washes (Gibco), the sections were permeabilised by a twenty minute incubation with 0.2% Triton-X 100 (Sigma). The slides were washed again in 0.01M PBS three times before blocking with 10% serum for one hour; donkey, goat or chicken blocking serum (Sigma) was used based on the secondary antibody host animal.

Slides were washed again three times with 0.01M PBS and then incubated with the primary antibody (Table F.2) overnight at 4°C. Two sections on each slide were demarcated as controls and were not incubated with primary antibody, but underwent all other steps.

The following day, slides were washed twice with 0.05% Tween-20 (Sigma-Aldrich) and then 0.01M PBS. Secondary antibody was diluted 1 in 400 in 0.1% Triton X-100 and added to the slides for 2 hours. After PBS wash, slides were then counter-stained with 4',6-diamidino-2-phenylindole (DAPI; Invitrogen). Coverslips were applied with ProLong Diamond Antifade Mountant (Life Technologies). The slides were then imaged on a confocal microscope (LSM 710, Zeiss), using the Zen 2009 software (Zeiss).

2.7.3 Immunocytochemistry

immunocytochemistry (ICC) is the identification and localisation of proteins in fixed cell cultures. The method utilises antigen specific primary antibodies and marker-signalling secondary antibodies in the same manner as IHC. The ICC protocol follows the steps of IHC detailed above. The difference being that HEK293T cells fixed on 10mm circular glass cover slips undergo the steps in individual wells on a 24-well plate. At the end of the antibody and wash steps, the circular cover slips are affixed to a polysine glass slide using ProLong Diamond Antifade Mountant.

2.7.4 Microscopy

The confocal microscope (Leica, Microsystems GmbH) allows high resolution and high contrast images of tissue and cell sections. Lasers are used to excite individual secondary signalling antibodies (i.e. DAPI or Alex Fluor 568) or endogenous fluorophores (i.e. GFP). A pinhole limits out of focus light and emission band pass filters can be used to enhance image colour channel specificity. Z-stack imaging allows high-definition 3D images in thicker tissue sections. Confocal image acquisition is slower than Evos microscopy and is

more appropriate for high magnification, high-definition images (40×, 63×)

The EVOS FL Auto 2 Cell Imaging System (Evos; Thermo-fischer scientific) uses fixed wavelength light emitting diode (LED) light sources. Image contrast can be both fluorescence and transmitted light. Automated Evos software workflows allow high volume screening of retinal sections. Automated image-stitching allows low-magnification images of whole retinal sections to be collected easily. The lack of a pinhole and lack of emission band filters results in a lower quality image at higher magnifications. The LED light source is less specific than the laser excitation wavelengths in confocal microscopy and signal overlap can occur. The mono-focal images lack the definition of confocal Z-stack images of 20μM retinal sections.

2.7.4.1 Confocal laser microscopy

Before use, the lasers were allowed to warm up for five minutes: the DAPI laser, the AlexFluor568 laser for red secondaries and the AlexFluor488 laser for endogenous GFP. White light was also used to obtain Nomarski differential interference contrast information in the images. Images were acquired using the Zen software (Leica).

The IHC slides were protected from incidental light exposure to reduce bleaching; laser exposure time was also minimised during image acquisition. Slides were screened using the 20× or 40× magnification, before obtaining detailed images of higher quality. The focal plane and Z-stack range was determined the 4',6-diamidino-2-phenylindole (DAPI) channel. In the red channel, the pinhole size was set to 1 Airy Disc unit (AU) and standardised across all other channels. The gain and saturation were adjusted to avoid pixel intensity saturation in any part of the image. Identical settings were used between slides and were re-loaded for future imaging sessions to allow reliable comparison of images.

2.7.4.2 Evos LED microscopy

The Evos microscope uses multiple proprietary light cubes. The DAPI light cube excites at 357/44nm, stimulating emission at 447/60nm. The GFP light cube excites 470/22nm and stimulates emission at 510/42nm. The RFP light cube excites at 531/40nm, stimulating emission at 593/40nm; the RFP cube is compatible with AlexFluor568 fluorescent secondary dyes.

Incidental light exposure was minimised, as was LED exposure time. White light microscopy was used to locate samples on the slide; the 2D location of sections on the slide was annotated in the software for multi-point imaging. The DAPI channel was used to set the focal plane. The saturation for each colour channel was manually adjusted to avoid signal saturation; identical settings were used across multiple slides to allow comparison. Multiple images were collected from each section and stitched together with contrast-adjusted by the Evos software.

2.7.5 Image analysis

2.7.5.1 Confocal microscope images of ICC/IHC

Image files were exported from the Zen software in *.lsm* file format and opened in Fiji ImageJ. For exemplar images, brightness contrast of individual colour channels was manually adjusted to a standardised level. Red, green, blue and Nomarski channels were merged; Z-stacks were merged together at median intensity. A scale bar and colour-matched primary antibody names were added for easy reference.

2.7.5.2 Evos images

Evos images were automatically handled and formatted using the inbuilt Evos software; stitched multi-panel images were similarly prepared.

2.7.5.3 cSLO images

cSLO images were exported from the Eye Explorer software as .tiff files and analysed using Fiji ImageJ. Manual counts of fluorescent cell numbers were performed using the cell counter plugin. Binary counts of toxicity changes in ICGA images were performed by visual inspection of the image. Automated threshold, segmentation and particle count workflows were also utilised.

2.7.5.4 OCT images

OCT images were analysed manually using the Eye Explorer software (Heidelberg). The radial OCT image for each eye was loaded, the vertical section chosen (0-180°) and the vertical:horizontal ratio was changed from 1:1 pixel to 1:1μM to avoid distortions of the measurement. The calliper tool was used to measure 1500μM from the optic nerve head, thereby standardising the radial distance of each thickness measurement (approximately halfway from optic nerve to fundus image edge). Two measurements were taken from the OCT image: a) total retinal thickness was measured from the inner margin of the nerve fibre layer to the inner margin of the RPE and b) outer retinal thickness was measured from the inner margin of the outer nuclear layer to the inner margin of the RPE.

2.8 Statistical analysis

All statistical and graphical analysis was performed using the statistical programming language `R` (v3.4) [138] operating in the graphical user interface RStudio [139]. All graphs were produced using the `ggplot2` package [140]. Datasets were imported from raw .csv files or .xlsx files exactly as they were recorded during each experiment. Data was cleaned using the `tidyverse` packages [141]. All `R` code was version controlled on GitHub to ensure reproducible research.

2.8.1 Analysis of non-repeated measures and non-complex datasets

After being cleaned, non-repeated measures datasets were evaluated for normality, number of groups and number of variables, then analysed accordingly using the base `stats` package in `R`:

- Analysis of two groups of parametric data was performed using the t-test function `t.test()`, specifying either paired and unpaired data.
- Analysis of two groups of non-parametric data was performed using the Wilcoxon signed rank test (paired data) and Wilcoxon rank sum test (unpaired data; also known as Mann-Whitney test). The function `wilcox.test()` was used from the base `stats` package.
- Odds ratios and contingency tables were assessed with Chi squared testing using the `chisq.test()` function.
- Non-parametric data across three or more groups - without repeated measures - was analysed using the Kruskal-Wallis test function `kruskal.test()` in the `PMCMR` package. Post-hoc testing applied Dunn's multiple comparisons using the `dunn.test()` function in the `dunn.test` package.
- Analysis of variance between three or more normally distributed groups - without repeated measures - was determined using the linear model function `lm()`.

  This function provides degrees of freedom and F-test values as in traditional ANOVA. It also iteratively fits coefficients and intercepts for each individual variable, group and variable-group interaction as specified in multivariate datasets. This allows more granular analysis of effect sizes, P-values and interactions than traditional ANOVA.

- Analysis of variance between multiple groups with repeated measures is detailed in subsection 2.8.2.

2.8.2 Hierarchical modelling of complex repeated measures datasets

Complex datasets containing repeated measures of multiple variables on individual subjects were analysed using hierarchical modelling. Models were fitted using the `nlme` package [142]. The `nlme` package is referred to throughout this thesis; it is an open-source statistical package for performing restricted maximum likelihood (REML) hierarchical regression modelling. This type of statistical analysis is detailed elsewhere [143]. Such modelling is more appropriate than classical ANOVA methods for analysing complex data with repeated measures and pairing, such as occurs in longitudinal studies on subjects treated in only one eye.

Many thanks to Professor Dan Lunn at the University of Oxford for his formal face-to-face statistical advice that was incorporated into these analyses.

Linear hierarchical models were fitted using the `lme()` function. Non-linear hierarchical models were fitted using the `nlme()` function. Further details are provided in the relevant chapters.

After initially fitting a model, normality of the model residuals was assessed by a quantile-quantile plot using the `qqnorm()` function. Outliers were manually reviewed and the original experimental notes checked for evidence of data entry errors or excludable sources of methodological error; any exclusions are detailed in the relevant chapter. Unexplained outliers were retained in the final analysis.

To further explore model normality, a Box-Cox profile likelihood [144] was generated using the `boxcox()` function from the `MASS` package. The profile likelihood of lambda, the exponent of a power transformation, was reviewed and log, square root or inverse transformations were applied as appropriate to achieve normality and satisfy the assumptions of the REML modelling.

The homoscedasticity of the model residuals was then assessed by a

residual plot - plotting actual versus predicted residual values. The `nlme` package — described earlier — uses REML regression modelling, but if the residuals plot revealed the funnel-shape of heteroscedasticity, an appropriate weighting was included in the fitted model (weighted least squares regression). Alternatively, if the residuals plot demonstrated systematic over- or under-prediction of values, then the model was fully revised.

2.8.3 Fitting functions to ERG response curves

The amplitude of the leading edge of the photoreceptor b-wave is a function of intensity, as broadly described by a saturating exponential function [145]. This saturating exponential relationship is best described as a *Michaelis-Menten* equation, after the original description of enzyme dose-effects relationships in biochemistry [146]. The intensity-amplitude relationship in electroretinography (ERG) testing is also described by a *Naka-Rushton* equation (Equation 2.2) following log-transformation of the stimulus intensity [147]. That is, a tanh (sigmoidal) function fits the b-wave response amplitude to a log of the stimulus intensity (Figure 2.6).

$$Response = \frac{R_{max} \times I^n}{(I^n + I_{50})} + b \quad (2.2)$$

$Response$	Amplitude (μV) of b-wave
R_{max}	Asymptote of response function
I^{n}	Log of stimulus light intensity
I_{50}	Stimulus intensity for half of R_{max}
b	Background signal

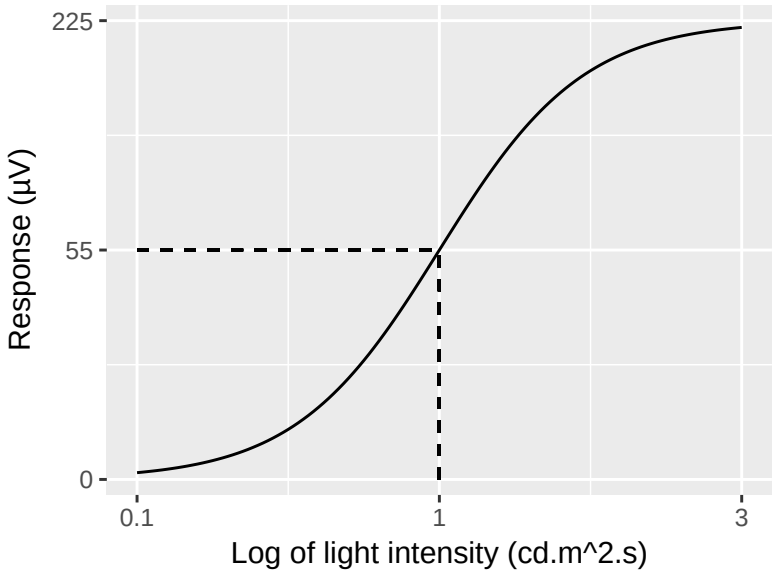


Figure 2.6 | Sigmoidal curve function. Sigmoidal curve function of the relationship of stimulus light intensity to electrophysiological response during ERG testing. The dotted line represents the midpoint of the sigmoidal curve. The axis values are approximate wild-type values derived from the uninjected eyes.

During statistical analysis, additional variation in the non-linear model must be accommodated:

2.8.4 Interpreting P-values

P-values were interpreted on a continuous scale and were not falsely dichotomised [148]; the common α value of 0.05 was used where appropriate. P-values were interpreted alongside *"...elements of scientific judgement about the plausibility of a hypothesis and study limitations that are normally banished to the discussion section: results of identical or similar experiments, proposed mechanisms, clinical knowledge..."* [149].

3

CONE PHOTORECEPTOR FUNCTION LOSS MUTATION

3.1 Introduction

A colleague in my laboratory noticed that a particular colony of inbred mice (of 129S6/SvEvTac origin) had poor light-adapted visual responses. I hypothesised that a novel genetic mutation affecting cone photoreceptors might be responsible.

Cone photoreceptors facilitate daytime vision, colour perception and central visual acuity [150, 151]. The cone phototransduction cascade and homeostatic functioning of cones has multiple linked steps and a single cone gene mutation can cause loss of cone function [152]. Mice are valuable for the identification and investigation of genes and mutations that may affect normal cone photoreceptor function, particularly in achromatopsia [116]. Mouse models also facilitate the development of retinal gene therapy [153, 31].

There have been nine mouse models of cone photoreceptor function loss (cpfl) reported (Table 3.1) since *cpfl1* was first described by Chang et al [113]. The *cpfl* retinal phenotype and underlying genetic basis is varied, but all nine models display partial or complete loss of cone function from birth, sometimes with progressive cone cell loss [111, 112, 113, 114, 33, 115, 117, 118, 119, 25].

This phenotype models human achromatopsia [152]. This chapter details the novel *cpfl10* mouse model discovered in this lab and its importance for understanding *CNGB3* achromatopsia.

The original *cpfl1* phenotype was characterised in detail by Chang et al [25] and Fischer et al [118]. *cpfl1* mice show virtually absent photopic due to InDel mutations in the *Pde6c* gene. There is progressive loss of cone photoreceptors demonstrated on IHC, culminating in almost complete loss at 5 months. SLO shows substantial reduction in fluorescent tagged cone numbers by 8 weeks. The identification of *Pde6c* as the causative murine gene was accompanied by the first published human cases of *PDE6C* achromatopsia [113]. A clear example of novel gene discovery in mice facilitating a better understanding of human disease.

Gnat2^{cpfl3} was the first *cpfl* mouse model to assist in developing retinal gene therapy for achromatopsia. Human cases of *GNAT2* achromatopsia were first reported by Kohl et al [22] and Aliganis et al [23]. The autosomal-recessive Gnat2^{cpfl3} mutation in mice is caused by a missense mutation in exon 6 of *Gnat2* [111]. Homozygous mice exhibit less than 25% normal cone function, which is extinguished by nine months. Gnat2 levels disappear on IHC over the same timeframe, but there is no cone photoreceptor loss.

The Gnat2^{cpfl3} mouse model was rescued using an AAV5-PR2.1-*Gnat2* vector (PR2.1 refers to the human LM opsin promoter) just one year after it was first described [31]. This was the first example of successful gene therapy for achromatopsia in an animal model. The *Gnat2* vector expressed mouse transgene under control of a human red-green opsin promoter fragment that targeted expression to cones. Photopic ERG function was significantly improved at 2-3 months and the improvement was sustained after 6-7 months. Treated mice also demonstrated functional rescue during OMR testing. However, no human *GNAT2* vector has yet been developed for clinical trials.

A human gene therapy trial for *CNGA3* achromatopsia (NCT02935517) began with the AAV rescue of the *cpfl5* mouse model in 2012 ([35]). The *cpfl5* model shows no photopic ERG function due to a missense mutation in exon 5 of *Cnga3*

[33]. IHC shows abnormal migration of the cone somata to the outer plexiform layer from PNW3, but no evidence of degeneration. This model was rescued using a AAV5.CBA.CNGA3 vector injected into the subretinal space. Treatment restored cone-specific ERG and cone-mediated visual acuity [35].

Table 3.1 | Summary of the Cpfl mouse models

model	Gene	Mutation	Annotation	Inheritance	ERG phenotype	Retinal phenotype	Histological phenotype	Important publications
cpfl1	Pde6c	InDel	c.864_865ins116 and c.1042delT	AR	virtually absent cone response at 4 weeks	Normal	photoreceptor changes at 3 weeks, almost complete cone loss by 5 months	[113] [25] [118]
cpfl2	(Chr 3)	-	-	AD	start to decrease at 2 months gone by 4 months of age	Retinal spots	Retinal waves and rosettes	[117]
cpfl3	Gnat2	Missense	c.596G	AR	25% of normal at 3 weeks, completely extinguished by 9 months	Dilated vessels	Reduced alpha-transducin levels no cone loss up to 5 months	[111] [31]
cpfl4	Chr17	-	-	AD	Cone–mediated photoresponses start to decrease PNW4, gone by PNW16, but rod–mediated photoresponses are normal up to 8 months of age	Progressive white retinal spots	large waves and rosettes in the central retina at 8 months of age	[115]
cpfl5	Cnga3	Missense	Exon 5	AR	Absent cone ERG	Normal	Cone somata migration to OPL from 3 weeks	[33]
cpfl6	Hcn1	Unknown	Unknown	AR	Abnormal cone-mediated photoresponse at PNW6. Normal rod-mediated photoresponses from PNW6 to PNM11.	Not examined	Normal retinal structure at PNM2. Mild peripheral retinal degeneration at PNM11.	[154] [155]
cpfl7	(Chr 19)	-	-	AR	Abnormal light-adapted ERG response and a normal a-wave but lower b-wave dark-adapted ERG response starting at PNW3	Not examined. Neurological motor defects	Ganglion cell disruption retinal segment degeneration in the peripheral retina at 3 months of age	[112]
cpfl8	Syne2	Missense	c.13978C	AR	Substantially diminished cone b-wave and reduced rod b-wave	Not examined	Reduced cone cell numbers. Mislocalised Horiztonal, Bipolar and Mueller cells	[119]
cpfl9	Unknown	-	-	AR	Substantically diminished cone photoreceptor function			[114]

3.2 Aims & objectives

The aim of this chapter is to characterise the phenotype and genotype of the cone phototransduction dysfunction in a novel mouse model of isolated cone blindness (*cpfl10*).

The objectives of this chapter are to:

1. Measure the electrophysiological retinal phenotype of the affected mice using electroretinography testing
2. Measure the functional retinal phenotype using optomotor response testing
3. Classify the structural macroscopic retinal phenotype using OCT and cSLO imaging
4. Categorise the phenotype as degenerative or stable based on IHC microscopy of photoreceptors
5. Classify the Mendelian inheritance pattern of the phenotype
6. Identify the causative mutation and affected gene of the abnormal cone photoreceptor function loss phenotype
7. Measure the effect of the causative mutation on cone phototransduction mRNA expression
8. Measure the effect of the causative mutation on retinal expression of the affected protein
9. Determine if the model is a candidate for re-expression AAV gene therapy

3.3 Materials & methods

3.3.1 Animals

The cone photoreceptor function loss 10 (*cpfl10*) phenotype was identified in a particular colony of inbred mice of 129S6/SvEvTac origin; the colony had been

bred in isolation for two decades. Strain-matched 129S2/SvHsd control mice were commercially obtained. C57Bl/6 mice for backcross breeding were also commercially obtained from Charles River. TKO mice for complementation testing were obtained from a local colony described earlier. All animals were housed and handled as detailed in section 2.1.

3.3.2 *In vivo* procedures

ERG, OCT, OMR and SLO *in vivo* tests were performed as described in section 2.2. Cursor a-wave and b-wave placement in ERG test traces was performed on the Espion Multifocal software. Calliper measurement of OCT retinal thickness was performed on the Heidelberg Eye Explorer software. Overhead videos of the OMR head-tracking behaviour was analysed and counted by a single observer.

3.3.3 Molecular techniques

3.3.3.1 Re-sequencing and genotyping

Targeted re-sequencing of known achromatopsia genes was performed on gDNA extracted from tail or ear tissue as detailed in subsection 2.3.1. Custom primer pairs were designed to amplify the exonic and adjacent intronic DNA. Amplicons were gel extracted and sent for commercial Sanger sequencing. The previously published point mutations in *Gnat2* [111] and *Syne2* [119] were only resequenced at the previously affected sites. Thank you to Dr Christina Zeitz at Institut de la Vision in Paris for the *Gnat2* primer pairs. After identifying the causative mutation in *Cngb3*, genotyping of all F2 and any other affected mice was performed using the primers:

- FW-5'-TTCTCTCCACACCAGTGCAC-3'
- RC-5'-ACACTGACAATGTTCTATCCACAGA-3'

Manual review of the Sanger chromatogram was performed in the Geneious software and het, hom or wt status was determined visually. A number of the

sequenced *Cngb3* exon 6 amplicons also underwent restriction digest with the ApaLi enzyme (New England Biolabs). Restriction fragment length polymorphism (RFLP) allowed mutant allele status to be corroborated by a second assay (Figure 3.5).

3.3.3.2 Retinal gene qPCR

Neurosensory retinas from *cpfl10* and strain-matched 129S2/SvHsd controls were harvested, the RNA extracted and reverse transcribed to cDNA as detailed in subsubsection 2.3.7.1. qPCR plates were performed as detailed subsubsection 2.3.8.3, using primer pairs selected for reliable efficiency in chapter 4. qPCR test plates were set-up to distribute different genes and samples across multiple plates to avoid systematic bias. Results were analysed in R using hierarchical linear modelling.

3.3.4 Immunohistochemistry

IHC was performed as detailed in subsection 2.7.2. Three commercially available CNGB3 primary antibodies Table F.2 were optimised and the final stains were performed with the most specific of these.

3.3.5 *In silico* modelling of Cngb3

The Visual Molecular Dynamics (VMD) freeware [156] was used to *in silico* assemble and analyse previously published models of mouse *Cngb3* (UniProt: Q9JJZ9) and Human *CNGB3* (UniProt: Q9NQW8). *Cngb3* was also examined in context using the CNGB3/A3 heterotetramer model (Swiss model ID: 5h3o.1) built from 3.5-Å-resolution single-particle electron cryo-microscopy structure of a cyclic-nucleotide-gated channel from *Caenorhabditis elegans* [157].

3.4 Results

3.4.1 Origin and phenotype of the mouse *cpfl10* mutant

The *cpfl10* phenotype can be easily identified by ERG. For all mice tested in the original colony (n=12), dark-adapted rod responses were equivalent to wild-type (regression, p=0.4) and light-adapted cone responses were completely absent or substantially reduced (Figure 3.3a).

3.4.2 Inheritance pattern

Complementation breeding of the *cpfl10* mice with a *Cnga3*$^{-/-}$ colony produced offspring with normal cone function. All of the phenotyped Cnga3$^{-/-}$,*cpfl10* outcross progeny (n=21) showed normal light-adapted ERG. The lack of complementation showed the cpfl10 mutation is not allelic to Cnga3 (X^2 = 38.7, df=1, p<0.001). In outcrosses with C57Bl/6 mice, *cpfl10* segregated as an autosomal recessive trait (Figure 3.1).

None of the C57Bl/6 outcross F1 progeny (129SB6F1) displayed a deficit in cone ERG function (n=28), excluding a dominant inheritance pattern (X^2=57, p<0.001). Approximately a quarter in the F2 generation (n=15/59) showed the original *cpfl10* phenotype, confirming an autosomal recessive inheritance pattern (X^2=13, p<0.001). Intercross of two affected F2 mice showed full penetrance of the phenotype in the subsequent F3 generation (n=6).

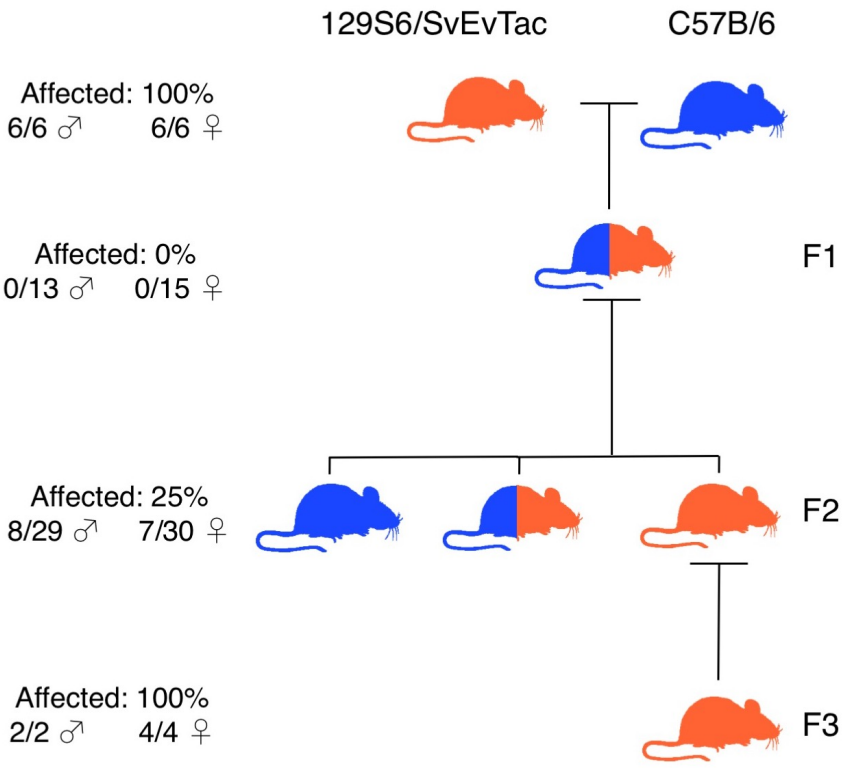


Figure 3.1 | Outcross breeding plan. Graphical representation of the incidence of the *cpfl10* ERG phenotype across generations during the backcross-intercross breeding with C57Bl/6 mice (n=105 mice). 'Affected' refers to the percentage of mice in each generation with absent or profoundly reduced cone ERG function. The exact numbers of affected mice in each generation are provided by gender.

3.4.3 Retinal phenotype

A further one hundred and fourteen mice derived from out-crosses and back-crosses of *cpfl10* were phenotyped; sixty-six mice were genotyped. The relationship between the causative mutation (NM_013927)c.692G>A; p.(R231H); subsection 3.4.5) and the electrophysiological phenotype is shown in Figure 4.3.

Regarding b-wave response amplitude. In scotopic conditions, at a single-flash 0.001 cd.m^2.s^{-1} stimulus, the response amplitude of wt mice (347 μV $\pm$ 40.5; n=28) have a similar b-wave amplitude (p=0.53) to the heterozygous (372 μV $\pm$ 24.7; n=22) and homozygous mutant mice (270 μV $\pm$ 32.4; n=32). In photopic conditions, at a single-flash 25cd.m.s^{-1} stimulus, heterozygous mice (180μV $\pm$ 10.9, n=34) and wt mice (175μV $\pm$ 12.8, n=42) have a similar b-wave amplitude

(p=0.42). Whereas the homozygous mutant mice (35.7μV $\pm$ 4.79; n=34) have a significantly diminished b-wave response (p<0.001). This significant difference is maintained across all other photopic stimulus intensities.

Regarding b-wave implicit times. In scotopic conditions, at a single-flash 0.001 cd.m^2.s^{-1} stimulus, the implicit time of wt mice (106 ms $\pm$ 4.14; n=28) is similar (p=0.37) to the heterozygous (109 ms $\pm$ 0.995; n=22) and homozygous mutants (112 ms $\pm$ 2.16; n=32). In photopic conditions, at a single-flash 25cd.m.s^{-1} stimulus, the implicit time of wt mice (51.7 ms $\pm$ 2.6; n=42) is similar (p=0.61) to heterozygous mice (48.8 ms $\pm$ 0.998; n=34). However, both genotypes have an implicit time that is significantly different (p<0.01) to homozygous mutants (95.3 ms $\pm$ 4.07; n=34). This saignificant difference is maintained across all other photopic stimulus intensities.

The *cpfl10* retinal fundus is macroscopically normal on cSLO imaging when compared with a commercially obtained 129S2/SvHsd colony wild-type (Figure 3.3). Infrared, blue laser autofluorescence (BAF) and ICGA imaging modalities show normal vasculature and photoreceptor reflectance patterns (P50 to P72). On the OCT, mutants show normal retinal architecture. Regarding the thickness of the whole retina on OCT, homozygous mutants (194μM $\pm$ 4; n=6) are indistinguishable (p=0.83) from wt mice (193μM $\pm$ 9; n=5). Similarly, the outer retinal thickness in homozygous mutants (0.055μM $\pm$ 0.002; n=6) and wt mice (0.058μM $\pm$ 0.002; n=5) are similar (p=0.73). IHC staining for cone arrestin at P70 shows normal retinal appearance and cone morphology (Figure 3.3) at PND70. Longitudinal changes in the cone photoreceptor morphology were not measured and a slow degeneration cannot be excluded.

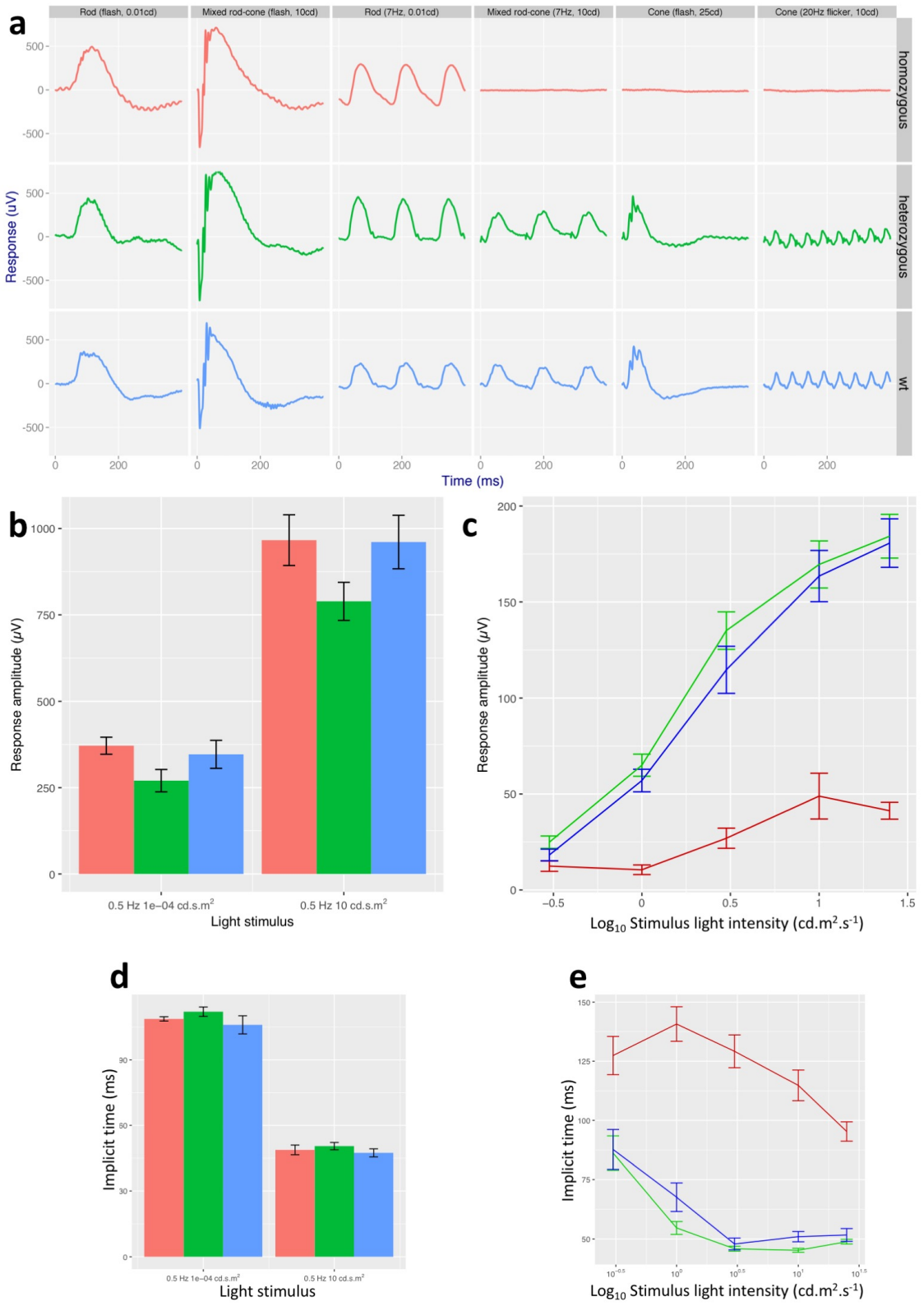


Figure 3.2 | *cpfl10* ERG phenotype-genotype correlation. a, Representative ERG results for mice genotyped as homozygous (red), heterozygous (green) or wild-type (blue) for the (NM_013927)c.692G>A;p.(R231H) mutation. **b,** Dark-adapted rod-isolating test steps were the same regardless of mutation status (n=65 mice). **c,** The irradiance response curve (IRC) for the light-adapted cone-isolating ERG test steps (n=65 mice) shows that heterozygous mice have normal cone function.**d,** Rod b-wave latency and **e,** cone b-wave latency for the same mice.

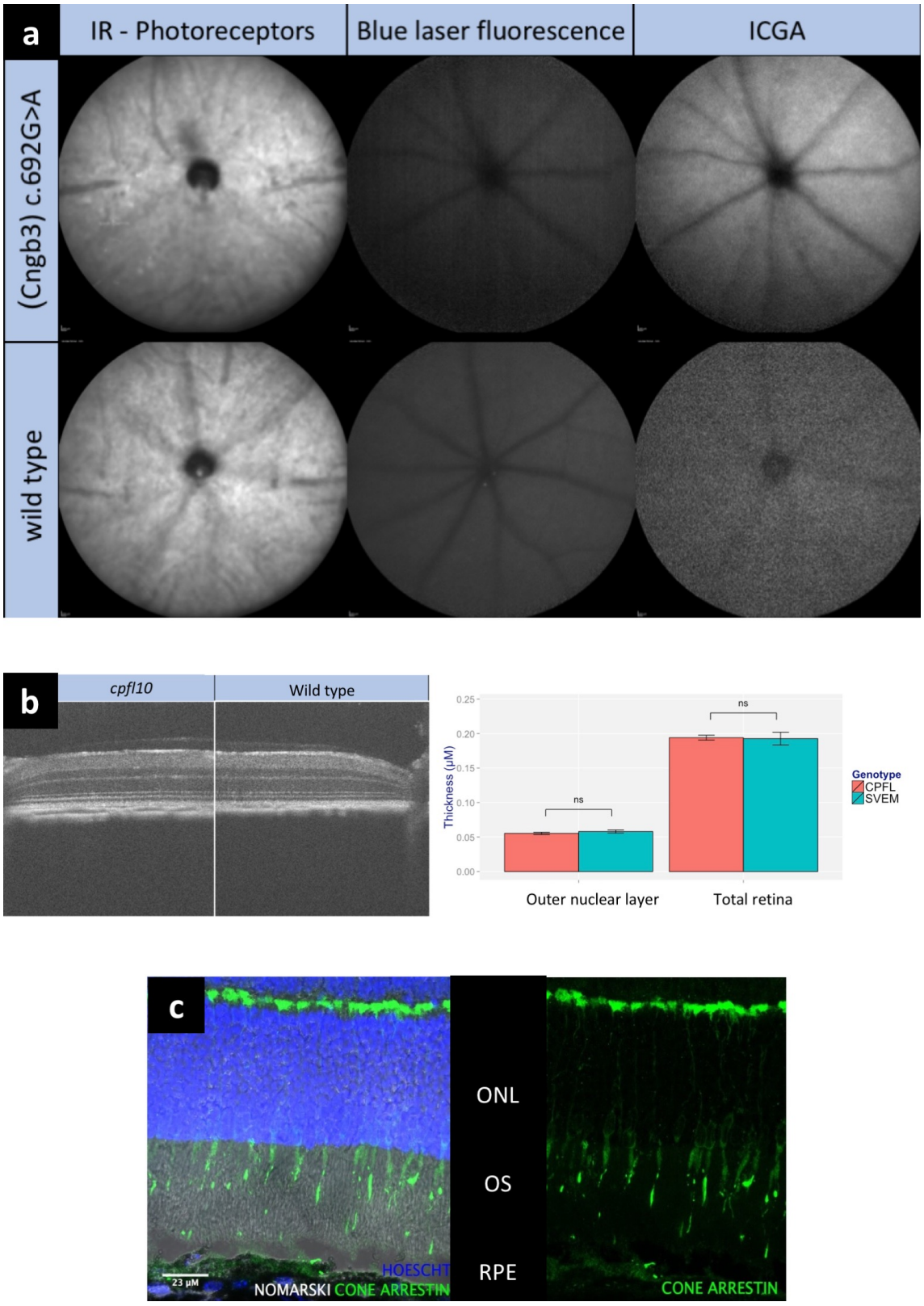


Figure 3.3 | Retinal phenotype. **a,** *En face* confocal scanning laser ophthalmoscopy images show no obvious macroscopic retinal changes. **b,** Representative optical coherence tomography cross-sections show equal retinal thickness (PND56) that is consistent across all mice measured (n=10 mice). **c,** Immunohistochemical staining for *Arr3* shows grossly normal cone morphology at PND70.

3.4.4 Effect of the cpfl10 mutation on mRNA expression

Re-sequencing of genes known to cause achromatopsia is time consuming. Identifying genes that were down-regulated in the retinal transcriptome of *cpfl10* mice would provide a starting point for targeted re-sequencing. A single down-regulated gene in the transcriptome might suggest that gene holds the causative mutation.

To this end, the retinal transcriptome of *cpfl10* mice (n=6) and strain-matched 129S2/SvHsd controls (n=3) was analysed using qPCR (Figure 3.4). The *ActB* reference values across all test plates were reliable and correlated as expected to the total amount of RNA in the test sample. The maximum variance of *ActB* for any given sample across all test plates was 0.3 Cq and the maximum variance between the two most extreme *ActB* values across all samples was 0.65 Cq.

The relative expression of Rhodopsin was significantly lower in cpfl10 mice (hierarchical linear model; P=0.025). This difference was not due sample quality variation as explained above. As noted earlier, the rod ERG function in homozygous *cpfl10* mutants was not significantly different to heterozygous or wild-type litter-mates. No rod ERG function data was recorded for the 129S2/SvHsd strain-matched controls to determine if the significant difference in *Rho* mRNA was correlated with a difference in rod b-waves. One explanation may be that the 129S2/SvHsd controls have a different rod photoreceptor transcriptome and phenotype; more appropriate controls may have been heterozygous or wild-type litter-mates. It is unlikely that a missense mutation in a cone-specific gene would affect Rhodopsin expression in the absence of a cone-rod dystrophy. Mice were all collected at the same time of day; neither had been recently dark adapted beforehand nor recently undergone ERG testing.

All cone-specific genes were significantly down-regulated (hierarchical linear model; P<0.001 for each cone gene). *Cngb3* exhibited the least down-regulation, showing approximately 80% of control expression. *Arr3*

showed the greatest down-regulation, with less than 25% of control expression. Cone arrestin helps reset the cone phototransduction cascade pathway. Without *Cngb3*-mediated phototransduction activity, there would be reduced need for *Arr3* activity.

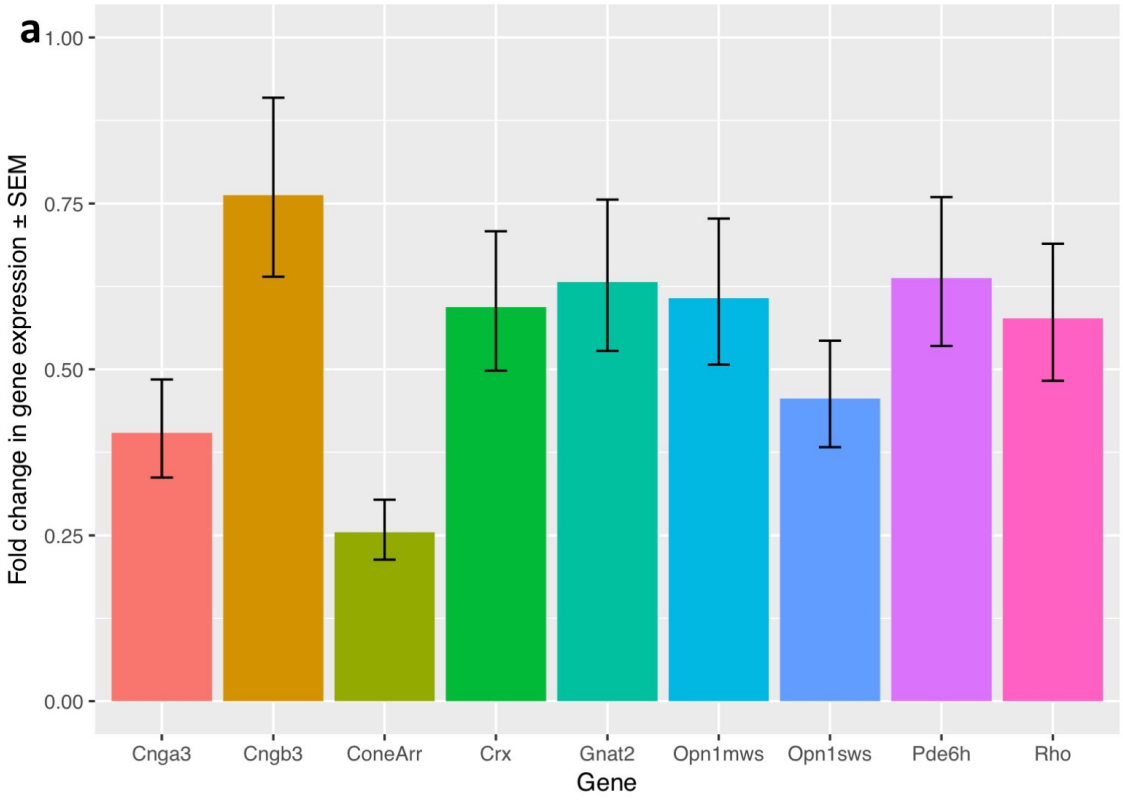


Figure 3.4 | Mutation effect on mRNA. a, All retinal genes were significantly down-regulated in *Cngb3*$^{cpfl10/cpfl10}$ mice compared to strain-matched 129S2/SvHsd controls (hierarchical linear model; P<0.001 for each gene). *Arr3* had the greatest reduction, yet *Cngb3* was least affected.

3.4.5 Mutation analysis

Targeted re-sequencing revealed that affected mice did not carry any of the spontaneous mutations previously found in other inbred lines. No mutations were detected in affected mice during sequencing of 100% of exonic *Gnat2* gDNA and the known *Gnat2*^{cpfl3} exon 6 mutation was excluded [111]. No mutations were found in 70% of exonic *Hcn1* gDNA, which had been previously linked to achromatopsia [154]. The *Syne2* mutation (c.13978C>T;p.Q4660*) was excluded [119]. *Cnga3* was not sequenced as it was excluded earlier by complementation breeding and testing.

A novel missense mutation was identified in exon 6 of the *Cngb3* gene, resulting in a substitution of Histidine for Arginine. The full mutation notation is (NM_013927) c.692G>A; (p.R231H). The mutation introduces a unique AgaLI restriction site that can be exploited in a genotyping RFLP assay to confirm the Sanger sequencing results Figure 3.5.

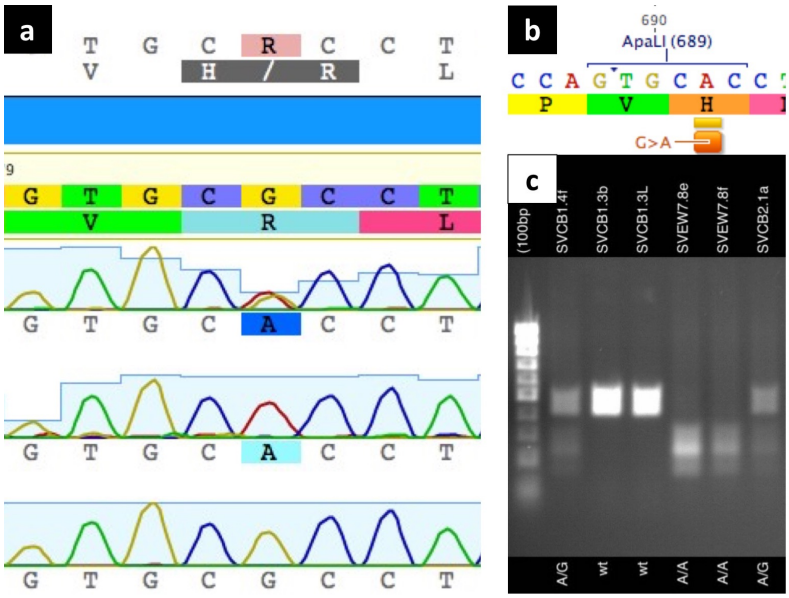


Figure 3.5 | cpfl10 genotyping. **a,** The chromatogram for the c.692G>A mutation is shown for heterozygotes *(top)*, homozygotes *(middle)* and wild-type litter mates *(bottom)*. **b,** The c.692G>A mutation introduces a novel ApaLI restriction site in the *Cngb3* gene sequence. **c,** A restriction fragment length polymorphism assay can thus identify homozygous, heterozygous or wild-type mice; wt band = 470bp, mutant band = 250bp + 190bp fragments. Confirmed Sanger results displayed below each lane show 100% concordance.

Re-sequencing of all F2 progeny (n=59 mice) demonstrated that homozygous (NM_013927) c.692G>A mutations fully co-segregated with the *cpfl10* phenotype (n=15/15). The mutation was also 100% penetrant in the F3 generation. Despite being fully penetrant, the homozygous mutant allele appears to have variable expressivity. Figure 3.6 shows that whilst all homozygous mice across multiple generations have profoundly diminished cone ERG, some individual mice (n=5 out of 17 mice) have a detectable ERG b-wave at the 25 candela single-flash test step. The background noise in ERG testing (approximately 50μV) may be masking any residual cone function in the other 12 mice without visible b-waves.

OMR testing in photopic conditions isolates cone function. OMR showed that all *cpfl10* mice (n=6) have residual cone function (Figure 3.6). This OMR cone function is significantly reduced compared to strain-matched wild-type controls (n=6; Kruskal-Wallis with Dunn's test, P=0.015). However, this residual cone

function is not significantly different to the TKO mice (n=3) without any retinal function (Kruskal-Wallis with Dunn's test, P=0.077). However, this non-significant difference may reflect an underpowered comparison.

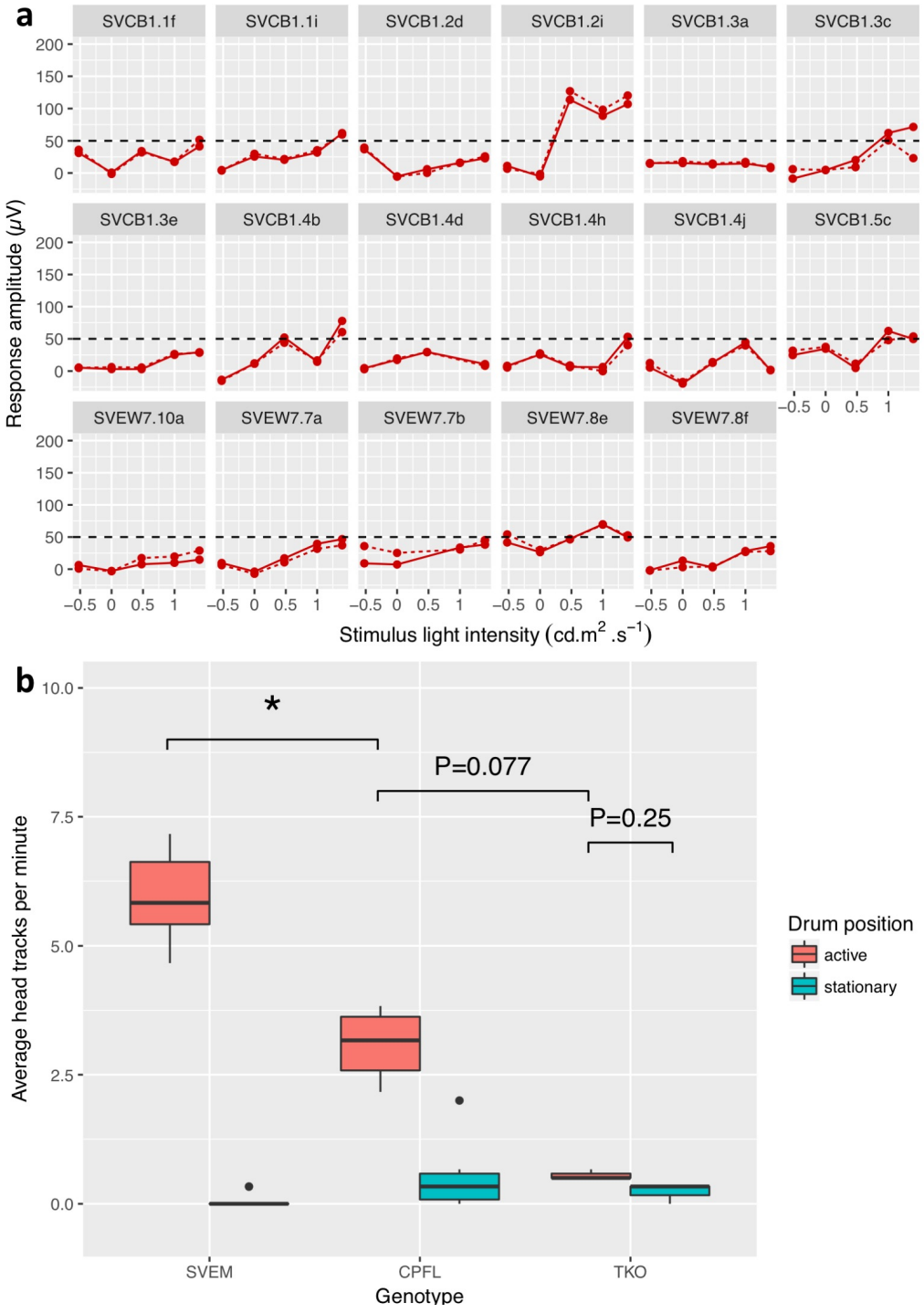


Figure 3.6 | Expressivity of the cpfl10 mutation. **a,** Individual irradiance response curve plots for the homozygous mutant mice (n=17) shows that some mice (n=5) have some residual cone response. The b-wave amplitude at 25cd (log 1.5cd) flash stimulus for these mice is above the 50μV background noise represented by the horizontal dotted line. **b,** Optomotor response testing shows that cone-mediated head-tracking behaviour for homozygous mutant mice (n=6) is diminished compared to wild-type controls (n=6). The diminished cone-function in homozygous mutants appears more than TKO mice (n=3) without retinal function (p=0.077).

The p.(R231H) Arginine residue in Cngb3 is highly conserved across species (Figure 3.7). This Arginine is the first extracellular amino acid immediately adjacent the first transmembrane domain of the Cngb3 protein. The Arginine residue in the same location in Cnga3 is highly conserved across species too. Fewer than 25% of residues are conserved between both Cnga3 and Cngb3 across multiple species (Figure 3.7). The CNG channels are heterotetramers and thus important residues and protein domains share similarities between both component proteins.

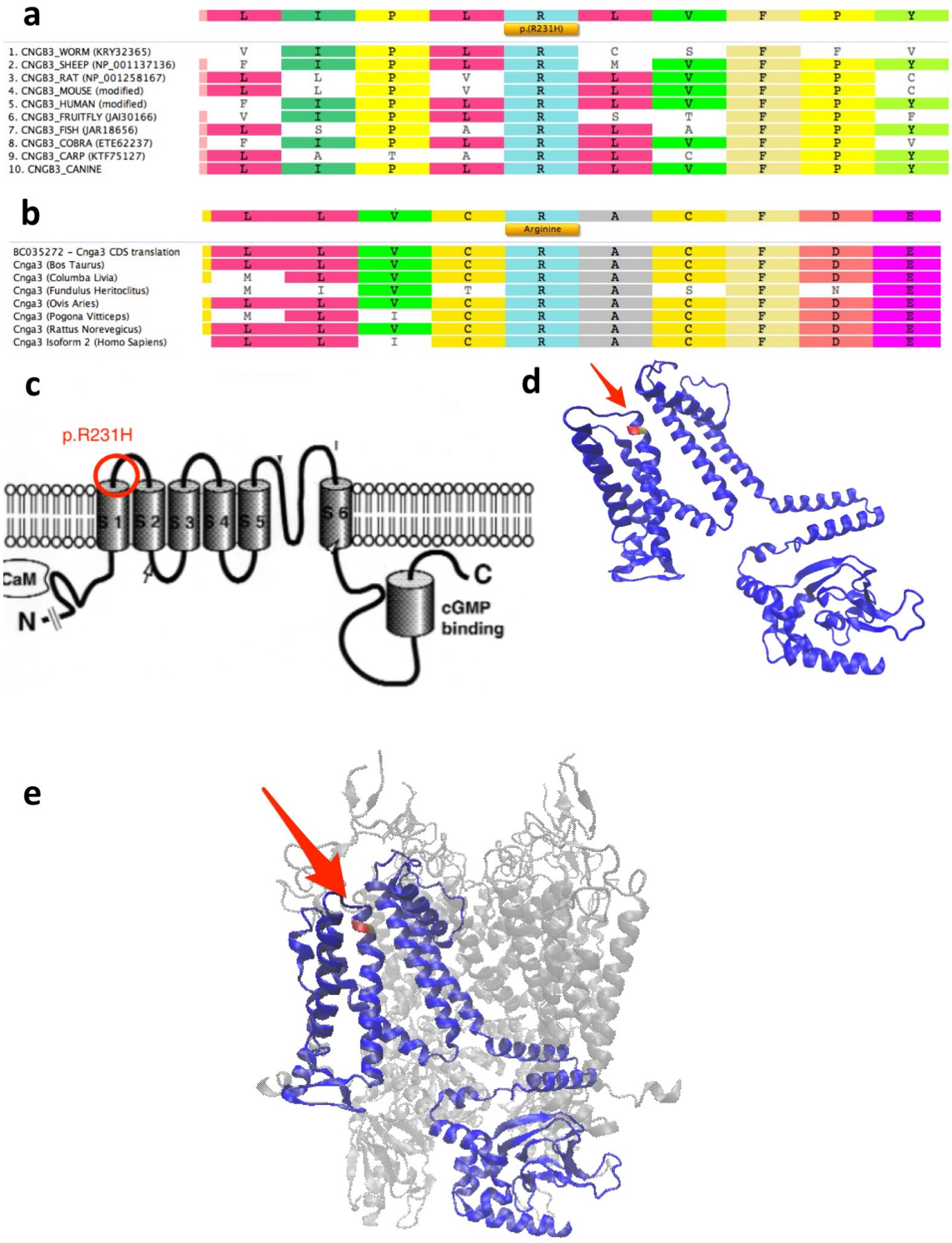


Figure 3.7 | Arginine conservation across species. **a,** The p.(R231H) missense mutation occurs at an Arginine residue conserved across all vertebrates. **b,** The equivalent Arginine residue in *CNGA3* is also highly conserved across vertebrates and other more distant species. **c,** The mutation (red) affects the initial residue of the first extra-cellular loop of Cngb3 *Image reproduced from [158].* **d,** Structural modelling of Cngb3 shows the affected residue (red arrow) and **e,** in the context of the CNG heterotetramer.

3.4.6 Effect of the cpfl10 mutation on protein expression

The previously described Cngb3 knock-out mouse does produce Cngb3 protein [36]; yet this IHC was performed using a custom-generated antibody that is not commercially available. All three of the commercially available antibodies to human CNGB3 (Table F.2) were tested on Opn1.GFP wild-type murine retinal sections at a range of concentrations (1/100, 1/500 and 1/1000). A non-specific binding pattern was observed for two of the anti-CNGB3 antibodies, (Figure 3.8 and Figure 3.9).

ABIN571515 also showed non-specific staining patterns using the normal protocol (Figure 3.10). Yet, when also tested in Opn1.GFP mice at different concentrations of Triton-X detergent permeabilisation incubation (0.1%, 0.2% and 0.3%) there was some success. Figure 3.10 demonstrates isolated instances of GFP and Cngb3 signal co-localisation in the region of the cone photoreceptor outer segments when using 0.3% Triton-X. This is likely a genuine signal, but would require further optimisation to reliably stain all cone photoreceptor outer segments.

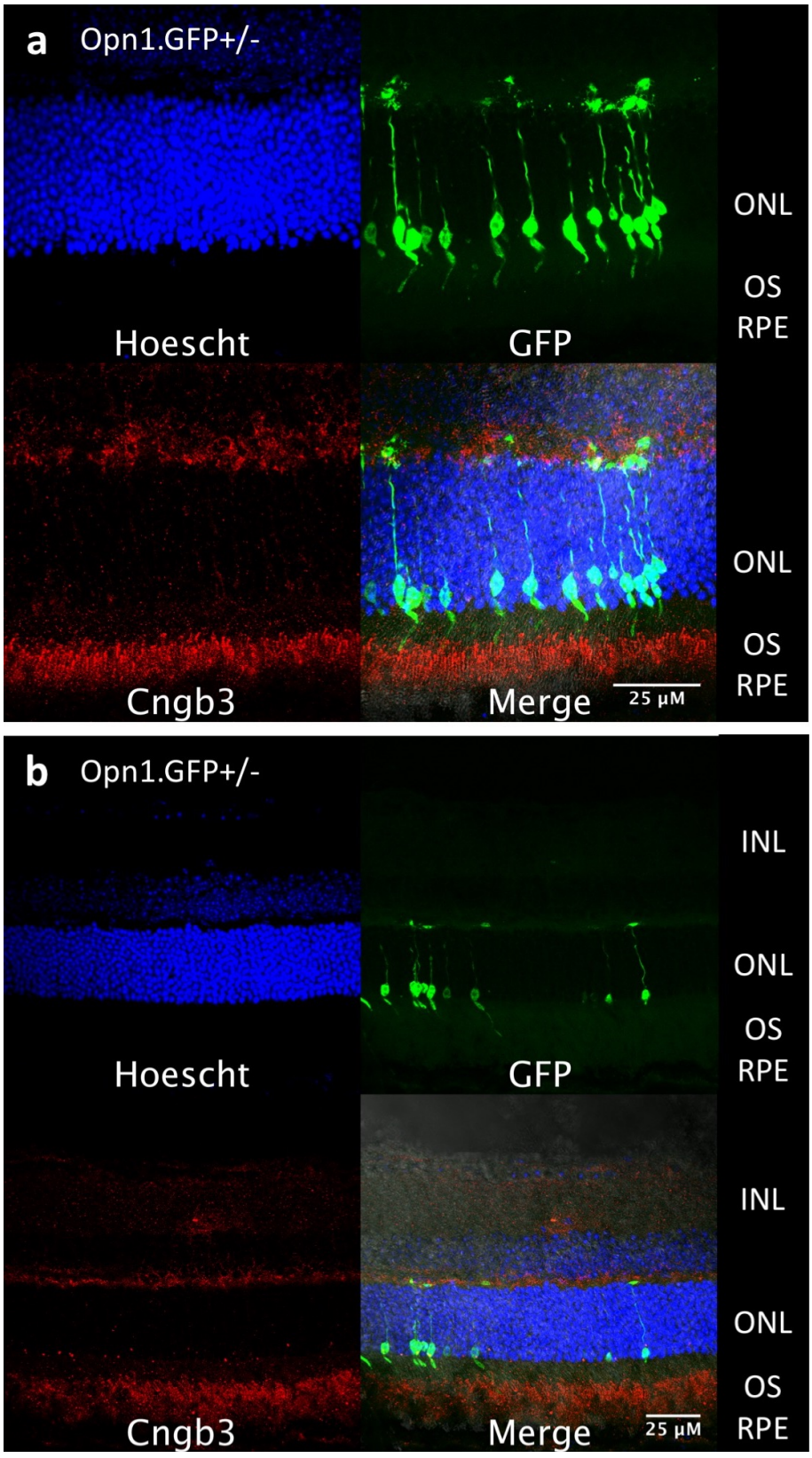


Figure 3.8 | Cngb3 IHC with antibody orb156415. **a,** 63x objective lens Z-stack of a retinal section in Opn1-GFP$^{+/-}$ control mice expressing endogenous GFP in cones. Anti-Cngb3 primary antibody (orb156415) yielded only non-specific staining. **b,** 40x objective lens Z-stack of a different Opn1-GFP$^{+/-}$ mouse showing the same non-specific Cngb3 antibody staining.

The partially-optimised ABIN5715 antibody protocol with a 0.3% Triton-X incubation step was applied to *cpfl10* retinal sections (Figure 3.11). In *cpfl10* mouse retinas showed a non-specific staining pattern without any evidence of GFP and Cngb3 signal co-localisation. Co-localisation was not observed in *cpfl10* mice across two different retinas, examining multiple sections and anatomical locations.

Given the difficulties in optimising any available commercial antibody for Cngb3 IHC, the absence of immunostaining in the *cpfl10* mouse is inconclusive. There is insufficient evidence to make a firm conclusion either way and more work is required to better optimise the antibodies or obtain better options.

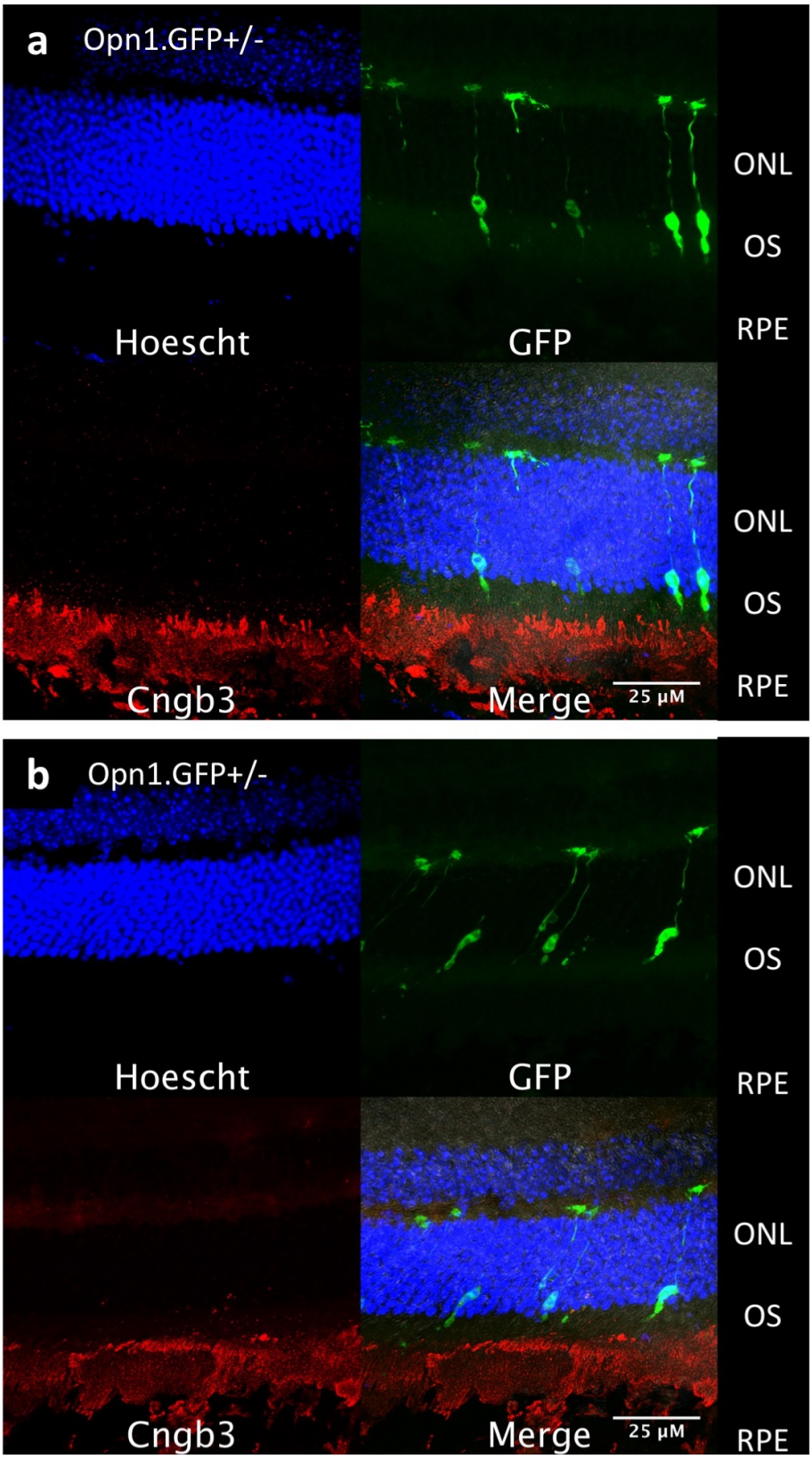


Figure 3.9 | Cngb3 IHC with antibody CPBT-31596RH. a, 40x objective lens Z-stack of a retinal section in Opn1.GFP$^{+/-}$ control mice expressing endogenous GFP in cones. Anti-Cngb3 primary antibody (CPBT-31596RH) yielded dense non-specific staining localised to an area of retinal detachment in the sample, but no outer segment localisation. **b,** 63x objective lens Z-stack of a different region showing the same non-specific Cngb3 antibody staining.

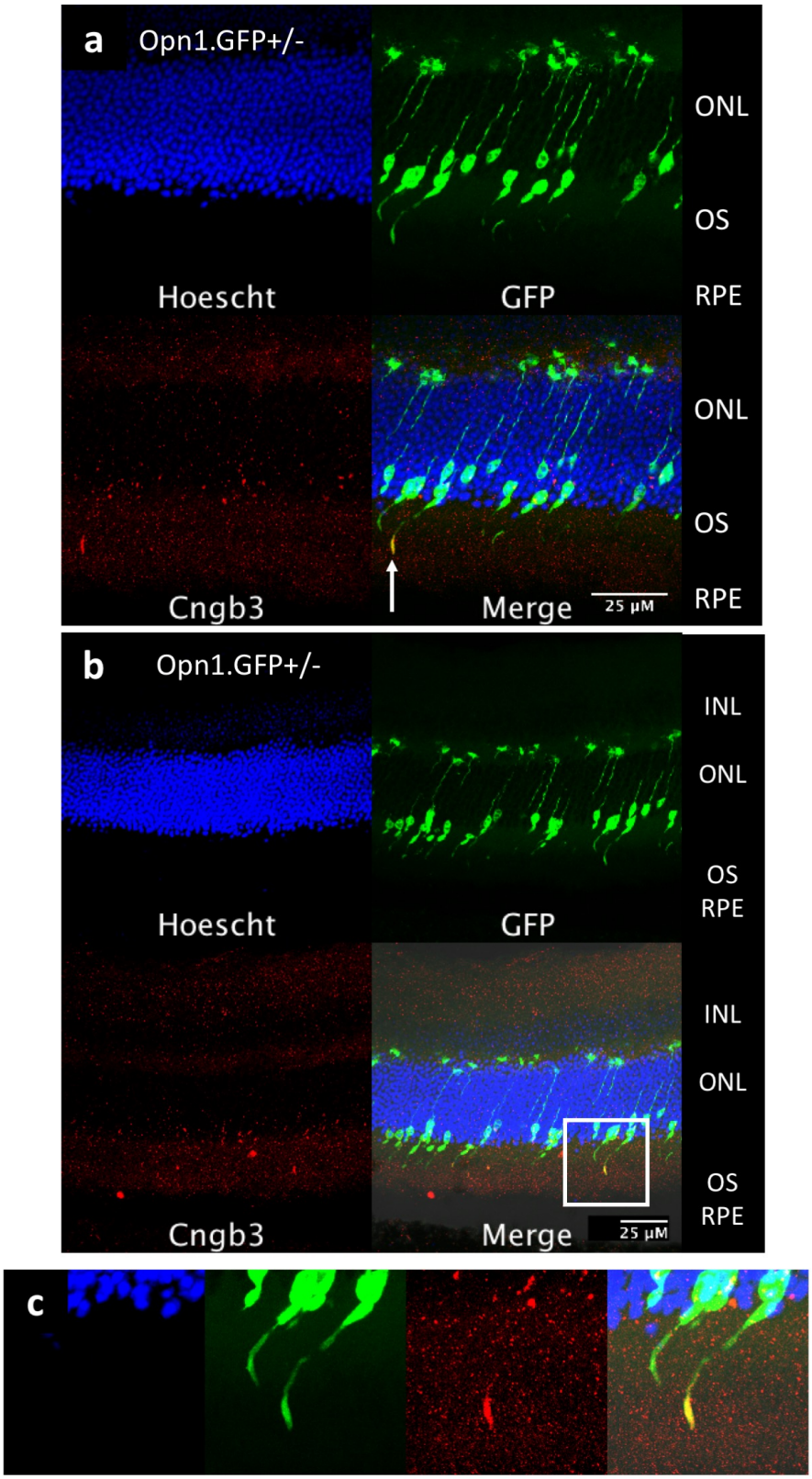


Figure 3.10 | Cngb3 IHC with antibody ABIN5715. **a,** 63x objective lens Z-stack of a retinal section in Opn1-GFP$^{+/-}$ control mice expressing endogenous GFP in cones. Anti-Cngb3 primary antibody (ABIN571515) yielded largely non-specific staining, with isolated co-localisation with cone OS (arrow). **b,** 40x objective lens Z-stack of a different Opn1-GFP$^{+/-}$ mouse. **c,** Enlarged region of interest showing Cngb3 and GFP co-localisation in OS.

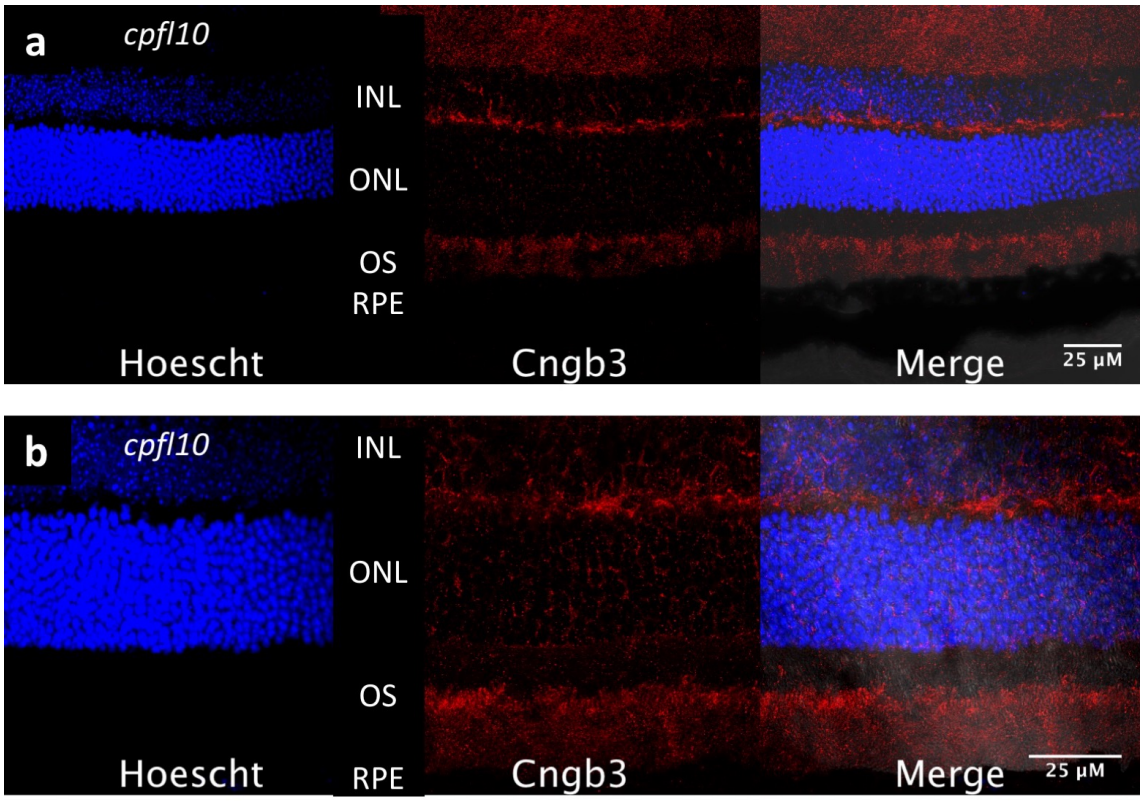


Figure 3.11 | Cngb3 IHC on *cpfl10* mice. a, *cpfl10* mouse retinal section stained with anti-Cngb3 antibody (ABIN571515) and imaged with a 40x objective lens shows no specific pattern of staining. **b,** *cpfl10* mouse retinal section stained with different anti-Cngb3 antibody (orb156415) produced no discernible localisation either.

3.5 Discussion

To our knowledge, this is the first naturally occurring mouse model of achromatopsia. resulting from a mutation in *Cngb3*. A spontaneously occurring G>A nucleotide substitution in exon 6 of *Cngb3* mutates a conserved Arginine residue. The missense mutation is located at the beginning of the first extra-cellular loop of the β-subunit of the cone-specific cyclic nucleotide gated heterotetramer membrane channel. Theoretically, a diminished ability of the mutant membrane channel to close could therefore impair hyperpolarisation in the cone phototransduction cascade. This mechanism could be explored further by transfecting cell cultures with plasmid expressing the *cpfl10* mutant sequence and performing patch-clamp recordings on the cells to assess the contribution of CNG channels in the membrane potential.

Normal cone function is lost in Cngb3$^{cpfl10/cpfl10}$ mice. The severity of cone function loss is more severe than the incomplete achromatopsia observed in the CNGB3$^{-/-}$ mice. This model contains a targeted deletion in exon 6 resulting in a premature stop codon c.733_749del; (p.A247*) and yet still reliably retains 20-30% of wild-type ERG function [159].

Cngb3 forms a heterotetramer with Cnga3; Cngb3 is the minor component and plays a modulatory role [5]. In murine retinal sections, Cngb3 and Cnga3 co-localise and are expressed exclusively in cone photoreceptors [160]. Cnga3 and Cngb3 are expressed exclusively in the cone photoreceptors; Cngb1 and Cnga1 are specific to rod photoreceptors. Immuno-precipitation of Cnga3 from mouse retinas can also be successfully co-stained for Cngb3, showing the necessary role of Cngb3 in forming CNG channels [160]. The subunit configuration of cone CNG channels can be either 3A:1B [4, 6] or an equal 2A:2A configuration [4]. Regardless, a normally functioning CNG channel requires at least one normal Cngb3 subunit, a clear mechanism by which the *cpfl10* mutation could impair cone function.

The affected Arginine residue is one of only 48 residues in human CNGB3 conserved across all vertebrates. Missense mutations account for 4% of all human CNGB3 achromatopsia mutations, but there are currently no reported human cases of mutation at this residue [161]. The genetic cause of achromatopsia in nearly 10% of the Pinegalap islander population is also a *CNGB3* missense mutation at a highly conserved residue. c.1304C>T; (p.S433F). The *Cngb3^{cpfl10}* mouse model provides a more appropriate pre-clinical model for developing genetic treatments for missense mutations in humans than the existing *Cngb3$^{-/-}$* deletion-truncation mouse model. Furthermore, this model may be beneficial in further exploring and understanding any differences in treatment effect observed in the current *CNGB3* clinical trials (NCT03001310 and NCT02599922). For example, *CNGB3* gene therapy vectors might be more effective in cases of premature stop codons rather than missense mutations because of how the mutated transcript and

peptide are handled by cellular machinery. NMD mechanisms might prevent excess protein accumulation. Such a difference could be explored in a direct AAV comparison in the two different missense and truncation mouse models of *Cngb3* achromatopsia.

The qPCR analysis of the retinal transcriptome did not accelerate the targeted re-sequencing process. All of the cone phototransduction genes were down-regulated, but *Cngb3* was least affected. The results of this qPCR analysis were confounded by the strain differences between the *cpfl10* mice and 129S2/SvHsd controls, despite being of similar origin. The genetic drift over time in the isolated *cpfl10* colony appears to have resulted in widespread significant differences in the retinal transcriptome, including *Rho* levels, that invalidate the 129S2/SvHsd mice as controls for this experiment. Instead, heterozygous or wild-type litter mates of the F2 progeny would likely yield more appropriate controls.

Given the difficulties in optimising any available commercial antibody for Cngb3 IHC, the absence of immunostaining in the *cpfl10* mouse is inconclusive. There is insufficient evidence to make a firm conclusion. More work is required to better optimise the existing three commercial antibodies for use in mouse retinas or a collaboration establish to obtain a Cngb3 antibody optimised in another laboratory. Clearly measuring the protein expression and localisation of Cngb3 would add important information to the understanding of the *cpfl10* model and mechanisms of cone dysfunction.

In silico analysis of the mouse mutation predicted a 'deleterious' effect, with a PROVEAN score [162] of -4.985, well beyond the cut-off of -2.5. Based on cross-species conservation, the predicted human mutation (NM_019098)c.764G>A; p.(R239H) was explored using peer-reviewed Poly-Phen II [163] *in silico* tools and a score of 1.000 predicted this equivalent mutation to be 'probably damaging' in humans.

There is substantial evidence to support the claim that the identified *Cngb3* missense mutation causes the phenotype. If additional evidence were required,

a causative autosomal-recessive mutation in mice can further validated in three ways. Firstly, complementation breeding with another affected mouse line to produce compound heterozygotes that reproduce the phenotype. Secondly, apply CRISPR-Cas9 or another DNA editing technology to delete or mutate the same nucleotides and confirm this changes leads to the same phenotype. Thirdly, rescue the phenotype using gene therapy rescue to express a functional copy of the mutated gene (not effective in dominant negative or gain-of-function dominant mutations). Two of the previously described cone photoreceptor function loss (cpfl) mouse models have been functionally rescued using AAV gene therapy [34, 31]. These additional levels of evidence have diminishing utility when the identified mutation is a previously published causative mutation for this phenotype.

The *Cngb3*$^{cpfl10/cpfl10}$ mutation is fully penetrant but has variable expressivity. The five homozygous mutants demonstrating detectable residual cone ERG b-waves likely represent baseline 'noise' ($\approx \pm 30\mu$V) in the ERG recording system exceeding, and thus masking, the small amplitude of residual b-waves in mutant mice. This explanation is supported by the small sample of mutant mice that demonstrated a positive response on OMR testing in cone-isolating conditions.

However, these five mice may represent variable phenotype expressivity. Diminished residual cone function may be retained in a stochastic manner. Genetically identical *C. elegans* subjects have highly variable mutant gene transcription that can expose otherwise buffered stochastic variability in gene expression, leading to pronounced phenotypic variation [164]. In the same way, stochastic variation in the *Cngb3*$^{cpfl10/cpfl10}$ cone cell transcriptome may randomly permit residual b-waves.

The *cpfl10* mouse model is a striking example of the effect of a single gene in the cone phototransduction cascade impairing cone function when altered. There are two examples where AAV expression of a functional *Cngb3* phototransduction enzyme rescued cone function [165, 36]. In the instance of lost cone photosensitivity in RP, a similar AAV-mediated expression of cone

phototransduction genes might improve or prolong cone photosensitivity.

3.6 Conclusion

This chapter identified the new *cpfl10* mouse model of achromatopsia. Tsing ERG and OMR testing, the electrophysiological and functional vision phenotype was characterised as an stationary and isolated complete cone dysfunction. Through a detailed breeding program, *Cnga3* was excluded as the causative mutation through complementation breeding and the inheritance pattern was shown to be recessive. Targeted re-sequencing identified the causative mutation as (NM_013927)c.692G>A; p.(R231H) and excluded other published human and mouse mutations. The causative mutation fully co-segregated with the cone phenotype, is a fully conserved residue across species and scores very highly on two different *in silico* causative mutation prediction algorithms. mRNA and protein expression analysis was inconclusive because of technical constraints.

Given that *Cngb3* is known to cause achromatopsia in both mice and humans — and given that the other common mutations have been excluded — it is reasonable to conclude that the *cpfl10* mouse model is caused by the mutation (NM_013927)c.692G>A; p.(R231H).

4

CONE CELL QPCR

4.1 Introduction

The core hypothesis of this thesis is that, in RP, the loss of photosensitivity in cone photoreceptors occurs much earlier than cone cell death and is driven by down-regulation of select cone phototransduction genes. Furthermore, this loss of cone photosensitivity can be reversed by supplementing the cone photoreceptor transcriptome by exogenous over-expression of select cone phototransduction genes.

In considering a restorative therapy that might reactivate dormant cones in end-stage RP, it is important first to establish the molecular changes that occur in these cells as a result of rod loss. The relationship between declining cone photosensitivity and changes in cone-specific gene expression in RP has not been studied in detail. This chapter will correlate the timing and magnitude of change in cone-specific genes to phenotypic changes in retinal structure and function.

The molecular approach of re-expressing down-regulated genes or RNA transcripts has been successful in oncology. There are multiple examples of genes or gene clusters that have been re-expressed in tumour cells, resulting in correction of down-regulation deficits and phenotypic changes [166, 167, 168,

169]. In retinal research, cone rescue has been demonstrated by correcting gene pathway down-regulation [62]; although this paper used pharmacological mechanisms rather than AAV gene therapy techniques.

Whole transcriptome analysis of gene pathway changes has been performed in mouse models of RP using Affymetrix microarray [62]. The insulin/mTOR pathway was the most down-regulated gene cluster at the onset of cone death. Insulin treatment prolonged cone survival, but electrophysiological and functional differences were not measured. Review of the raw Affymetrix data (personal communication; C Punzo and C Cepko) identified that a number of cone phototransduction genes, as well as *Crx*, were also down-regulated during degeneration.

What precise difference in cone-specific genes would be observed in degenerate retinas when examined with greater sensitivity and greater accuracy using the qPCR technique? How would this down-regulation correlate with phenotypical changes and would such differences reveal an appropriate candidate gene for over-expression gene therapy treatment?

4.1.1 RNA quantification technologies

Early RNA quantification technology compared RNA expression using Northern Blot. RNA molecules were separated by molecular weight using gel electrophoresis and then transferred by capillary transfer to a blotting membrane [170]. RNA molecules were identified on the blotting membrane using hybridisation probes [170]. The Northern Blot technique is constrained by the low number of targets, risk of RNA degradation and low sensitivity due to signal strength. The subsequent development of RNase protection assays improved sensitivity, particularly in partly degraded samples [171].

Techniques that first reverse transcribe RNA to cDNA are more robust as the information contained in the transcriptome is stabilised and invulnerable to degradation [172]. The qPCR, microarray and RNA-seq techniques all quantify cDNA levels [173].

4.1.1.1 Microarray

Microarray technology is capable of parallel gene expression profiling, providing higher throughput than qPCR [173]. Microarray testing surfaces use an ordered array of nucleotide probes to target pre-determined fragments of the transcriptome [174, 175]. Prepared cDNA is exposed to the probes, which then hybridise the appropriate target [175]. Hybridisation is then detected using fluorescent or luminescent signals; relative signal strength measures differential transcript expression [175].

Microarray performance is limited by issues of cross-hybridisation, non-specific hybridisation and limited dynamic range [176]. Low target mRNA concentration may result in false negatives, thus microarray has a lower sensitivity than qPCR. Similarly, high target mRNA concentration may saturate the probe, making it difficult to identify increased or high-concentration expression [177]. The confounding effect of sensitivity dynamic range is target dependent [177]. The volume of data produced by microarray also requires more sophisticated *in silico* analysis techniques than the qPCR $\triangle\triangle$Cq method [178].

4.1.1.2 RNA-seq

RNA-Seq, or whole-transcriptome shotgun sequencing, performs parallel in-depth nucleotide sequencing of prepared transcriptome cDNA fragments [179]. RNA-seq allows *de novo* assembly of the transcriptome sequence, whereas microarray requires knowledge of the transcriptome target nucleotide sequences *a priori* in order to design the hybridisation probes [179]. RNA-Seq is therefore able to identify alternative isoforms, genetic variants and SNPs, and confirm predicted intron-exon boundaries [176]. RNA-seq is dorsal to microarray in detecting RNA at low concentrations and the results of these two techniques correlate well [176]. Recent work has shown equivalent accuracy and precision in differential transcriptome analysis between RNA-Seq and qPCR [180].

However, sequencing individual RNA-Seq samples remains expensive, particularly after including multiple biological replicates [179]. Furthermore, the

high-volume sequencing data generated requires complex specialist *in silico* analysis [181]. This large financial and analysis burden would only be justified if the study sought to achieve more a focussed analysis of differential cone gene expression.

4.1.1.3 qPCR

Reverse transcription qPCR (RT-qPCR) uses the polymerase chain reaction to amplify starting concentrations of specific genes. Dyes included in the reaction mixture produce increasing fluorescent signal as amplification proceeds [182]. Measuring this detectable signal during the exponential amplification phase allows highly specific quantification of target nucleotide starting concentration [182, 183, 184].

There is no significant systematic difference in specificity or sensitivity between the main fluorescent dyes - SYBR, Taqman (hydrolysis probes) or LightCycler (dual hybridisation probes) - when appropriately optimised beforehand [185, 186, 187]. The MIQE consensus guidelines recommend avoiding proprietary Taqman probes with unpublished sequences [184]. The SYBR green qPCR system permits full control of the primer nucleotide sequence and is more cost effective.

When examining small numbers of target genes, such as the cone phototransduction cascade, qPCR is more rapid, sensitive, displays a broader dynamic range and is less complex to analyse than microarray.

4.1.2 Selection of qPCR test genes

All genes involved in the cone phototransduction cascade were included in the final test panel. Down-regulation of some or all of these genes may underpin the loss of cone phototransduction. Additionally, *Crx* was included because of its role in photoreceptor differentiation and cone opsin expression, as detailed in subsubsection 1.1.3.2. In particular, mice with *Crx* mutations have down-regulation of genes in the phototransduction cascade [15]; an important

action to reverse if *Crx* down-regulation occurs in RP mice. Related transcription factors, such as upstream *Otx*, *RorB2* and *Trb2*, were initially excluded from testing in the face of the high-volume of experiments.

4.1.2.1 Crx isoforms 1 and 2

The full length NM_001113330.1 (Crx mRNA isoform 2) and NM_007770.4 (Crx mRNA isoform 1) share 97.5% homology. The differences are confined to the first 125bp of the transcript, prior to the first exon. *Crx* mRNA primers were designed to regions downstream of the non-homologous region to capture both isoforms in the final results.

4.1.3 Correlating gene expression analysis to phenotype

Changing gene expression is better understood alongside phenotypic data. The rate of loss of the outer retina during RP degeneration will mark the major phases of rod death and will be measured with OCT. The magnitude and pattern of *in vivo* GFP expression changes will estimate the major phases of cone death and will be measured with cSLO. The loss of normal cone electrophysiology (ERG) and functional cone vision (OMR) will highlight the functional relevance of down-regulated cone genes.

4.2 Aims & objectives

This first aim of this chapter is to characterise the cone phototransduction dysfunction in an existing Rhodopsin knockout mouse model of Retinitis Pigmentosa (*Rho*$^{-/-}$) and correlate these changes to changes in gene expression. The second aim of this chapter is to identify one or more candidate cone genes for therapeutic over-expression in *Rho*$^{-/-}$ mice to prevent or delay cone phototransduction dysfunction.

The objectives of this chapter are:

1. Assess the retinal electrophysiology and function in the Rho$^{-/-\ B6TgOPN1LW\text{-}EGFP+/-}$ mice mice compared to wild-type strain-matched controls using ERG and OMR
2. Measure the retinal architecture and thickness, with OCT, in Rho$^{-/-\ B6TgOPN1LW\text{-}EGFP+/-}$ mice over the stages of retinal degeneration
3. Measure the effect of the B6$^{TgOPN1LW\text{-}EGFP}$ allele on retinal electrophysiology using ERG
4. Develop a reproducible method for manually quantifying cone survival *in vivo* by measuring B6$^{TgOPN1LW\text{-}EGFP}$ signal in *en face* cSLO retinal images over time
5. Measure the sampling bias in using FACS to isolate cones in B6$^{TgOPN1LW\text{-}EGFP+/-}$ mice
6. Establish the exact nucleotide sequence of GFP in B6$^{TgOPN1LW\text{-}EGFP+/-}$ mice, thereby allowing accurate primer design
7. Measure and map the dorsal-ventral distribution gradient of GFP in the cones of B6$^{TgOPN1LW\text{-}EGFP+/-}$ mice
8. Rationalise whether the FACS technique or double-normalisation to GFP qPCR signal is the most appropriate control for the larger qPCR experiment characterising cone phototransduction genes

9. Design a large cohort of primer pairs for the chosen cone phototransduction genes and test each pair in an optimisation experiment to select the most efficient test primer pair for each gene

10. Measure the magnitude and timeline of changes in cone phototransduction cascade gene expression levels in Rho$^{-/-\ B6TgOPN1LW\text{-}EGFP+/-}$ mice using qPCR

11. Correlate the changes in gene expression to the changes in structural and functional phenotype

12. Identify one or more candidate genes for therapeutic over-expression in Rho$^{-/-\ B6TgOPN1LW\text{-}EGFP+/-}$ mice using an AAV vector

13. Identify the most appropriate time-points to perform subretinal injections on Rho$^{-/-\ B6TgOPN1LW\text{-}EGFP+/-}$ mice to maximise the chance of gene therapy success

14. Rationalise the optimal time-points for functional testing in AAV treated Rho$^{-/-\ B6TgOPN1LW\text{-}EGFP+/-}$ mice to detect any treatment benefit

4.3 Materials & methods

4.3.0.1 Animals

Animals were maintained as detailed in section 2.1. Three genotypes of mice were used in the OCT, SLO, ERG, OMR and qPCR experiments: Rho$^{-/-\ B6TgOPN1LW\text{-}EGFP+/-}$ hybrids, B6$^{TgOPN1LW\text{-}EGFP+/-}$ and wt (B6$^{TgOPN1LW\text{-}EGFP-/-}$ litter-mates). The genotype status of each mouse was confirmed using the eartag PCR genotyping technique.

4.3.0.2 *In vivo* procedures

ERG, OCT and cSLO were performed on anaesthetised mice using the protocols detailed in section 2.2. OMR was performed on unrestrained conscious mice using the protocol described in subsection 2.2.5.

4.3.0.3 FACS

The subsection 2.3.6 details how B6$^{TgOPN1LW\text{-}EGFP+/-}$ retinas were dissociated using Papain, filtered and pre-stained with Propidium Iodide. FACS was performed on external equipment with assistance from a technician in defining the fluorescence gates and collecting the final samples.

4.3.0.4 IHC

IHC was performed using *Arr3* primary antibody, DAPI stain and Alexa-Fluor568 secondary antibody as per the protocol detailed in subsection 2.7.2. Full details of the antibodies and blocking serums are available in Table F.2. Images were acquired using the confocal microscope as outlined in subsubsection 2.7.4.1 and analysed using ImageJ Fiji (Table E.1).

4.3.1 qPCR

qPCR quantification of messenger RNA (mRNA) expression aims to quantify the inherent variation in mRNA between different conditions at a given time or over multiple time-points. However, measured mRNA levels can also vary due to sampling error or variation in extraction and purification techniques [172]. mRNA can be degraded by incorrect pre-processing or during isolation steps; techniques may also purify inhibitor molecules or alter reverse transcription efficiency [183]. Suitable normalisation techniques must be used in order to control for these sources of error, many of which should be combined in the same protocol [188].

4.3.1.1 Sampling error

Firstly, the processed tissue must have a uniform volume between samples and each be a representative sample of the larger organ [184]. For example, colon biopsies not being standardised for size, depth and location of collection [189]. In the case of whole retina sampling, the extraction and processing of the full neurosensory retina is a complete enumeration of retinal cells; a census not a

sample.

Secondly, the cell type of interest must constitute a stable proportion of the total sample collected. For example, the declining number of T-cells as a proportion of whole blood samples in HIV+ patients as the disease progresses [190]. Similarly, the cone photoreceptor population changes minimally as wild-type mice age, but declines over time in diseased $Rho^{-/-}$ $B6TgOPN1LW\text{-}EGFP^{+/-}$ mice. It would be misleading to directly compare these mice on retinal volume alone and controlling for declining cone cell population requires a cell-type specific marker.

The $B6^{TgOPN1LW\text{-}EGFP}$ mice express green fluorescent reporter protein in a subpopulation of cone photoreceptors and can be used to normalise relative differences in declining cone populations. FACS pre-processing or double-normalisation to GFP transcript levels are two alternative methods that will be compared.

4.3.1.2 RNA integrity and quantification

Poor RNA integrity significantly affects qPCR performance [191]. Slight differences in RNA integrity between samples can cause 2- to 7-fold differences in relative gene expression [192]. This difference is neutralised if the samples have equivalent levels of degradation [193]. Important considerations include preventing RNA degradation, measuring degradation after processing, measuring purity and standardising

RNA can be degraded by ribonucleases (RNases), which are present in biological materials and are a frequent contaminant of laboratory workspaces and equipment. UV light alters RNA by introducing crosslinks. The proprietary RNAlater stabilisation solution inactivates RNases and has been shown not to cause systematic differences in gene expression profiles after storage for 1 week at room temperature [194] and up to many months at -20°C (manufacturer guidance).

After processing the sample, overall RNA degradation can be estimated

using the 28S:18S area ratio; degradation is greater the further the ratio deviates from 2 [192]. Traditional Ethidium bromide agarose gel quantification of 28S and 18S ribosomal RNA (rRNA) band density requires high volumes of precious RNA sample (2μg). Microfluidic capillary electrophoresis can quantify the ratio with smaller quantities of RNA (200pg) [192], but is not available in this laboratory. Alternatively, spectrophotometry wavelength ratios (A_{260}/A_{230} and A_{260}/A_{280}) is a quick method for estimating sample purity and quantity, but has limitations, particularly in the presence of impurities [192].

Using spectrophotometry ratios, the quantity and quality of RNA will be formally assessed prior to reverse transcription. There is a positive correlation between the RNA concentration isolated and the qPCR estimation of the amount of test gene cDNA [188].

4.3.1.3 Appropriate reference genes

The final resolution of qPCR is determined by the error of the reference gene. The normalisation error for a single unvalidated control gene can differ by 3.0- and 6.4-fold differences in 25% and 10% of cases respectively [195]. Multiple reference genes can substantially reduce this reference error; three or more proper reference genes are recommended to reduce this error and give reliable normalisation [195]. However, each additional reference gene increases the number of qPCR test plates by 50%, a significant consideration in a project already planning 45 or more 96-well test plates.

Actb encodes a highly-conserved cytoskeletal protein involved in cell motility and integrity. *Gapdh* encodes a catalyst of carbohydrate metabolism. Both genes are ubiquitously expressed in all murine tissues at greatly varying reads per kilobase transcript per million mapped reads (RPKM) [196, 197]. Multiple primer pairs for both reference genes will compared on positive control samples during the optimisation step and an appropriate primer pair selected for the final reference.

4.3.1.4 Primer efficiency

qPCR primer efficiency estimates can vary by up to 42% across multiple test plates with insufficient technical replicates [182]. However, primer efficiency is reproducibly stable on a single platform, particularly when using technical triplicates and a dilution series produced using large volumes to minimise pipetting error [182]. Equivalent primer efficiency between targets is vital for producing reliable $\triangle\triangle$Cq analysis of differential gene expression.

4.3.1.5 qPCR technical methods

Retinas were harvested from 4-5 B6$^{\text{TgOPN1LW-EGFP+/-}}$ and Rho$^{\text{-/-}}$ B6TgOPN1LW-EGFP+/- mice at 2, 6, 12, 17 and 25 weeks of age. Retinas were harvested from 3-4 B6$^{\text{TgOPN1LW-EGFP-/-}}$ mice at 2, 6, 12 and 17 weeks of age.

Retinal samples were extracted from mice as detailed in subsubsection 2.3.7.1 and transferred directly into RNAlater and stored at -20$degree$C until mRNA extraction. All workspaces and equipment were pre-treated with RNAseZap wipes at each step. Both retinas of each mouse were combined for RNA extraction and cDNA transcription.

qPCR was performed as detailed in subsubsection 2.3.8.3. All reactions were performed as technical triplicates; negative and positive controls were included across plates. Primers were optimised on B6$^{\text{TgOPN1LW-EGFP+/-}}$ positive control samples, across a robust 3-5 point 10-fold dilutions series.

The MIQE consensus guidelines [184] are the gold standard for replicable and reproducible qPCR gene expression studies. The guidelines provide a checklist of 56 pieces of essential information that should be provided with each qPCR experiment. A further 27 pieces of desirable information should also be volunteered where available. These details are provided throughout the methods.

4.3.1.6 Statistical analysis of qPCR

A hierarchical quadratic polynomial linear model was fitted to the final data set using the statistical methods described in subsection 2.8.2. Assistance was provided in person by Professor Dan Lunn at University of Oxford Department of Statistics.

The .csv results files were combined into a single data frame for analysis using the `dplyr`and `tidyr` package in the `R` programming language. All data-cleaning and other handling before modelling was explicitly recorded as per reproducible research guidelines [198, 199, 200].

4.4 Results

4.4.1 *In Vivo* OCT measurements

A cross-sectional case-control study of the natural history of OCT measurements was performed on both eyes in $B6^{TgOPN1LW\text{-}EGFP+/-}$ and $Rho^{-/-\ B6TgOPN1LW\text{-}EGFP+/-}$ mice (n=33 mice). Figure 4.1 shows that $B6^{TgOPN1LW\text{-}EGFP+/-}$ controls did not degenerate over time (p=0.40) and did not differ on the ventral-dorsal axis (p=0.71).

$Rho^{-/-\ B6TgOPN1LW\text{-}EGFP+/-}$ mice degenerated rapidly ($p<0.001$) and the outer retina was completely lost by 17 weeks of age. After 17 weeks there was no further loss in the total retinal thickness, showing that the degeneration was confined to the outer retina. There was no difference in the rate of degeneration between the ventral and ventral retina (p=0.19).

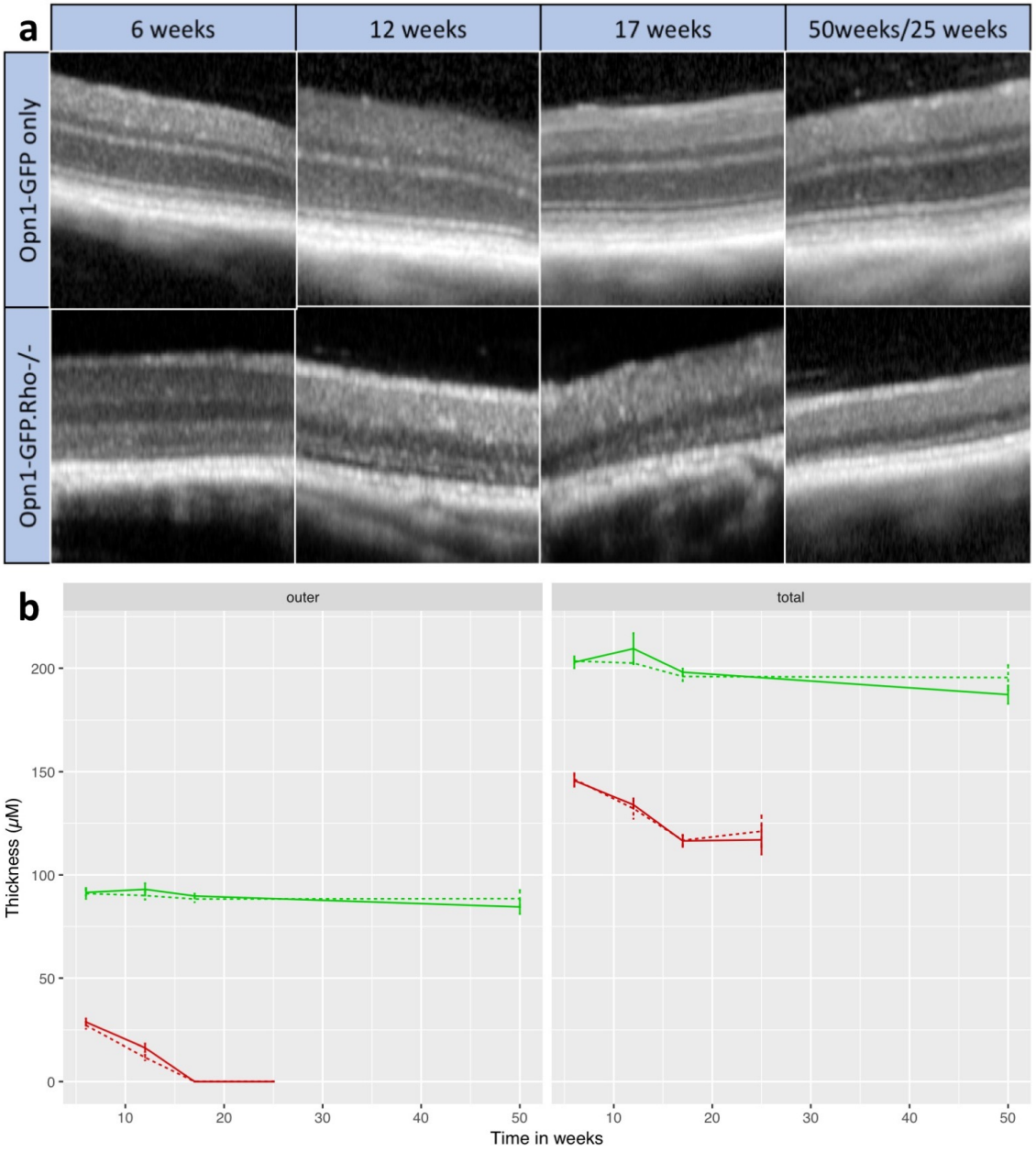


Figure 4.1 | OCT phenotype. a, Representative OCT images show stable retinal thickness in the control B6$^{TgOPN1LW\text{-}EGFP+/-}$ mice up to 50 weeks (top row; green), but rapidly declining outer retinal thickness in the Rho$^{-/-}$ B6TgOPN1LW-EGFP$^{+/-}$ mice (bottom row; red). **b,** Manual measurement of the total retinal and outer retinal thickness (n=33 mice) shows no difference in the mean thickness (μM$\pm$SEM) between the dorsal (solid line) and ventral (broken line) retina.

4.4.2 Validation of *In vivo* cSLO manual counts

A cross-sectional case-control study of the natural history of *in vivo* retinal GFP signal was performed on a different cohort of mice using SLO. B6$^{TgOPN1LW\text{-}EGFP}$ mice were compared to Rho$^{-/-}$ B6TgOPN1LW-EGFP$^{+/-}$ mice at 6, 12, 17 and 25 weeks

(n=45 mice). Figure 4.2 shows how semi-crescent regions of interest were then systematically sampled from the *en face* SLO image as described elsewhere [201]. The sample surface area was sufficiently constrained for manual counting, whilst also avoiding spherical aberration in the image periphery. Semi-crescent sampling also minimised the effect of dark retinal vessels on count values in each region of interest, as well as excluding the optic disc and adjacent pixels.

Discrete circular fluorescent signals larger than approximately 30 pixels, termed *particles*, were counted manually using the ImageJ counter plugin; overlapping particles were counted as discrete occurrences where appreciable. A small pilot count in images captured at 60%, 70%, 80%, 90% and 100% detector sensitivity revealed that images captured at 100% sensitivity yielded higher particle counts yet equivalent coefficient of variance. This was likely a product of the wider dynamic range at higher sensitivity detecting weaker GFP signals; a more representative sample of the remaining cell population. Thus the final manual counts were sampled from images captured at 100% detector sensitivity.

The 100% sensitivity images (n=90) were quality controlled before performing manual counts. A total of 10 images were excluded due to poor technical quality (11%); namely, media opacities casting shadow or severe chromatic aberration. Severe chromatic aberration occurred in four images with severely defocussed fluorescent particles and equivalent dioptric focus in sequential IR and BAF images.

There is no published methodology for manual or automated counting of GFP signal in SLO images of mouse retina. New methodologies should be evaluated for accuracy, precision, repeatability and variability.

Variability within individual mice and reliability of the counts is explored in (Figure 4.2); a Bland-Altman plot [48] shows the difference between the corresponding regions of the left and right eye. Theoretically, the differences between eyes are minimised by reproducible examiner counting technique and equivalent rates of cell loss between eyes in a given mouse. However, the

differences between the left and right eyes are not normally distributed (Shapiro-Wilk, p=0.002) and skewed because of higher outlier counts in the right eye, particularly at higher mean counts.

The precision of the manual count technique in this dataset varies by age, as best conveyed by the coefficient of variation (cv). The cv expresses the standard deviation as a percentage of the sample mean; variation relative to observation size. The cv in mice at 6 weeks is 23%, but increases in $Rho^{-/-\ B6TgOPN1LW\text{-}EGFP+/-}$ mice to 60% from 17 weeks onwards. The increasing cv in $Rho^{-/-\ B6TgOPN1LW\text{-}EGFP+/-}$ mice over time may reflect the migration of macrophages into the retina as part of the degenerative process; an increasing background artefact that masks that true trajectory of the final period of cone loss and may reduce the accuracy of this technique in this final phase.

Inter-observer variability was not assessed for manual counts of the primary dataset, but was evaluated against a different dataset. Test-retest variability was not assessed, but could have been evaluated by repeated measures on the same mice on sequential days. There is no gold-standard of *in vivo* cone imaging by which to measure accuracy.

4.4.2.1 Results of cSLO manual counts

A hierarchical linear model was fitted to the SLO manual count data as described in subsection 2.8.2 and the graphical model predictions are shown in Figure 4.2. The $B6^{TgOPN1LW\text{-}EGFP+/-}$ mice showed fewer particles in the ventral region (-46$\pm$11; p=0.002), but no significant reduction in particle count over time (p=0.665). $Rho^{-/-\ B6TgOPN1LW\text{-}EGFP+/-}$ mice began with an equivalent number of particles as controls and the ventral region also showed significantly fewer particles than the dorsum (-56$\pm$12; p<0.001). The ventral reduction was more severe in $Rho^{-/-\ B6TgOPN1LW\text{-}EGFP+/-}$ mice than controls (-10$\pm$16.9; p<0.001). $Rho^{-/-\ B6TgOPN1LW\text{-}EGFP+/-}$ mouse particle count declined over time (-1.4$\pm$0.1/day; p<0.001) and approached zero shortly before 25 weeks.

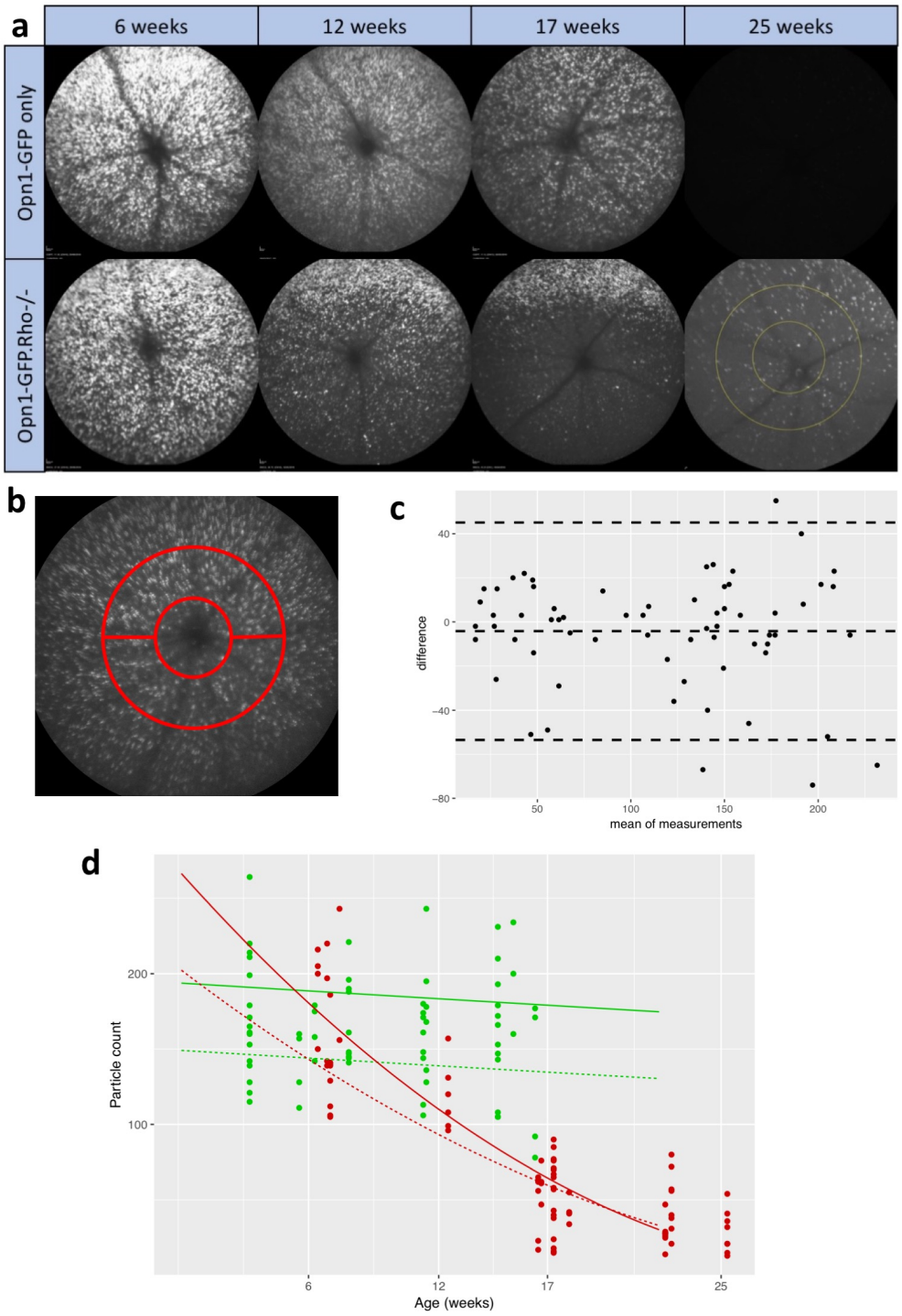


Figure 4.2 | SLO phenotype. **a,** Representative *en face* SLO images show declining GFP signal in Rho$^{-/-}$ B6TgOPN1LW-EGFP$^{+/-}$ mice (bottom row). Opn1.GFP expression is greater dorsally [127]. **b,** Semi-crescent regions were sampled for manual particle counts using the ImageJ counter plugin. **c,** Bland-Altman plot showing the difference in manual counts between the left and right eyes of the same mouse. **d,** Scatterplot of Rho$^{-/-}$ B6TgOPN1LW-EGFP$^{+/-}$ (red) and B6$^{TgOPN1LW-EGFP+/-}$ (green) manual particle counts (n=45). Linear model overlay shows significant difference between the dorsal (solid line) and ventral (broken line) retina in both genotypes (linear model, $p<0.001$), as well as the significantly faster decline in Rho$^{-/-}$ B6TgOPN1LW-EGFP$^{+/-}$ mice over time ($p<0.001$).

4.4.3 *In vivo* cone function

4.4.3.1 Cone electrophysiological function

Additional mice (n=66) underwent a cross-sectional case-control study to explore the natural history of ERG function in $Rho^{-/-\ B6TgOPN1LW\text{-}EGFP+/-}$, $B6^{TgOPN1LW\text{-}EGFP+/-}$ and $B6^{TgOPN1LW\text{-}EGFP-/-}$ mice. ERGs were performed one week before the cSLO measurements detailed earlier. Figure 4.3 shows the scotopic rod response in $Rho^{-/-\ B6TgOPN1LW\text{-}EGFP+/-}$ mice is absent from birth. The scotopic 10^{-4} candela flash is not significantly different between $B6^{TgOPN1LW\text{-}EGFP+/-}$ and $B6^{TgOPN1LW\text{-}EGFP-/-}$ mice (t-test; p=0.79).

Hierarchical linear modelling of the cone irradiance response curve was performed as detailed in subsection 2.8.2. The asymptote of $B6^{TgOPN1LW\text{-}EGFP-/-}$ mice does not decline significantly from baseline over time (p=0.069), but the asymptote of the $B6^{TgOPN1LW\text{-}EGFP+/-}$ mice does decline significantly from baseline (p<0.001). Both the $B6^{TgOPN1LW\text{-}EGFP+/-}$ and $Rho^{-/-\ B6TgOPN1LW\text{-}EGFP+/-}$ mice asymptotes decline over time compared to $B6^{TgOPN1LW\text{-}EGFP+/-}$ (p<0.001) and the $Rho^{-/-\ B6TgOPN1LW\text{-}EGFP+/-}$ mouse asymptote declines more than twice as rapidly than $B6^{TgOPN1LW\text{-}EGFP-/-}$ mice (p<0.001). In $Rho^{-/-\ B6TgOPN1LW\text{-}EGFP+/-}$ mice, the mid-point of the curve changes significantly over time compared to $B6^{TgOPN1LW\text{-}EGFP-/-}$ (p<0.001) as the response curve flattens with the degeneration. The curve flattens less dramatically in $B6^{TgOPN1LW\text{-}EGFP+/-}$ mice as well, approaching significance over time (p=0.053).

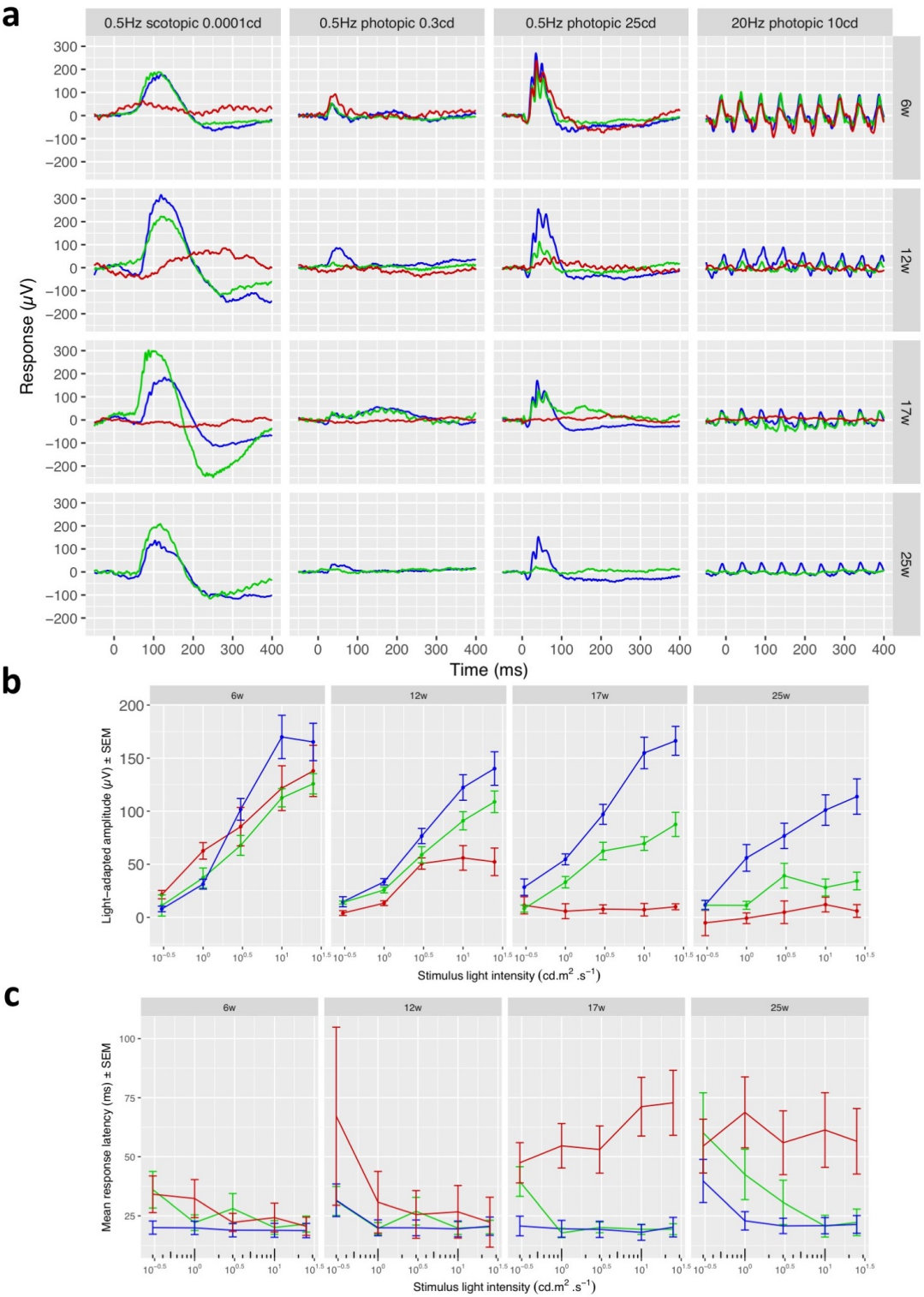


Figure 4.3 | ERG phenotype over time. **a,** Representative ERG traces in anaesthetised Rho$^{-/-}$ B6TgOPN1LW-EGFP+/- (red), B6$^{TgOPN1LW-EGFP+/-}$ (green) and B6$^{TgOPN1LW-EGFP-/-}$ (blue) mice at each time point. **b,** The irradiance response curve (±SEM) in B6$^{TgOPN1LW-EGFP+/-}$ mice drops significantly below B6$^{TgOPN1LW-EGFP-/-}$ at 17 weeks (p=0.03; n=66 mice). **c,** The mean latency of the photopic ERG b-wave is no different between genotypes at 6 weeks, but differs over time as the scotopic cone response declines and is extinguished. Grouped data shown as mean ± SEM.

4.4.3.2 Cone optomotor response function

Optomotor response testing was performed on Rho$^{-/-\ B6TgOPN1LW\text{-}EGFP+/-}$ mice to track the change in cone function over time. Time-points were selected at 6, 12 and 17 weeks to mirror the other natural history work. An additional 10 week time-point was added to further explore the loss of cone function observed around this time on ERG.

Figure 4.4 shows that head-tracking behaviour in scotopic conditions was present at the 6 week baseline (5.1 $\pm$ 0.7 per minute) and significantly different compared to stationary stimulus null test conditions (0.13 $\pm$ 0.08). Head-tracking behaviour did not change significantly from baseline at 10 weeks of age. However, at 12 weeks of age, head-tracking behaviour dropped significantly to 2.8 $\pm$ 0.65 ($p<0.01$). This reduced head-tracking behaviour was still significantly different to null stimulus conditions ($p<0.01$). The distinction between positive and null test condition head-tracking behaviour was lost at 17 weeks. Control mice (Figure 2.3) continue to demonstrate unchanged head-tracking behaviour beyond 17 weeks.

This OMR data confirms the findings of the ERG data, showing the cone function in Rho$^{-/-\ B6TgOPN1LW\text{-}EGFP+/-}$ mice is largely extinguished shortly before 12 weeks. It highlights that residual cone function exists around 12 weeks, as suggested by reduced ongoing head-tracking behaviour.

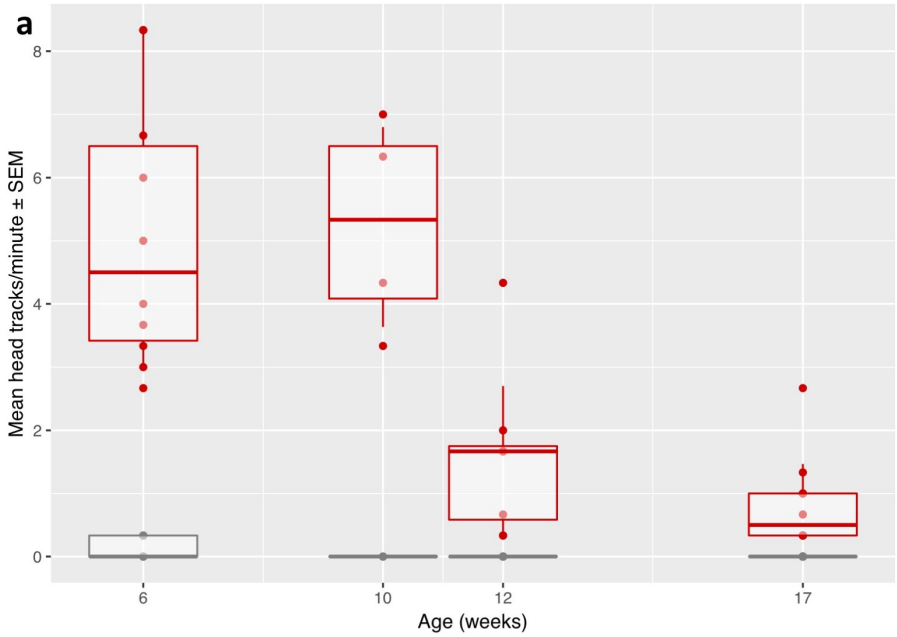


Figure 4.4 | Cone function. a, Optomotor response testing of Rho$^{-/-\ B6TgOPN1LW\text{-}EGFP+/-}$ mice (n=13) shows mean head tracking behaviour when the drum stimulus is active (red) or stationary (grey). Mean head tracks are consistent at 6 and 10 weeks, but reduced significantly at 12 weeks onwards ($p<0.01$). Data represented as a boxplot with mean and interquartile range; individual measured values are shown as overlaid dot points to highlight outliers.

4.4.4 Cone sampling bias caused by GFP

4.4.4.1 Proportion of cones expressing GFP on IHC

A dorsal-ventral gradient of GFP expression in cones exists in B6$^{TgOPN1LW\text{-}EGFP+/-}$ mice [127]. IHC was performed on B6$^{TgOPN1LW\text{-}EGFP+/-}$ mice (PND50-60) to explore how well *Arr3* primary antibody co-localised with cone GFP expression in our local colony. Figure 4.5 shows that in this single dorsal sample, all cones are labelled for both GFP and *Arr3*. However, co-localisation declined ventrally as shown by the original authors; this declining proportion was not quantified. This IHC shows that *Arr3* is an appropriate antibody for cone identification in later AAV experiments. However, it is not known whether *Arr3* expression, and thus binding, would be down-regulated in advanced Rho$^{-/-\ B6TgOPN1LW\text{-}EGFP+/-}$ degeneration.



Figure 4.5 | GFP expression on IHC. Representative images of *Arr3* staining in the dorsal retina of B6$^{TgOPN1LW\text{-}EGFP+/-}$ mice. The overlaid signals show that the GFP and *Arr3* signals co-localise in all of the cone photoreceptors in this dorsal section.

4.4.4.2 Proportion of GFP cones isolated using FACS

A pilot study was performed to validate the findings of the original authors and explore the possibility of using fluorescence-activated cell sorting (FACS) in isolating the cone photoreceptors before qPCR.

The original authors of the B6$^{TgOPN1LW\text{-}EGFP}$ mouse paper [127] demonstrated successful FACS isolation of cone photoreceptors from dissociated mouse retinas. Their data showed RT-PCR testing of the sorted cell fraction also showed little or no Rhodopsin mRNA contamination, but only ≈15,000 cones were isolated. This represented less than 10% of the total 180,000 cone photoreceptors in the retina [121]. Presumably, this isolated cone fraction would also skew towards dorsal M-cones, due to the geographic variation of GFP expression in the model [127, 128]

The yield of our pilot study of FACS was ≈27,000 cells from both eyes of individual B6$^{TgOPN1LW\text{-}EGFP}$ mice Figure 4.6. This number is consistent with the original cell counts obtained in Fei et al [127]. The potential bias introduced by only sampling a tenth of the total cone photoreceptor population, skewed towards M-cones, is substantial. As such, FACS was not used in the final cone qPCR analysis. The qPCR test results outlined below was performed on unsorted whole neurosensory retina samples.

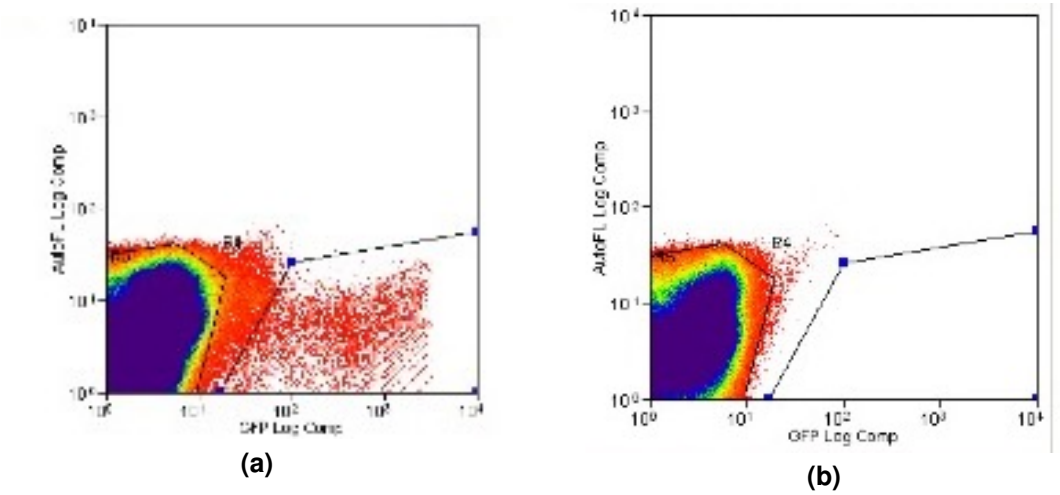


Figure 4.6 | FACS pilot study. a, FACS results from GFP-expressing mouse retina and **(b)** wild type controls. The x-axis shows the log fluorescence of the cells and the bounded area (bottom right of each plot) defined the population of retinal cells differentially sorted as GFP positive.

4.4.5 Sequencing the B6$^{TgOPN1LW\text{-}EGFP}$ transgene

The nucleotide sequence of enhanced GFP in the B6$^{TgOPN1LW\text{-}EGFP}$ mouse model was not included in the original publication [127]. Multiple variants of GFP exist [202] and qPCR test primers could only be designed once the B6$^{TgOPN1LW\text{-}EGFP}$ allele was fully sequenced.

The original genotyping primers used for confirming allele expression were used to amplify the first portion of the GFP sequence from gDNA. After sequencing the initial portion, downstream primers were designed to all known variants of GFP. Amplicons were produced from some primer pairs and the amplification-sequencing process was repeated along the length of the gene. BLAST search of the final nucleotide sequence matched dozens of plasmid constructs (ID: KX247384.1, MF379629.1, MF944225.1) all containing an enhanced GFP variant (NCBI ID: ATG88206.1) qPCR primer pairs were manually designed on this GFP sequence.

4.4.6 Optimisation of cone qPCR primer pairs

Multiple primer pairs for each of the 10 test genes were manually designed and BLAST searched on NCBI to exclude homology. Of the primer pairs designed,

thirty-two non-homologous pairs were each tested on at least two occasions for reproducible qPCR efficiency above 90% on standardised retinal transcriptome samples. This lengthy process is summarised as the best two efficiencies for each primer pair in Table H.1. The primer pair with reproducible efficiency closest to 100% for each test gene was selected for the test qPCR (Table 4.1). The melt curves showed single peaks, confirming a pure amplicon product and excluding non-specific signal (Figure 4.7).

Table 4.1 | The optimised primer pairs used in cone gene expression qPCR testing

Primer pair	Direction	Nucleotide sequence (5'-3')
B-actin pair 3	Forward	AGCCATGTACGTAGCCA
	Reverse	GAAGCTGTAGCCACGCT
Cnga3 pair 1	Forward	TAGACATGCTGGTTCGAGC
	Reverse	GTTGGTCCTTGTCTCTGTG
Cone Arrestin pair 1	Forward	GTGGATGATGTGGACACTG
	Reverse	CTGGATGCTGGTGGGTTC
Cone pde6h pair 1	Forward	GAGTCCTCCAGCACCAAG
	Reverse	TCCCGAACTGAGCAAGCT
Gnat2 pair 1	Forward	CTGACAAGGAAGCCAAGACT
	Reverse	CAGGATGGACTGCAGCAC
Opn1sw pair 1	Forward	ACAGTCTTCATCGCCA
	Reverse	CAAGTAGCCAGGACCAC
Cngb3 pair 1	Forward	AGCCAGCTCTCAGACTGCA
	Reverse	ACAGTTCCAGTTATACGCA
Opn1mw pair 3	Forward	AGCCAGCTCTCAGACTGCA
	Reverse	GCAACTGCCAAGTTCACCAG
Crx pair 4	Forward	CACGTGAGGAGGTTGCTCTT
	Reverse	GTAGAGGGTCTCGGGGATGT
Rho pair 1	Forward	TGCTCAACTTGGCCGT
	Reverse	GCGGAAGTTGCTCATCG

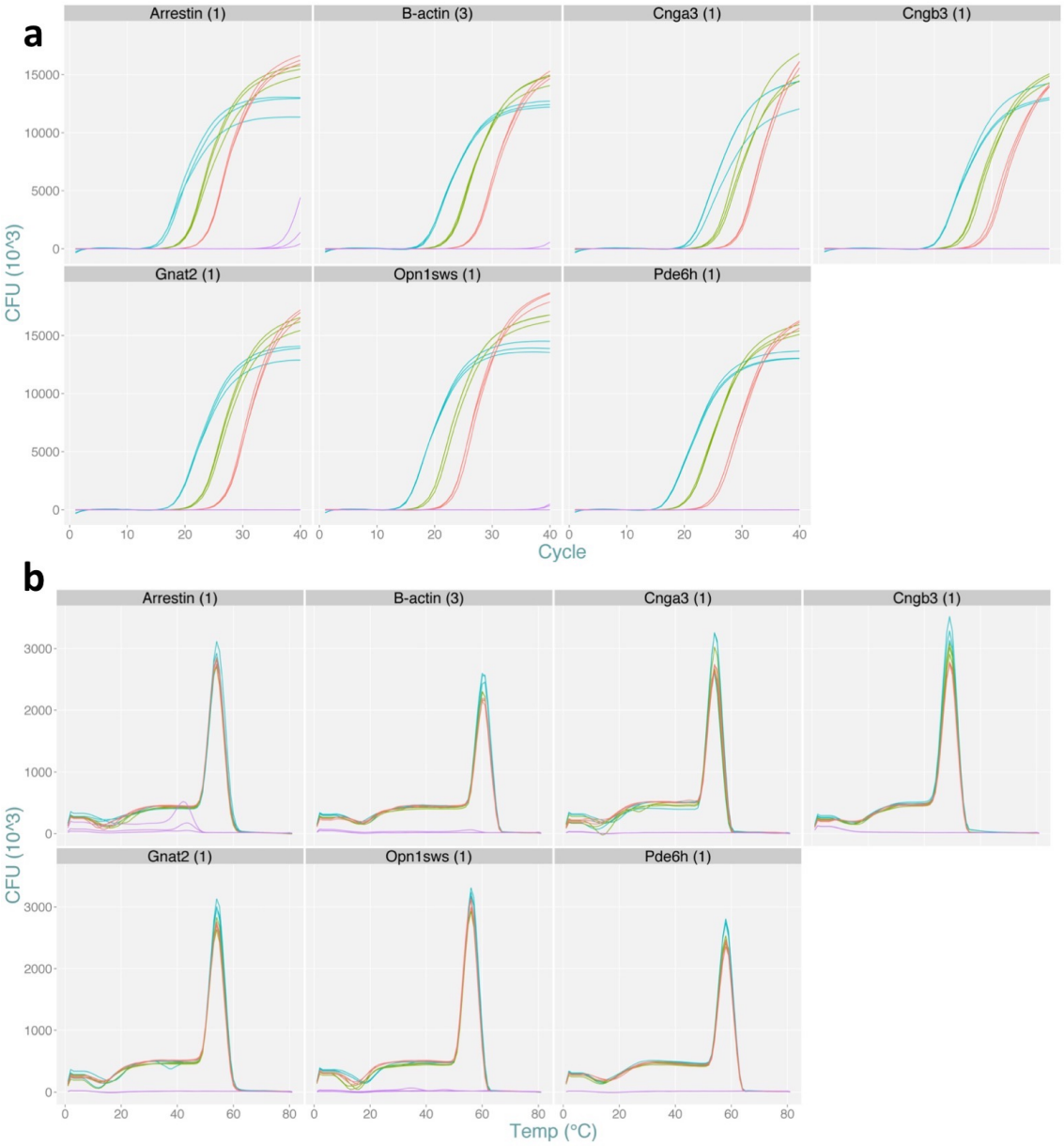


Figure 4.7 | qPCR test primer melt curves. a, Amplification curves for 7 of the 10 optimised primer pairs used in the test plate data collection; efficiencies of 90-105% were derived from these datasets. **b,** Melt curves showing overlaid data from multiple dilution series of different retinal transcriptome positive controls. Each primer pair produces a single peak without background signal, confirming specificity and low false negative rate.

4.4.7 mRNA isolation from retinal sample

Figure 4.8 shows the mRNA concentration that was extracted from each of the 94 mice across the three genotypes and five time-points. In six $Rho^{-/-}$ B6TgOPN1LW-EGFP+/- mice, the total mRNA isolated from the samples was insufficient to add 3000ng/μL to each reverse transcription reaction. These six

mice were combined into time-point matched pairs to form three composite samples of sufficient total mRNA.

The quality of the isolated mRNA was confirmed by the 230/260 and 260/280 ratios on spectrophotometry. Samples were only reverse transcribed to cDNA if the 260/280 ratio approached 2.0 and there was minimal evidence of contamination at 230nm. All samples satisfied this quality control step and were converted to cDNA.

4.4.8 qPCR test plates

All qPCR reactions on a single biological replicate were performed as technical triplicates. There were 2930 qPCR reactions performed as 1176 technical triplicates of raw data collected across 42 qPCR test plates. Technical triplicates were identified as outliers if the range of Cq values exceeded 0.2 cycles. We can describe the effect of a 0.2 cycle variation on absolute measurement accuracy as $1 \pm (2^{-0.2})$, which represents a maximum of 13% to 15% variation. The MIQE guidelines provide no formal threshold for identifying outlier technical replicates [184].

520 technical triplicates had a Cq variance greater than 0.2 cycles, which represents 44.4% of total reactions. Automated removal of the most extreme value in each of these triplicates was performed using the `outliers` package in `R`. After removal of the most extreme value, 31 of these technical duplicates had a range of Cq values above 0.2 cycles, which represented 2.6% of all qPCR reactions performed. Ongoing analysis was performed on the remaining dataset.

4.4.8.1 Negative controls

Negative control triplicate wells were included on each test plate. Molecular biology H2O was used as a negative sample alongside the normal reaction mix to demonstrate a minimal or absent non-specific background signal.

Table 4.2 shows that none of the negative controls for any of the test genes in the qPCR test plates reproducibly measured Cq values below 35. There was

some recurring primer-dimer formation at low quantities in the *Rho* and *cGFP* primer pairs, which generated Cq values above 35 cycles. Ultimately, all of the eleven primer pairs produced a reliable true positive signal and incidental contamination was excluded.

Table 4.2 | Numbers of negative control wells with detectable signal.

Target	No signal measured	Signal measured	Mean Cq
Bactin	48	11	39.05
cGFP	12	9	37.12
Cnga3	12	0	
Cngb3	12	0	
ConeArr	10	2	37.23
Crx	13	5	37.84
Gnat2	11	1	37.19
Opn1mw	21	0	
Opn1sw	17	4	38.57
Pde6h	11	1	36.98
Rho	3	9	37.07

4.4.8.2 Positive controls

Positive control triplicate wells were included on each test plate. A standard sample of $B6^{TgOPN1LW\text{-}EGFP+/-}$ retinal cDNA was used as a positive sample alongside the normal reaction mix to demonstrate a consistent positive signal on an unchanged sample, despite some expected inter-plate variation.

Figure 4.8 shows that the majority of positive control wells measured tightly clustered results within and across all test plates. Eight test genes showed variance less than 0.1 cycles across all test plates. It is not possible to comment reliably of the between-plate reproducibility of *Arr3* and *Gnat2* because different positive control samples were used across test plates.

4.4.8.3 Reliability of the *Actb* reference gene

The reference gene should optimally exist in a steady state across time and disease models. Figure 4.8 shows the changes in *Actb* over time by mouse genotype. A hierarchical linear model analysis of variance of *Actb* and genotype showed that expression of the *Actb* reference gene in $B6^{TgOPN1LW\text{-}EGFP-/-}$ and

B6$^{TgOPN1LW\text{-}EGFP+/-}$ mice was not significantly different over time (p=0.20), nor between these two genotypes (p=0.96). *Actb* levels in Rho$^{-/-\ B6TgOPN1LW\text{-}EGFP+/-}$ mice did decline significantly over time (p=0.01), but were not significantly different from B6$^{TgOPN1LW\text{-}EGFP-/-}$ mice (p=0.08) or B6$^{TgOPN1LW\text{-}EGFP+/-}$ mice (p=0.15).

Detailed plots of *Actb* normality in Figure 4.8 show a unimodal frequency distribution in all genotypes at 2 weeks. This normality disintegrates into a worsening right-skew distribution over subsequent the time-points. The right-skew correlates with declining *Actb* expression and lower Cq values in the outlier values.

Figure 4.8 highlights the decline in mRNA concentration isolated from Rho$^{-/-\ B6TgOPN1LW\text{-}EGFP+/-}$ samples over time. mRNA concentrations decline significantly from baseline over time (linear model, $p<0.001$); most likely a product of the very high mRNA concentrations observed at 2 weeks of age.

Actb Cq values plotted against sample mRNA concentration shows a weak correlation ($R^2 = 0.19$) between gradually rising *Actb* Cq values and declining total sample mRNA. Decline and *Actb* Cq values are correlated with

In summary, *ActB* expression profiles between mice show variance but are not significantly different to one another over time. *ActB* exists in a sufficiently steady state to be a reliable solitary reference gene.

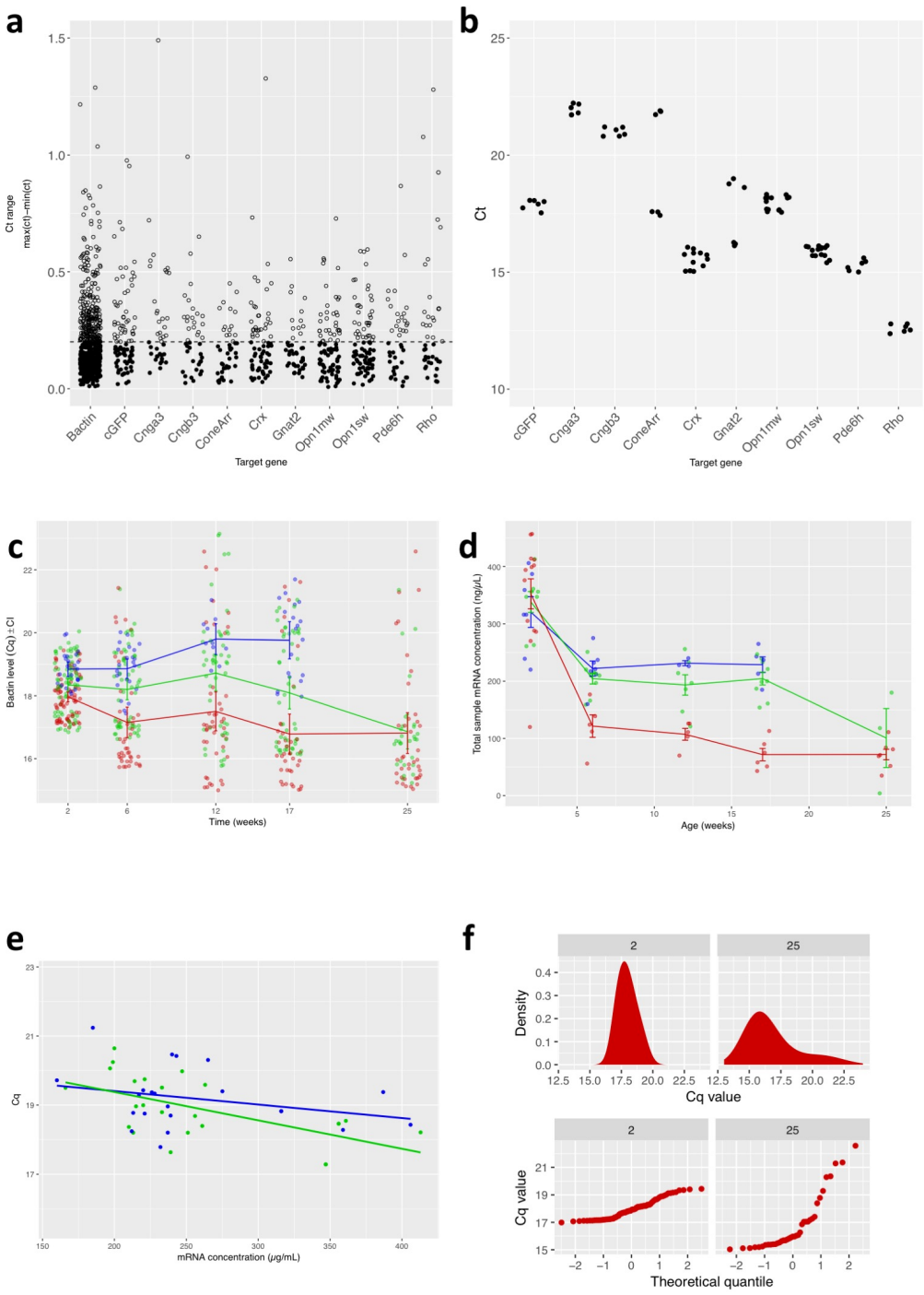


Figure 4.8 | **qPCR quality control.** **a,** Technical triplicates with Cq variance above 0.2 cycles were identified (unfilled circles) and the most extreme value excluded as per the protocol. **b,** Positive control samples showed reproducible Cq values across the test plates. **c,** *Actb* housekeeper Cq values (± 95% CI) showed no significant difference over time between Rho$^{-/-}$ B6TgOPN1LW-EGFP$^{+/-}$ (red), B6$^{TgOPN1LW\text{-}EGFP+/-}$ (green) and B6$^{TgOPN1LW\text{-}EGFP-/-}$ (blue) mice. **d,** Changes in the total mRNA (±SEM) isolated from both retinas of each mouse demonstrate the contribution of the degenerative process on mRNA concentrations. **e,** Linear correlation shows a weak relationship between this changing mRNA concentration and the *ActB* Cq value. **f,** Density and qqnorm plots highlight changes in Rho$^{-/-}$ B6TgOPN1LW-EGFP$^{+/-}$ Cq value frequency distribution between 2 and 25 weeks.

4.4.8.4 *Rho* transcript expression

Fei et al ([127]) did not detect *Rho* transcript in the retinal transcriptome of the $Rho^{-/-\ B6TgOPN1LW\text{-}EGFP+/-}$ mice using RT-PCR gels. Yet Figure 4.9 shows that qPCR is sensitive enough to detect a *Rho* transcript in the retinal transcriptome of $Rho^{-/-\ B6TgOPN1LW\text{-}EGFP+/-}$ mice. All negative controls did not produce signal. Also, this finding was made on multiple occasions in many different samples over different years - exogenous contamination is an unlikely explanation.

In subsubsection 4.4.9.1, the hierarchical model fitted to the qPCR dataset for statistical analysis. A 2.5-fold increase in Rhodopsin expression from baseline was suggested in the the $B6^{TgOPN1LW\text{-}EGFP+/-}$ mice (P=0.067). As anticipated due to the pol2:neo disruption of *Rho*, Rhodopsin transcript levels were significantly reduced over 1000-fold at 2 weeks in $Rho^{-/-\ B6TgOPN1LW\text{-}EGFP+/-}$ mice. *Rho* levels declined over time ($p<0.001$) and the rate of decline accelerated over time ($p=0.075$).

Figure 4.9 shows the *Rho* transcript correlated with declining ONL thickness on OCT measurements. Transcript levels continued declining even after the ONL was no longer detectable on OCT imaging. This correlation makes the authenticity of the Rho transcript more likely - exogenous contamination is unlikely to behaviour follow a temporal pattern like this.

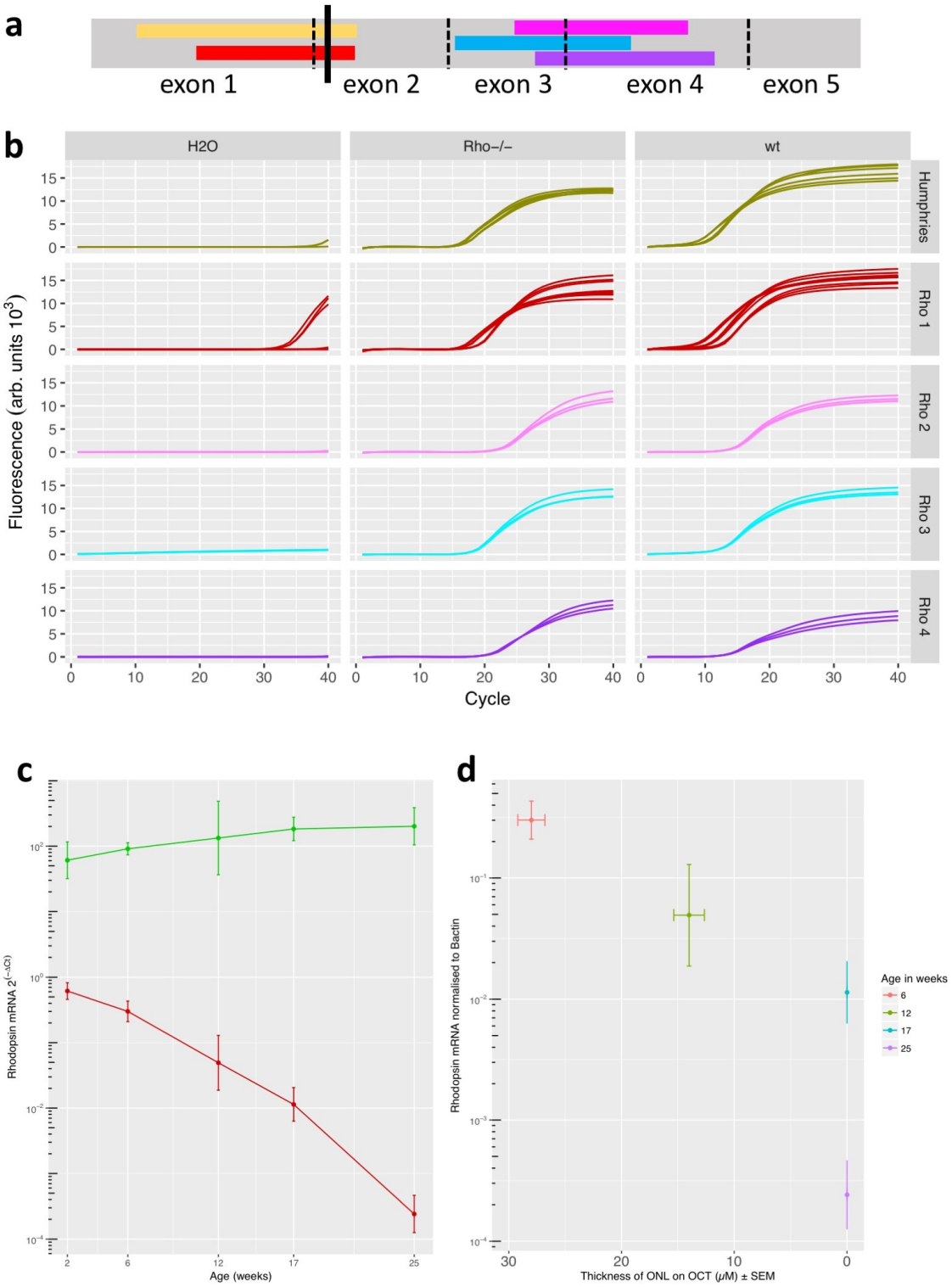


Figure 4.9 | Rhodopsin transcript. **a,** Graphical representation of a *Rho* gene fragment showing the the pol2:neo insertion site and the location of the downstream qPCR reverse primers. **b,** qPCR amplification curves from Rho$^{-/-\ B6TgOPN1LW\text{-}EGFP+/-}$ mice, showing that all primer pairs targeting *Rho* downstream of the disruption cassette produce an amplicon. **c,** qPCR ΔCt values over time for primer pair 'Rho 1' in Rho$^{-/-\ B6TgOPN1LW\text{-}EGFP+/-}$ (red) and B6$^{TgOPN1LW\text{-}EGFP+/-}$ (green) mice showing reduced quantities of *Rho* transcript. **d,** Correlation of OCT-measured ONL thickness and qPCR ΔCt values (mean$\pm$SEM) over time; notably, *Rho* transcript continues to decline after the loss of ONL on OCT. Data shown as mean values $\pm$ SEM.

4.4.9 Hierarchical model of the cone qPCR data

4.4.9.1 Fitting the model

The temporal change in test gene expression consistently reached a peak at, or around, 2 weeks of age across all tested cone genes. Following this peak, the levels of cone gene expression dropped in the Rho$^{-/-\ B6TgOPN1LW\text{-}EGFP+/-}$ mice. The B6$^{TgOPN1LW\text{-}EGFP+/-}$ mice then either fell or remained steady. The fitted linear model included this quadratic polynomial relationship.

A two-level hierarchical polynomial model was fitted to the qPCR dataset using the `nlme` package in `R`. Formal statistical advice was provided by Professor Dan Lunn at the University of Oxford statistics department. A quadratic form of the polynomial model was fitted by using the `poly()` function in `R` to generate polynomial values for the five time points (2, 6, 12, 17 and 25 weeks). Uncorrected test gene Cq was taken to the dependent variable, with housekeeping gene (*Actb*) Cq as the first explanatory variable, with interactions included between mouse genotype, the gene being tested, the linear time value and quadratic time value (Equation 4.1).

$$y = \beta_1 + \beta_2 x_1 + \beta_3 x_2 + \beta_4 x_3 + \beta_5 x_4 + \beta_6 x_5 \quad (4.1)$$

y	Test gene Cq
x_1	Housekeeping gene Cq
x_2	Test gene name
x_3	Mouse genotype
x_4	Time linear
x_5	Time quadratic

Figure 4.10 shows some non-normality in the model residuals. A Box-Cox profile likelihood did not suggest a transformation (λ = 1) and manual exploration of Tukey's power ladder for transformations did not improve the residuals. The residual non-normality appeared concentrated largely in a subset of Rho$^{-/-\ B6TgOPN1LW\text{-}EGFP+/-}$ mice and appears to relate to the loss of *ActB* normality described in subsubsection 4.4.8.3. Manual review of those mice did not reveal a cause for outlier status and no exclusions were made. A plot of the model

residuals against fitted values (Figure 4.10) showed homoscedasticity and no weighting was required.

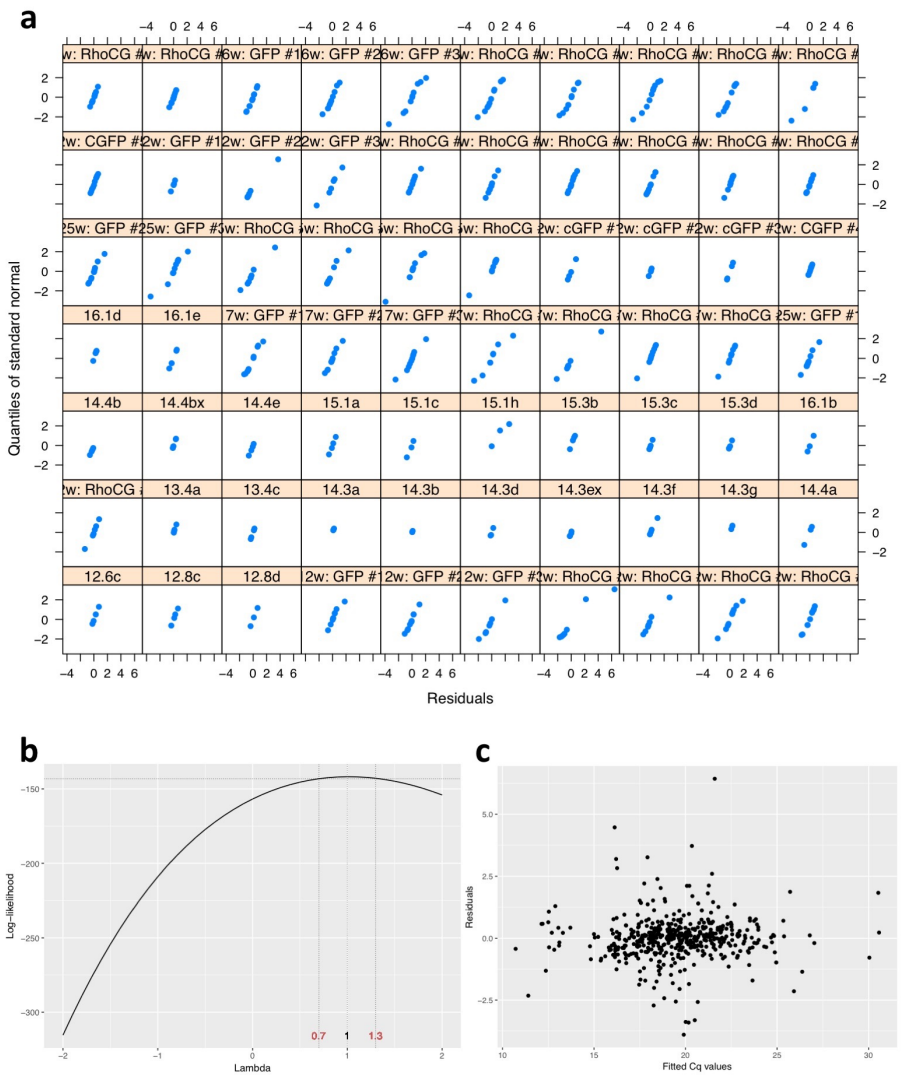


Figure 4.10 | Polynomial model diagnostic tests. **a,** Model residuals showed some non-normality that was concentrated in a subset of mice, but no experimental basis was identified for exclusion. **b,** The Box-Cox profile likelihood did not suggest any transformation. **c,** A plot of fitted values against residuals showed homoscedasticity.

4.4.9.2 Results of the polynomial model

The full statistical output of the polynomial model is listed in Table 4.3 and the data is graphically displayed in Figure 4.11. All contrasts are expressed as relative changes in $Rho^{-/-\ B6TgOPN1LW\text{-}EGFP+/-}$ mice compared to the $B6^{TgOPN1LW\text{-}EGFP+/-}$ mice as a reference. The analysis of the *Rho* transcript was detailed above.

Cone photoreceptor expression of *GFP* in $B6^{TgOPN1LW\text{-}EGFP+/-}$ and $Rho^{-/-\ B6TgOPN1LW\text{-}EGFP+/-}$ mice declined over time (p=0.043). However, the decline was not significantly different between the two genotypes overall, nor did the rate of change differ significantly between genotypes.

Crx expression increased 3-fold in $B6^{TgOPN1LW\text{-}EGFP+/-}$ mice over time (p=0.01). *Crx* was the most down-regulated cone gene in $Rho^{-/-\ B6TgOPN1LW\text{-}EGFP+/-}$ mice, showing a significant 4-fold reduction overall for the genotype, a reduction over time and a increase in the rate of reduction over time.

Both cone opsin genes showed no significant change in expression over time in $B6^{TgOPN1LW\text{-}EGFP+/-}$ mice. In $Rho^{-/-\ B6TgOPN1LW\text{-}EGFP+/-}$ mice, *Opn1sw* was the most down-regulated of the two cone opsins; a significant 8-fold reduction in expression overall, significant reduction over time and in the rate of reduction over time. *Opn1mw* was not significantly reduced in $Rho^{-/-\ B6TgOPN1LW\text{-}EGFP+/-}$ overall (3-fold; p=0.32), but expression did decline over time from baseline in $Rho^{-/-\ B6TgOPN1LW\text{-}EGFP+/-}$ mice (p=0.011). An increased rate of change in *Opn1mw* was suggested over time in $Rho^{-/-\ B6TgOPN1LW\text{-}EGFP+/-}$ mice (p=0.08).

The expression of *Gnat2* followed a different pattern to all of the other genes. *Gnat2* expression increased 3.5-fold over time in the $B6^{TgOPN1LW\text{-}EGFP+/-}$ mice. *Gnat2* expression was 2.3-fold higher in $Rho^{-/-\ B6TgOPN1LW\text{-}EGFP+/-}$ mice than in controls (p=0.05) and increased significantly over time. *Gnat2* expression closely followed the quadratic arc over time, largely due to the profound increase in expression between the 2 and 6 week time-points.

Pde6h expression did not differ between genotypes. There was no change over time in $B6^{TgOPN1LW\text{-}EGFP+/-}$ mice, but a change from baseline in the

Rho$^{-/-\ B6TgOPN1LW\text{-}EGFP+/-}$ mice. However, the difference between the genotypes was not significant and the rate of change in Rho$^{-/-\ B6TgOPN1LW\text{-}EGFP+/-}$ mice was not significantly different over time.

Cngb3 expression did not differ between genotypes. *Cngb3* did not change over time in B6$^{TgOPN1LW\text{-}EGFP+/-}$ mice, but did change from baseline in Rho$^{-/-\ B6TgOPN1LW\text{-}EGFP+/-}$ mice. There was no significant difference in rate of change between the genotypes.

Cnga3 showed no significant difference between genotypes, nor any significant change over time in either genotype, nor any significant difference in rate of change.

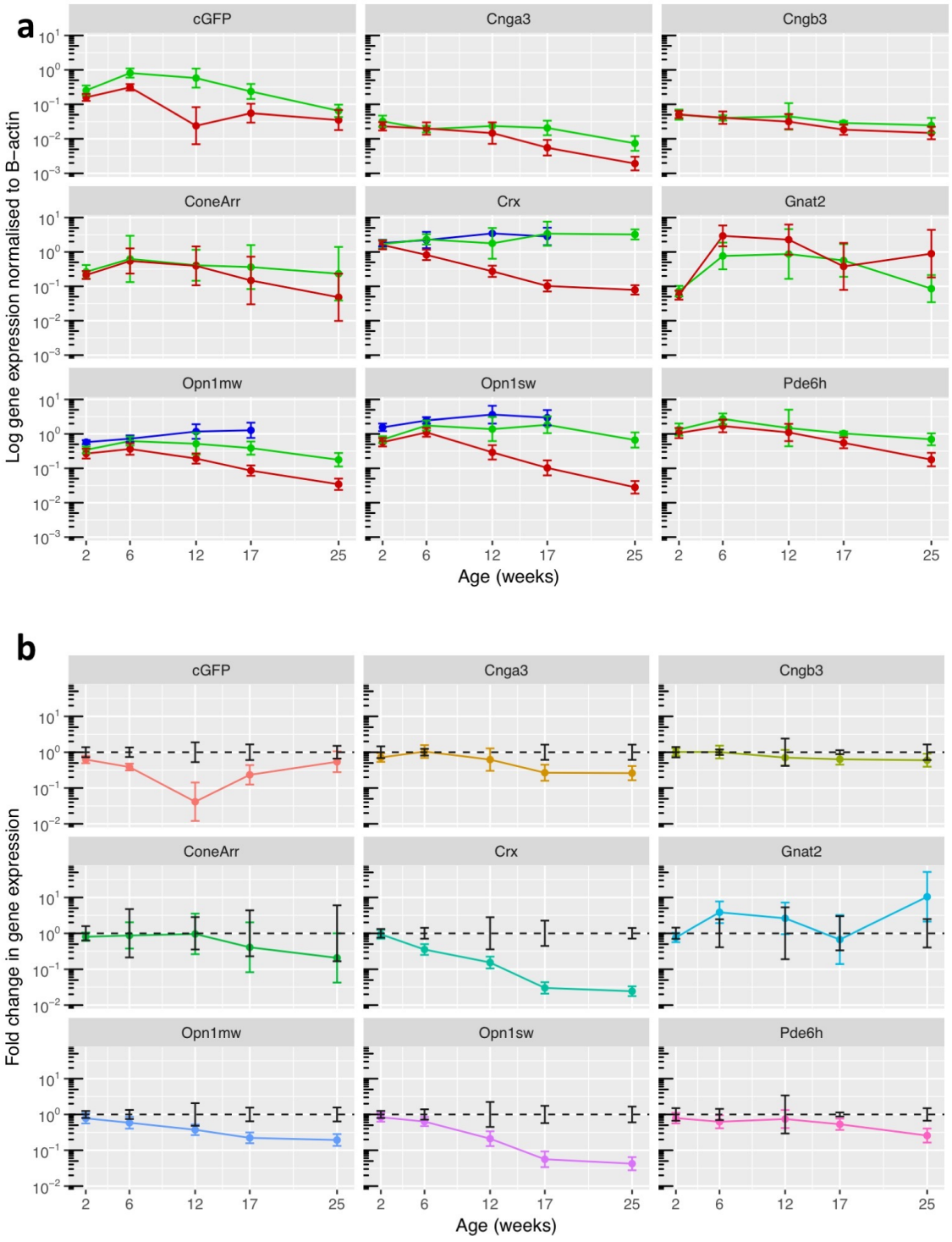


Figure 4.11 | Cone qPCR results. **a,** The gene expression values over time for Rho$^{-/-\ B6TgOPN1LW\text{-}EGFP+/-}$ (red), B6$^{TgOPN1LW\text{-}EGFP+/-}$ (green) and B6$^{TgOPN1LW\text{-}EGFP-/-}$ (blue) mice as displayed as $2^{\Delta Cq}$. ΔCq is calculated by subtracting the matched reference gene *ActB* value from the test gene value. **b,** The same gene expression data showing $\Delta\Delta$Cq values calculated by normalising Rho$^{-/-\ B6TgOPN1LW\text{-}EGFP+/-}$ expression to the B6$^{TgOPN1LW\text{-}EGFP+/-}$ mice (grey broken line with SEM bar); B6$^{TgOPN1LW\text{-}EGFP+/-}$ mouse data is not included in this bottom panel. All data shown as mean values $\pm$ SEM.

Table 4.3 | The statistical output of the polynomial model of cone cell qPCR data comparing $Rho^{-/-}$ to $GFP^{+/-}$ Opn1.GFP mice over time and rate of change.

	cGFP		Crx		Opn1mw		Opn1sw		Cnga3		Cngb3		ConeArr		Gnat2		Pde6h		Rho	
	Effect	p-value	Effect	p-value	Effect	p-value	Effect	p-value	Effect	p-value	Effect	p-value	Effect	p-value	Effect	p-value	Effect	p-value	Effect	p-value
intercept	15.000		11.682		14.271		12.788		18.410		17.408		14.921		14.714		12.332		7.482	
Bactin	0.286		0.286		0.286		0.286		0.286		0.286		0.286		0.286		0.286		0.286	
$Rho^{-/-}$	0.629	0.091	2.039	0.000	0.364	0.320	1.424	0.000	0.114	0.789	-0.492	0.242	1.864	0.000	-1.182	0.005	0.010	0.981	11.141	0.000
Time	1.249	0.043	-1.653	0.010	0.101	0.868	-0.634	0.297	0.417	0.545	-0.217	0.752	0.059	0.931	-1.804	0.010	0.201	0.771	-0.785	0.254
$Time^2$	0.923	0.096	-0.993	0.084	0.186	0.734	0.180	0.742	-0.251	0.722	-0.331	0.625	0.069	0.919	0.838	0.219	0.239	0.735	-1.342	0.067
$Rho^{-/-}$ over time	-0.078	0.927	4.433	0.000	1.476	0.086	3.636	0.000	1.471	0.110	0.651	0.476	3.253	0.002	0.133	0.884	1.018	0.267	10.017	0.000
$Rho^{-/-}$ over $time^2$	-1.176	0.152	0.391	0.666	1.228	0.135	1.215	0.139	1.401	0.139	0.990	0.282	0.244	0.803	2.296	0.013	1.506	0.112	1.709	0.075

Each individual gene is displayed in columns showing the magnitude of effect and p-value of each variable (fixed effect) in the hierarchical model. The $Rho^{-/-}$, time and $time^2$ polynomial fixed effects are reported, along with their interactions. The y-intercept and *Bactin* fixed effects are provided for completeness.*This table shows the full results of the polynomial model fitted to the repeated-measures qPCR dataset. The details of how the model was fitted are provided in subsection 2.8.2 and subsubsection 4.4.9.1. All results are reported as the effect size and p-value of the $Rho^{-/-}$ mice compared to the Opn1.GFP control mice (baseline).*

Each individual gene is displayed in columns showing the magnitude of effect and p-value of each variable (fixed effect) in the hierarchical model. The $Rho^{-/-}$, time and $time^2$ polynomial fixed effects are reported, along with their interactions. The y-intercept and Bactin fixed effects are provided for completeness.

4.4.10 Correlation of *Crx* and *Rho* changes

Declining *Crx* and *Rho* transcript levels can be correlated with linear regression. Figure 4.12 shows a linear regression of the relationship between these two genes in the Rho$^{-/-}$ B6TgOPN1LW-EGFP$^{+/-}$ genotype. Variation in the *Rho* transcript levels significantly correlate with *Crx* levels by $\approx$ 25% ($p<0.001$); however, this numerical relationship is correlated not causative. In a linear regression, *Rho* transcript levels correlate strongly with variation in *Crx* levels ($R=0.88$). Cone photoreceptors account for only 3% of the total retinal cell population. As such, it is not possible to say with confidence that the significant reductions in *Crx* levels observed are solely a product of rod photoreceptor death. Loss of cone cell derived *Crx* may still be a substantial and significant contributing factor.

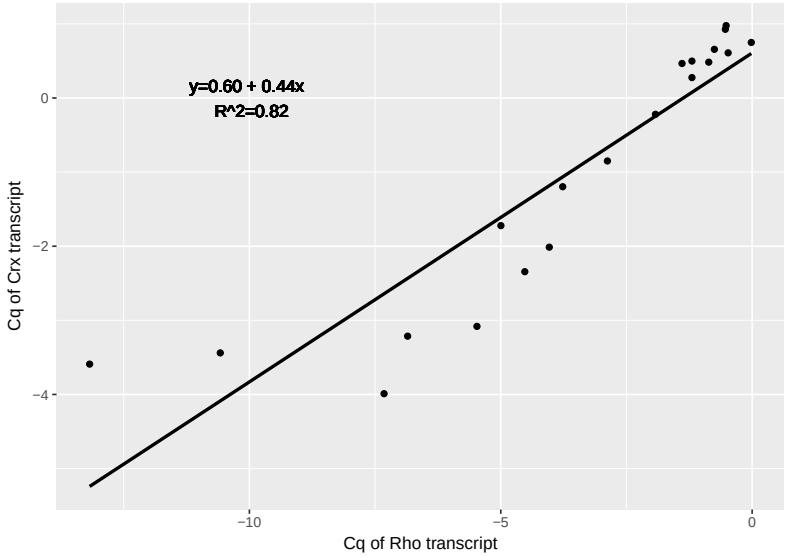


Figure 4.12 | Correlation of *Crx* and *Rho*. *Crx* transcript levels decline significantly with falling *Rho* levels ($p<0.001$). The *Rho* transcript levels only account for 82% of the variation observed in *Crx* levels.

4.5 Discussion

4.5.1 Validation of the OCT for rod measurements

This chapter confirmed that outer segments are not visible in Rho$^{-/-\ B6TgOPN1LW\text{-}EGFP+/-}$ mice. It is known that the outer segments never develop in the absence of Rhodopsin protein [132]. The rate at which the outer retina is lost in this model was also quantified; there is no difference between the dorsal and ventral retina in this model. The data support the continued use of the dorsal subretinal injection method, with no need to deliver the vector ventrally.

4.5.2 Validation of SLO manual counting technique

This chapter validated a manual counting technique for assessing the change in fluorescent cone signal over time in *en face* SLO images of the retina collected at 100% detector sensitivity. The results from 45 mice showed that, as anticipated from cone IHC work by Punzo et al [62], particle counts in Rho$^{-/-\ B6TgOPN1LW\text{-}EGFP+/-}$ mice decline rapidly around 12-17 weeks. Here we show that in some mice the cones appear to be fully extinguished by 17 weeks, before the end of the major phase of cone death [62]. However, this apparent early extinction of fluorescent signal may simply represent the lower limits of SLO detection or the cessation of GFP protein production in cones preceding IHC cell loss by some weeks.

The manual count technique validated the original description by Fei et al [127] that the ventral retina of B6$^{TgOPN1LW\text{-}EGFP+/-}$ mice has fewer fluorescent cones. This ventral difference was even more pronounced in Rho$^{-/-\ B6TgOPN1LW\text{-}EGFP+/-}$ mice. The *in vivo* particle count in B6$^{TgOPN1LW\text{-}EGFP+/-}$ mice is not significantly different up to 17 weeks of age, which suggests that the previously described cone loss [128] is a late occurrence closer to the 35 week time point described in the paper.

The count technique had acceptable precision for measuring such a large change between these two genotypes. However, the increasing coefficient of variance over time may mask subtle changes in cone photoreceptor survival in later AAV rescue experiments. The coefficient of variance increases at later time-

points and thus at lower particle counts. This increasing variance may be caused by new white particles developing in images at later time-points. This rising false positive signal observed in multiple images may mask the lower cell count as it approaches zero. This false positive white dot signal was detected in most but not all $Rho^{-/-\ B6TgOPN1LW\text{-}EGFP+/-}$ mice and may represent migration of macrophages into the retina; auto-fluorescent macrophages have been observed on SLO in other degenerative retinal diseases [203].

The small systematic difference in average counts between the eyes (Left>Right) could have resulted from: a) cataract occurring slowly during testing, as the left eye was imaged after the right, b) differences in the contact lenses altering signal in one eye more than the other. Issues that can both be overcome by randomisation or faster technique.

Low detector sensitivity was identified as an important source of sampling error. Low detector sensitivity resulted in loss of lower-fluorescent particles in the image. 100% detector sensitivity was shown to yield the most number of discrete particles without the loss of discrete particle margins that was observed at 108% sensitivity. Pixel greyscale value saturation occurs more often at 100% sensitivity, but this would only affect the normal distribution of the results if a mean greyscale technique were applied, not a manual count.

Chromatic aberration was identified as an additional source of error in *in vivo* counting. In some cases, large aberrations resulted in defocussed images that were unusable due to loss of any discrete margins around the particles. The issue of chromatic aberration in SLO images has been described previously [201]. It can be avoided by manually dialling the dioptric focus to optimise image clarity before acquisition.

4.5.2.1 Cone function outcome measures

This chapter confirmed previous findings that the photopic ERG is extinguished in most $Rho^{-/-\ B6TgOPN1LW\text{-}EGFP+/-}$ mice at 12 weeks; scotopic ERG was never measurable as expected. This chapter identified that $B6^{TgOPN1LW\text{-}EGFP+/-}$ mice lose

half of their photopic ERG function by 17 weeks of age. Dominant cone dystrophy had been previously described in these mice due to insertion of the B6$^{TgOPN1LW\text{-}EGFP}$ transgene in the region of the North Caroline Macula Dystrophy locus [128], but the timeline of cone function loss was unknown. Lipinski et al [128] describe a diminished photopic ERG flash response b-wave at P245 in both heterozygous and homozygous B6$^{TgOPN1LW\text{-}EGFP}$ mice; the preceding timeline of declining cone function was not characterised.

The decline in B6$^{TgOPN1LW\text{-}EGFP}$ mouse scotopic ERG function is more rapid and severe than the minimal decline cone GFP fluorescent measured on cSLO (Figure 4.2). This is consistent with the findings in Lipinski et al [128] in which the cone dysfunction predominantly affected S-cones, located in the ventral retina. Whereas, the observed pattern of slowly declining GFP expression is concentrated in the dorsal retina, which is majority M-cones.

4.5.3 Suitability of *Actb* as a single qPCR reference gene

The MIQE guidelines [184] emphasise the importance of internally validating the reference gene across genotypes and time. *Actb* levels are reliable across all time-points for the non-degenerate B6$^{TgOPN1LW\text{-}EGFP\text{-}/\text{-}}$ and B6$^{TgOPN1LW\text{-}EGFP+/\text{-}}$ mice. *Actb* satisfies the required standard for a suitable reference gene in the B6$^{TgOPN1LW\text{-}EGFP+/\text{-}}$ and B6$^{TgOPN1LW\text{-}EGFP\text{-}/\text{-}}$ mouse strains.

However, *Actb* levels in Rho$^{-/-\ B6TgOPN1LW\text{-}EGFP+/\text{-}}$ mice do vary over time. Mice collected at the 25 week time-point show the most extreme variation, suggesting that the underlying retinal degeneration underpins the reduced expression and loss of normality. For this reason, it is likely that no reference gene would be expressed in a steady state over time in Rho$^{-/-\ B6TgOPN1LW\text{-}EGFP+/\text{-}}$ mice. This is a potential source of error in the late time-point gene analysis work that cannot be controlled for. However, if the *ActB* reference gene caused artifactual global up- or down-regulation in relative test gene expression, this would be obvious in the final expression graphs. Such a systematic bias was not observed.

4.5.4 Nonsense-mediated decay of mutant Rhodopsin mRNA

The qPCR results above show reduced, but ongoing, levels of *Rho* transcript; a finding that contradicts the original paper [132]. Other authors have confirmed no Rho protein expression in this model [62, 132]. Thus these findings are consistent with nonsense mediated decay (NMD), whereby a premature stop codon results in reduced mRNA levels and no protein product. The pol2:neo cassette is approximately 3.1kB in length [132], although the exact sequence was not available at the time of publishing. It is not known if the insertion cassette would create a frameshift of downstream Rhodopsin signal or whether the expression cassette itself contains a premature stop codon.

Interestingly, the residual *Rho* transcript levels correlate with the declining outer nuclear layer thickness on OCT. Punzo et al [62] demonstrated that a scattered single layer of rod nuclei persist beyond 17 weeks in the $Rho^{-/-\ B6TgOPN1LW\text{-}EGFP+/-}$ model. OCT is likely not sensitive enough to detect such residual rod cells. This could explain why the *Rho* transcript continues to decline after the OCT no longer detect changes in the photoreceptor layer.

4.5.5 GFP as an internal control

The $B6^{TgOPN1LW\text{-}EGFP}$ allele was included in this experiment as an internal control. The declining total cone photoreceptor population in $Rho^{-/-\ B6TgOPN1LW\text{-}EGFP+/-}$ mice could confound the qPCR gene expression analysis. Without GFP as an internal control, it would not be known whether falling cone gene expression could be a product of either gene down-regulation across cones or the ongoing death of cone photoreceptors.

Pilot studies of IHC confirmed the original findings that GFP expression in cones varies along a dorsal-ventral gradient [127]. Also, the previously unknown nucleotide sequence of the GFP transgene was determined. However, pilot FACS showed showed substantial sampling bias and ultimately FACS was not used as

a way of internally controlling cone sampling. Instead, GFP transcript expression measured on qPCR acted as an internal control for double-normalising qPCR $\triangle$Cq values.

Whole retinal expression of GFP transcript declined over time in both genotypes. Unexpectedly, the qPCR results showed that Rho$^{-/-\ B6TgOPN1LW\text{-}EGFP+/-}$ mice did not down-regulate GFP expression faster than controls. Paradoxically, the SLO particle counts clearly showed the GFP signal being extinguished by 17-25 weeks in most mice. This lag between the GFP transcript levels on qPCR and functional GFP protein expression on SLO suggests that the loss of the *in vivo* fluorescence occurs due to down regulated translation. The mismatch is unlikely to be caused by increased GFP transcript degradation or reduced GFP transcription at the genome.

Evidence against reduced GFP transcription can be found in the mouse opsin expression analysis. The significantly reduced *Opn1mw* and *Opn1sw* transcript levels in Rho$^{-/-\ B6TgOPN1LW\text{-}EGFP+/-}$ mice did not correlate with a significant reduction in human OPN1LW-promoter driven GFP expression. This may be because the promoter-mediated down regulation mechanisms do not recognise exogenous human OPN1LW fragment. Alternatively, it may suggest that the mechanisms for down-regulating endogenous opsins are due to transcript degradation.

Because the GFP transcript levels did not vary significantly by Rho$^{-/-\ B6TgOPN1LW\text{-}EGFP+/-}$ status, double-normalisation of cone gene $\triangle$Cq values to GFP values did not alter the kinetics of relative cone gene expression, nor the statistical outcomes. As such, this technique was not included in the final hierarchical model analysis presented in subsubsection 4.4.9.2.

4.5.6 Gene expression peak from 2 to 6 weeks

Seven of the cone-specific genes showed rising expression between 2 and 6 weeks, before declining thereafter. This distinct polynomial expression profile may arise from the continued development and neuroplasticity of the retina in young pups. The eye are not fully open until 3 weeks after birth and retinal synaptic

connections are still being made in the first few weeks [204].

Punzo et al [62] deliberately sought genes that were up-regulated in RP at early ages before later down-regulation. This polynomial expression profile confirms that the genes of interest are cone-specific, as they are not immediately down-regulated by rod death beginning at birth. Notably, *Crx* and *Cngb3* did not demonstrate an initial peak. *Crx* likely because of the ongoing loss of transcript with the loss of rods. Fluctuations in *Cngb3* may not have been large enough to register given the error limit.

4.5.7 Expression of Crx

Crx was significantly down-regulated in $Rho^{-/-\ B6TgOPN1LW\text{-}EGFP+/-}$ mice at an accelerating rate from 6 weeks onwards. There was no contribution of the $B6^{TgOPN1LW\text{-}EGFP}$ allele to this down-regulation, it was purely driven by the $Rho^{-/-\ B6TgOPN1LW\text{-}EGFP+/-}$ status. The down-regulation of *Crx* preceded changes in other cone genes.

Crx is a photoreceptor-specific transcription factor that activates cone photoreceptor gene expression by binding directly to the promoter or enhancer regions of the target gene [132]. During embryological development, expression of Otx shortly precedes Crx expression and coinciding cone photoreceptor development. Crx expression peaks in mice pups at p5 [7]. Studies examining mRNA expression in various models of Crx knock-out mice demonstrate down-regulation of genes involved in the photo-transduction cascade. Particularly, Opn1mws, Opn1sws, Gnat2, Cone Arrestin and Pde6c [15]. This same pattern of cone gene down-regulation was observed in the $Rho^{-/-\ B6TgOPN1LW\text{-}EGFP+/-}$ mice, following the significant down-regulation of *Crx* from 6 weeks onwards.

The inclusion of rod photoreceptors as well as cones photoreceptors in the final test sample confounds the cause of the reduced *Crx* transcript, as both photoreceptor types express *Crx*. This confounding could be reduced by FACS pre-processing to remove rod photoreceptors. However, FACS sorting

introduces a separate source of confounding as detailed in subsubsection 4.4.4.2. The loss of a large majority of the cone photoreceptor population during FACS may alter the results unpredictably; alternatively, it may select against those cone photoreceptors with down-regulated *Crx* expression, which are simultaneously down-regulating GFP expression.

Correlation of declining *Crx* levels with falling *Rho* transcript did not explain all of the variance in *Crx*. This experiment is limited because it is not possible to quantify what contribution the cone photoreceptors made to the observed decline in *Crx* levels. It would be possible to explore the effect of declining *Crx* on cone photosensitivity by over-expressing the gene using an AAV vector.

4.5.8 Expression of Opsin genes

The expression of both cone opsins in $Rho^{-/-\ B6TgOPN1LW\text{-}EGFP+/-}$ mice declined significantly from baseline. This finding is in keeping with previous work showing that Opsin proteins are down-regulated and mislocalised on IHC [62]. The decline in opsin expression continues beyond 12, well after the loss of global retinal photopic sensitivity as measured by full-field ERG and OMR. Potentially, some residual cones with photosensitivity might be detectable with multifocal ERG testing or patch-clamping dissociated photoreceptor cells.

There appears to be an intrinsic loss of *Opn1mw* expression in $B6^{TgOPN1LW\text{-}EGFP+/-}$ mice. It does not significantly diverge from $B6^{TgOPN1LW\text{-}EGFP-/-}$ expression levels. However, the difference in *Opn1mw* down-regulation in $Rho^{-/-\ B6TgOPN1LW\text{-}EGFP+/-}$ mice does not reach significance over time. Whereas the decline in *Opn1sw* expression in $Rho^{-/-\ B6TgOPN1LW\text{-}EGFP+/-}$ mice is significantly different over time. This observation contradicts the fact that the cone dystrophy caused in $B6^{TgOPN1LW\text{-}EGFP+/-}$ mice affect S-cones more than M-cones [128].

4.6 Conclusion

This chapter identified the unexpected presence of a detectable *Rho* transcript in $Rho^{-/-\ B6TgOPN1LW\text{-}EGFP+/-}$ mice and quantifies the time line of cone function loss in $B6^{TgOPN1LW\text{-}EGFP+/-}$ mice.

This chapter developed and validated a manual counting technique for monitoring *in vivo* SLO assessment of GFP signal in the retina; this technique was used to demonstrate the timing and magnitude of cone loss in $Rho^{-/-\ B6TgOPN1LW\text{-}EGFP+/-}$ mice.

This chapter identified *Crx* and the cone opsins as the most down-regulated genes in retinas of $Rho^{-/-\ B6TgOPN1LW\text{-}EGFP+/-}$ mice. These genes are potential candidates for over-expression gene therapy to correct this deficiency and, potentially, restore cone photosensitivity.

5

CREATION AND VALIDATION OF AAV VECTORS

5.1 Introduction

The main hypothesis of this thesis explores whether the loss of cone photosensitivity observed in chapter 4 can be reversed by supplementing the cone photoreceptor transcriptome by exogenous over-expression of select cone phototransduction genes. This chapter is a crucial step towards answering this hypothesis, as it deals with the method by which the cone phototransduction genes will be over-expressed.

Figure 4.11 showed that murine *Crx* and cone opsins are the most substantially and earliest down regulated cone genes. This down-regulation coincides with the loss of cone photosensitivity in Figure 4.3. As detailed in subsection 4.5.7, both *Crx* and the cone opsins play important roles in cone photoreceptor gene expression and photosensitivity.

In keeping with the core hypothesis of this thesis, the human homologues *CRX* and *OPN1LW* have been selected for over-expression to potentially rescue or prolong cone photosensitivity.

5.1.1 Delivery mechanism

The intracellular delivery of DNA coding sequence or RNA molecules is achieved with gene therapy vectors. Vectors can be broadly classified as either viral or non-viral. The four main viral vectors are lentivirus, retroviruses, Adenoviral (Ad) and Adeno-associated virus (AAV). These viral vectors are either integrating (lenti-, retro-), whereby their DNA content is integrated into the host cell DNA; or non-integrating (adeno-, AAV), whereby they are maintained as an episome in the nucleus. Non-viral vectors can be as simple as the technique of electroporation of unpackaged DNA into cells. Typically though, non-viral vectors refer to liposomes (spherical vesicles with a lipid bilayer) and recent efforts to develop synthetic lipid or polymer nanoparticle vectors [205].

5.1.2 Choice of viral vector

As outlined by Somia et al ([206]), selection of an optimal viral vector should consider the following qualities:

- Easy production
- Sustained transgene expression
- Immunologically inert
- Tissue specific targeting
- Sufficient transgene payload capacity
- Integration or segregation of transgene
- Capacity to transfect replicating and non-replicating cells

Pioneering gene therapy work in the late twentieth-century initially utilised retrovirus and Ad vectors. The first human gene therapy trial utilised a retroviral vector to transduce T-cells *ex vivo*; modified cells expressed the 1.7kB adenosine deaminase (ADA) cDNA as a successful treatment for severe combined immunodeficiency (SCID) [207].

Retroviral vectors have two limits that make them ineffective as retinal gene therapy vectors. Most importantly, retroviruses have limited ability to transfect non-dividing cells, such as photoreceptors; although the relationship between infectivity and cell cycle stage depends on the class of virus [208]. Also, there are examples of retrovirus transgene silencing *in vivo* [209].

Adenoviral (Ad) vectors were developed for their capacity to deliver a large genetic payload, whilst also avoiding integration into the host genome; unregulated transgene integration has been shown to cause mutagenesis and carcinogenesis in mice [205]. For further safety, Ad serotypes are made non self-replicating by deletion of the E1 and E3 genes or complete removal of all intrinsic genes ('gutless' Ad). These recombinant Ad vectors were first used in the delivery of functional CFTR gene for cystic fibrosis in animals [210] and transient CFTR expression in human nasal epithelium [211]. In retinal research, Ad serotypes 2 and 5 were first shown to successfully transduce murine photoreceptors *ex vivo* and *in vivo* [212]. More recent work has exhibited the variety of retinal cell transduction specificity for the many different Ad serotypes [213].

There were early concerns about Ad immunogenicity [214] and immune-mediated death of transduced cells. These concerns reached a peak in 1998 following the death of an otherwise healthy eighteen-year-old during a phaseI Ad vector trial to treat ornithine transcarbamylase deficiency [215, 206]. Although the cause was unclear, prior Ad exposure and antibodies were thought to contribute significantly [206].

In this context, an Adeno-associated virus (AAV) vector was first used to transduce retinal photoreceptors in 1996 [216]. AAV.CMV.lacZ vector successfully expressed *LacZ* transgene in photoreceptors, as detected by X-Gal staining. AAV vectors are capable of transducing non-replicating retinal cells without integration [217] and less immunogenic potential, although recent work is starting to question this assumption [218]. The total AAV vector payload is limited at 4.7kB, packaged as a single strand of DNA.

AAV is not a self-replicating virus and is dependent upon external helper genes provided directly by Ad or, during lab manufacturing, *in trans* plasmids containing the additional genes. Furthermore, to create space for the transgene expression cassette, the *Rep* and *Cap* genes are also externalised during manufacture, making AAV replication *in vivo* impossible. To date, all but two clinical trials of retinal gene therapy have used AAV vectors [219, 220, 66, 65].

5.1.3 Rationale for transgene selection

5.1.3.1 Human genes function in mice

There is evidence that the mouse phototransduction cascade can be triggered by OPN1LWS human visual pigment [221]. Mouse phototransduction cascade can also be activated by other non-murine opsins [95]. Development of a vector using human opsin or other genes is therefore an established approach in mice and would also allow easier transition to clinical trials if successful.

5.1.3.2 CRX

The gene expression assay in chapter 4 identified *Crx* as the most profoundly down-regulated gene examined. As detailed in subsubsection 1.1.3.2, *Crx* is necessary for cone opsin expression and interacts with other transcription factors (Rorβ2 and Trβ2) to modulate these opsins. Furthermore, *Crx* auto-regulates expression and down-regulated *Crx* have been shown to potentiate further *Crx* down-regulation [11, 8]. AAV over-expression of human *CRX* may slow or halt the *Crx* down-regulation in photoreceptors and prevent the cone opsin down-regulation observed.

5.1.3.3 OPN1LW

The gene expression assay in chapter 4 identified *Opn1sw* and *Opn1mw* as the next most down-regulated genes. Other studies confirm this early pattern of cone opsin down-regulation during RP [62]. Human opsins can stimulate the murine phototransduction cascade [221] and, if successful, are more readily translatable

to the clinic than murine opsin vectors. Of the three human cone opsins, OPN1LW has the least nucleotide and amino acid homology with the murine opsins. As such, isolation of the human transgene in treated mouse samples may be more readily achieved using qPCR and IHC.

Previous studies have shown that ectopic expression of both human Rhodopsin [102] and the Halorhodopsin transmembrane channel [95] can restore photosensitivity in degenerate retinas. These two important studies suggest that, similarly, ectopic cone opsin expression may restore photosensitivity.

5.1.4 Rationale for promoter selection

Promoters used in gene therapy expression cassettes can be either constitutive, tissue-specific or regulatable. None of these choices is perfect for this project. Regulatable promoters are useful for clinical situations in which constitutive protein expression may be deleterious; in such cases, small-molecules (i.e. Tetracycline) can be administered to turn off or on the transgene expression. However, retinal gene therapy with CRX or OPN1LW to prolong cone photoreceptor photosensitivity requires constant transgene expression within cones.

As demonstrated in the gene expression study of chapter 4, cone-specific promoters and endogenous cone genes are down-regulated during RP. A finding confirmed in other work [222, 62]. Cone-specific promoters, such as the *ARR3* fragment, are known to localise transgene expression to cones. Yet, they may also be silenced by the same underlying process down-regulating endogenous cone genes. A constitutive promoter such as CAG overcomes the potential problem of transgene silencing because it is not down-regulated in the same way [223]. CAG is a synthetic promoter assembled from a) Cytomegalovirus early enhancer element, b) the promoter, first exon and first intron of the Chicken β-actin gene, and c) the splice acceptor of the rabbit β-globulin gene.

However, constitutive expression of these transgenes may have off-target effects, these could be beneficial or deleterious. However, it has been shown that ectopic expression of photosensitive opsins or membrane channels can confer useful light sensitivity to degenerating or blind retinas. Melanopsin has been shown to improve mouse visual function [103]. Ectopic expression of human rhodopsin is beneficial to visual function in mice [102]. Even bacterial ectopic expression of Halorhodopsin channels can restore cone photoreceptor sensitivity [95].

5.1.5 Rationale for including intron-exon and WPRE elements

Transgene expression efficiency can be further modulated by regulatory elements such as intron-exon splice sites and the Woodchuck hepatitis virus post-transcriptional regulatory element (WPRE) [224, 51]. Intron-exon splice sites encourage binding of transcriptional machinery, thereby driving more transcription and expression. Intron-exon sites are included in the synthetic CAG promoter [223].

The primary benefit of Woodchuck hepatitis virus post-transcriptional regulatory element (WPRE) is the improved transduction at lower dose; an efficiency improvement that helps reduce AAV immunogenicity. WPRE is thought to enhance the efficiency of transcript termination and has been shown to enhance transgenic GFP expression in *ex vivo* human retinal cultures and transgenic *REP1* expression in deficient mice [51]. WPRE was included in the first gene therapy vector approved for use in the European Union, Glybera [225]. WPRE is also currently used in the REP1 vector being tested in phase I/II choroideremia trials [65]. The primary benefit of WPRE is the improved transduction at lower dose, thereby reducing immunogenicity.

5.1.6 Rationale for capsid serotype AAV^{Y733F}

Early AAV serotypes for murine retinal gene therapy were wild-type AAV2 or AAV5 [216]. Targeted mutation of capsid Tyrosine residues helps bypass Tyrosine-mediated immune response to AAV [136]; although the innate immune response still responds to AAV vectors [218]. Tyrosine capsid mutants also display differing specificity for various tissue types [226] and retinal cell types. AAV8^{Y733F} has been shown to more strongly target retinal photoreceptors that other wild-type and mutant AAV8 or AAV9 capsids [136]. However, direct comparison with the AAV5^{Y719F} capsid showed no difference in cone rescue [227]. None of the capsid types exclusively targets photoreceptors and all vectors delivery the expression cassette to RPE during subretinal injections [228].

Regarding clinical translation, serotype efficacy for retinal transduction also varies by species. AAV8 has also been shown to be more effective than AAV2 for retinal gene expression in non-human primate (NHP) [229]. For this reason, AAV8^{Y733F} is the most appropriate capsid selection in an experiment targeting murine photoreceptors and considering clinical translation.

5.2 Aims & objectives

This first aim of this chapter is to create and validate an AAV vector to deliver human *CRX*.

The second aim of this chapter is to create and validate an AAV vector to deliver human *OPN1LW*.

The objectives for the first aim of this chapter are:

1. Produce a pAAV.CAG.CRX.WPRE.pA plasmid by cloning human *CRX* coding sequence into an existing AAV plasmid construct.

2. Sequence the cloned *CRX* plasmid to exclude mutations, amplify the plasmid in E. Coli and confirm the ITRs are intact by Xma1 restriction

digest and re-sequencing

3. Produce AAV2/8^{Y733F}.CAG.CRX.WPRE.pA virus vector using HEK293 cell cultures transduced with the *CRX* plasmid, along with existing Helper and RepCap plasmids

4. Confirm the AAV2/8^{Y733F}.CAG.CRX.WPRE.pA virus vector has high-fidelity capsid using SDS-PAGE and sufficient titre (>1 $\times$ 10^{10}gc/mL) using qPCR

5. Optimise the CRX antibodies and techniques for WB and IHC on HEK293 cells and cell lysate, following cell transfection with pAAV.CAG.CRX.WPRE.pA plasmid

6. Validate the virus vector functions correctly, by demonstrating expression of the exogenous CRX protein in HEK293 cells transducted with AAV2/8^{Y733F}.CAG.CRX.WPRE.pA vector

The objectives for the second aim of this chapter are:

1. Produce a pAAV.CAG.OPN1LW.WPRE.pA plasmid by cloning human *OPN1LW* coding sequence into an existing AAV plasmid construct.

2. Sequence the cloned *OPN1LW* plasmid to exclude mutations, amplify the plasmid in E. Coli and confirm the ITRs are intact by Xma1 restriction digest and re-sequencing

3. Produce AAV2/8^{Y733F}.CAG.OPN1LW.WPRE.pA virus vector using HEK293 cell cultures using the custom *CRX* plasmid, along with existing Helper and RepCap plasmids

4. Confirm the AAV2/8^{Y733F}.CAG.OPN1LW.WPRE.pA virus vector has high-fidelity capsid using SDS-PAGE and sufficient titre (>1 $\times$ 10^{10}gc/mL) using qPCR

5. Optimise the OPN1LW antibodies and techniques for WB and IHC on HEK293 cells and cell lysate, following cell transfection with pAAV.CAG.OPN1LW.WPRE.pA plasmid

6. Validate the virus vector functions correctly, by demonstrating expression of the exogenous OPN1LW protein in HEK293 cells transducted with AAV2/8^{Y733F}.CAG.OPN1LW.WPRE.pA vector

5.3 Materials & methods

5.3.1 Genetic components

5.3.1.1 Human CRX gene

Homo Sapiens Crx gene was ordered from a commercial source (Origene, Cat# SC126270, NCBI reference NM_000554). The CRX clone was delivered as ion-exchange column purified, transfection-ready dried plasmid DNA. The sample was reconstituted and stored at -20°C.

5.3.1.2 Human OPN1LW gene

Homo Sapiens long wavelength sensitive cone opsin (OPN1LW) was a kind gift from Dr Michelle McClements. The coding DNA sequence had been previously spliced together from human gDNA. The sample was re-sequenced before cloning to confirm the nucleotide sequence matched the GenBank reference BC156643.1.

5.3.1.3 Plasmid backbone

The pAAV.CAG.GFP.WPRE.pA was a kind gift from lab colleagues. Details can be found in subsubsection 2.4.2.1.

5.3.2 Molecular techniques

5.3.2.1 PCR and Agarose gels

PCR amplification of transgene inserts was performed using oligonucleotide primers that also introduced the Kozak consensus sequence and restriction digest sites. PCR was performed using KOD HotStart MasterMix as outlined elsewhere (subsection 2.3.2). CRX was amplified using a 2 minute *hot-start* 95°C step, following by 30 cycles of: denaturing at 95°C for 15 seconds, annealing at 58°C for 10 seconds and extension at 70°C for 20 seconds. Secondary structure formation by CRX was overcome by 1% Dimethyl sulfoxide (DMSO) addition during PCR.

OPN1LW was amplified using a 2 minute *hot-start* 95°C step, following by 35 cycles of: denaturing at 95°C for 15 seconds, annealing at 60°C for 10 seconds and extension at 70°C for 20 seconds.

1.5% Agarose gels and DNA band extractions were performed as explained in subsection 2.3.3.

5.3.2.2 Restriction digests and ligation

Restriction digests of plasmids and transgene inserts was performed (see subsection 2.4.4) using bacterial endonuclease enzymes: PstI, HindIII, SalI and EcoRV enzymes (NEB). Linearised single-enzyme digested and circular undigested plasmid control experiments were performed in parallel. During ligation (see subsection 2.4.4, secondary structure formation by CRX was overcome by the addition of 1% DMSO.

5.3.2.3 XL-10 cell transformation and amplification

Following transgene ligation into the digested backbones, ultracompetent XL-10 cells were transformed with these plasmids as detailed in subsection 2.4.6. Successfully transformed bacteria were amplified in culture and plasmid concentrates extracted using commercial mini-prep or mega-prep kits.

5.3.3 AAV production

See section 2.5 for full methodological details and Table 5.2 for final plasmid transfection concentrations.

5.3.4 Cell culture and histological analysis

5.3.4.1 HEK293T cell transfection with plasmid

HEK293T cells were transfected with GFP, CRX or OPN1LW plasmids using TransIT-LT1 transfection reagent as detailed in subsection 2.6.2. For ICC, transduced cells were cultured on 10mm glass cover slips inside 24-well plates. Cells were fixed with 4% PFA and then easily transferred to glass slides after

ICC protocol in culture wells. For WB, transduced cells were resuspended in PBS, centrifuged gently at 1000g for 10 minutes, re-suspended in fresh PBS and then centrifuged again before freezing the cell pellet at -80°C.

5.3.4.2 ICC protocol

ICC was performed on HEK293T cells on glass cover slips as detailed in subsection 2.7.3. Briefly, HEK293T cells transfected with transgene plasmid were PFA fixed, permeabilised, blocked and incubated with primary antibodies. The slides were then washed, incubated with secondary fluorescent antibodies and then DAPI counter-stained. They were then mounted on glass slides for confocal microscopy, as detailed in subsubsection 2.7.4.1.

5.3.4.3 HEK293T cell transduction with AAV

HEK293T cells were seeded into 6-well plates and transduced with AAV as detailed in subsection 2.6.3. An MOI of 5,000 and 10,000 was used for each AAV batch. Cell pellets were were collected by suspension in PBS and then centrifugation at 1000g for 10 minutes.

5.3.4.4 Western Blot

WB was performed as detailed in subsection 2.3.10. Briefly, HEK293T cell pellets and wild type retinas were homogenised in RIPA buffer. Prepared samples and recombinant protein controls were loaded into a gel alongside a protein size ladder. An electric current was passed through the buffer and the proteins diffused down the gel proportional to size. The proteins were transferred to a membrane and then stained with specific primary antibodies and label-signalling secondary antibodies.

5.4 Results

5.4.1 Design of AAV plasmids

The desired plasmids were first designed *in silico* using commercial Geneious software (v7). Primers were designed to amplify each transgene, whilst simultaneously introducing the Kozak consensus sequence and the relevant restriction sites for subsequent insertion into the plasmid.

For both the OPN1LWS and CRX cloning strategy, the restriction enzymes PstI and HindIII were chosen. These enzymes cut the plasmid backbone only once, whilst also having no cut site in the transgene CDS. The final primer designs are visible in Figure 5.1. Whilst trouble-shooting the CRX cloning, a second cloning strategy was designed using overlap PCR to join the CRX and WPRE components before a PstI/SalI digest.

During the cloning of CRX, the transgene proved difficult to ligate prior to transformation of XL-10 cells. *In silico* analysis of CRX transgene CDS secondary structure demonstrated strong hairpin formation (Figure 5.1). The subsequent addition of DMSO to the PCR amplification resulted in higher amplicon yield. The addition of DMSO during the ligation of CRX transgene into the plasmid backbone resulted in successful colonies containing the correct plasmid sequence.

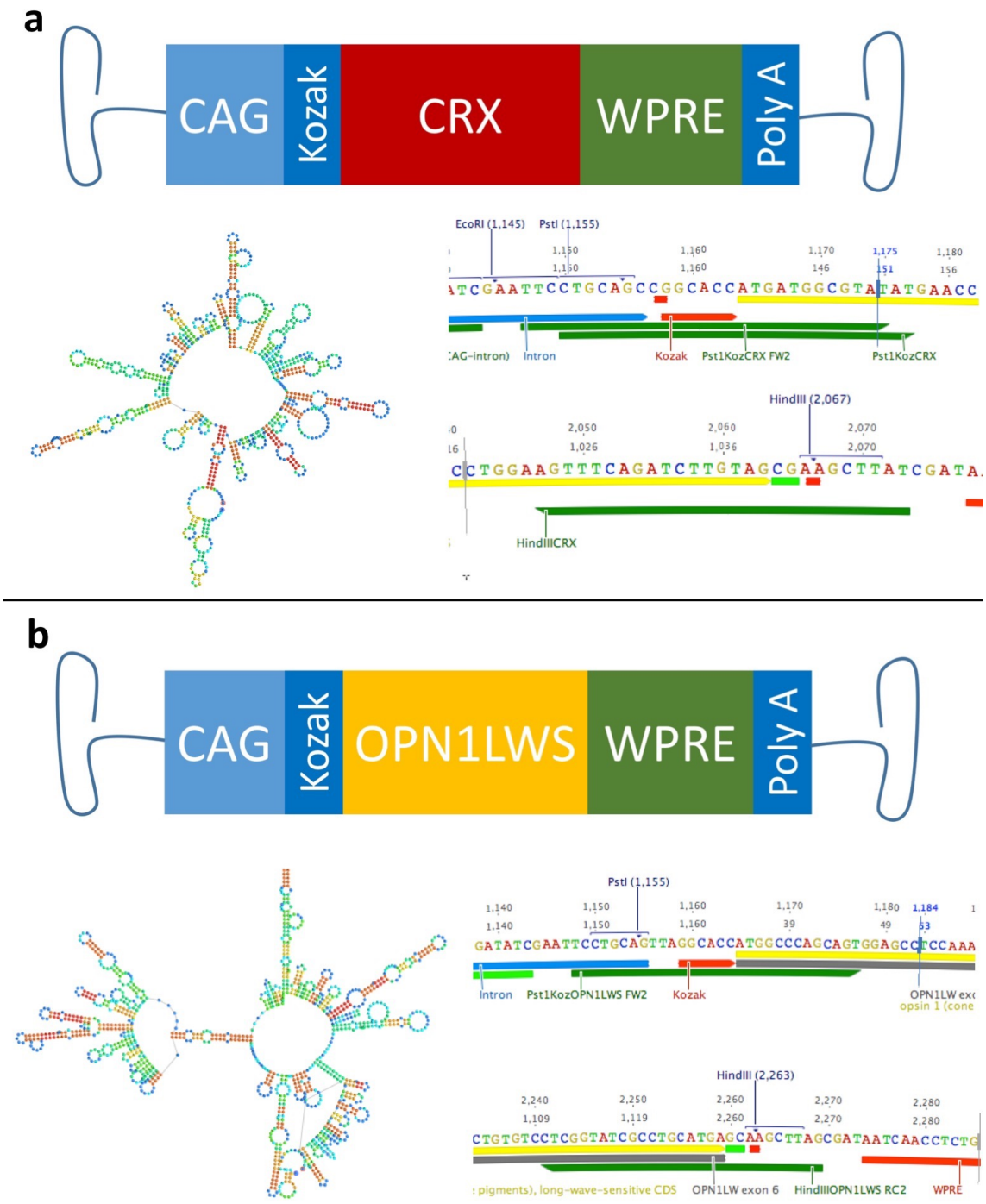


Figure 5.1 | AAV plasmid cloning strategies. The pAAV.CAG.CRX.WPRE.pA expression cassette **(A)** was cloned into an existing vector backbone using primers that introduced the PstI and HindIII restriction sites to the transgene. The Kozak consensus (GGCACCATG) was also introduced. *CRX* has a strong secondary structure formation as showing the folding model (left-side). The pAAV.CAG.OPN1LW.WPRE.pA expression cassette **(B)** was also created using PstI and HindIII restriction sites introduced by primers. The *OPN1LW* secondary structure *in silico* model predicted much weaker bonds than *CRX*.

5.4.2 Cloning the AAV.CAG.OPN1LW.WPRE.pA plasmid

As detailed in Figure 5.2, PCR of OPN1LW produced amplicons approximately 1100bp in size and introduced the Kozak sequence and restriction sites. The correct amplicon band size was confirmed on agarose gel and amplicon purity was optimal at a 60°C annealing temperature. The OPN1LWS amplicons, as well as the recipient vector backbone, were digested using PstI and HindIII restriction enzymes. The correct digest fragments were demonstrated on Agarose gel. After extraction, the digested transgene fragment was then ligated into the digested vector backbone, before being used to transform Ultracompetent XL-10 cells.

The cultured XL-10 cells showed successful positive controls transformed with pAAV.CAG.GFP.WPRE. The negative transfection control showed a low background of colony growth due to undigested vector. A ligation control plate demonstrated the digested GFP fragment was re-ligated into the plasmid backbone. OPN1LWS test plasmid produced good numbers of colonies for further processing.

24 colonies were chosen and cultured overnight before plasmid extraction with commercial mini-prep kit (144-315ng/μL). The plasmid extract of each colony culture was digested with Xma1 enzyme to confirm intact viral ITRs and screen for OPN1LW insertion. OPN1LW introduces an additional XmaI cut-site into plasmid, creating distinct three-band pattern. CAG.GFP.WPRE plasmid positive control showed correct XmaI digestion; 19 of the 24 OPN1LW cultures showed expected XmaI digest.

Colony 1 sequencing confirmed un-mutated transgene and the culture was mega-prepped to produce high concentration plasmid (1458ng/μL). Full plasmid sequencing excluded any mutations, including the early ITRs. Repeat XmaI digestion confirmed intact ITR digest sites. The transgene plasmid was ready to proceed to AAV production.

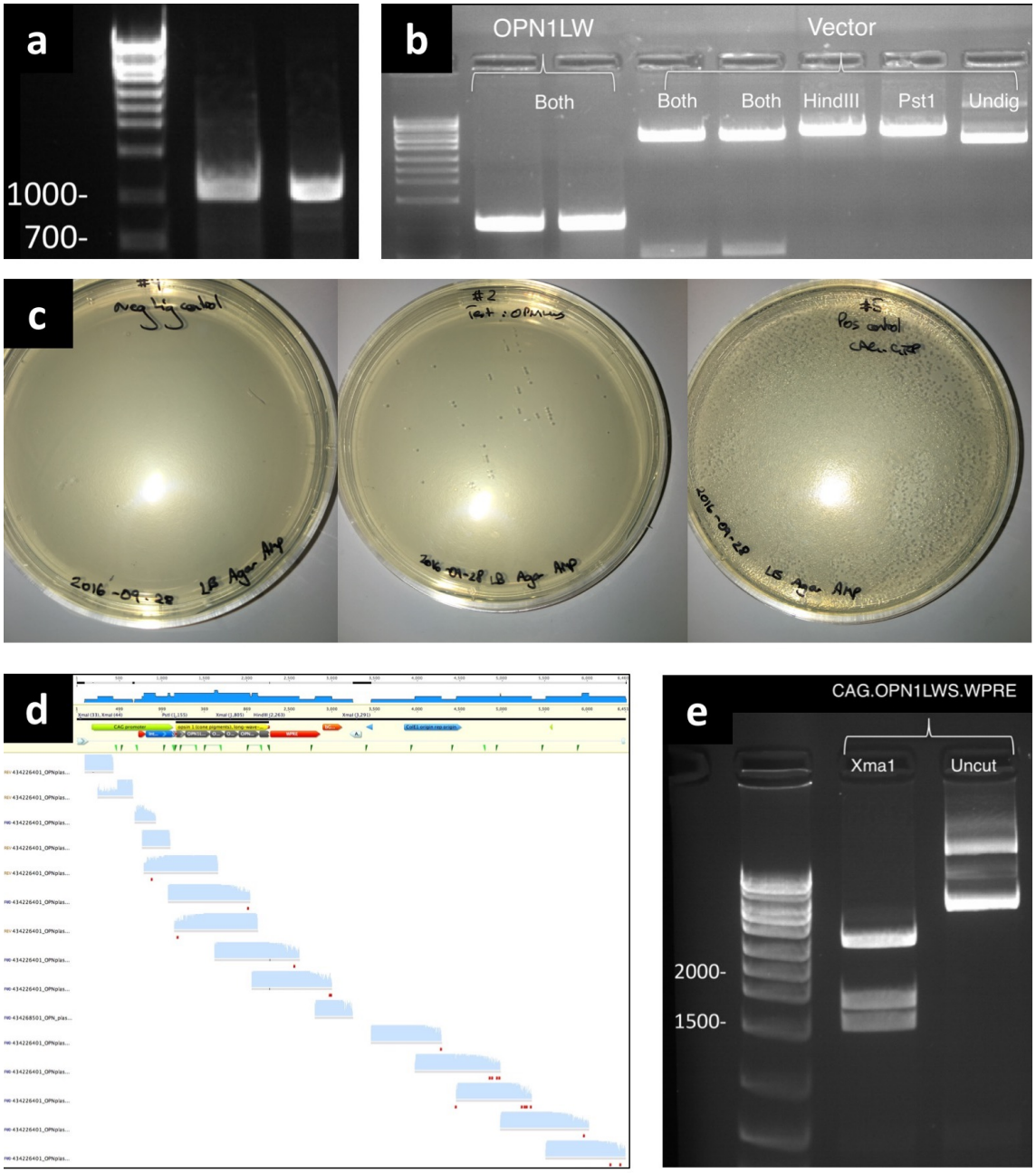


Figure 5.2 | Cloning the OPN1LW plasmid.a, The 1100bp *OPN1LW* amplicon was PCR amplified using custom primers that introduced restriction sites. **b,** Agarose gel showing the amplicon and vector plasmid after digestion with PstI and HindIII enzymes; the agarose gel also shows positive and negative controls. The double-digested insert and backbone were then extracted from the gel and ligated in a separate reaction. **c,** Agar culture plates showing XL-10 bacterial colonies after transformation. There are no colonies in the negative control, but high growth in the *OPN1LW* ligation test plate and positive control. **d,** Sanger sequencing reads (light blue) of the final pAAV.CAG.OPN1LW.WPRE plasmid (top annotations) mega-prep showed good coverage and no mutations. **e,** Agarose gel showing XmaI digest of the pAAV.CAG.OPN1LW.WPRE plasmid produced three bands as expected, demonstrating the middle of the ITRs are intact.

5.4.3 Cloning the AAV.CAG.CRX.WPRE.pA plasmid

As detailed in Figure 5.3, PCR of CRX produced amplicons approximately 900bp in length on Agarose gel and introduced PstI and HindIII cut sites. In the alternative overlap PCR strategy, CRX was joined to WPRE during PCR to produce a 1500bp product whilst also introducing PstI and EcoRV cut sites. The ultimately successful PstI/HindIII restriction digest of CRX and the recipient plasmid can be seen in Figure 5.3(C).

Strong secondary structure bonds in CRX (subsection 5.4.1) were ultimately overcome by the addition of DMSO during both PCR and the ligation reaction. Ligated CRX plasmid grew ample colonies compared to low negative control background during XL-10 transformations.

24 colonies were chosen and cultured overnight before plasmid extraction with commercial mini-prep kit (112-293ng/μL). The plasmid extract of each colony culture was digested with SacI and XmaI enzyme to confirm intact viral ITRs and screen for CRX insertion. CRX introduces an additional XmaI cut-site into plasmid, creating a distinct three-band pattern; SacI is unique to CRX in this plasmid design. CAG.GFP.WPRE plasmid positive control showed correct XmaI digestion pattern (Figure 5.3e); only colony 1 and 6 of the 24 cultures showed CRX insertion. Sequencing revealed an InDel mutation in colony 1.

CAG.CRX.WPRE colony 6 sequencing confirmed un-mutated transgene and the culture was mega-prepped to produce high concentration plasmid (1666ng/μL). Repeat XmaI digestion confirmed intact ITR digest sites. Full plasmid sequencing excluded any mutations, including normal ITRs. The transgene plasmid was ready to proceed to AAV production.

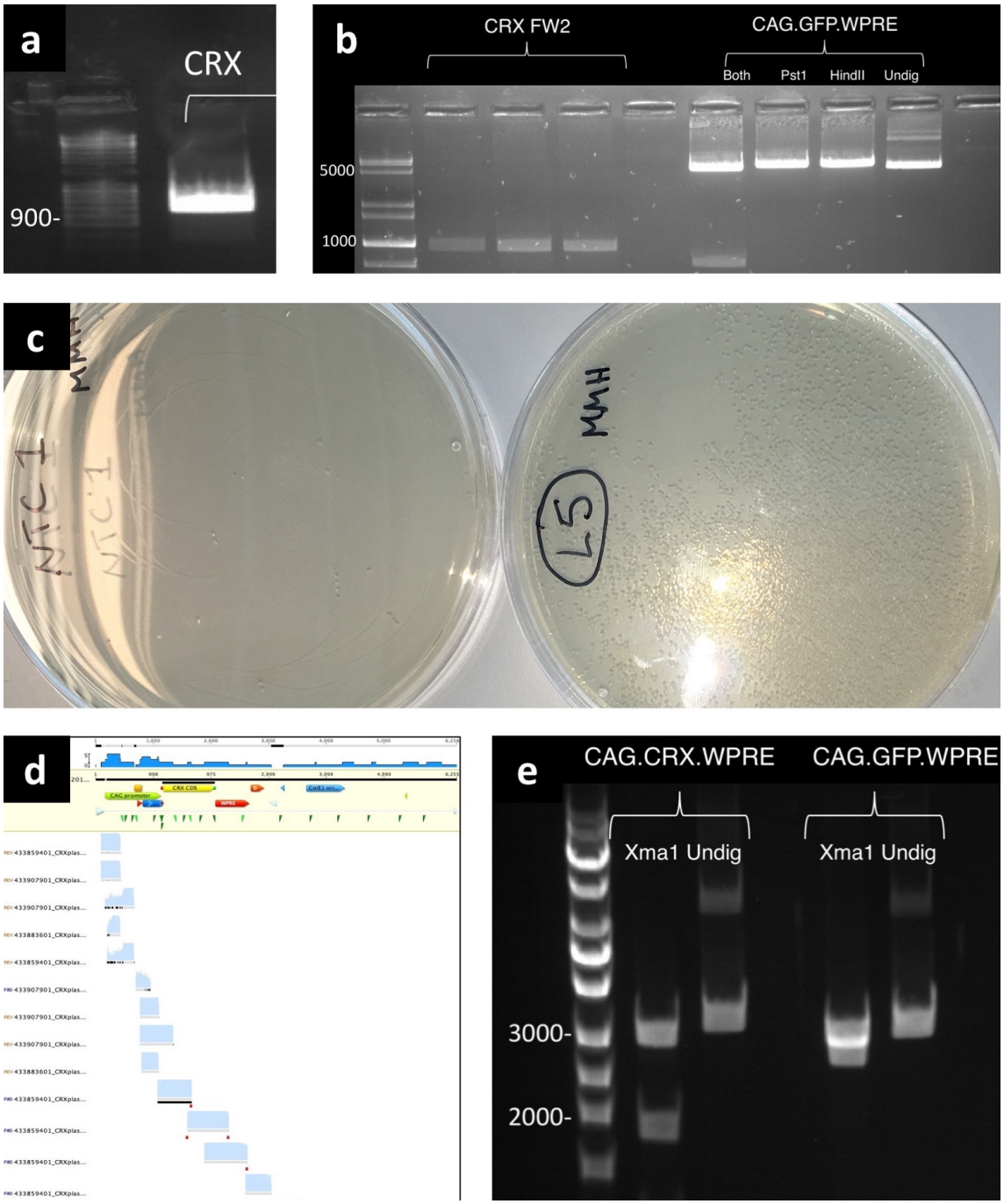


Figure 5.3 | Cloning the CRX plasmid. a, Agarose gel showing the 900bp *CRX* PCR amplicon produced using custom primers that introduced restriction sites. **b,** Agarose gel showing the amplicon and vector plasmid after digestion with PstI and HindIII enzymes; the agarose gel also shows positive and negative controls. The double-digested insert and backbone were then extracted from the gel and ligated in a separate reaction. **c,** Agar culture plates showing XL-10 bacterial colonies after transformation. There are no colonies in the negative control (NTC), but high growth in the *CRX* ligation test plate. **d,** Sanger sequencing reads (light blue) of the final pAAV.CAG.CRX.WPRE plasmid (top annotations) mega-prep showed good coverage and no mutations. **e,** Agarose gel showing XmaI digest of the pAAV.CAG.CRX.WPRE plasmid produced three bands as expected, demonstrating the middle of the ITRs are intact.

5.4.4 Validation of plasmid promoter

CAG promoter driven transgene protein expression was confirmed experimentally before AAV production. Transgene ICC/IHC antibodies were also optimised. Plasmid-transfected HEK293T cell cultures were fixed before undergoing ICC protocol detailed in subsection 2.7.3. Some transfected wells were pelleted and set aside at -80°C for WB optimisation. Three primary antibodies for each transgene (full technical details: Table F.2) were optimised for ICC at different concentrations as detailed in Table 5.1.

Table 5.1 | Optimised ICC antibodies.

Antibody name	Secondary serum	Dilution
1) CRX AB54635	Donkey	1/200
2) CRX SC-81958	Donkey	1/200
3) CRX PA5-32182	**Donkey**	**1/500**
1) AB65: OPN1LWS C-term	**Donkey**	**1/1000**
2) AB27: OPN1LWS N-term	Donkey	1/200
3) PA1: Mouse opsin1	Goat	1/1000

Antibodies highlighted in bold showed optimal results and were used for further in vitro and in vivo work at these concentrations.

The negative control HEK293T culture showed no background fluorescence. As exemplified in Figure 5.4, the GFP-transfected positive control HEK293T cells showed strong cytoplasmic GFP signal. CRX expression was predominantly nuclear, as expected for a transcription factor. OPN1LW expression showed a mix of cytosolic and nuclear staining patterns. The appearance of circular nuclear CRX may also represent cytoplasmic staining in unhealthy HEK293T cells with retracted cytoplasmic processes.

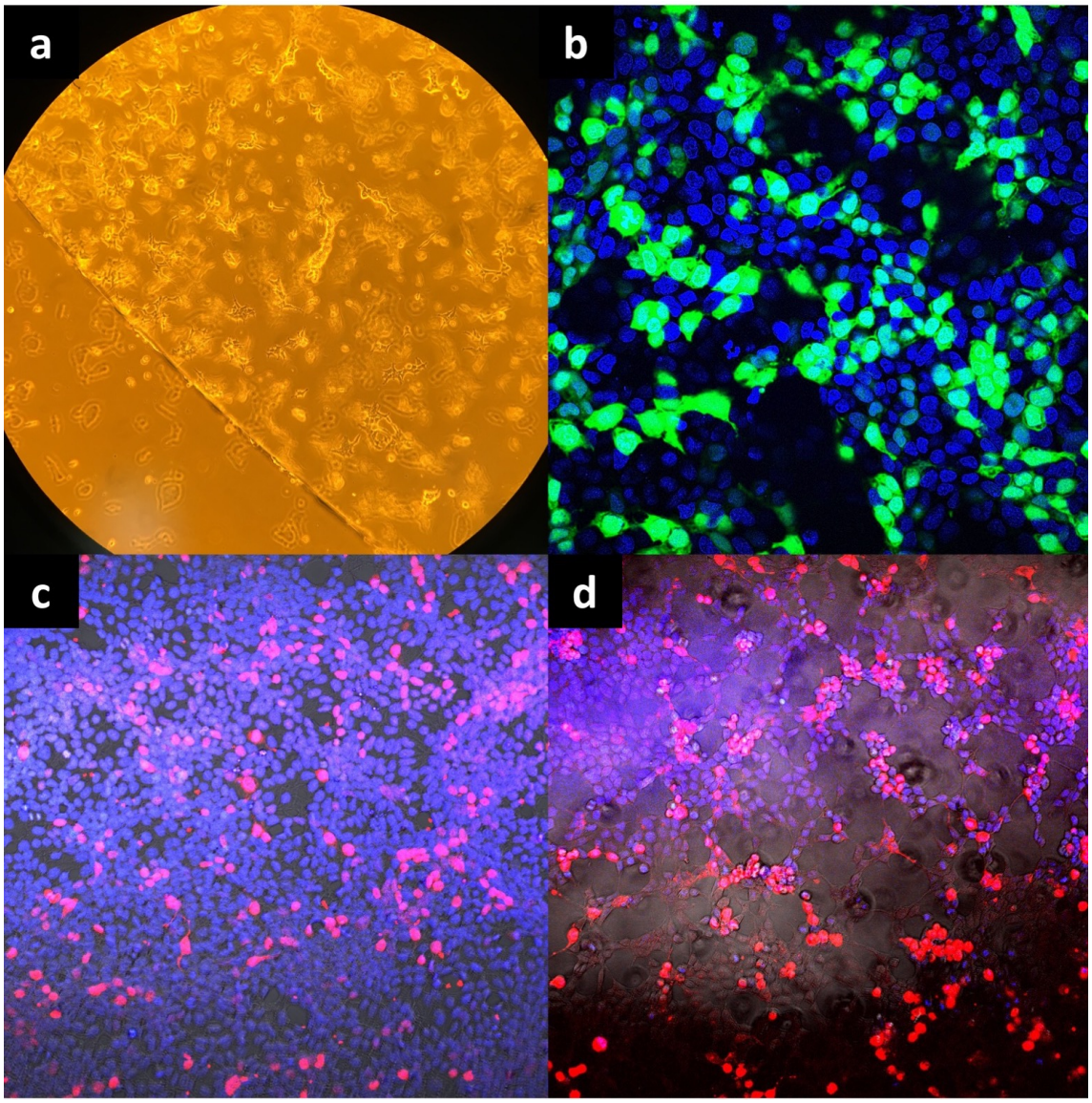


Figure 5.4 | Validation of plasmid promoters. **a,** Semi-confluent HEK293T cells cultures grown on transferrable glass cover slips (the glass edge is visible) were transfected with plasmids. Immunocytochemistry demonstrated that the **b,** GFP control plasmid, as well as **c,** CRX and **d,** OP1LWS test plasmids produced protein in the cells.

5.4.5 AAV8^{Y733F} production

Before commencing AAV production, two additional plasmids were prepared. Previously cloned RepCap AAV8^{Y733F} was amplified from a communal Glycerol stock of transformed XL-10 cells (1494ng/μL). Helper plasmid (pAdΔ6) was amplified from communal glycerol stock of transformed XL-10 cells (1243ng/μL).

Batches of both OPN1LW and CRX AAV were produced simultaneously from two hyperflasks each. Hyperflasks were seeded from HEK293T subcultures at

Table 5.2 | Plasmid concentrations for transfections during AAV production.

Plasmid	Size (kb)	ng/μl	μl per hyperflask	μl per 2 flask transfection
Helper Plasmid #2	15.4	1237	213.9	427.8
AAV2 Y733F	7.3	1494	84.0	167.9
CAG.OPN1LWS.WPRE	6.4	1458	75.4	150.8
Helper Plasmid #1	15.4	1237	214.6	429.3
AAV2 Y733F	7.3	1494	84.2	168.5
CAG.CRX.WPRE	6.3	1666	65.2	130.4

passage 44. Final plasmid transfection concentrations are listed in Table 5.2. Despite being cultured from the same cell population, the subjective health of the HEK293T cells in the OPN1LWS hyperflasks appeared suboptimal; a higher number of detached cells and patchy confluence.

The first batch of AAV produced (AAV-batch-1) showed suboptimal SDS-PAGE (see subsubsection 5.4.6.2) with multiple unexpected bands. Further, the titre of OPN1LW was a log unit less than the CRX virus.

AAV was produced a second time (AAV-batch-2) to improve the capsid purity and raise the OPN1LW titre. A second batch of Helper plasmid was produced (1237ng/μL) to confirm the helper plasmid was not reducing AAV capsid purity. The same HEK293T cell sub-line at passage 45 was used. The OPN1LW hyperflask culture encountered similar subjectively suboptimal growth after transfection. The final titre for each vector was equivalent to batch 1.

5.4.6 AAV quality control

Both batch 1 and batch 2 of the CRX and OPN1LW AAV were tested by qPCR and SDS-PAGE before proceeding to functional assays.

5.4.6.1 qPCR titring of AAV concentration

Custom oligonucleotide primers were designed to both the CRX and OPN1LW transgenes, and the polyA tail. The efficiency of all primer pairs were tested on a plasmid concentration gradient (details in Appendix H).

The most efficient primer pair for each transgene, as well as the polyA primer

pair, were used to titre the AAV concentrate and the AAV wash from each batch (Figure 5.5). The final titre of each AAV solution was calculated from the average of both primer pairs as shown in Table 5.3.

Table 5.3 | Final titres for each batch of AAV.

Virus	Batch	AAV concentrate (gc/mL)	AAV wash (gc/mL)
AAV2/8.OPN1LW	1	6.06×10^{11}	6.30×10^{9}
	2	3.02×10^{11}	3.01×10^{10}
AAV2/8.CRX	1	5.64×10^{12}	2.04×10^{11}
	2	7.68×10^{12}	1.42×10^{11}

5.4.6.2 SDS-PAGE of AAV capsid

SDS-PAGE was performed on denatured AAV protein capsid (Figure 5.5). Strong bands at 87, 73 and 62kDa corresponded to the expected size of VP1, VP2 and VP3 capsid proteins. Unexpected protein contaminants were also observed at lower dilutions.

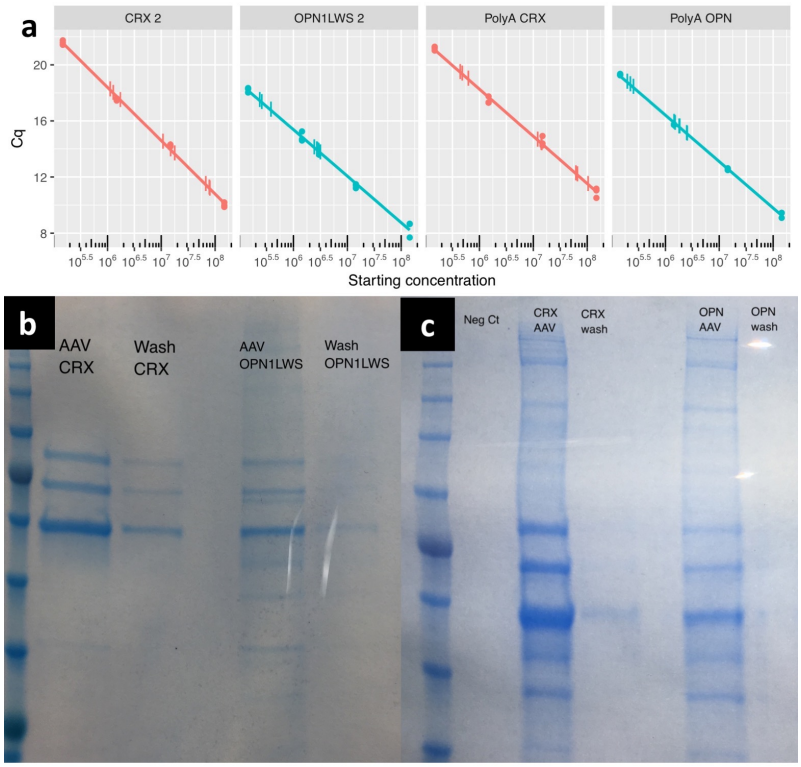


Figure 5.5 | AAV quality control. **a,** AAV concentrate and AAV wash titres (vertical lines) were measured against a reference dilution series of known plasmid concentrations (filled circles). Two different primer pairs were used for each AAV; one targeting the transgene (Efficiencies: CRX #2 84%, OPN1LW #2 100%) and a common poly-A tail primer (Efficiency: 98-100%). The AAV capsid purity was assessed with SDS-PAGE for **b,** Batch 1 and **c,** batch 2. The strong bands at 87, 73 and 62kDa are expected capsid proteins VPN1, VPN2 and VPN3. Unexpected protein contaminants are also visible, but were more dilute in batch 1.

5.4.6.3 Western Blot optimisation on cell lysate

Three antibodies for CRX and four antibodies for OPN1LW (details in Table F.2) were trialled for optimal WB performance. Antibodies were tested on plasmid transfected HEK cell lysates (see subsection 5.4.4), commercially available recombinant protein (see Table F.2) and wild-type mouse retinas. No CRX antibodies differentiated between mouse and human protein on WB. CRX antibody AB54635 performed optimally in identifying human CRX at the expected size of 38kDa. All three OPN1LW antibodies tested failed to identify the expected 40kDa band. Figure 5.6 shows one of four attempts to optimise the OPN1LW antibodies. Multiple antibody concentrations, increased positive control recombinant protein loading and an alternative incubation-shaker technique (in place of the snap.id method) were each attempted in turn without success. A subsequent review of literature identified another red-green opsin antibody used successfully for WB (Thermofisher, PA1-9517). This antibody could be ordered and optimised if required.

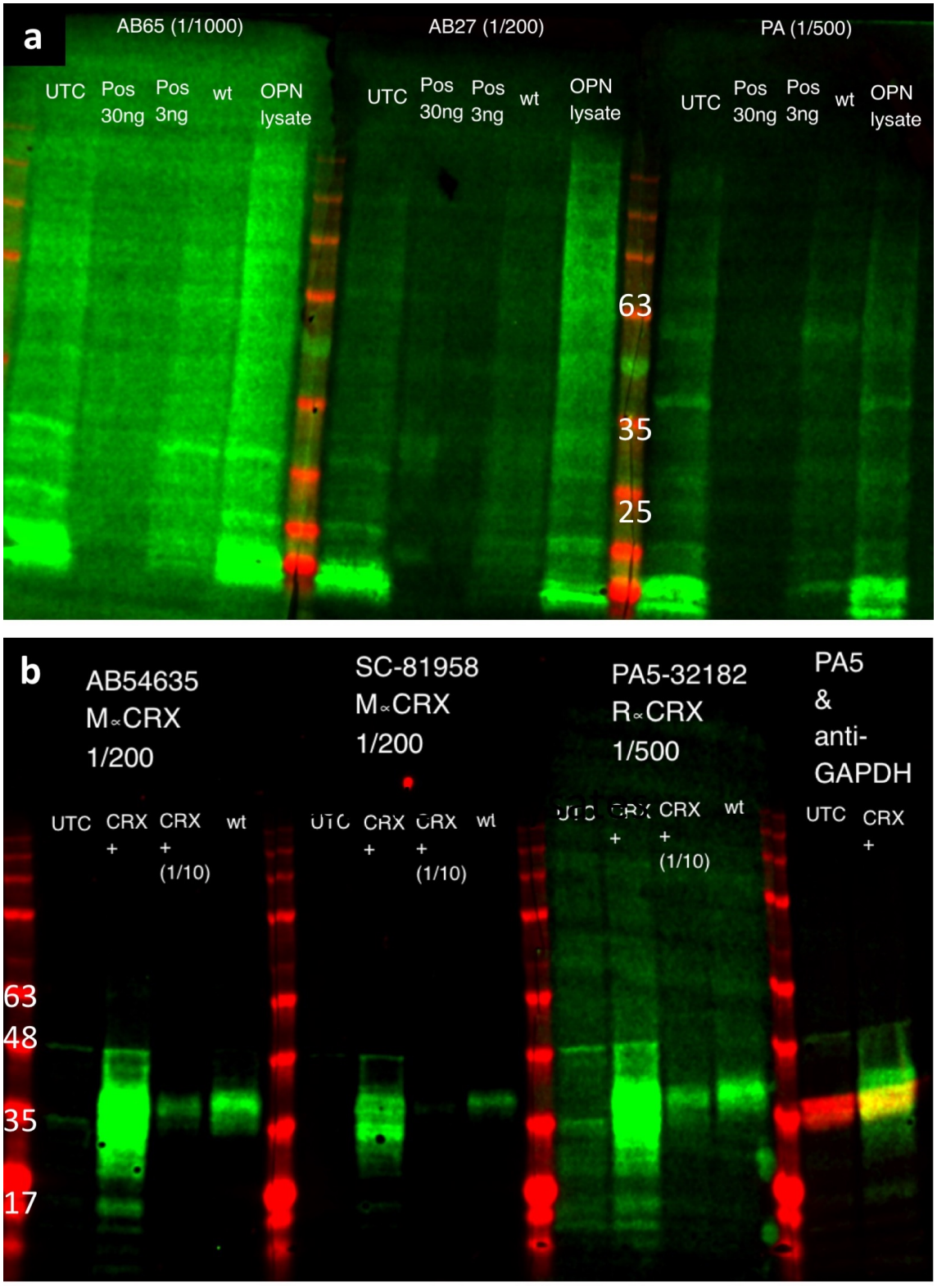


Figure 5.6 | **Western Blot optimisation. a,** OPN1LW antibody optimisation on plasmid transfected HEK cell lysates and recombinant protein. No band was identified by any of the three antibodies at the expected size of 40kDa. **b,** CRX antibody optimisation on lysates and recombinant protein shows the expected band at 37kDa.

5.4.7 Differentiating between species *in Vivo* with qPCR and IHC

In silico analysis of mouse *Opn1mw* mRNA (NM_008106.2) and human *OPN1LW* mRNA (NM_020061.5) reveals 83.7% homology, with nucleotide differences spread evenly across the transcript. Mouse *Crx* mRNA is alternatively spliced as isoform 1 (NM_007770.4) or isoform 2 (NM_001113330.1); however, the coding sequence of both isoforms share 87.5% homology with human *CRX* coding sequence. Similarly, the nucleotide differences are spread evenly across the transcript. In order to differentiate between exogenous human sequence and endogenous murine nucleotide sequence, sixteen qPCR primer pairs were compared. Pairs were chosen that accurately distinguished between human transgene plasmid and mouse retinal transcriptome nucleotide sequences Figure 5.7.

Table 5.4 | Non-homologous primers for differentiating between species.

Gene	Primer sequence
Human CRX	FW-5'-AGGGCCGTCTCTGACCTCC-3'
	RC-5'-GCTCGGAGACCCATAGGCG-3'
Mouse Crx	FW-5'-CACGTGAGGAGGTTGCTCTT-3'
	RC-5'-GTAGAGGGTCTCGGGGATGT-3'
Human OPN1LW	FW-5'-GGTCTCTGGCTACTTCGTGC-3'
	RC-5'-ACCAGATCCAGGAGAAGGCA-3'
Mouse Opn1mw	FW-5'-GACACTGGACCACTATGAG-3'
	RC-5'-ACTGATAGTGCTGGCA-3'

In silico analysis of human OPN1LW protein shows 87% amino acid homology with the murine Opn1mw, spread equally across the peptide. There are no obvious divergent epitopes for easy differentiation on IHC. Mouse Crx protein (NP_031796.1) and human CRX protein (NP_000545.1) differ by only 10 amino acids, spread evenly across the 299aa peptide. This high level of homology increases the likelihood of transgenic human CRX interacting correctly with transcription machinery in murine photoreceptors. It also presents challenges for *in vivo* differentiation between mouse and human protein. The

antibodies showed that endogenous Crx is expressed in both the outer nuclear layer and the inner nuclear layer [9, 10]. None of the four antibodies tested for IHC against human OPN1LW nor the three antibodies tested against human CRX gave a completely negative signal in murine retinal sections (Figure 5.8). No antibodies were identified that could exclusively identify human transgenic proteins during later *in vivo* experiments.

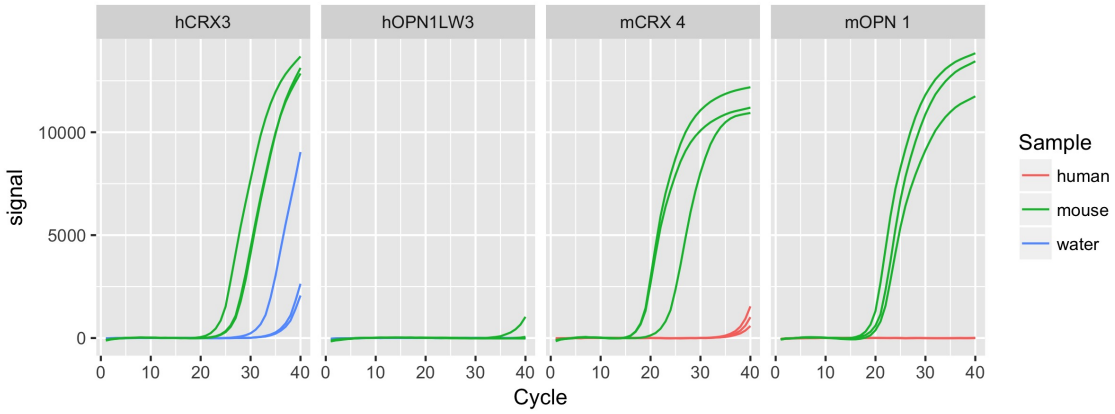


Figure 5.7 | Differentiating species on qPCR. Primer pairs designed to differentiate between non-homologous regions of human and mouse *CRX* and *OPN1LW*. Fourteen primer pairs were tested against samples of the murine retinal transcriptome and stock plasmids containing the human transgenes to identify these four optimal primers for differentiation.

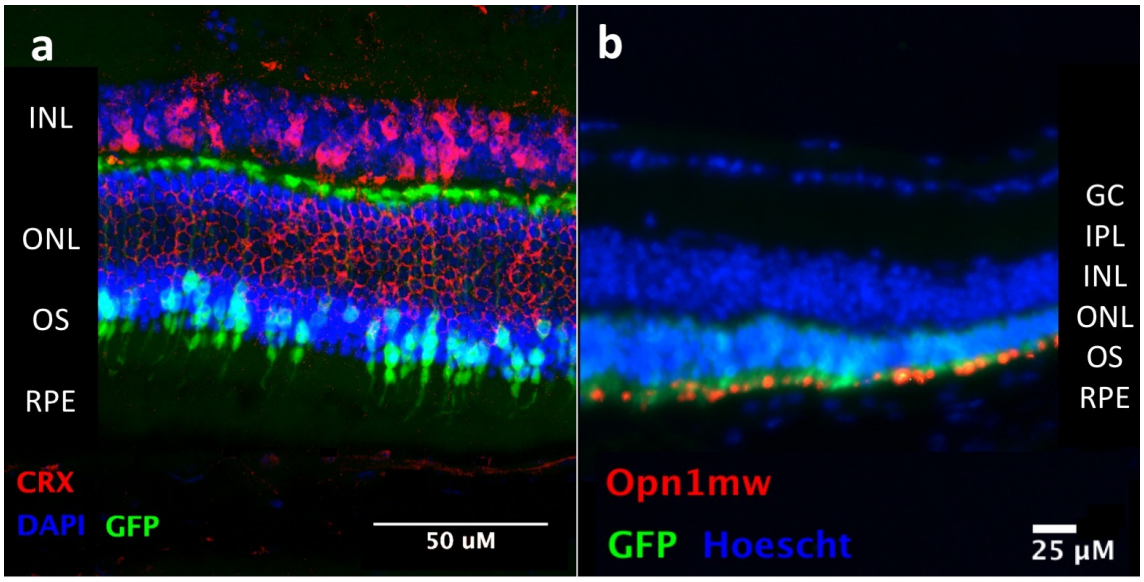


Figure 5.8 | **Differentiating species by IHC. a,** 63x lens objective Z-stack of a Opn1.GFP mouse retina (green cones) showing endogenous Crx nuclear staining; none of the three antibodies could distinguish between species. **b,** Low-power 10x lens objective image of an Nrl.GFP retina (green rods) showing endogenous Opn1mw staining pattern scattered infrequently with cones (only 3% of photoreceptors); none of the antibodies distinguished between species.

5.5 Discussion

In this chapter, two recombinant AAV plasmids were designed and cloned, allowing AAV vector production and functional validation *in vitro* before proceeding to *in vivo* testing.

pAAV.CAG.OPN1LW.WPRE.pA was cloned successfully and amplified without introducing mutations to the transgene, ITRs or other important components. Both batches of AAV2/8.OPN1LW had comparable titre, but were 10-fold less than the AAV2/8.CRX produced at the same time. The reduced AAV2/8.OPN1LW titre was unexpected but may reflect a toxic effect of the opsin transmembrane protein on HEK293T cells. The subjective appearance of reduced HEK293T density in the OPN1LW hyperflasks during production, as well as the appreciably smaller OPN1LW cell-pellet isolated during harvesting could be consistent with some HEK293T toxicity from OPN1LW expression. Ultimately, batch 1 of AAV2/8.OPN1LW had better capsid purity and was selected for use *in vivo*.

pAAV.CAG.CRX.WPRE.pA proved difficult to clone, possibly due to strong secondary structure formation in the CRX transgene that ultimately responded to the addition of dimethyl sulfoxide (DSMO). Both batches of AAV2/8.CRX had comparable titre, but the first batch of AAV had greater capsid purity.

The highest titre of any AAV batch (7.68×10^{12} gc/mL) produced was 10-fold lower than the maximum titres achieved in our lab for other transgenic AAV using the same protocol and equipment (10^{13} gc/mL). This titre difference may be a product of experience, but was not improved by production of a second batch. Similarly, new aliquots of helper and RepCap plasmids were amplified for the second batch of AAV, but provided no improvement. The titre difference may be explained by the overall health of the HEK293T cell cultures at high passage counts (p44 and p45). The cultures did not survive in 1% FBS DMEM medium during transduction experiments, an environment in which they normal cope when at lower passage counts. This poor cell health may also explain why both batches

of AAV had some faint additional SDS-PAGE bands.

IHC confirmed that the CAG constitutive mammalian promoter was functional in both plasmids and all AAV batches produced. Both AAV constructs successfully drove transgenic protein expression in HEK293T cells. CRX protein was largely localised to the nucleus of the cells as expected for a transcription factor. The OPN1LW protein was localised to both the HEK293T cell cytoplasm and nucleus and there was limited evidence of OPN1LW signal at the membrane on high power views. This may reflect an inability of opsin protein to be correctly inserted into the membrane without photoreceptor molecular machinery. Alternatively, it may reflect the death of any HEK293T cells that did insert opsin into the membrane, as suspected as a possible cause for the lower titre.

It was not possible to optimise antibodies that differentiated between human OPN1LW and mouse cone opsins in either IHC or WB . This will create difficulties in reliably identifying human OPN1LW transgene expression in mouse cone photoreceptors during *in vivo* testing. Alternatively, an OPN1LW vector also containing internal ribosome entry site (IRES) and a reporter gene could have been used to identify transduced cone photoreceptors [230]. Similarly, the use of a small epitope tag fused to the transgene protein (e.g. *Myc* or flag) could also identify transduced cone photoreceptors and the localisation of exogenous opsins in those cones [231]. However, N-terminus epitope tags may interfere with normal cone opsin functions; particularly, N-terminus changes may alter the downstream signalling to transducin outlined in subsection 1.1.2.

It was possible to identify qPCR primer pairs that differentiated human *CRX* and *OPN1LW* transgenes from mouse *Crx* and *Opn1mw* in the retinal transcriptome. Transgene expression in the retina of treated mice can now be clearly identified, allowing the time-dependent and titre-dependent magnitude of transgene transcription to be quantified. It will also allow any qPCR testing of injected retinas to isolate any up-regulation in endogenous cone genes from the gene therapy; an important distinction in exploring if treatment corrects the gene expression changes observed in chapter 4.

5.6 Conclusion

In this chapter, two recombinant AAV were produced and functionally validated *in vitro* before subsequent functional testing *in vivo* in the next chapter. The first batches of AAV2/8^{Y733F}.CAG.CRX.WPRE.pA and AAV2/8^{Y733F}.CAG.OPN1LW.WPRE.pA have adequate titre (CRX: 5.64 $\times$ 10^{12} gc/mL, OPN1LW: 6.06 $\times$ 10^{11} gc/mL) and acceptable capsid purity. Both AAV produce protein in transfected and transduced mammalian cell cultures and are expected to function *in vivo*. IHC and WB antibodies for the human CRX and OPN1LW proteins have been optimised for assessing *in vivo* protein expression. Both vectors are ready to proceed to pilot testing *in vivo* in Rho$^{-/-}$ mice.

6

PILOT STUDY OF AAV

6.1 Introduction

The core hypothesis of this thesis is that, in RP, the loss of photosensitivity in cone photoreceptors occurs much earlier than cone cell death and is driven by down-regulation of select cone phototransduction genes. Furthermore, this loss of cone photosensitivity can be reversed by supplementing the cone photoreceptor transcriptome by exogenous over-expression of select cone genes; specifically *CRX* and *OPN1LW*.

In chapter 4, a detailed analysis of the cone phototransduction transcriptome in Rho$^{-/-\ B6TgOPN1LW\text{-}EGFP+/-}$ mice was analysed alongside detailed phenotypic data about cone photosensitivity. This data demonstrated that *Crx* and the cone opsins are the most down-regulated genes and precede the loss of cone photosensitivity. As such, the human homologues *CRX* and *OPN1LW* were selected for over-expression gene therapy in mice to rescue or prolong cone photosensitivity.

In chapter 5, the human homologues *CRX* and *OPN1LW* were cloned into plasmid constructs and used to manufacture AAV2/8^{Y733F}.CAG.CRX.WPRE.pA and AAV2/8^{Y733F}.OPN1LW.CRX.WPRE.pA virus vectors. These virus vectors underwent quality control and demonstrated adequate capsid purity and sufficient titre. Both virus vectors also produced in exogenous protein in

transfected HEK293 cells.

In this chapter, the first Rho$^{-/-}$ mice will be injected with each two AAV vector to explore the effects of each vector *in vivo*. Pilot studies are an important step before performing a full randomised controlled trial of a treatment [232, 233]. A pilot study allows the study protocol to be tested and adjusted prior to the full study; the AAV preparation, equipment, surgical technique, functional measures and molecular endpoints can all be optimised. The randomisation technique, post-operative care and exclusion criteria can be finalised. Furthermore, the pilot data collected will estimate the location and precision of the outcome measures; this data will guide the sample size calculations for the outcome measures in full trial.

6.2 Aims & objectives

The objective of this chapter is to deliver both AAV vectors to the subretinal space of Rho$^{-/-}$ mice and demonstrate that each vector produces exogenous protein in the correct cell types and cellular locations.

1. Demonstrate reproducible subretinal surgical delivery of AAV vectors
2. Estimate the effect of each AAV treatment on retinal electrophysiology using ERG; this information will underpin power calculations in the next chapter
3. Estimate the effect of each AAV treatment on the macroscopic retinal appearance and architecture using cSLO and OCT
4. Optimise the immunohistochemistry techniques for injected eyes
5. Demonstrate retinal expression of the transgene for both AAV vectors
6. Decide upon the final dose selection for the full study in the next chapter

6.3 Materials & methods

6.3.1 Mouse model

The Rho$^{-/-}$ mouse model was used, following on from the chapter 4 characterisation experiments. Due to time constraints and difficulty with breeding pairs prior to the pilot study, the Nrl-L-EGFP$^{+/-}$:Rho$^{-/-}$ colony was used in place of the Rho$^{-/-\ B6TgOPN1LW\text{-}EGFP+/-}$ colony. The Nrl-L-EGFP$^{+/-}$:Rho$^{-/-}$ mice express GFP reporter in the rod photoreceptors, yet still demonstrate the rod degeneration phenotype.

The Nrl-L-EGFP$^{+/-}$:Rho$^{-/-}$ colony are similar, but not identical, to the Rho$^{-/-\ B6TgOPN1LW\text{-}EGFP+/-}$ colony. The first difference is a positive, these mice do not demonstrate the inherent cone degeneration described in GFP cone colony [128]. Secondly, these mice are easier to detect patterns of AAV-mediated photoreceptor damage on cSLO; the diffusely green fundus shows photoreceptor dropout more easily following injections.

However, the Nrl-L-EGFP$^{+/-}$:Rho$^{-/-}$ colony cannot undergo cSLO *in vivo* quantification of cone GFP survival. So too, the cones are not intrinsically labelled on IHC and - without additional antibodies - can only be identified by the gaps they leave between the green rods.

6.3.2 Study design

The pilot study was performed on two cohorts of Nrl.GFP,Rho$^{-/-}$ mice (n=18). All mice received an un-randomised PBS sham injection in the right eye. The fellow eye was randomised to receive either AAV2/8.CAG.CRX.WPRE at 1×10^{9}gc/mL or AAV2/8.CAG.OPN1LW.WPRE at 1×10^{8}gc/mL. Mice were randomised as described in subsection 6.3.5.

A first cohort - from a single litter - of 6 mice received subretinal injections of AAV at 3 weeks of age, underwent terminal ERG testing 3 weeks later and were sacrificed the same day for WB analysis. A second cohort of 12 mice - from two litters - received subretinal injections at 3 weeks of age, underwent a recovery

ERG 3 weeks later and a terminal OCT procedure the following week (4 weeks post injection). Eyes were collected for IHC the same day as OCT imaging.

The injected litters contained a mix of Nrl-L-EGFP$^{+/-}$:Rho$^{-/-}$ and Nrl-L-EGFP$^{-/-}$:Rho$^{-/-}$ mice. GFP genotype was not established before treatment and GFP phenotype was only confirmed later during cSLO imaging (n=12/18 mice).

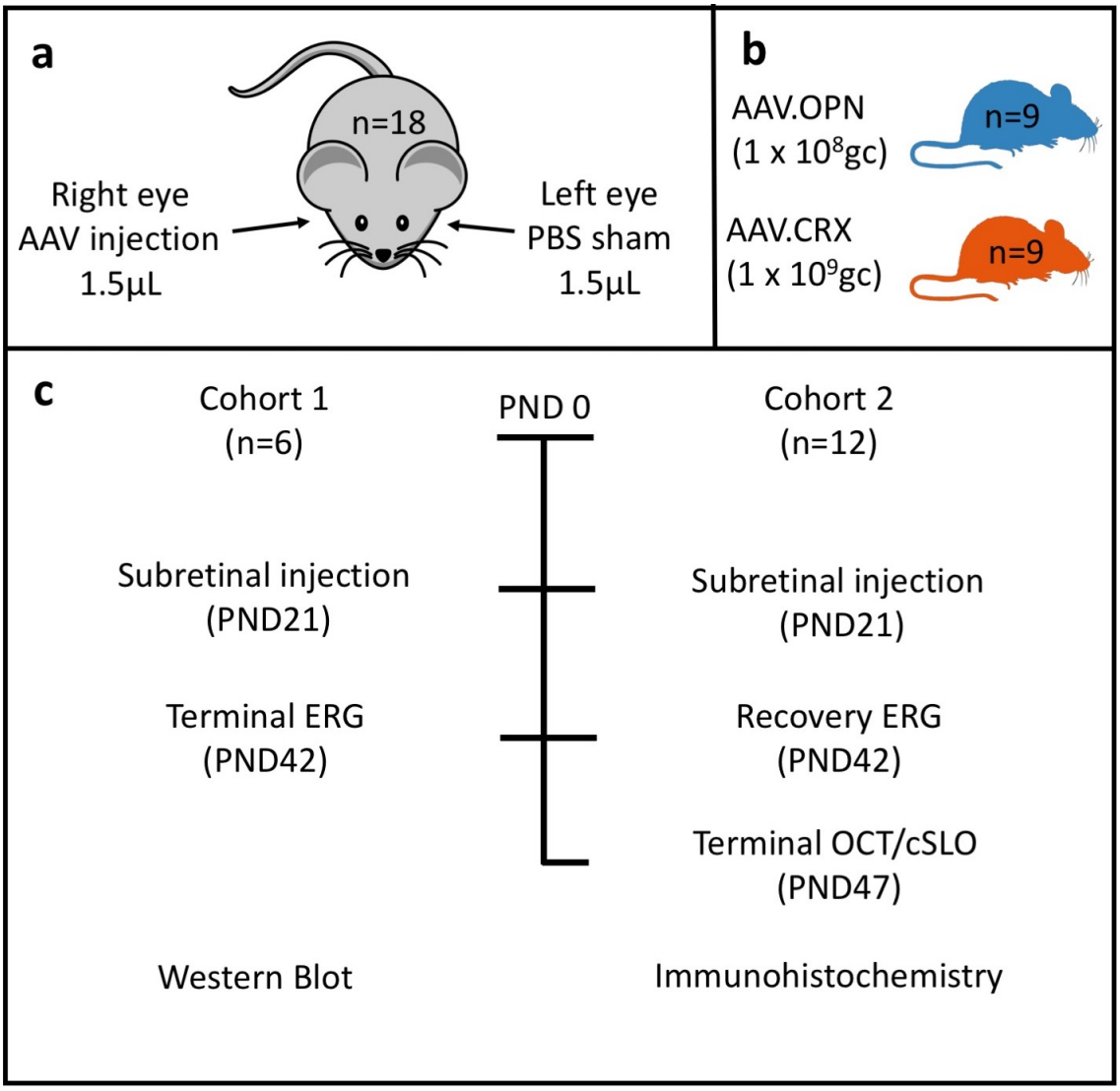


Figure 6.1 | Pilot study design. **a,** Left eyes received PBS sham and right eyes received a randomised AAV treatment. **b,** Designated colours for the AAV.OPN (blue) and AAV.CRX (orange) treatment groups. These colours are consistently used in graphically representing the outcome results. **c,** Schematic of the functional testing and tissue endpoints for the two cohorts of mice in the pilot trial; both AAV treatment groups were distributed equally between both cohorts. *PND: Post-natal day*.

6.3.3 Route of delivery

AAV treatment can be delivered to the retina by subretinal or intravitreal injection. Intravitreal delivery is performed with a small-gauge injection via the pars plana in anaesthetised mice. Depending upon capsid serotype, intravitreal AAV may transduce only Ganglion cells or transduce all retinal layers. Intravitreal Y733F capsid mutant vector can transduce photoreceptors [136] and quad-capsid mutants combined with miRNA show more specific photoreceptor-only transduction [234]. The inner limiting membrane appears to affect the efficiency of outer retina transduction from intravitreal injections, but can be disrupted by added protease [235]. With added protease, intravitreal AAV5 can transduce RPE [235].

Subretinal delivery is performed by a small-gauge trans-scleral injection in a hypotonous globe as described in subsection 2.2.2. Subretinal delivery is more effective at transducing photoreceptors and the RPE than inner retinal cells [236]. However, trans-scleral subretinal injections complicated by a retinotomy can result in intravitreal reflux of AAV and off-target inner retinal transduction. In this pilot study, AAV was delivered by subretinal injection.

6.3.3.1 Subretinal injections

Subretinal injections were performed at 3 weeks of age on both eyes of Nrl-L-EGFP:Rho$^{-/-}$ mice as described in subsection 2.2.2. AAV was defrosted on the day on injection and diluted in a tissue culture hood using sterile PBS. AAV.CRX was diluted to to 1×10^{9} and AAV.OPN to 1×10^{8}. A separate aliquot of sterile PBS was prepared in the culture hood for sham injections. All preparations were transported and stored on ice prior to injection.

The subretinal injections were performed on anaesthetised mice as described in subsection 2.2.2. Mice were recovered in a heated box and checked post-operatively on day 1, day 3 and every week thereafter. No complications were observed requiring intervention.

6.3.4 Dose and volume selection

The pre-clinical mouse experiments underlying some of the current retinal gene therapy clinical trials used 1 $\times$ 10^9gc [153] , 8 $\times$ 10^9gc [36], 2 $\times$ 10^8gc [237] or 6 $\times$ 10^9gc [34]. Outer retina transgene expression using AAV vectors occurs successfully at doses as low as 1×10^7gc [216]. A dose-dependent increase in transgene expression occurs with increasing titres [136], but vector-mediated toxicity will invariably be observed at very high concentrations.

The AAV tyrosine capsid mutants can achieve higher transgene expression compared to wild-type capsid AAV delivered at 100-fold higher titres [136]. Also, expression is increased at lower titres (i.e. 1×10^8gc/mL) by WPRE [51], a regulatory element included in both the AAV.CRX and AAV.OPN vectors.

The final volume of suspension was chosen as 1.5μL for mice injected at PND21, in keeping with previous work within our laboratory and elsewhere [36]. Larger volumes can cause retinal stretching, particularly in younger mice, which can be harmful. Smaller volumes are more difficult to work with using the equipment.

In this study, AAV was delivered at a dose of 1 $\times$ 10^9gc (AAV.CRX) and 1×10^8gc (AAV.OPN) in a 1.5μL volume of PBS.

6.3.5 Randomisation

Randomisation of the mice to treatment groups balances the groups, robustly eliminates confounding bias, and is the basis for uncorrected statistical testing of the difference in treatments [232]. Unbiased randomisation in a trial typically involves allocating each participant a unique number and then performing random number sampling without replacement (e.g. pseudorandom number generator software) from this allocated range. Restrictions may be introduced to ensure equal sizes for the treatment groups.

In this study, mice were alternately allocated to an AAV treatment after being randomly selected from the cage; true randomisation was not performed.

Restrictions were placed on treatment allocations - more than half of each cohort could receive one of the two particular AAV treatments.

6.3.6 Outcome measures

The initial data gathered in a pilot study provides estimates of the mean values for each outcome measure, as well as the variance, expressed as SEM or CI. This information can be used for power calculations ahead of the full randomised experiment. The outcome measures chosen for the pilot trial are those optimised during the natural history study; ERG, OCT and cSLO. The tissue endpoints were IHC and WB.

6.3.6.1 Electroretinography

ERG was performed on anaesthetised mice (n=18/18) three weeks following subretinal injections (mean age PND42$\pm$2). Testing and waveform analysis were performed as detailed in subsection 2.2.6.

6.3.6.2 OCT and cSLO

OCT measurements of retinal thickness were collected on anaesthetised mice as detailed in section 2.2. Measurements were only taken on the second cohort of mice (n=12/18) four weeks following subretinal injections (mean age PND47$\pm$2).

cSLO images of the macroscopic retinal appearance under IR, BAF and ICGA imaging conditions were collected on the same anaesthetised mice during the same imaging session. The cSLO protocol is detailed in subsection 2.2.3. BAF images at 70% detector sensitivity were analysed in ImageJ using a previously published protocol to quantify the effect of treatment on the GFP signal [201]. Regions of interest were sampled from the *en face* image using a 250-450 pixel annulus and then divided into dorsal and ventral halves. Mean greyscale values were measured for each region and expressed as integers (range: 0 to 255 arb. units).

6.3.6.3 Immunohistochemistry

Eye cups were collected following terminal OCT at seven weeks of age (mean age PND47±2). Eye cups were treated and preserved at -80°C as detailed in subsection 2.7.1.

Eye cups were later cryo-sectioned and stained with anti-CRX (#PA5-32182) or anti-OPN1LW (#ABIN651110) primary antibody, AlexFluor568 anti-Rabbit (#A10042) secondary and Hoescht. This protocol had been previously optimised in chapter 5, using the standard protocol in subsection 2.7.2. Details of the antibodies and blocking serums are listed in Table F.2.

6.3.6.4 Statistical analysis

All data handling and statistical analysis was performed using R software. ERG, OCT thickness and cSLO BAF mean greyscale values were all analysed using a hierarchical linear model, as detailed in subsection 2.8.2. The presence of pigmentary changes on IRAF images were assessed by chi-squared test on a contingency table. IHC expression intensity and patterns were only assessed qualitatively.

6.4 Results

6.4.1 Surgical outcome criteria

Criteria were developed for assessing the quality of the surgical delivery of the AAV vector. A successful surgery delivered the full volume of vector into the subretinal space and was not complicated by any item in the exclusion criteria. Figure 6.2 shows exemplar images of successful surgery and Table 6.1 details these criteria as they were applied during the pilot trial

All signs could be readily observed intra-operatively. The score was allocated by the surgeon at the time of the procedure and was not validated by a second observer; the inter-observer variability is unknown.

AAV treatment or PBS sham was delivered successfully into the subretinal

space, except one mouse that received less than 1.5μL of AAV.OPN (1×10^8gc). The delivery of this smaller volume was caused by an unintentional retinotomy permitting vector reflux into the vitreous. The final quantity delivered cannot be reliably quantified. In the absence of any other complications such as bleeding, this mouse was included in the final analysis in the pilot.

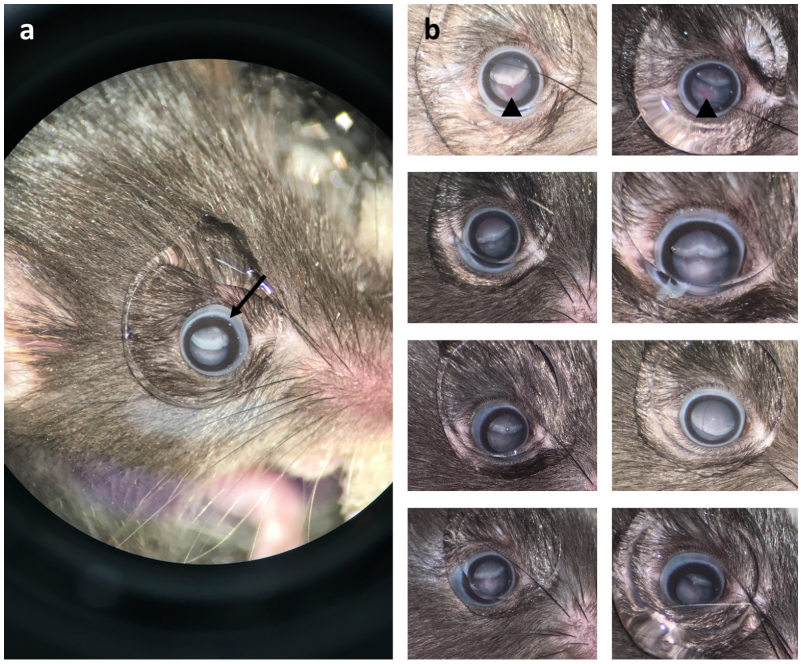


Figure 6.2 | Surgical outcomes. **a,** View down the operating microscope of the right side of an anaesthetised mouse immediately following trans-scleral delivery of 1.5μL of AAV to the subretinal space. The trans-scleral approach of the 35G needle is indicated by the arrow. **b,** Panel of images showing eight mice injected with AAV. In the top two images, arrowheads indicate the presence of epiretinal blood. In the bottom right image, the subretinal bleb is smaller than normal due to incomplete delivery of the vector.

Table 6.1 | Inclusion and exclusion criteria for surgical success

Surgical stage	Inclusion criteria	Exclusion criteria
Pre-op	Normal anterior segment Binocular	Anterior segment pathology Monocular
Intra-op vector deliver	Subretinal delivery of full 1.5μL volume	Visible reflux of fluid into vitreous Appreciable reduction in subretinal bleb size suggesting reflux into vitreous Vector delivery directly into vitreous Vector delivery into another location not subretinal Equipment malfunction or error preventing delivery of exactly 1.5μL of vector
Intra-op complications	Absence of excludable haemorrhage * retinotomy permitted without reflux	Subretinal haemorrhage, any size (observe 60 secs) Intravitreal haemorrhage, obscuring more than one-quarter of visible retina Epiretinal haemorrhage, obscuring more than one-quarter of visible retina Lens touch, lens dislocation or cataract Intraocular anterior segment haemorrhage Extra-ocular haemorrhage, ongoing Retinal tear or more than one retinotomy, with or without vector reflux Incarceration of iris in the corneal wound for A/C tap
Post-op	Normal behaviour as per licence	Failure to recover fully from anaesthesia Endophthalmitis (at any stage post-operatively) Incarceration of iris in the corneal wound for A/C tap Development of permanent cataract

6.4.2 Effect on ERG function

In summary, subretinal injection of AAV.OPN (1×10^8gc) and AAV.CRX (1×10^9gc) significantly reduces scotopic and photopic retinal pathway response within 3 weeks of treatment. Comparison with the sham injected eyes shows this effect is not due to the mechanical effect of retinal detachment or the presence of subretinal fluid. Full statistical analysis below.

6.4.2.1 Mesopic and scotopic function

Nrl-L-EGFP$^{+/-}$:Rho$^{-/-}$ have no intrinsic scotopic retinal function in the absence of rhodopsin protein. The natural history study in chapter 4 confirmed the absence of this retinal function. The mean scotopic 10^{-4} candela flash response in the sham-injected eye of the AAV.CRX group (26.5mV$\pm$10.2, n=9) and the AAV.OPN group (31.6mV$\pm$8.7; n=9) was no different to mean baseline noise (approximately 30mV) and not different between groups (5mV $\pm$ 25; p=0.85).

Figure 6.3 shows the mesopic ERG test results for the two groups of mice treated in the pilot trial (n=18 mice). All ERG b-wave values are written as the measured mean (mV) $\pm$ SEM. Linear mixed-effects (lme) modelling using REML was the statistical method used to accomodate the within-mouse inter-eye (L and R) correlation; p-values are derived from this model. Differences are written as mean $\pm$ standard error for the *fitted* values in the model.

The mesopic function of the sham-injected eyes did not differ between groups. The mean mesopic 10 candela flash response in sham-injected eye of the AAV.CRX group (147.3mV $\pm$ 27.7; n=9) and the AAV.OPN group (149.0mV $\pm$ 25.5; n=9) did not have a significant difference (1mV $\pm$ 24; p=0.95; lme model). These findings are consistent with both cohorts of mice being similar at baseline and being affected similarly by the subretinal PBS and mechanical effect of detachment.

For the 10 candela scotopic stimulus, the mean response in AAV.CRX treated eyes (80.9mV $\pm$ 22.1; n=9) as significantly less than the fellow sham eyes (-66mV $\pm$ 21; p=0.033; lme model). The AAV.OPN injected eyes (103.4mV $\pm$ 21.1; n=9)

also showed a significant reduction compared to the fellow sham eyes at this stimulus (-45mV $\pm$ 21; p=0.035; lme model). The reduction in scotopic ERG function from AAV treatment is either masked at low stimulus intensities or is only evident for mixed rod-cone stimulus such as 10 candela 0.5Hz flash.

6.4.2.2 Photopic function

Figure 6.3 shows the cone ERG IRC for the mice treated in the pilot trial (n=18). All ERG b-wave values are written as the measured mean (mV) $\pm$ SEM. P-values are given for a non-linear mixed-effects model was fitted to the ERG cone IRC data as described in subsection 2.8.2. Negative b-wave values were constrained to zero and interactions were included for the effect of treatment group and treatment status on asymptote, as well as treatment group on x-mid transition point. Model residuals were normally distributed (p=0.20; Shapiro-Wilk) and there was no heteroscedasticity. Differences are written as mean $\pm$ standard error for the *fitted* values of the model.

The cone function of sham-injected eyes did not differ between the two AAV treatment groups. The mean photopic 25 ($10^{1.4}$) candela flash b-wave in the sham-injected eye of the AAV.CRX group was 137.8mV $\pm$ 27.6 (n=9) and the AAV.OPN group was 125.2mV $\pm$ 24.7 (n=9). The IRC model showed the asymptote of the sham eyes in the AAV.OPN group was similar to the sham eyes in the AAV.CRX group (-19.4mV $\pm$ 24.4; p=0.427; nlme). This is expected as all mice were selected from the same colony, randomised to injection and tested at the same ages.

Treatment with either AAV vector reduced the asymptote of the ERG irradiance response curve. The mean photopic 25 ($10^{1.4}$) candela flash b-wave in the treated eyes of the AAV.CRX group was 45.7mV $\pm$ 11.0 (n=9). This asymptote was significantly less than the contralateral sham eyes (difference of -101.1 $\pm$ 12.3; p<0.001; nlme model). Hence, these ERG findings confirmed that the AAV.CRX (10^9gc) reduced photopic retinal function at 3 weeks.

The mean photopic 25 ($10^{1.4}$) candela flash b-wave in the treated eyes of the

AAV.OPN group was 60.2mV $\pm$ 17.6 (n=9). This asymptote was significantly less than the contralateral sham eyes (difference of -72.0mV $\pm$ 10.1; p<0.001; nlme model). Hence, these ERG findings confirmed that the AAV.OPN (10^8gc) reduced photopic retinal function at 3 weeks. The amount by which each vector reduced the photopic ERG function was similar (p=0.427).

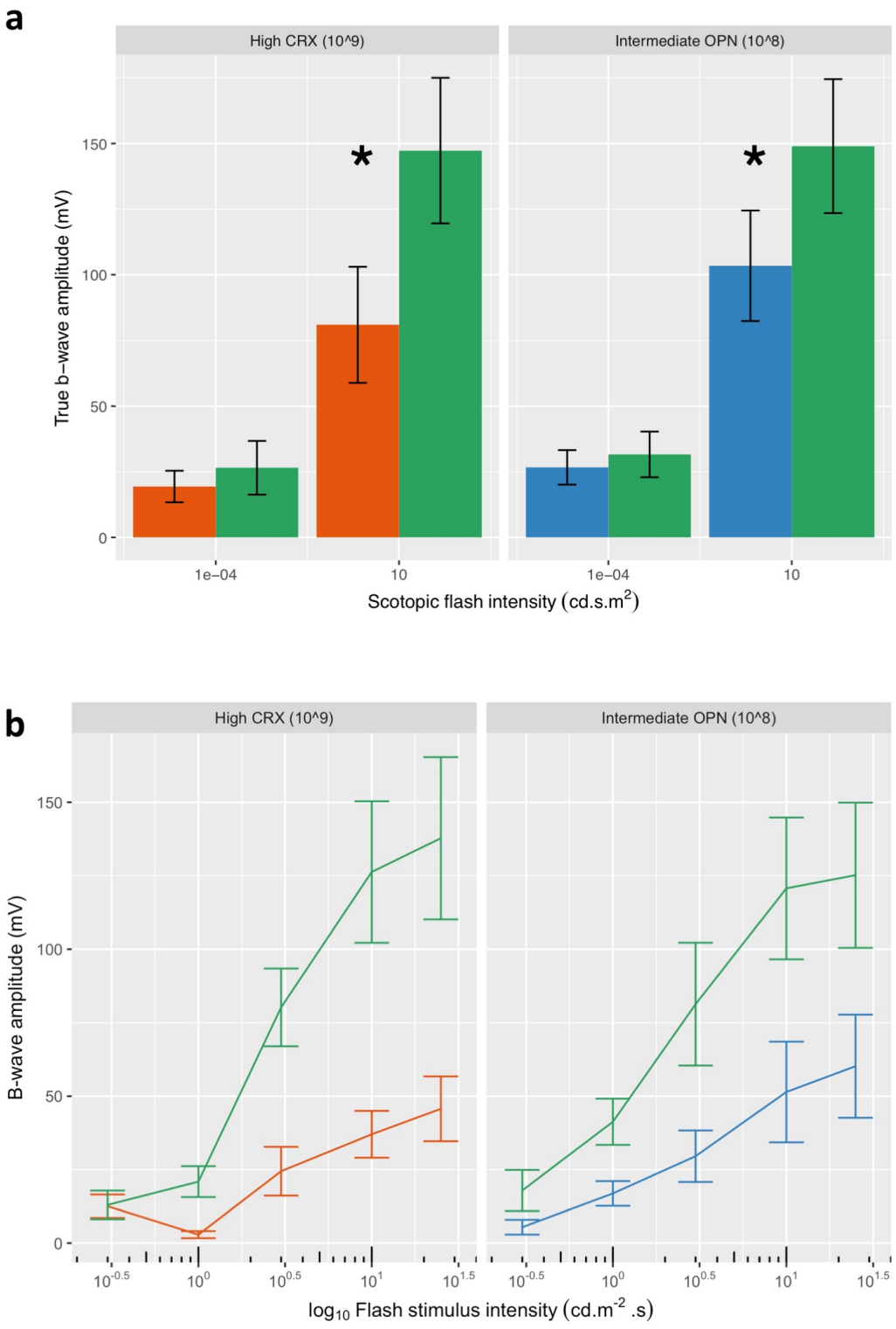


Figure 6.3 | Pilot study ERG results. **a,** ERG results for scotopic single-flash rod-isolating test steps showing true b-wave amplitude for AAV.CRX (10^9) (orange) and AAV.OPN (10^8) (blue) treated eyes compared to the contralateral PBS sham treated eyes (green). B-wave amplitude is significantly reduced in both groups of AAV treated eyes at 10 candela stimulus. **b,** ERG results for the photopic single-flash cone-isolating $\log_{10}$ irradiance response curve. Both groups of AAV treated eyes show significantly reduced sigmoidal asymptote and x-mid inflection compared to PBS sham eyes. All data presented as mean ± SEM. *p<0.05

6.4.3 Retinal architecture on OCT

Overall, dorsal subretinal injections of either AAV vector caused a large and significant reduction in the total and, especially, outer retinal thickness compared to sham injected eyes. This reduction was more severe in the dorsal retina, but is also significant in the ventral retina which is beyond the area of injection. In the dorsal retina it appears to follow a dose-dependent effect.

Figure 6.4 shows a representative OCT image and graphically displays all OCT data collected in the pilot study. All OCT thickness measurements are written as the measured mean (μM) $\pm$ SEM. Linear mixed-effects (lme) modelling using REML was the statistical method used to accomodate the within-mouse inter-eye (L and R) and intra-eye (dorsal and ventral) correlations; p-values are derived from this model analysis. Differences are written as estimate $\pm$ standard error for the *fitted* values in the model.

6.4.3.1 Effect of sham injections

The mean dorsal total retinal thickness in sham injected eyes (n=6) in the AAV.CRX group (155.7μM $\pm$ 3.7) and the AAV.OPN group (154.8μM $\pm$ 2.9) was not significantly different (p=0.924). Similarly, the mean dorsal outer retinal thickness in the sham injected eyes in the AAV.CRX group (47.5 μM $\pm$ 5.8) and the AAV.OPN group (48.2 μM $\pm$ 3.0) was not significantly different (p=0.939). Similarly, there was no significant difference between the dorsal and ventral retinal thickness in sham injected eyes of either AAV.CRX (p=0.92) or AAV.OPN (p=0.94). Compared to untreated mice assessed at a similar time-point in chapter 4, there is no evidence that PBS sham injections at PND21 affect the natural rate of retinal degeneration in the Nrl-L-EGFP$^{+/-}$:Rho$^{-/-}$ mice. The PBS sham injections show that the mechanical detachment of the retina and the presence of the PBS (used to suspend AAV before injection) do not alter retinal thickness 3 weeks after injection.

6.4.3.2 Effect of AAV.CRX treatment

In contrast, AAV.CRX (1×10^9gc) eyes (n=6) had a reduced dorsal outer retinal thickness of 15.7μM $\pm$ 4.3, which was significantly less (-31μM $\pm$6; p<0.001) than the contralateral sham eye. Notably, the loss of retinal thickness was not confined to the outer retina. AAV.CRX treated eyes had a reduced dorsal total retinal thickness of 94.3μM $\pm$ 11.9 that was significantly different from the contralateral sham eye (-61μM $\pm$6; p<0.001). The reduced retinal thickness was not confined to the site of the subretinal injection in the dorsal retina. The ventral total retinal thickness in AAV.CRX treated eyes (138.7μM $\pm$ 8.8) and contralateral sham eyes (159.0μM $\pm$4.3) was also significantly different (19.2μM $\pm$6.1; p=0.002). Compared to the damage dorsally, this loss was significantly less severe ventrally (-44.3 μM $\pm$ 6.1; p<0.000). This may be because the ventral retinal loss in AAV.CRX treated eyes was caused entirely by the loss of outer retina (20.3μM $\pm$ 6.6; p<0.001), showing there was no significant loss of the inner retinal layers ventrally. All of these findings are consistent with a dose-dependent toxicity due to AAV.CRX (1×10^9gc) treatment.

6.4.3.3 Effect of AAV.OPN treatment

Similarly, AAV.OPN (1×10^8gc) treated eyes (n=6) had a reduced dorsal total retinal thickness of 127.2μM $\pm$ 6.9, which was significantly less (27.7μM $\pm$ 6.1; p<0.001) than the contralateral sham eye. This damage was not fully explained by the significant difference in dorsal outer retinal thickness (19.5μM $\pm$ 6.1; p=0.002), showing that the inner retinal layers were also damaged by the AAV.OPN treatment. The damage to the dorsal retina total thickness was less severe than in the AAV.CRX treated eyes (-32.8μM $\pm$ 8.5; p=0.003). This is consistent with either the 10-fold difference in AAV dose or a dose-independent difference in how the *CRX* transgene thins the retina.

Further evidence for a dose-dependent effect is shown in the ventral retinal thickness of the AAV.OPN treated eyes. Similar to the AAV.CRX treated eyes, the ventral total retinal thickness (143.8μM $\pm$ 8.5) is significantly reduced

compared to the sham eye (-22.0 μM $\pm$ 7.2; p=0.012). Unlike AAV.CRX treated eyes, this retinal thinning compared to sham eyes is not fully explained by the loss in the outer retina (8.167μM $\pm$ 7.126; p=0.278). The severity of retinal thinning ventrally is equivalent to the loss observed in the AAV.CRX treated retinas (p=0.55). The dose-dependent or transgene-dependent effect observed in the dorsal retina does not hold true in the ventral retina, despite evidence of thinning here.

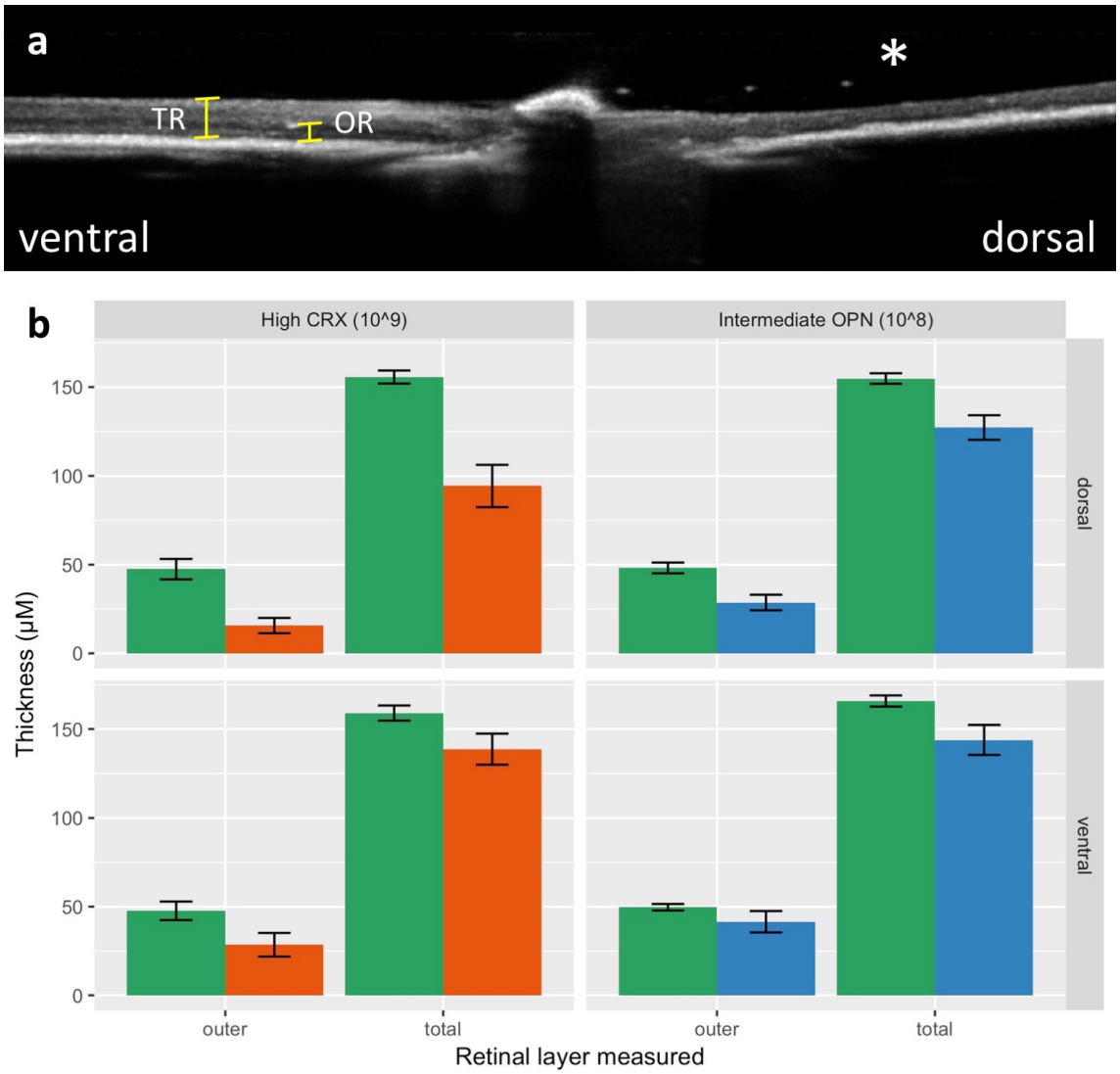


Figure 6.4 | Pilot study OCT. a, Representative OCT image showing a radial cross-section from ventral (left) to dorsal (right) retina through the optic nerve of an injected eye. The retina is thinner dorsally at the location of the AAV injection ('*'). Calliper measurements of the total retina (TR) and outer retina (OR) were collected as indicated. **b,** Manual measurements of both total and isolated outer retinal thickness on OCT, displayed by dorsal or ventral location. The retinal thickness is significantly less than sham injected eyes in AAV treatment groups, both dorsally (hierarchical linear model; $p<0.001$) and even ventrally ($p<0.01$) . All data shown as mean ± SEM.

6.4.4 Macroscopic appearance of the retina *in vivo* on cSLO

6.4.4.1 GFP signal on BAF

Overall, dorsal subretinal injections of either AAV vector caused a large reduction in GFP signal in Nrl.GFP^{+} mice. This reduction is more severe in the dorsal retina,

but also occurs in the ventral retina.

Figure 6.5 shows representative cSLO images and the data collected from the images; only a subset of mice in each group were GFP^+ (n=4 each group). All cSLO greyscale measurements are written as the measured mean (arb. units) $\pm$ SEM. Linear mixed-effects (lme) statistical modelling using REML accommodated the within-mouse inter-eye (L and R) and intra-eye (dorsal and ventral) correlations; all p-values are derived from this model analysis. The linear model satisfied the tests outlined in subsection 2.8.2 and the residuals were normally distributed(Shapiro-Wilk; W=0.96; p=0.459). Differences are written as estimate $\pm$ standard error for the *fitted* values in the model.

In detail, the mean greyscale values in the dorsal area of PBS sham injected eyes in the AAV.CRX group (86.0 $\pm$ 20.8; n=4) and the AAV.OPN group (78.5 $\pm$ 21.7; n=4) were no different (-7.5 $\pm$ 33; p=0.83). Similarly, the mean greyscale value in the ventral area of the PBS injected eyes was not different between the two groups (-1.5 $\pm$ 33; p=0.97). There is no significant difference between the dorsal and ventral GFP signal in PBS sham injected eyes in the AAV.CRX group (10 $\pm$ 8; p=0.27) or the AAV.OPN group (16 $\pm$ 8.5; p=0.087). These results are consistent with PBS sham injections and the mechanical detachment having no substantial effect on the Nrl.GFP signal 3 weeks following injections. An appropriate baseline from which to measure the isolated effects of the individual AAV treatments.

In contrast, the mean greyscale value in the dorsal retina of AAV.CRX (1×10^9gc) treated eyes (38.5 $\pm$ 19.6; n=4) was significantly different to the contralateral sham eye (-47.5 $\pm$ 10; p=0.003). The ventral retina of AAV.CRX (1×10^9gc) was also significantly less than sham (-34.25 $\pm$ 10; p=0.14). The reduction in dorsal GFP signal was also significantly more severe than the ventral retina (-23.25 $\pm$ 8.5; p=0.019), consistent with the dose-dependent effect demonstrated in the dorsal-ventral gradient of retinal thinning on OCT.

The AAV.OPN (1×10^8gc) treated retina had a dorsal greyscale value (47.2 $\pm$ 21.3; n=4) significantly lower than the contralateral sham treated eyes (-31.25 $\pm$

9; p=0.020). The ventral retina (66.5 $\pm$ 27.3; n=4) also showed a similar pattern of significant reduction compared to sham (-28 $\pm$ 10; p=0.031). Once again, the dorsal retina was more severely affected (p=0.087), consistent with a dose-dependent gradient.

6.4.4.2 Pigmentary pattern on ICGA

Figure 6.5 shows the characteristic pigmentary changes observed in the fundus of AAV treated mice, but not present in the sham injected eyes. All of the AAV.CRX (10^9gc) injected eyes that underwent ICGA cSLO imaging (n=4/4) showed pigmentary changes. This is significantly correlated with the AAV.CRX treatment (Chi-square; p=0.034).

Similarly, all of the AAV.OPN (10^8gc) injected eyes that underwent ICGA cSLO imaging (n=5/5) showed pigmentary changes concentrated in the dorsal retina. This is significantly correlated with AAV.OPN treatment (Chi-square; p=0.011). Qualitatively, the total amount of pigmentary change appeared correlated to the severity of GFP signal reduction.

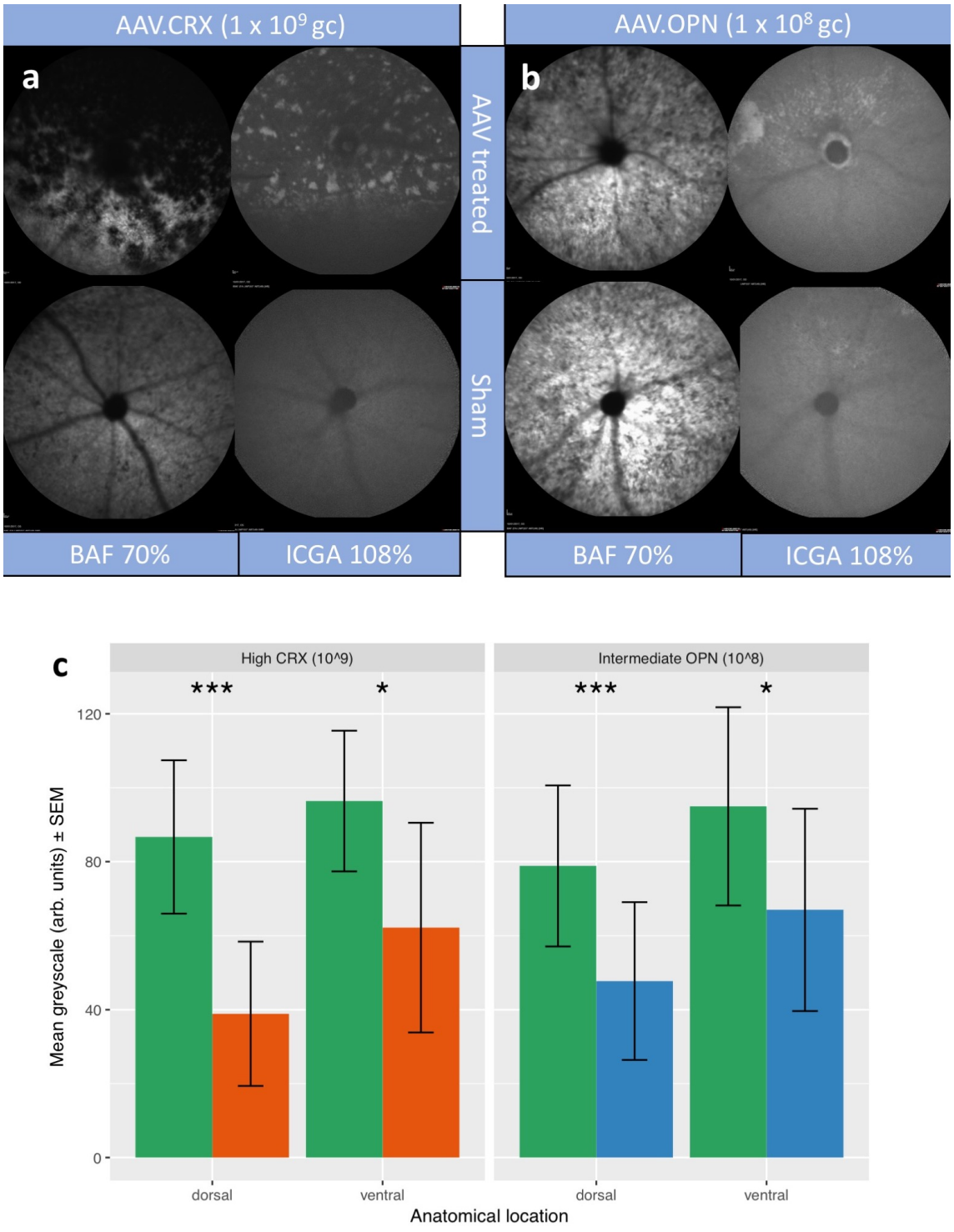


Figure 6.5 | Pilot study cSLO. a, *En face* retinal images showing AAV.CRX (1×10^9gc) treated eye (top row) and sham injected eye (bottom row) in the same mouse. Images show rod-specific GFP fluorescent signal (first column) and ICGA images (second column). GFP signal is reduced superiorly in the injected eyes and this correlates to the signal changes in the ICGA images. **b,** The same pattern was observed in AAV.OPN (1×10^8gc) treated mice. **c,** Quantification of the mean greyscale signal using a published ImageJ workflow in sham (green), AAV.CRX (orange) and AAV.OPN (blue) treated eyes. Compared to sham eyes, injected eyes show a significant reduction in GFP signal (hierarchical linear model; $p<0.001$; n=8 mice) and also a reduction in the inferior retinal signal ($p<0.05$). Data shown as mean $\pm$ SEM. *$p<0.05$. ***$p<0.001$

6.4.5 Transgene expression on IHC

Overall, AAV.CRX and AAV.OPN both express exogenous transgene in the area of the dorsal subretinal injection.

Figure 6.6 shows the CRX transgene protein staining pattern in a representative AAV.CRX (10^9gc) injected eye compared to the sham treated contralateral eye. Qualitatively, the sham eyes showed no appreciable change in Nrl.GFP expression, and outer retinal appearance, between the dorsal injection site and the ventral uninjected retina. There was widespread nuclear-staining of endogenous Crx protein in the outer nuclear layer of sham injected eyes that did not appear different in the dorsal retina. The AAV treated eyes showed high intensity CRX nuclear staining in the dorsal retina and an obvious difference between the injected dorsal retina and the uninjected ventral retina. The regions of high CRX staining were associated with loss of the rod photoreceptors, as shown by the reduced or absent GFP signal.

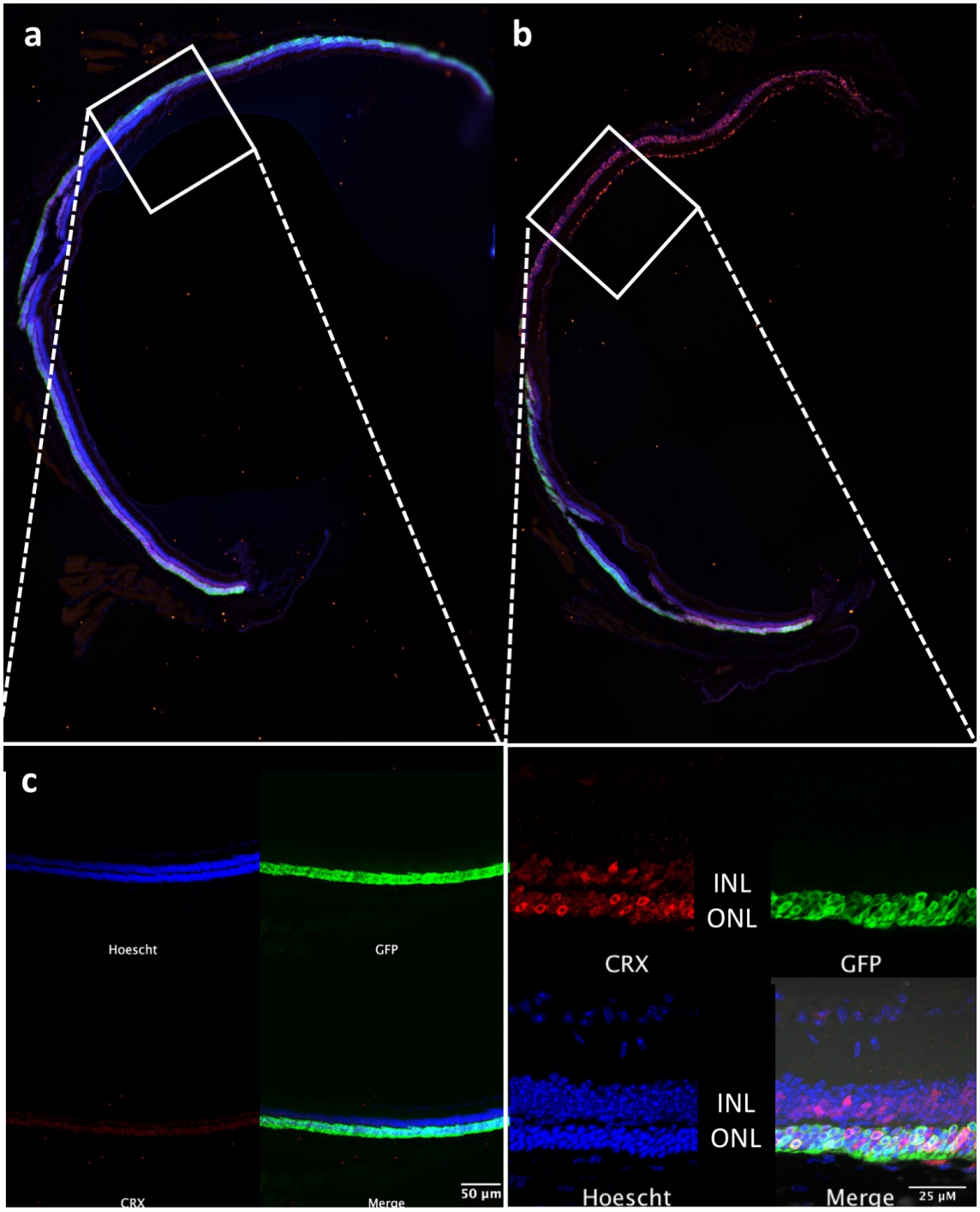


Figure 6.6 | CRX IHC on injected mice. **a,** Low-power view of a PBS sham injected retina of an Nrl-L-EGFP$^{+/-}$:Rho$^{-/-}$ mouse (which has green rod photoreceptors) showing diffuse background Crx signal in photoreceptors and the inner nuclear layer. **b,** AAV.CRX injected contralateral eye of the same mouse showing high intensity CRX transgene staining in the superior retina at the site of the AAV injection that does not extend to the inferior retina. **c,** Higher-powered field (20x) from the same mouse showing the faint background staining of CRX. **d,** High-powered field (63x) from the injected eye showing the more intense CRX staining in the injected region.

Figure 6.7 shows the OPN1LW transgene protein staining pattern in a representative AAV.OPN (10^8gc) injected eye compared to the sham treated contralateral eye. The sham injected eye shows no suggestion of altered GFP expression or outer retinal loss dorsally. There is a scattered endogenous Opn1mw signal in outer segments. The AAV injected eye shows dorsal loss of GFP and outer retina. Immediately below this damaged region is an area of OPN1LW expression in the outer retina or RPE. This high intensity region of expression does not continue into the ventral retina, where only scattered endogenous Opn1mw signal is observed.

No quantitative analysis was performed on mean signal strength or area of signal. The inability of the optimised IHC antibodies to differentiate between the endogenous mouse protein and exogenous human transgene was explored and described in chapter 5; this confounding factor must be accounted for when interpreting the IHC.

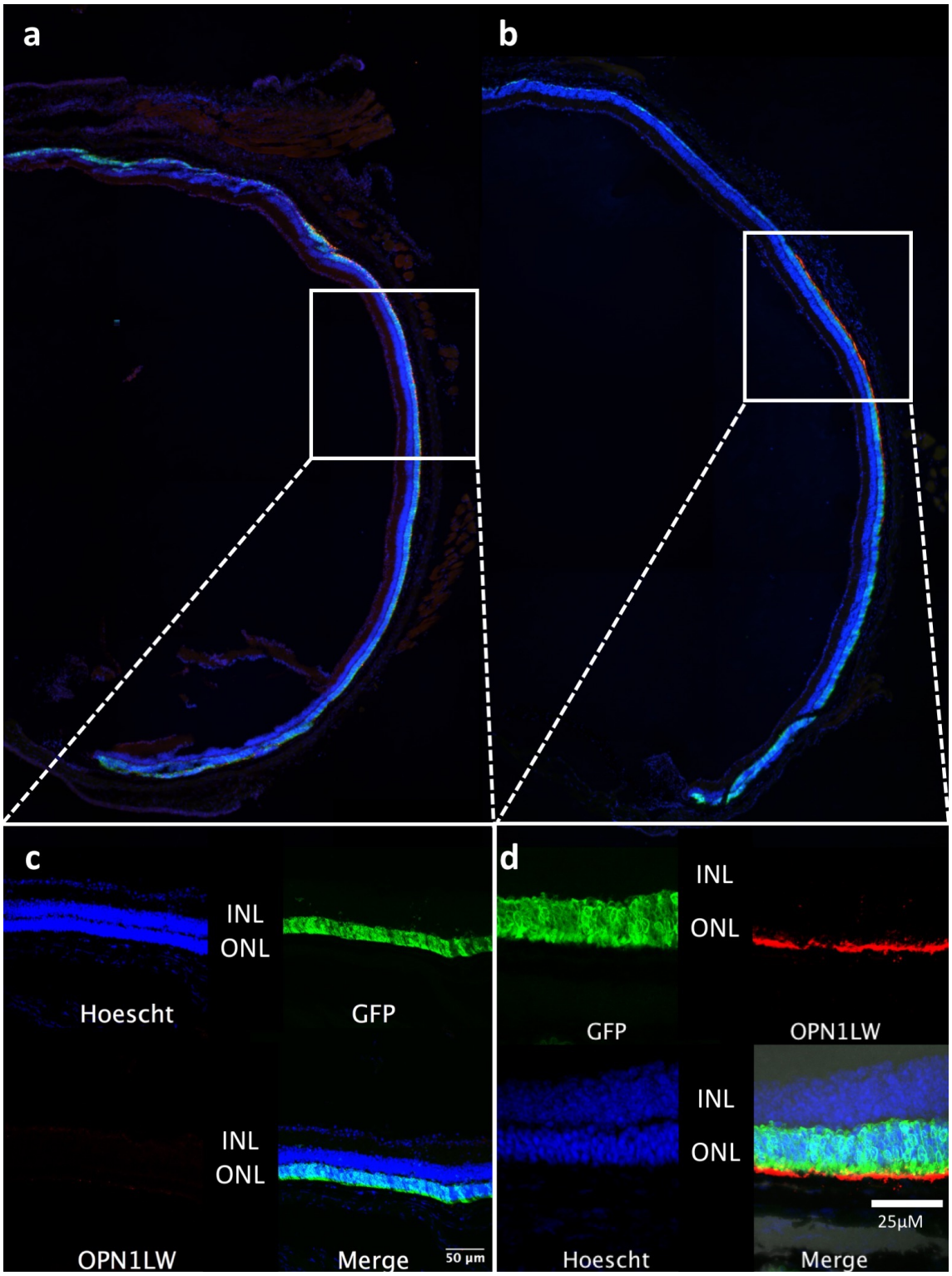


Figure 6.7 | OPN1LW IHC on injected mice. a, Low-power view of a PBS sham injected retina in a Nrl-L-EGFP$^{+/-}$:Rho$^{-/-}$ mouse showing scattered background outer segment Opn1sw expression. **b,** The AAV.OPN1LW injected contralateral eye of the same mouse showing severe loss of the outer retina and endogenous GFP signal superiorly and immediately below, a discrete area of OPN1LW expression in transduced outer retina/RPE. **c,** Higher-power field emphasises the minimal opsin staining in the outer segments. **d,** High-power view emphasises the continuous high intensity OPN1LW expression in the outer retina/RPE.

6.5 Discussion

This chapter was a pilot study designed to answer questions that would guide the planning and execution of the full treatment experiment in chapter 7. Eighteen Nrl-L-EGFP:Rho$^{-/-}$ mice were treated with PBS sham injections in one eye and randomised AAV treatment injections in the fellow eye.

This chapter demonstrated that a reproducible subretinal surgical delivery of the AAV vector could be achieved by a single surgeon. The chapter estimated the location and precision of sham and AAV treated eye values for the ERG, OCT and cSLO functional outcomes. Optimised IHC techniques were successfully applied to injected eyes and there was convincing evidence that both AAV vectors produce transgenic protein. The evidence of AAV-mediated retinal damage at higher doses emphasises the need for a range of doses in the full experiment.

6.5.1 Surgery

The surgical technique for subretinal delivery of AAV vector was practiced and optimised during this experiment; surgeries were faster and less difficult at the end. Timing of vector dilution, average per-mouse times and equipment redundancy were optimised.

The surgical inclusion-exclusion criteria (Table 6.1) were developed through experience, discussion with colleagues and observation of other surgeries during this time. A continuous score (i.e. out of 10 or a percentage) for the quality of surgery could have then been included in a multivariable regression of outcomes, as well as acting as exclusion criteria. The Apgar score for assessing newborn babies first proposed in the 1950s was an early example of . Continuous scores such as this have been developed to successfully predict post-operative morbidity in human surgery [238]. However, such scores require a large cohort of patients (or mice) to successfully validate the value of the scores in predicting outcomes. There are no currently published scores for grading the quality of subretinal surgical delivery in mice. In humans, there are

only case series about subretinal injection and subsequent visual outcomes [97], but no scoring systems.

As such, a continuous score was avoided because of challenges with inter-observer variability. In particular, it would be challenging to visually estimate the proportion of vector delivery (i.e. 60% or 90%) in cases of reflux into the vitreous or supra-choroidal space. Differences in the tilt of the mouse eye visual axis, as well as the posterior/anterior location of the subretinal bleb, change the apparent proportion of the delivered volume (see Figure 6.2). Instead, a binary yes-no criteria were developed to allow easy removal of mice that did not receive a full vector dose by identifying simple signs of vector reflux.

Similarly, a binary exclusion criteria was developed to identify mice that suffered complications that would confound *in vivo* functional tests or tissue testing. Small areas of vitreal or epiretinal blood were permitted as these complications were the most frequent despite practice and, based on the experience of others, did not grossly affect outcomes. This surgical score will be applied to all injected mice in the next chapter.

6.5.2 Transgene expression

As explored and discussed in chapter 5, antibodies that could differentiate between transgenic human and endogenous mouse proteins for CRX and OPN1LW were not identified. This non-specific target signal places caveats on interpreting the IHC results. Considering the anatomical location and gradient of the signal in relation to the dorsal injections is a useful adjunct in the absence of specificity. High signal immediately adjacent damaged dorsal retina was considered a sign of transgene expression. Transgene expression at the site of injection was presumed to have been erased by the death of the transduced cells. As described below, the mechanism of this cell death is unknown.

The AAV2/8.CAG.CRX.WPRE vector expressed CRX protein in the injected eyes at a dose of 1×10^9gc. This expression was localised to the nuclei of the cells as expected for a nuclear transcription factor. In the nuclei, CRX binds to the

promoter sequences of CRX, cone opsins and other genes to increase expression [7]. It is possible that this increased CRX signal in the dorsal retina of the AAV treated eye is a mix of exogenous transgene and up-regulated endogenous Crx responding to the positive-feedback loop of more CRX. Without an antibody to distinguish between species, this possibility is unknown.

CRX expression was also observed in the inner retina of the AAV injected eyes; signal was seen in the inner nuclear layer. Without a co-staining primary antibody for bipolar, horizontal or ganglion cells, the cellular specificity of this expression is unknown. This inner retina CRX expression was observed in mice with and without retinotomy, suggesting that the AAV vector was able to reach cells beyond the outer limiting membrane without a traumatic conduit. This inner and outer retina transduction pattern has been described previously without traumatic surgery [136]. There was no evidence of RPE cell transduction, which differs from the AAV.OPN vector expression pattern in RPE cells.

The AAV2/8.CAG.OPN1LW.WPRE vector expressed OPN1LW protein in the injected eyes at a dose of 1×10^9gc. This expression was localised to the outer segments of the photoreceptors and RPE immediately adjacent the area of damaged outer retina. The presumed area of transgenic OPN1LW expression was a densely concentrated contiguous signal around the damaged retina. Whereas the un-transduced ventral retina showed background scattered endogenous cone opsin signal. In the absence of the Opn1.GFP reporter allele, cone-specific expression could not be established.

Based on location, the OPN1LW signal also appeared localised to RPE cells, but a primary RPE-65 antibody was not used to confirm cellular co-localisation. Transduction of RPE cells by subretinal injection of AAV has been shown elsewhere [136]. OPN1LW signal may occur in the RPE cells due to primary expression of the transgenic protein or by phagocytosis of the transgene from transduced photoreceptor outer segments [239]. The absence of the transgene from RPE underneath the damaged dorsal photoreceptors makes the latter hypothesis less likely assuming these photoreceptors were damaged by

transgene over-expression and not capsid-induced immune destruction. Since immunostaining of opsins recognises the protein in the folded, membrane bound state, it is likely that RPE does translate the OPN1LW protein, but that it is not trafficked appropriately and therefore not detected with this method.

6.5.3 Evidence of AAV mediated damage

Multiple observations show retinal damage mediated by the AAV vectors: the significantly reduced rod and cone pathway ERG function, the total and outer retinal thinning on OCT, the reduced or absent dorsal GFP signal, the dorsal pigmentary changes on the IRAF cSLO images, and the loss of dorsal photoreceptors observed on IHC.

The pattern of ventral retinal thinning and reduced ventral GFP signal showed that the AAV-mediated retinal damage was not confined to the dorsal subretinal injection site. Dorsal subretinal injections have been previously shown to transduce ventral retinal cells at equivalent doses [136]. The IHC did not clearly demonstrate ventral transgene expression. Yet, the lack of species differentiation by the antibodies may be masking exogenous gene expression in the ventral retina.

The ventral damage was less severe than the dorsal retinal damage for both AAV vectors, which is consistent with a dose-dependent effect because the injection was into the dorsal retina. That is, the ventral retinal cells were exposed to a lower MOI of AAV and thus incurred less damage. Further suggesting a dose-dependent effect, the severity of retinal thinning and GFP signal loss was less severe in the AAV.OPN treated eyes. AAV.OPN was delivered at a 10-fold lower dose than AAV.CRX, thus this may represent be a dose-dependent difference. Alternatively, the difference may be a product of differing pathways by which over-expression of each human transgene causes damage. Demonstrating a dose-response relationship in the large randomised experiment will answer this question.

There are multiple possible mechanisms contributing to the retinal damage

observed in these AAV treated eyes. The exact cause is not clear; more information from a full randomised trial about the dose response and expression pattern is required.

The use of a ubiquitous CAG promoter to express cone photoreceptor genes introduces the risk of deleterious non-photoreceptor expression. Ubiquitous promoters can express transgenes in any retinal tissue type [136] and, as described in subsubsection 6.3.6.3, this off-target expression in RPE cells and the inner nuclear layer is identified in our treated mice. Theoretically, *CRX* expression elsewhere could induce transcription of photoreceptor genes by promoter binding, which could in turn alter non-photoreceptor cellular function or survival.

It is possible that an immune response contributed to the damage. However, there was no objective evidence of auto-fluorescent macrophages on cSLO BAF images in areas of lost GFP signal. Such a macrophage signal was observed in late-stage $Rho^{-/-}$ mice and is a known feature in retinal degeneration [203]. A primary antibody to identify macrophages was not included in the IHC protocol.

The exogenous human transgene and protein may stimulate an immune response response from the host mouse. Yet, subsection 5.4.7 details how the interspecies homology of *CRX*-*Crx*and *OPN1LW*-*Opn1mw* are each more than 90%. It is unclear whether the acquired immune defences of mice could identify human protein given that the six commercially available primary antibodies tested in chapter 5 were unable to do so. The innate immune defences do respond to AAV vectors through poorly understood mechanisms [218]. Reassuringly, other authors have previously shown that human transgenes - with even less interspecies homology - can be used to rescue mouse phenotypes without immune complications [153, 237, 165].

If an immune response did cause the observed retinal damage, then it is more likely to be mediated by the capsid proteins of AAV. AAV is, in a large part, used as a vector due to its low immunogenicity compared to Adenovirus or Lentivirus vectors [215, 206]. The capsid purity of the AAV.CRX and AAV.OPN

vectors injected in these mice are shown in subsubsection 5.4.6.2. As described in chapter 5, a fresh repeat vector preparation with new plasmids and in new cultures did not improve the capsid purity measured on SDS-PAGE. The faint additional bands observed may represent incorrectly synthesised capsid proteins or other unknown contaminants that could stimulate an immune response following injection. However, detailed discussion with colleagues both before and after the pilot trial reached a consensus that the capsid purity was equivalent to other AAV preparations using the same protocol that had subsequently been used successfully in mouse trials.

It is unlikely that surgical damage or retinal bleeding caused this consistent pattern of loss. Firstly, the surgical inclusion and exclusion criteria described in Table 6.1 showed no major complications in any mice in the pilot study. Secondly, the effect on the treated retinas is so consistent, substantial and widespread that it is unlikely to be related to irregular surgical mistakes.

6.5.4 Exploring the IRAF changes in the full trial

The pigmentary changes on IRAF cSLO images will be monitored in the randomised dose-response experiment in the next chapter. The mechanism underlying the changes is not known, but the changes appear to consistently occur in regions of retinal damage. A detailed exploration of the underlying mechanism or cellular/proteinaceous make-up of the changes is not warranted. The pigmentary changes on IRAF cSLO are simply another indicator of retinal damage alongside BAF cSLO, OCT and ERG changes.

6.5.5 Future dose selection

The OCT and BAF cSLO data suggests dose dependent retinal damage. To explore this possibility further and to examine whether a lower AAV dose can avoid or minimise toxicity, a number of lower doses will be trialled in the full study. Transgene expression is known to occur successfully at a 1×10^7gc dose [136, 216]; this dose will be the lowest used in the subsequent full study. The final

doses for both AAV will be 10^7, 10^8 and, for AAV.CRX, 10^9.

Trialling different doses in the subsequent study will dilute any potentially pro-inflammatory capsid proteins or contaminants contributing to retinal damage. It will also demonstrate dose-dependent transgene expression on IHC, which will help confirm successful retinal transduction in the absence of antibodies that can differentiate the interspecies homology.

6.5.6 Effect of a different mouse model

For logistical reasons and time constraints, the Nrl-L-EGFP$^{+/-}$:Rho$^{-/-}$ mouse model was used in place of the Rho$^{-/-\ B6TgOPN1LW\text{-}EGFP+/-}$ mouse model originally characterised for gene selection. This introduces a confounding factor. Genetic drift in the B6$^{TgOPN1LW\text{-}EGFP}$ and Nrl-L-EGFP colonies before cross-breeding with the Rho$^{-/-}$ lines may interact with the AAV vectors to produce different outcomes; particularly, the evidence of retinal damage from the AVV vectors. So too, the differential expression of GFP reporter protein in rods or cones may interact with the AV vector in unexpected ways.

6.5.7 Rationale for proceeding to full trial

The question of whether the AAV2/8.CAG.CRX.WPRE or AAV2/8.CAG.OPN1LW.WPRE vectors are beneficial to cone photoreceptors in Rho$^{-/-}$ mice over the full duration of retinal degeneration remains unanswered. What if lower doses of these two vectors avoid retinal damage and provide benefit?

Furthermore, it is possible that the initial retinal damage caused to the treated dorsal retina overshadows beneficial transduction of adjacent surviving retina. Longer term follow-up of treated mice may unmask functional or structural benefits at later time-points as this watershed effect becomes apparent.

The specific effect of the AAV treatments on the cone photoreceptors has also not been explored. Trialling lower doses of the AAV vectors on Rho$^{-/-\ B6TgOPN1LW\text{-}EGFP+/-}$ mice will allow longitudinal tracking of cone survival *in*

vivo.

6.6 Conclusion

This chapter shows that the AAV2/8.CAG.CRX.WPRE and AAV2/8.CAG.OPN1LW.WPRE vectors successfully transduce mouse retinas following subretinal injection and express transgenic protein. There is evidence of a dose-dependent damage to the retina from these AAV that needs to be explored further at lower doses and over a longer time-frame in the full randomised trial. This effect also needs to be explored in the original $Rho^{-/-\ B6TgOPN1LW\text{-}EGFP+/-}$ mouse model.

7

FULL STUDY OF AAV EFFICACY

7.1 Introduction

The core hypothesis of this thesis is that, in RP, the loss of photosensitivity in cone photoreceptors occurs much earlier than cone cell death and is driven by down-regulation of select cone phototransduction genes. Furthermore, this loss of cone photosensitivity can be reversed by supplementing the cone photoreceptor transcriptome by exogenous over-expression of select cone genes; specifically *CRX* and *OPN1LW*.

Candidate cone genes were identified by analysing the transcriptome and phenotype of an RP mouse in chapter 4. In chapter 5, the *CRX* and *OPN1LW* human transgenes were packaged into separate AAV8 viral vectors and validated *in vitro*. In chapter 6, these two AAV8 viral vectors were injected into a small pilot cohort of RP mice and shown to express the transgenes. This chapter will conclude this line of work by testing the efficacy of each AAV8 virus vector in prolonging or rescuing cone photosensitivity in the $Rho^{-/-\ B6TgOPN1LW\text{-}EGFP+/-}$ mouse model over time.

Randomised control experiments are the gold-standard for testing the efficacy of an intervention. The CONSORT consensus guidelines detail the expected standards in clinical RCTs [240] and the ARRIVE guidelines provide

similar guidance for *in vivo* testing of a new treatment in mice [241]. Randomisation of the mice to treatment groups balances the groups, robustly eliminates confounding bias, and is the basis for uncorrected statistical testing of the difference in treatments [232]. Controls should allow comparison between AAV treatment and natural history of the disease (uninjected) to identify any treatment effect. Similarly, controls should allow comparison between AAV treatment and subretinal injections of only PBS (sham) to exclude any effect from the mechanical process of injections and the PBS used for suspending AAV.

7.2 Aim & objectives

The chapter aims to test if either the *CRX* or *OPN1LW* virus vectors can prolong or rescue cone photosensitivity in a mouse model of RP. This aim will be explored through the following objectives:

1. Successfully deliver subretinal AAV2/8.CAG.CRX.WPRE (henceforth AAV.CRX) and AAV2/8.CAG.OPN1LW.WPRE (henceforth AAV.OPN) vector to the full number of $Rho^{-/-\ B6TgOPN1LW\text{-}EGFP+/-}$ mice pre-determined in the power calculation, allowing for attrition due to a 20% surgical failure rate

2. Exclude structural retinal toxicity at lower doses using OCT and cSLO imaging

3. Measure cone survival *in vivo* using cSLO BAF imaging

4. Determine if either vector at any dose improves photosensitivity by assessing injected mice with ERG at 3 weeks after injection

5. Determine if either vector at any dose prolongs photosensitivity by assessing injected mice with ERG at 9 weeks after injection, at around the time most $Rho^{-/-\ B6TgOPN1LW\text{-}EGFP+/-}$ mice lose cone ERG function

6. Further explore any evidence of prolonged cone photosensitivity by assessing injected mice with OMR at 9-12 weeks after injection

7. Confirm successful transgene mRNA expression at lower doses of 10^7 and 10^8 gc/1.5μL by measurement with qPCR

8. Confirm successful exogenous protein expression and cellular localisation at lower doses of 10^7 and 10^8 gc/1.5μL with IHC

9. Perform semi-quantitative assessment of cone photoreceptor survival on IHC

7.3 Materials & methods

7.3.1 Animals

The Rho$^{-/-\ B6TgOPN1LW\text{-}EGFP+/-}$ mouse model, origin and housing conditions are described in section 2.1.

Both Rho$^{-/-\ B6TgOPN1LW\text{-}EGFP+/-}$ and Rho$^{-/-\ B6TgOPN1LW\text{-}EGFP-/-}$ mice were included equally in this experiment to control for the effect B6$^{TgOPN1LW\text{-}EGFP}$ allele on retinal electrophysiology and cone survival. Each treatment group included two equal subgroups of GFP positive and negative mice. Both subgroups were initially analysed separately, but none of the outcome measures showed a difference between GFP positive and negative mice. As such, the final analysis presented in this chapter combines Rho$^{-/-\ B6TgOPN1LW\text{-}EGFP+/-}$ and Rho$^{-/-\ B6TgOPN1LW\text{-}EGFP-/-}$ mice into single groups based on treatment group only.

7.3.2 Subretinal injections

Subretinal injections of sterile PBS sham or AAV vector were performed as detailed in subsection 2.2.2. Surgical success was assessed using the inclusion-exclusion criteria detailed in Table 6.1 and failed surgeries excluded from the study as appropriate.

AAV was defrosted on the day on injection and diluted in a tissue culture hood using sterile PBS. AAV.CRX was diluted to to 1×10^9gc/1.5μL, 1×10^8gc/1.5μL and 1×10^7gc/1.5μL. AAV.OPN to 1×10^8gc/1.5μL and 1×10^7gc/1.5μL. A separate aliquot of sterile PBS was prepared in the culture hood for sham injections. All preparations were transported and stored on ice prior to injection.

7.3.2.1 Rationale for dose range

As described earlier in chapter 6, the high doses of AAV.CRX (1×10^9gc) and AAV.OPN (1×10^8gc) cause some dorsal retinal damage. This needs to be characterised in greater detail over a longer time period to explore the possibility

of a late-stage treatment effect in transduced surviving ventral retina.

Furthermore, lower doses of both AAV need to be trialled to explore safety and the possibility of functional benefit at lower doses. Previous successful transgene expression has been achieved at 10^7gc using AAV vectors [216, 136]. As such, the final doses for both AAV will be 10^7, 10^8 and, for AAV.CRX, 10^9. Further details of the treatment groups are provided in Figure 7.1.

7.3.2.2 Randomisation and blinding

For optimal randomisation, each mouse receiving a unique number and then a random number generation process (i.e. software, random number tables) allocate s each mouse number to a treatment group [242]. In this way, confounding effects are randomly distributed between groups [232]. Furthermore, treatment should be randomly allocated between left and right eyes to avoid systematic bias (such as the left-eye bias suggested in cSLO GFP counts in subsection 4.5.2). However, mice in this experiment received a sequentially allocated injection to the right eye only; standards of randomisation were constrained in this trial because of pragmatic considerations.

Firstly, concentrated AAV vector is a precious resource. Defrosting a full aliquot of both AAV.CRX and AAV.OPN for each injection cohort each time might exhaust stocks prematurely; defrosted AAV can not be used on subsequent injection days due to unstable storage once defrosted. As such, not every cohort of mice (i.e. groups of 1-3 litters weaned together) received a full mix of the six treatment groups. Rather, AAV.CRX and AAV.OPN were clustered in cohorts, although PBS sham mice were distributed evenly across all cohorts.

Secondly, mice were allocated to either an AAV injection or PBS sham injection according to the order they were withdrawn from the cage. This method of sequential allocation is not purely random. However, sequential allocation reduces the logistical burden on a single surgeon performing all steps; it thus helps to avoid record-keeping errors.

Furthermore, eye randomisation introduces risks around accurate

record-keeping and the possibility of confusing treated and untreated eyes between similarly-appearing mice. Alternatively, systematic error in functional testing can be minimised by using the same lens on both eyes and alternating which eye is tested first in sequential mice in the same testing session to minimise systematic influence of mild evolving cataract in the second eye imaged.

In human testing, the treatment should also be double-blinded to avoid inherent bias in the experimenter or placebo effect in the patient [243]. In mice, the placebo effect does not hold true, but inherent bias of the examiner remains a constraint [244]. However, blinding in mouse experiments introduces additional record-keeping burdens. A fellow researcher needs to be present to prepare and dilute the AAV treatments, possibly be present to help draw-up the injection during surgery and also maintain sealed treatment records to be unmasked at the end of the experiment. These were not insignificant logistical considerations in a trial that identified 114 mice to take to surgery over a period of 3-4 months. As such, no formal blinding process was undertaken. However, individual mice were difficult to recall as mouse cages were not labelled with the treatment details and each cage contained mice from multiple different treatment groups.

7.3.3 Adjusting for the B6$^{TgOPN1LW\text{-}EGFP}$ allele

Figure 4.3 describes the significant reduction in ERG function that occurs by PNW25 in mice that are heterozygous for the Opn1.GFP allele. The contribution of this functional difference could confound any treatment effect from AAV injections. As such, B6$^{TgOPN1LW\text{-}EGFP+/-}$ heterozygotes and B6$^{TgOPN1LW\text{-}EGFP-/-}$ wt litter mates were all included in the study to allow any confounding of ERG results to be identified, yet also allow *in vivo* cSLO measurement of the GFP signal.

7.3.4 Power calculations and sample sizes

A full trial should also be sufficiently powered to detect a treatment effect if it exists, or confidently exclude one if not present. Pre-experimental power calculations are reviewed in detail elsewhere [245, 148]

For this study, ERG was chosen as the most important functional outcome measure. It is a sensitive measure of organised photopic retinal pathway function. The Rho$^{-/-}$ mouse model characterisation in chapter 4 showed that ERG can detect more incremental changes in cone pathway function over time than OMR.

The ERG natural history study in chapter 4 measured a b-wave amplitude of μ_1 of 137.9mV $\pm$ 24.1 for a 25cd.s^{-1}.m^2 stimulus in untreated Rho$^{-/-}$ eyes at PND42; the time point of the 3 weeks post-op ERG for this trial. The same natural history experiments measured a μ of 165.2 $\pm$ 61.0 in wt control mice for the same age and conditions. In the context of these results, detecting a modest 20% improvement in ERG function 3 weeks post-injection would require n=82 — given α=0.05 and 1-β = 0.80.

The later time-point ERG at PNW12, 9 weeks after surgery, has a smaller remaining b-wave with a smaller standard deviation. At the 25cd.s^{-1}.m^2 stimulus, a treatment group of n=12 would detect a 50% improvement in b-wave function with 80% confidence (i.e. AAV-mediated prolongation of photopic cone function). Where possible, 2-3 additional mice were injected in treatment groups to control for attrition.

7.3.5 Study design

Figure 7.1 shows that the final study design contained six treatment groups (PBS, three doses of AAV.CRX and two doses of AAV.OPN1LW) spread across seven cohorts (i.e. 1-3 litters injected at a time). The left eye in each mouse was left uninjected and the right eye was randomised to one of the six treatment groups. This approach avoided the need to perform sham injections in every contralateral

eye because normalisation to the uninjected eye allowed single sham cohort to be compared to each other group individually.

There were also two phases to the study. The first phase involved subretinal injections for functional testing (n=83). The second phase involved subretinal injections exclusively for qPCR tissue endpoints (n=20).

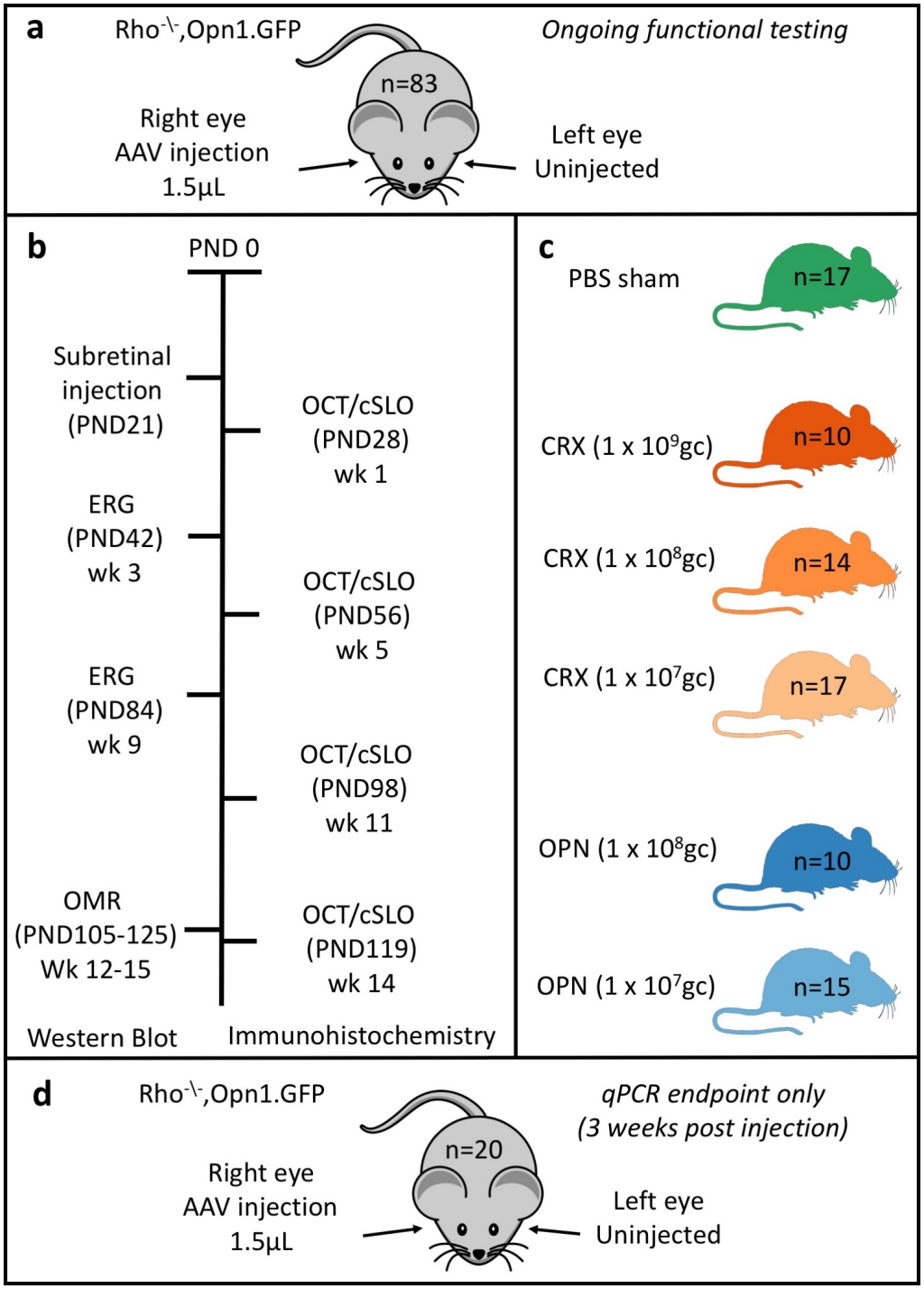


Figure 7.1 | Design of the study. **a,** 83 Rho$^{-/-}$ mice received a randomised AAV dose or PBS sham subretinal injection in the right eye. **b,** These 83 mice were tested *in vivo* over 4 months, using ERG, cSLO, OCT and OMR. Mice were sacrificed at the end for WB and IHC tissue endpoints. **c,** There were six treatment groups of mice; PBS sham, three doses of AAV.CRX and two doses of AAV.OPN. **d,** An additional 20 mice received subretinal injections, did not undergo functional testing, and were harvested for qPCR 3 weeks following subretinal injection.

7.3.6 *In vivo* functional testing

7.3.6.1 OCT and cSLO

Retinal imaging with OCT and cSLO imaging modalities was performed on anaesthetised mice as detailed in subsection 2.2.4 and subsection 2.2.3. Custom afocal contact lenses were used with viscous coupling media (Hypomellose) to prevent corneal desiccation and cataract formation; the same lens was changed between eyes for image collection to standardise the optics.

7.3.6.2 ERG

Retinal pathway electrophysiology was performed on anaesthetised mice as detailed in subsection 2.2.6. Mice were dark-adaption the night before before scotopic and mesopic testing. Mice underwent light-adaption in the middle of the testing protocol as described in Table 2.1.

7.3.6.3 OMR

Tectal visual reflexes of conscious mice were tested in photopic conditions as described in subsection 2.2.5. Manual counts of head tracking behaviour were assessed by a single observer from overhead video feeds.

7.3.7 Molecular techniques

7.3.7.1 Retinal samples and cDNA

Whole neurosensory retinas were taken from treated mice after euthanasia as detailed in subsubsection 2.3.7.1 in RNase-free conditions. RNA was isolated from samples using a commercial kit (Qiagen) as described in subsubsection 2.3.7.2 and 1500ng of total RNA per retina then reverse transcribed to cDNA subsubsection 2.3.7.3.

7.3.7.2 qPCR

qPCR testing of reverse transcribed retinal transcriptome was performed using primer pairs optimised earlier in subsection 5.4.7 to differentiate between

exogenous human transgene and endogenous mouse gene.

7.3.7.3 IHC

Samples for IHC were collected from treated mice as described in subsection 2.7.1 and stored at -80°C. Samples were then cryo-sectioned, mounted on slides and stained for CRX and OPN1LW expression using antibodies previously optimised in subsection 5.4.7.

7.3.8 Statistical analysis

7.3.8.1 Hierarchical non-linear modelling of the ERG IRC

Figure 2.6 is a representative sigmoid curve showing the relationship between stimulus light intensity and electrophysiological response in the retina. Equation 7.1 explains the sigmoidal response relationship between the log of stimulus light intensity (cd/m^{2}s^{-1}) and the magnitude (μV) of the recorded response. The equation was expanded to include as many treatment groups as required.

$$Response = \frac{Asym + a_1 z_1 + at_1 z_1 y + a_2 z_2 + ...}{1 + exp(\frac{xmid}{\phi})} \quad (7.1)$$

$Where:$

$Asym$	asymptote of sigmoidal curve
a_1	untreated eyes in group 1
z^1	treatment group 1
at_1	treated eyes in group 1
y	effect of injection across groups
a_1	untreated eyes in group 2
z^1	treatment group 2
...	*further treatment groups*
$xmid$	x-value of sigmoid midpoint
ϕ	steepness of the curve

7.4 Results

7.4.1 Surgical success and details of excluded mice

A total of 116 Rho$^{-/-}$ mice were identified at birth as candidates for the randomised study. Two mice were excluded after weaning due to anophthalmos or congenital corneal opacity. The remaining mice were genotyped for GFP status using ear tag biopsies as described in subsection 2.3.2 and 51% of mice were GFP$^{+/-}$ as anticipated. GFP positive and negative mice were allocated equally between the treatment groups.

114 mice were anaesthetised for surgery on the day of weaning at a mean age of PND22 $\pm$ 1. Figure 7.2 shows successful subretinal injections in representative mice. A total of 103 Rho$^{-/-}$ mice received successful subretinal injections of AAV or PBS sham in the right eye. The fellow eye was an uninjected control. The different injections were randomised to the right eye within cohorts (typically 1-2 litters) and the treatment groups were spread across the seven cohorts to spread the confounding factors.

82 of these mice were designated for functional testing over time, as described in Figure 7.1. A further 20 mice were collected 3 weeks later for qPCR analysis without undergoing functional testing.

14 mice were excluded from the trial due to one of the surgical complications defined in Figure 6.2. Specifically, these mice were excluded due to appreciable reflux of AAV into the vitreous (n=6), subretinal haemorrhage (n=4), large vitreous or epiretinal haemorrhages (n=2), slow recovery from anaesthesia (n=1), and persistent post-operative extra-ocular bleed (n=1).

Ultimately, 82 mice proceeded to functional testing with ERG, OCT, cSLO and OMR. 5 mice were culled prematurely during the post-operative functional testing period. Data already collected from these mice was included in the final analysis.

- One mouse was culled from the low CRX (10^7gc) group at PND89 due to slow recovery from anaesthesia following the 'wk9 ERG' test.

- One mouse was culled from the high CRX (10^9gc) group at PND88 after developing a corneal opacity that persisted for two days following the 'wk5 OCT' test.
- One mouse was excluded from the PBS sham group at PND46 due to slow recovery from anaesthesia following the 'wk3 ERG' test.

79 mice continued with functional testing until the late time-points and were ultimately all collected for WB or IHC after OMR testing.



Figure 7.2 | Surgical outcomes. Magnified images of subretinal AAV injections through dilated pupils in anaesthetised mice showing the varied bleb appearances for successful delivery of 1.5μL of AAV vector. Images were captured 60 seconds after vector delivery to allow late complications to develop and be identified. The last row of images show large subretinal haemorrhages - these were excluded. *Arrowheads: epiretinal haemorrhages smaller than exclusion criteria.*

7.4.2 Retinal architecture measured with OCT

OCT was performed (mean days post-op $\pm$ range) on treated mice at 1 week post-surgery (7 days $\pm$ 3), 5 weeks post-surgery (35 days $\pm$ 1) and 11 weeks post-surgery (87 days $\pm$ 5). A smaller cohort of mice underwent OCT at 17 weeks post-injection (142 days $\pm$ 1; n=12).

Overall, dorsal subretinal injections at the highest dose of either AAV vector caused a large and significant reduction in the total and, especially, outer retinal thickness compared to sham injected eyes. This is consistent with the findings of the pilot study. However, the magnitude of AAV.CRX mediated retinal thinning appeared generally dose-dependent and even the lowest AAV.CRX (1×10^7gc) dose caused some retinal loss. The lowest dose AAV.OPN (1×10^7gc) showed no toxicity, consistent with a dose dependent effect.

Figure 7.3 shows a representative OCT image and graphically displays all OCT data collected in the pilot study. All OCT thickness measurements are written as the measured mean (μM) $\pm$ SEM. Linear mixed-effects (lme) modelling using REML was the statistical method used to accomodate the within-mouse inter-eye (L and R) and intra-eye (dorsal and ventral) correlations, as well as the correlation of repeated measures over time. P-values below are derived from this model analysis. Differences are written as estimate $\pm$ standard error for the *fitted* values in the model. Model residuals were normally distributed (Shapiro-Wilk; p=0.159).

Regarding the baseline degeneration in untreated eyes. The uninjected eyes decline significantly over time as expected due to the inherent Rho$^{-/-}$ degeneration (-0.5μM/day $\pm$ 0.06; p<0.001). This decline of the uninjected eyes in the sham group is not significantly different to any of the five treatment groups (CRX9;p=0.630, CRX8;p=0.824, CRX7;p=0.860, OPN8;p=0.510, OPN7;p=0.710). This shows that the baseline characteristics of all mice and the inherent degeneration are equivalent across litters.

Regarding the effect of PBS sham injections. The mean dorsal total retinal

thickness in the sham group at week 1 in the uninjected eyes (162.5 $\pm$ 2.8; n=10) and the injected eyes (155.4 $\pm$ 2.4; n=10) suggests a difference (-8.7 $\pm$ 6.8; p=0.205). However, the sham injected eyes do not diverge from the uninjected contralateral eye with age either dorsally (0.056 $\pm$ 0.08; p=0.47) or ventrally (-0.03 $\pm$ 0.08; p=0.64). Overall, the mechanical effects of subretinal PBS fluid and detachment of the dorsal retina do not significantly affect retinal thickness.

Regarding the effect of dorsal AAV.CRX (1 $\times$ 10^9gc) subretinal injections. The total retinal thickness in the treated eye declined significantly from baseline over time (-0.8 $\pm$ 0.06; p<0.001) and declined significantly faster over time than the contralateral untreated eye (0.26 $\pm$ 0.07; p<0.001). The dorsal retina in these injected eyes was thinner than the ventral retinal overall (14.11 $\pm$ 7.4; p=0.058). Yet, the ventral retina of the AAV.CRX (1 $\times$ 10^9gc) treated eye still showed faster rate of retinal loss than the uninjected eye (0.22 $\pm$ 0.07; p=0.002). This shows that this treatment did not slow the degeneration, but actually accelerated it significantly. This acceleration was more severe dorsally at the site of injection, but also affected the ventral retina.

Regarding the effect of dorsal AAV.CRX (1 $\times$ 10^8gc) subretinal injections. The 1 $\times$ 10^8gc dose thinned the dorsal outer retina significantly (-14.4 $\pm$ 6.4; p=0.026), but the treatment did not accelerate the rate of loss (-0.08 $\pm$ 0.06; p=0.217). The total dorsal retina was not significantly different compared to the uninjected fellow eyes (-8.7 $\pm$ 6.2; p=0.17), nor did treatment accelerate the loss of the total retina (-0.06 $\pm$ 0.06; p=0.37).

Regarding the effect of dorsal AAV.CRX (1 $\times$ 10^7gc) subretinal injections. This dose initially thinned the dorsal total retina (-18.4 $\pm$ 6.04; p=0.003), but subsequently degenerated at a significantly slower rate than the uninjected eye (-0.18 $\pm$ 0.09; p=0.05). The treated eyes ended the study with equivalent surviving total dorsal retina (122.3μM $\pm$ 5.2) as the untreated eyes (121.3μ $\pm$ 7.0). The ventral retinal thickness was not affected by the injection (1.7 $\pm$ 6.04; p=0.8), nor the rate of degeneration affected (-0.07 $\pm$ 0.09; p=0.43). The magnitude of retinal thinning due to the AAV.CRX vector was not exactly dose

dependent. The thinning observed in the lowest dose AAV.CRX (1×10^7gc) group was at times and, in different locations, more severe than the 1×10^8gc and even the 1×10^9gc dose. However, the overall pattern appeared to favour a dose-dependent effect.

Regarding the effect of the dorsal AAV.OPN (1×10^8gc) subretinal injections. This treatment did not alter the total retinal thickness significantly overall (8.6 ± 9.8; p=0.38), but it did accelerate the rate of loss dorsally (-0.3 ± 0.1; p=0.005). The ventral retinal thickness measurements were not affected by this dose overall (p=0.756) or the rate of loss over time (p=0.181).

Regarding the effect of the dorsal AAV.OPN (1×10^7gc) subretinal injections. This treatment did not alter the total dorsal retina thickness overall (3.5 ± 7.7; p=0.65) or alter the rate of dorsal degeneration over time (-0.08 ± 0.09; p=0.40). Similarly, the ventral retina was not affected overall (p=0.60) or over time (p=0.70) at this dose.

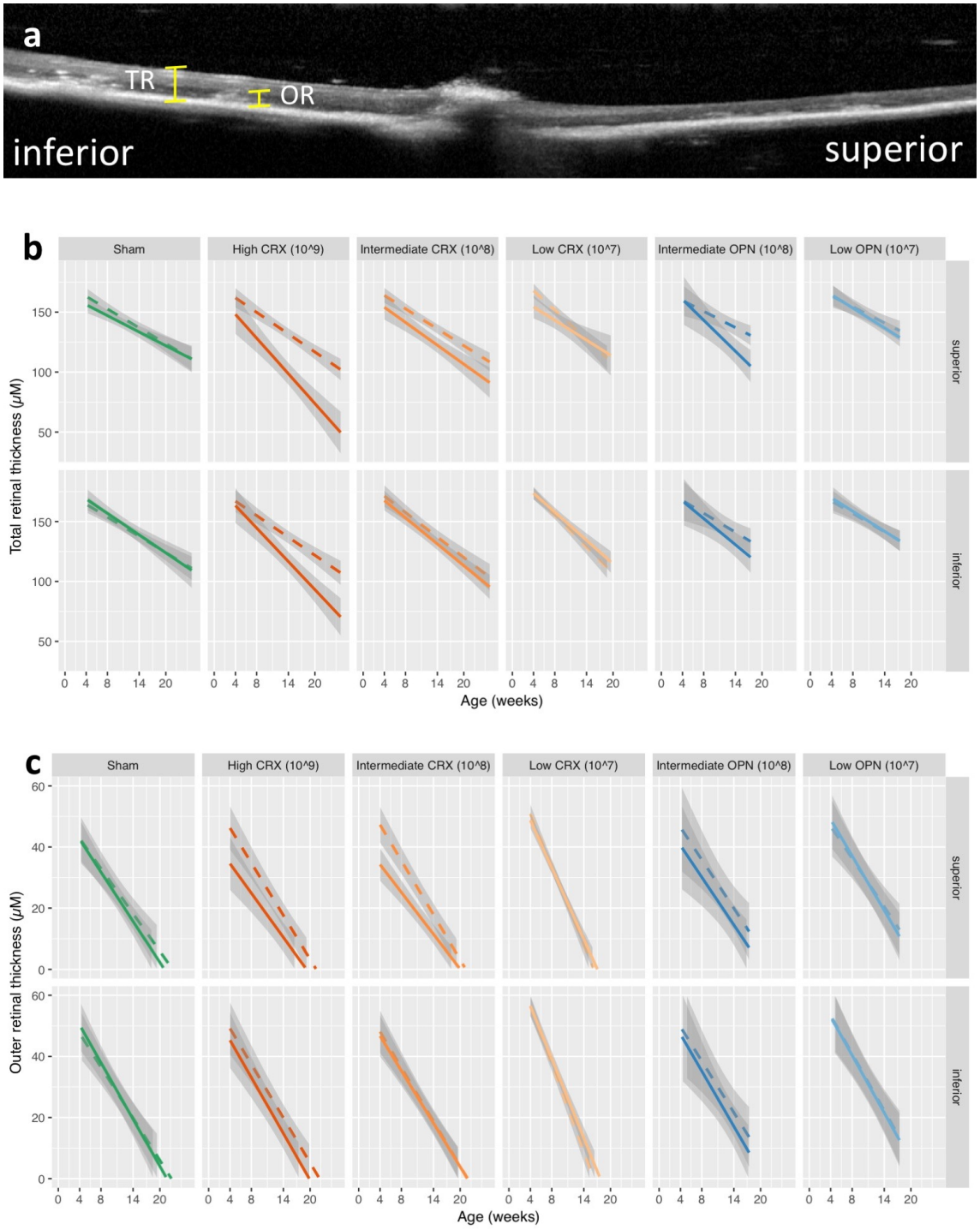


Figure 7.3 | Effect of AAV on retinal structure. a, Representative OCT image of an AAV injected eye at PND28 showing a cross-section through the optic nerve from ventral to dorsal retina. Callipers show the measurement technique for total retinal thickness (TR) and outer retinal thickness (OR). **b,** Mean total retinal thickness (TR) over time in the injected (solid line) and uninjected eyes (broken line), faceted by treatment group and anatomical location. **c,** Mean outer retinal thickness (OR) over time in the AAV treated and untreated eyes, faceted by treatment group and anatomical location. All data shown as mean ± 95% CI (grey shading).

7.4.3 Cone photoreceptor survival measured *in vivo* with cSLO BAF

cSLO imaging, using the IR, BAF and IRAF imaging modalities, was performed on treated mice during the same imaging session as the OCT image collection detailed above. Figure 7.5 and Figure 7.4 show representative images from the different treatment groups using the BAF modality at 100% sensitivity. The uninjected eyes showed a similar pattern of degeneration over time as the $Rho^{-/-}$ model natural history study in subsection 4.5.2.

Figure 7.6 shows the results of particle counts performed on semi-crescent regions of interest in cSLO BAF images at 1 and 5 weeks post injection. This method is described in subsection 4.4.2. The PBS sham injected eyes did not differ significantly from the contralateral uninjected eyes at 1 or 5 weeks (p=0.06). There was no significant difference between the dorsal and ventral retina at 1 and 5 weeks.

The injected eyes in each treatment group showed a variable response to AAV injections. None of the treatment groups showed a significant difference between the injected and uninjected dorsal retina.

Regarding the effect of AAV.CRX (1×10^9gc) treatment on GFP signal. At 1 week, treated eyes were similar to sham injected eyes. Uninjected control eyes showed decreased GFP signal that increased at week 5; this was likely artefact arising from technical issues with these images.

Regarding the effect of AAV.OPN (1×10^8gc) treatment on GFP signal. Overall, injected eyes appeared to have globally reduced GFP signal over time compared to uninjected eyes.

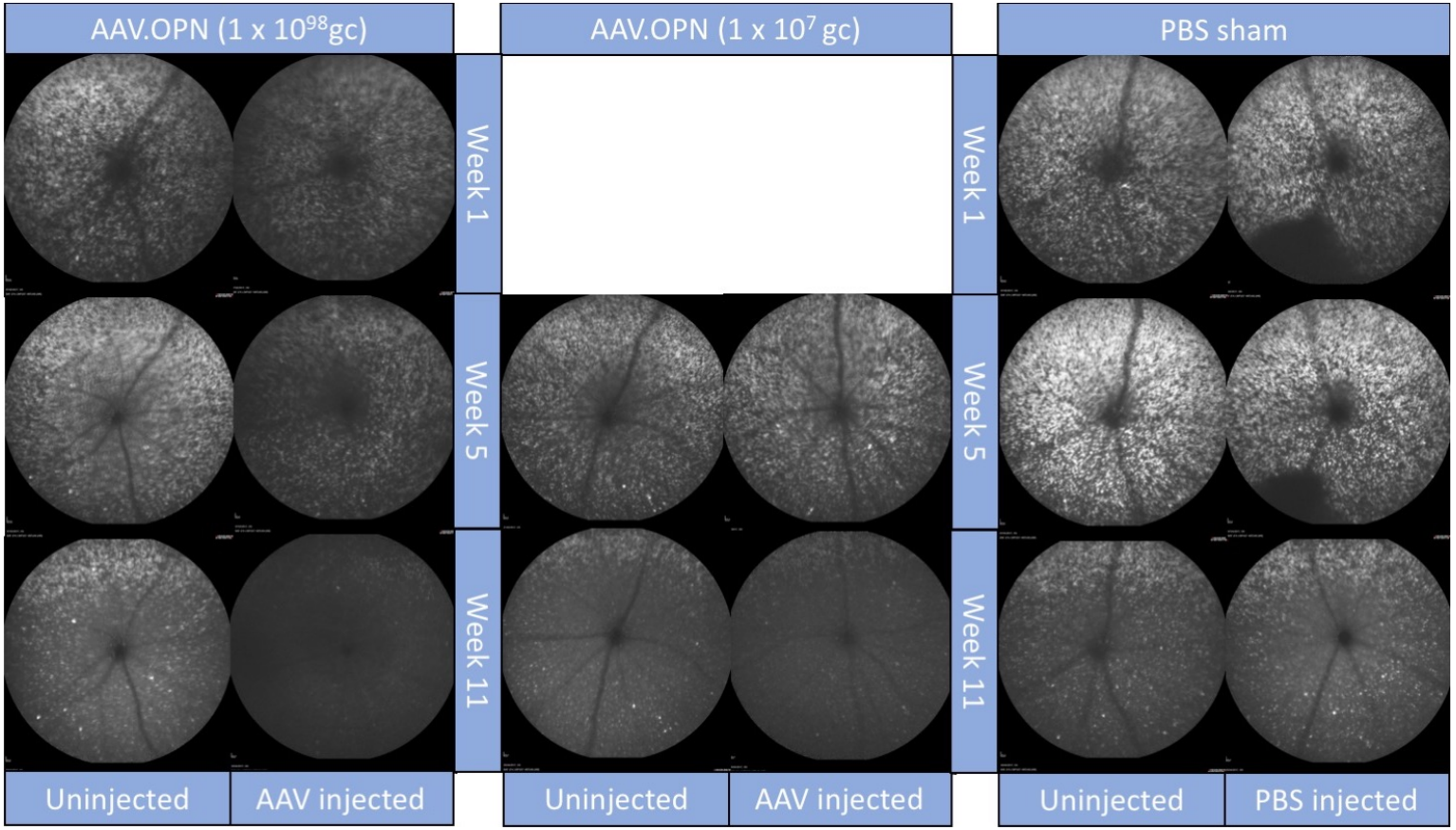


Figure 7.4 | Representative cSLO for AAV.OPN mice. cSLO images from selected mice treated with AAV.OPN1LWS or PBS sham injections demonstrating the appearance of the *in vivo* cone GFP signal over time. Some of the eyes treated with a dose of 1×10^8gc lost GFP signal on cSLO faster than the contralateral uninjected eye. However, there were many mice - more commonly at the 1×10^7gc dose - that showed no difference between the injected and uninjected eyes over time. Similarly, the PBS sham appeared to have no effect on GFP signal over time. A small ventral vitreous haemorrhage is visible in the PBS sham eye, showing resolution over time.

7.4.4 Pigmentary changes in treated retinas measured *in vivo* with cSLO IRAF

The pilot trial identified pigmentary changes in the AAV injected eyes that were absent in the PBS sham injected eyes. Colleagues had previously observed these changes appeared to correlate with retinal toxicity, although no findings have been published elsewhere. During cSLO BAF modality image acquisition, IRAF modality images were also captured for most mice. Pigmentary changes were never observed in uninjected eyes or PBS injected eyes, nor did they ever manifest in AAV injected eyes until at least 1 week after surgery.

However, pigmentary changes did occur in at least some of the AAV treated eyes in every treatment group except the lowest AAV.CRX (1×10^7gc) dose group. Figure 7.7 shows exemplar images and graphically represents the binary proportion of occurrence across treatment groups. The occurrence of a pigmentary changes on IRAF imaging follows a dose-related pattern.

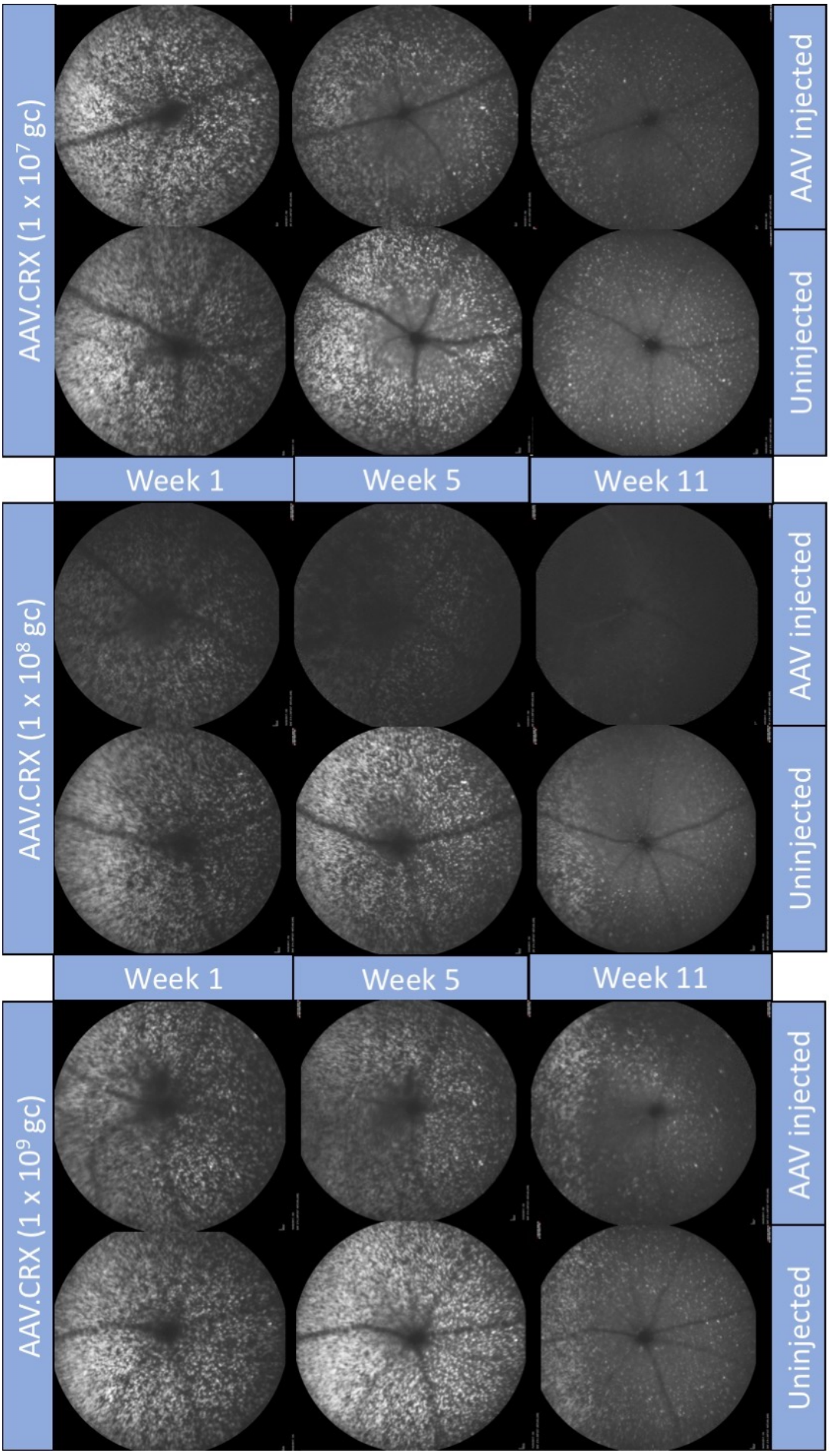


Figure 7.5 | Representative cSLO for AAV.CRX mice. Selected cSLO images showing GFP signal over time imaged at 100% sensitivity using the BAF modality. Eyes treated with AAV.CRX at a 1×10^9gc dose were, at times, equivalent to the uninjected eye over time. As observed in the pilot study, some AAV.CRX treated eyes did lose GFP signal at a faster rate than the uninjected eye. This was evident even at the lower dose of 1×10^8gc. However, the lowest 1×10^7gc dose rarely changed GFP signal over time.

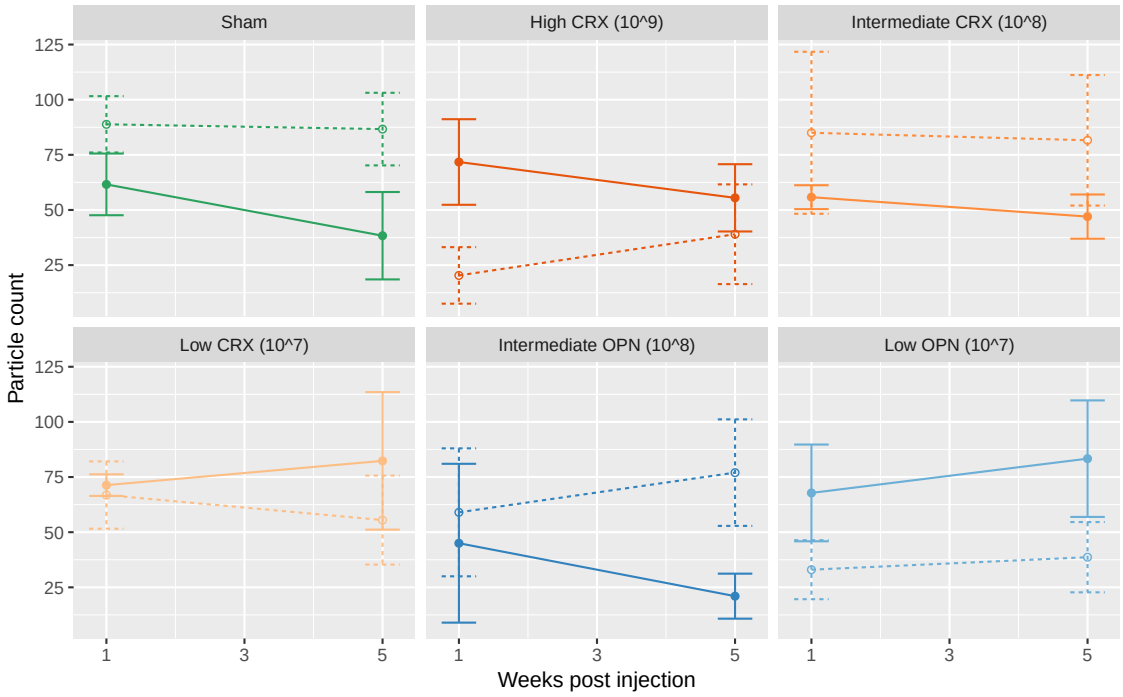


Figure 7.6 | Particle counts of cSLO BAF images. Counts of individual GFP signal points in the dorsal retinas of injected (solid line) and uninjected (broken line) Rho$^{-/-}$ B6TgOPN1LW-EGFP$^{+/-}$ retinas 1 and 5 weeks after treatment. 11 week data not shown as migrating autofluorescent macrophages artefact causes false high counts. Values are mean $\pm$ SEM.

7.4.5 Retinal function measured with ERG

ERG testing was performed (mean days post-op $\pm$ range) on treated mice at 3 weeks after surgery (22 $\pm$ 3; n=81) and 9 weeks after surgery (68 $\pm$ 6; n=49). Response amplitudes were manually measured at the leading edge of the b-wave and are written as the measured mean (μM) $\pm$ SEM. Implicit time measurements are written as the measured mean (ms) $\pm$ SEM.

7.4.6 Effect on mesopic and scotopic ERG function

Rho$^{-/-}$ have no intrinsic scotopic retinal function in the absence of Rhodopsin protein. The natural history study in chapter 4 confirmed the absence of this retinal pathway in our local colony of Rho$^{-/-}$ B6TgOPN1LW-EGFP$^{+/-}$ mice. Nonetheless, AAV treated mice were still dark-adapted overnight and tested in scotopic conditions during the ERG protocol at 3 weeks and 9 weeks. Treated mice were also tested in mesopic conditions using brighter flash stimulus against in a

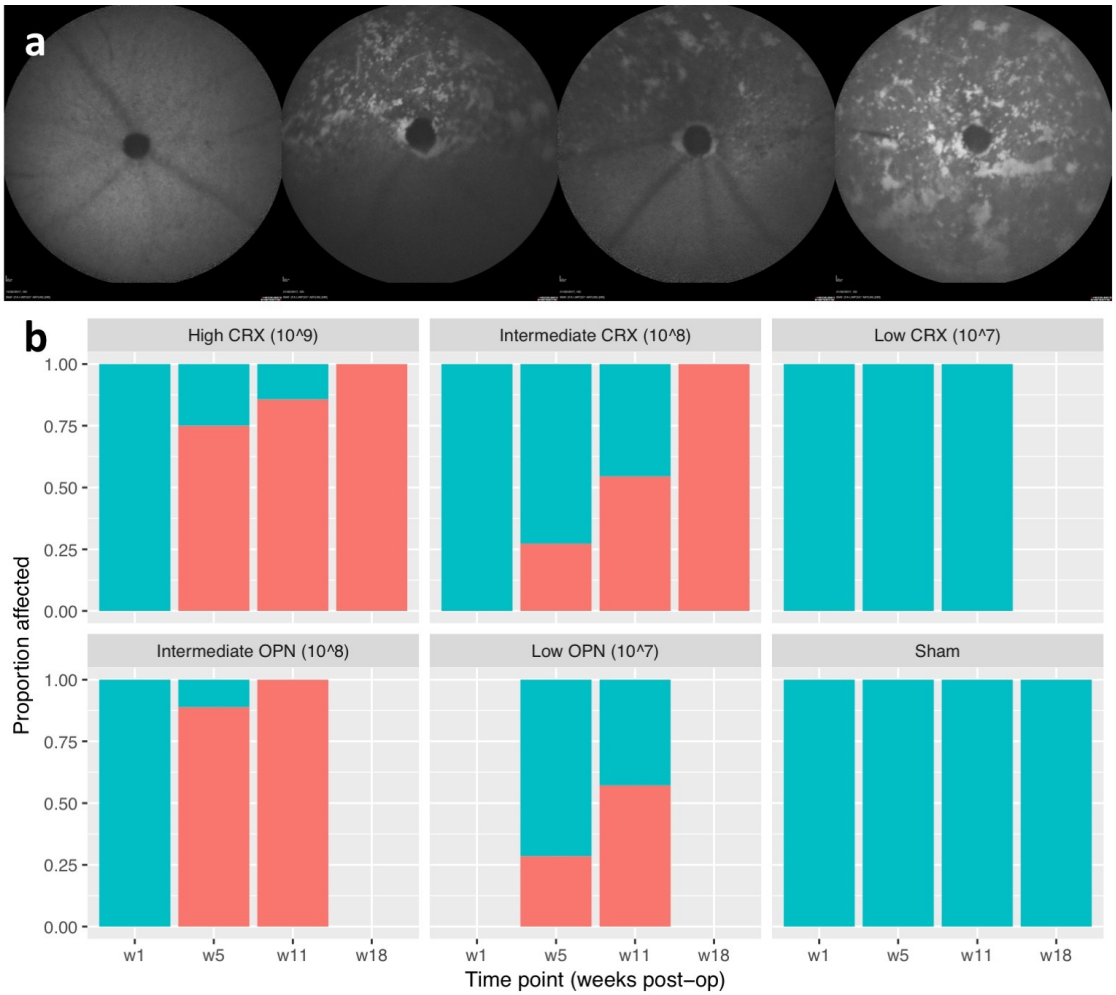


Figure 7.7 | Pigmentary changes on cSLO IRAF. a, Examples of the varying severity of pigmentary changes occurring in AAV injected eyes during the experiment, ranging from unchanged to changes encompassing some or all of the retina. No changes were observed in any of the uninjected eyes. **b,** The proportion of injected eyes showing the presence (red) or absence (green) of pigmentary changes in the injected eyes of mice suggests a dose-related response, with a delayed onset more than 1 week after surgery.

dark-adapted setting. The results of these scotopic and mesopic test conditions for 3 weeks and 9 weeks after surgery are displayed in Figure 7.8 and Figure 7.9 respectively. Linear mixed-effects (lme) modelling using REML was the statistical method used to accomodate the within-mouse inter-eye (L and R) correlations, as well as the repeated measures at two time points. P-values below are derived from this model analysis.

As anticipated, the scotopic 10^{-4} candela 0.5Hz flash did not produce an appreciable b-wave response in any of the mice. Forced-choice cursor placement produced a mean b-wave amplitude no greater than the mean

background noise in any of the groups.

The mesopic 10 candela 0.5Hz flash step did stimulate an appreciable b-wave response in mice 3 weeks after surgery, but without the typical deep a-wave observed in mice with functional rod pathways. In all mice, this mesopic b-wave declined significantly by 9 weeks after surgery in both the uninjected (-68.2 $\pm$ 14.0; p<0.001) and injected eyes (-49.6 $\pm$ 14.1; p<0.001). Generally, the forced-choice b-wave 10 candela flash step measurement at 9 weeks was no larger than the mean background noise.

Regarding the baseline characteristics of the mice in each treatment group at the 3 week ERG. The mean implicit times (mesopic 10cd stimulus) for the uninjected eyes in each AAV treatment group were not significantly different from the uninjected eyes in the sham group. Compared to the mean response amplitude (mesopic 10cd stimulus) of the uninjected eyes of the PBS sham group (177.1 $\pm$ 13.3), the AAV.CRX 1 $\times$ 10^9gc group (112.5 $\pm$ 24.1; n=9) was significantly lower (p<0.001). Conversely, the AAV.CRX 1 $\times$ 10^7gc group (218.5 $\pm$ 17.1; n=17) was significantly higher than the sham group (p=0.045). The AAV.CRX 1 $\times$ 10^8gc group, AAV.OPN 1 $\times$ 10^8gc and AAV.OPN 1 $\times$ 10^7gc groups showed no significant difference in the baseline characteristics. These baseline differences in some groups is an important confounding factor to consider whilst interpreting the results.

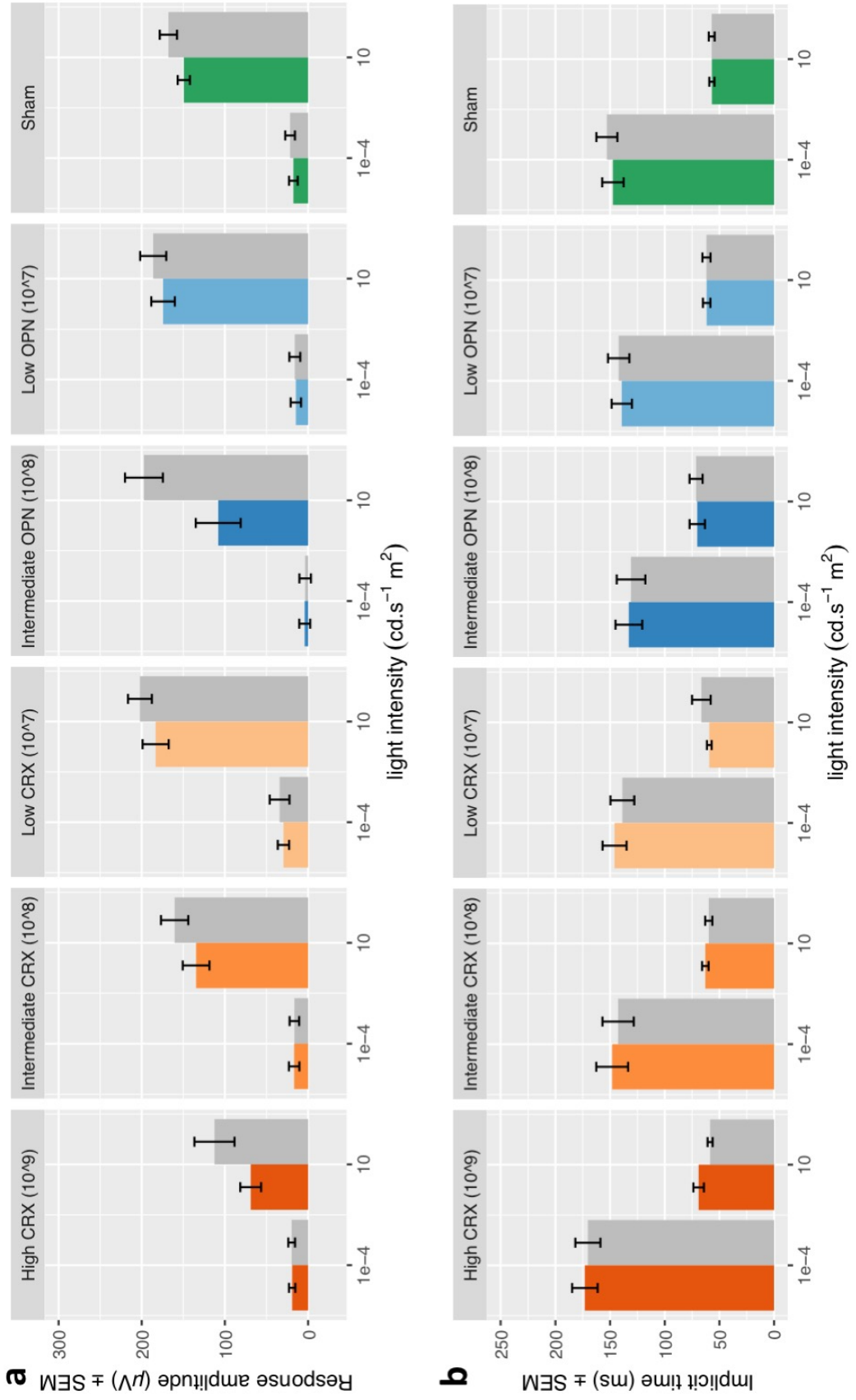


Figure 7.8 | Mesopic ERG function at 3 weeks. a, ERG b-wave response amplitude for uninjected (grey) and injected (solid colour) eyes tested in scotopic and mesopic conditions 3 weeks following surgery. Scotopic response is absent in Rho$^{-/-}$ mice as expected. Results are faceted by treatment group (Sham: green. CRX: Orange. OPN: Blue). **b,** Implicit times for the same ERG testing on uninjected (grey) and injected (solid colour) eyes 3 weeks after surgery. All data shown as mean ± SEM.

Regarding the effect of PBS sham injections on mesopic retinal function (n=17 mice). The mean response at 3 weeks in uninjected eyes (177.1 $\pm$ 13.3) and sham injected eyes (170.2 $\pm$ 21.9) was not significantly different (25.8 $\pm$ 14.4; p=0.074). The mean implicit time in uninjected eyes (57.0 $/pm$ 2.7) and injected eyes (56.9 $\pm$ 2.4) was not significantly different (p=0.95). 9 weeks following surgery, there was no difference between the eyes in response amplitude (p=0.17) or implicit time (p=0.78). This pattern was repeated at 9 weeks in all AAV treatment groups and likely reflects the natural history of the Rho$^{-/-}$ degeneration largely extinguishing mesopic retinal function by this age.

Regarding the effect of the AAV.CRX 1 $\times$ 10^{9}gc treatment on mesopic retinal function (n=9 mice). The mean response at 3 weeks in AAV injected eyes (39.8 $\pm$ 21.5) compared to uninjected eyes (112.5 $\pm$ 24.1) was significantly different (-72.6 $\pm$ 19.4; p<0.001). The mean implicit times of uninjected eyes (58.5 $\pm$ 2.3) and injected eyes (92.5 $\pm$ 23.9) at 3 weeks was significantly different (p=0.042). The AAV treated eye response did not decline significantly by 9 weeks (-0.08 $\pm$ 29.8; p=0.98) whereas the untreated eye response declined profoundly (-85.0 $\pm$ 29.8; p=0.005); this suggests that AAV.CRX 1 $\times$ 10^{9}gc treatment caused an almost complete loss of mesopic function at 3 weeks.

Regarding the effect of the AAV.CRX 1 $\times$ 10^{8}gc treatment on mesopic retinal function (n=13 mice). The mean response at 3 weeks in uninjected eyes (160.4 $\pm$ 16.4) and AAV injected eyes (149.5 $\pm$ 21.0) was not significantly different (-11.0 $\pm$ 18.3; p=0.55). The implicit times were not significantly different between eyes (p=0.45)

Regarding the effect of the AAV.CRX 1 $\times$ 10^{7}gc treatment on mesopic retinal function (n=17 mice). The mean response at 3 weeks in uninjected eyes (218.5 $\pm$ 17.1) and AAV injected eyes (183.3 $\pm$ 15.7) was significantly different (-35.3 $\pm$ 16.0; p=0.029). The implicit times were not significantly different between eyes (p=0.78)

Regarding the effect of the AAV.OPN 1 $\times$ 10^{8}gc treatment on mesopic retinal function (n=10 mice). The mean response at 3 weeks in uninjected eyes (213.8

$\pm$ 26.2) and AAV injected eyes (131.0 $\pm$ 33.4) was significantly different (-82.8 $\pm$ 20.8; p<0.001). The implicit times were not significantly different between eyes (p=0.57).

Regarding the effect of the AAV.OPN 1 $\times$ 10^7gc treatment on mesopic retinal function (n=15 mice). The mean response at 3 weeks in uninjected eyes (186.2 $\pm$ 15.7) and AAV injected eyes (174.3 $\pm$ 14.1) was not significantly different (-11.9 $\pm$ 17.0; p=0.49). The implicit times were not significantly different between eyes (p=0.95).

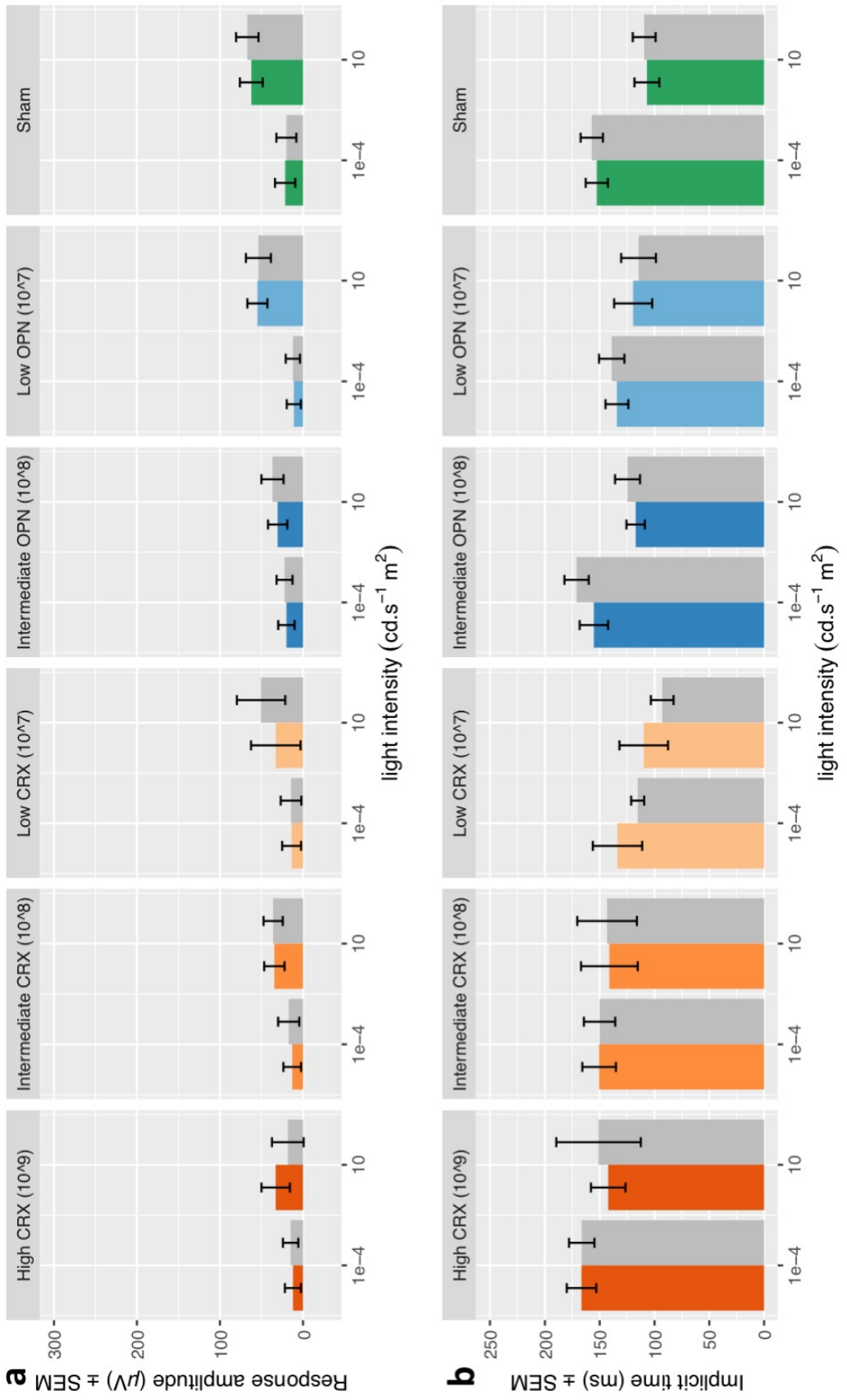


Figure 7.9 | Mesopic ERG function at 9 weeks. a, ERG b-wave response amplitude for uninjected (grey) and injected (solid colour) eyes tested in scotopic and mesopic conditions 9 weeks following surgery. Mesopic response is largely extinguished in Rho$^{-/-}$ mice as expected. Results are faceted by treatment group (Sham: green. CRX: Orange. OPN: Blue). **b,** Implicit times for the same ERG testing on uninjected (grey) and injected (solid colour) eyes 9 weeks after surgery. All data shown as mean ± SEM.

7.4.7 Effect on photopic ERG function

Figure 7.10 shows the photopic ERG irradiance response curve (IRC) and implicit times for the different treatment groups 3 weeks following injection. Figure 7.11 shows the photopic ERG IRC and implicit times for the different treatment groups 9 weeks following surgery. Non-linear mixed-effects (nlme) modelling using REML (see subsection 2.8.2, Figure 2.6 and Equation 7.1) was the statistical method used to accomodate the within-mouse inter-eye (L and R) correlations, as well as the repeated measures at two time points and saturating exponential cone response with light intensity. P-values below and the projected asymptote of the irradiance response curve are derived from this model.

Regarding the baseline characteristics of the mice allocated across the treatment groups. At 3 weeks, in the sham group (n=17), the asymptote of the uninjected eyes was 215.6μV $\pm$ 17.5. Table 7.1 shows that the asymptote of the photopic ERG IRC was not significantly different between the uninjected eyes of the sham group and the uninjected eyes of each AAV group. Yet, across the six cohorts (litter groups) of mice, the later cohorts typically demonstrated a larger photopic ERG response than the earlier cohorts. Mice from these later cohorts were disproportionately allocated to AAV.CRX (1×10^7) and AAV.OPN (1×10^7) groups. As such, the asymptotes in the uninjected eyes of these AAV groups were significantly different to the uninjected eyes of the AAV.CRX (1×10^8), AAV.CRX (1×10^9), and AAV.OPN (1×10^8). This source of confounding should be considered when assessing dose effects. However, comparison to the contralateral uninjected eye within a group or to the sham injected group does not need adjustment.

The midpoint of the sigmoid ERG IRC in uninjected eyes was 0.36 $\log_{10}$cd.s^{-1}.m^2 $\pm$ 0.02. Fitting an interaction between the treatment group and the midpoint did not show a significant difference between the groups (CRX9, p=0.903; CRX8, p=0.379; CRX7, p=0.634; OPN8, p=0.723; OPN7, p=0.528).

Table 7.1 | Baseline characteristics of the photopic ERG IRC asymptote across treatment groups.

Group	Value	Std.error	p-value
Sham	215.6	17.5	
CRX (10^9)	195.8	23.8	0.501
CRX (10^8)	187.6	19.9	0.288
CRX (10^7)	255.5	17.5	0.103
OPN (10^8)	208.8	22.6	0.813
OPN (10^7)	253.0	18.6	0.139

The slope of the sigmoid ERG IRC in uninjected eyes was 0.31 $\log_{10}$cd.s^{-1}.m^2 $\pm$ 0.01. Fitting an interaction between the treatment group and the midpoint did not significantly improve the log likelihood ratio of the model. Thus, in the final model, the effect of the subretinal injections on the photopic ERG response amplitude interacted only with asymptote.

Furthermore, the implicit time of the uninjected eyes did not vary significantly over stimulus intensity (p=0.76), nor between groups (CRX9, p=0.113; CRX8, p=0.168; CRX7, p=0.34; OPN8, p=0.16; OPN7, p=0.66).

Taken together, these findings demonstrate that the pre-surgery randomisation has largely avoided any confounding of baseline photopic ERG function. Although the litter-dependent variance between the higher and lower AAV dose groups should be kept in mind. The different effects of the subretinal injections on photopic ERG function can be assessed with uncorrected statistical testing.

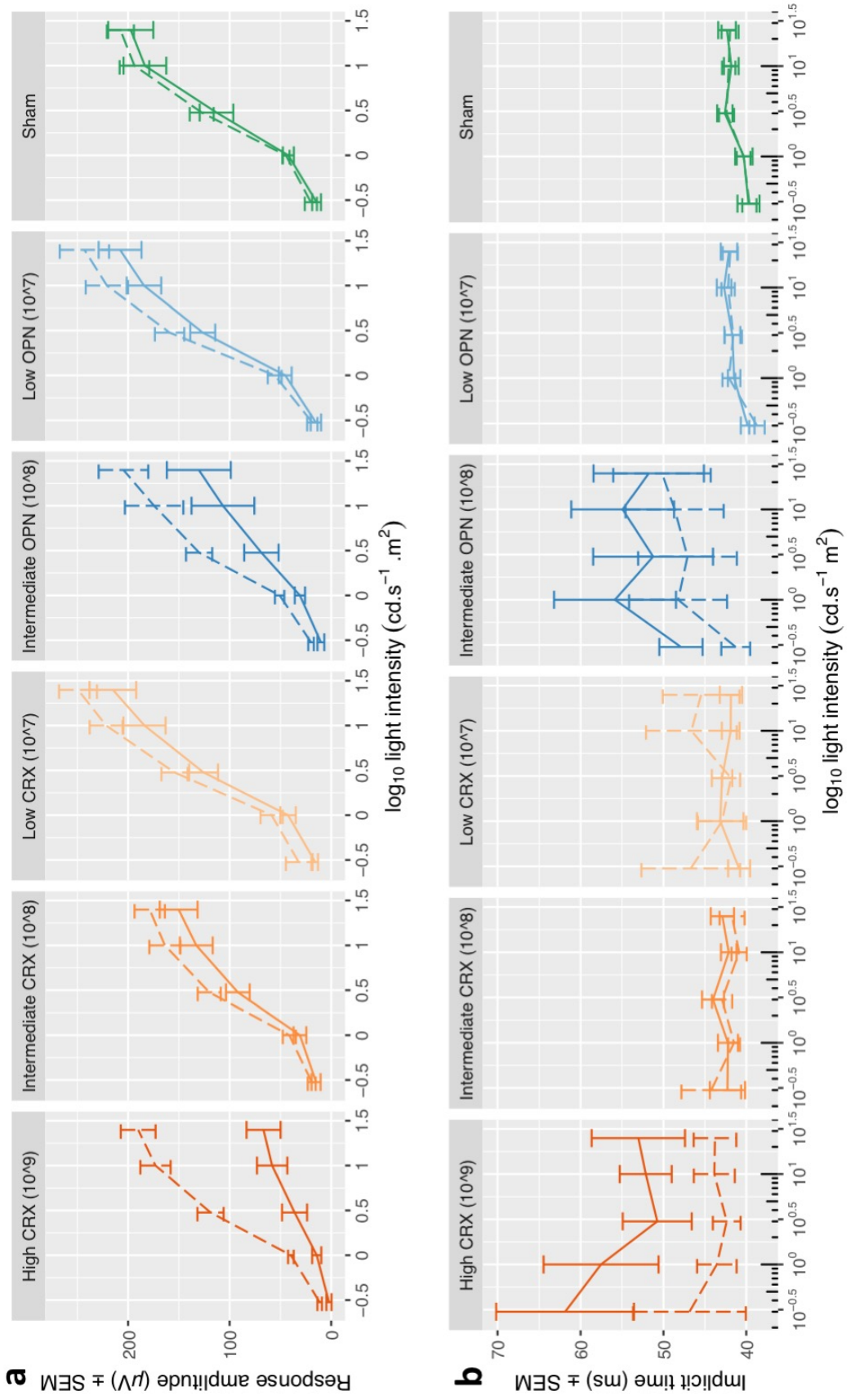


Figure 7.10 | Photopic ERG function at 3 weeks. a, Photopic ERG irradiance response curve (IRC) of mice in the treatment groups 3 weeks after injections, showing response for injected eyes (solid line) and uninjected eyes (broken line). Every group, including sham, showed significantly reduced function in the injected eye. **b,** Implicit times for the leading edge of the b-wave for the same photopic ERG data at 3 weeks. All data shown as mean ± SEM.

Regarding the effect of PBS injections on photopic retinal function (n=17 mice). Compared to the uninjected eye at 3 weeks, the asymptote of the treated eye was reduced (-13.4μV $\pm$ 6.8; p=0.051). At 3 weeks, the implicit time did not vary between injected and uninjected eyes (p=0.85). This is consistent with a mild reduction in retinal function due to the subretinal fluid and mechanical detachment. At 9 weeks, photopic retinal function was largely absent and the injected and uninjected eyes were both equivalent (p=0.72).

Regarding the effect of AAV.CRX (1×10^9) injections on photopic retinal function (n=10 mice). Compared to the uninjected eye at 3 weeks, the asymptote of the treated eye was reduced (-129.1 $\pm$ 9.5; p<0.001). At 3 weeks, the implicit time did not vary between treated and untreated eyes (p=0.85). At 9 weeks, photopic retinal function was largely extinguished and the injected and uninjected eye response amplitudes were both equivalent (p=0.63).

Regarding the effect of AAV.CRX (1×10^8) injections on photopic retinal function (n=14 mice). Compared to the uninjected eye at 3 weeks, the asymptote of the treated eye was reduced (-34.9 $\pm$ 7.8; p<0.001). At 3 weeks, the implicit time did not vary between treated and untreated eyes (p=0.46). At 9 weeks, photopic retinal function was largely extinguished and the injected and uninjected eye response amplitudes were both equivalent (p=0.66).

Regarding the effect of AAV.CRX (1×10^7) injections on photopic retinal function (n=17 mice). Compared to the uninjected eye at 3 weeks, the asymptote of the treated eye was reduced (-41.5 $\pm$ 6.9; p<0.001). At 3 weeks, the implicit time did not vary between treated and untreated eyes (p=0.50). At 9 weeks, photopic retinal function was largely extinguished and the injected and uninjected eye response amplitudes were both equivalent (p=0.13).

Regarding the effect of AAV.OPN (1×10^8) injections on photopic retinal function (n=10 mice). Compared to the uninjected eye at 3 weeks, the asymptote of the treated eye was reduced (-82.0 $\pm$ 9.0; p<0.001). At 3 weeks, the implicit time did not vary between treated and untreated eyes (p=0.19). At 9 weeks, photopic retinal function was largely extinguished and the injected and

uninjected eye response amplitudes were both equivalent (p=0.67).

Regarding the effect of AAV.OPN (1×10^7) injections on photopic retinal function (n=15 mice). Compared to the uninjected eye at 3 weeks, the asymptote of the treated eye was reduced (-41.4 $\pm$ 7.3; p<0.001). At 3 weeks, the implicit time did not vary between treated and untreated eyes (p=0.81). At 9 weeks, photopic retinal function was largely extinguished and the injected and uninjected eye response amplitudes were both equivalent (p=0.45).

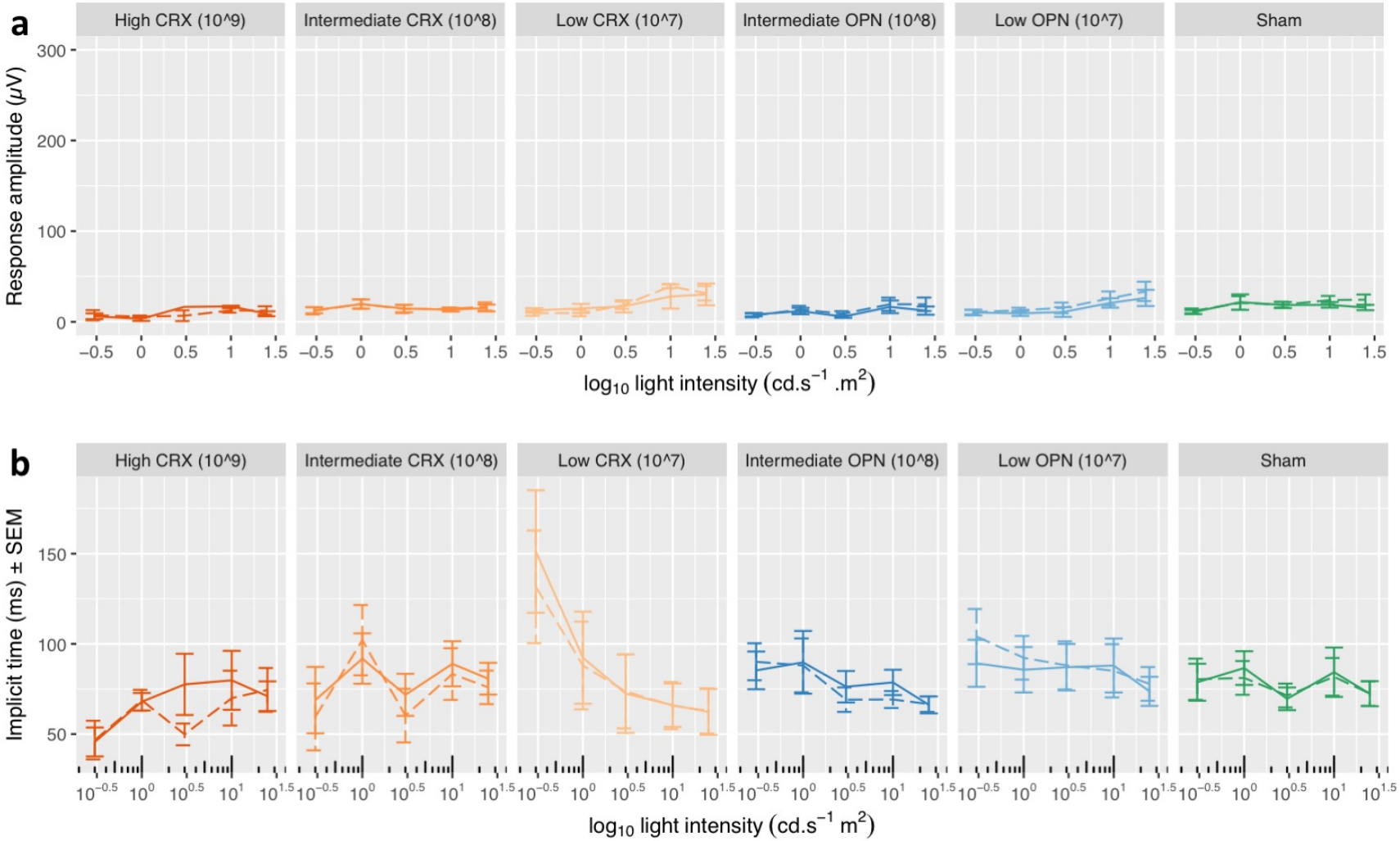


Figure 7.11 | Photopic ERG function at 9 weeks. a, Photopic ERG IRC of the treatment groups 9 weeks after injection, showing extinction of photopic retinal pathways due to Rho$^{-/-}$ degeneration and no evidence of extended photosensitivity. **b,** Implicit times for the leading edge of the b-wave for the same photopic ERG data at 9 weeks. All data shown as mean ± SEM.

7.4.8 Effect on OMR function in photopic conditions

OMR functional testing was performed (mean days post-op ± range) on treated mice at 12 to 13 weeks post-surgery (90 days ± 8). A separate cohort of control mice ($Rho^{-/-}$; n=5) underwent OMR testing at 6 weeks of age for comparison.

Figure 7.12 graphically displays the data from the OMR testing. All OMR measurements are written as the measured mean (head tracks/minute) ± SEM. The OMR measurements were not normally distributed (Shapiro-Wilk; W=0.7, p<0.001), as expected for a count variable with a fixed lower limit of 0. Statistical analysis would be appropriate with a Kruskal-Wallis test with Dunn's post-hoc comparisons to deal with the non-parametric data but would not accommodate the within-mouse inter-eye correlation. Alternatively, a linear mixed-effects (lme) model to accommodate the within-mouse inter-eye correlated data is still relatively robust for handling non-parametric data. The final fitted lme model satisfied the model tests for residual normality (Shapiro-Wilk; W=0.98, p=0.55) and homoscedasticity; p-values are derived from this model.

The untreated control mice at 6 weeks of age (n=5) showed equivalent head tracking behaviour for the left eye (5.0 ± 1.1) and right eye (5.2 ± 0.9), that were not significantly different (-0.2 ± 0.3; p=0.49). Yet, the head-tracking behaviour during stationary testing (0.1 ± 0.1) was profoundly and significantly less (p<0.005), thereby validating the test conditions. The head tracking behaviour for injected or uninjected eyes each treatment group were all significantly less than the control group (p<0.001).

Regarding the effect of PBS sham on OMR function in photopic conditions (n=3). The mean response of the uninjected eye (0.5 ± 0.2) and injected eye (1.1 ± 0.4) were not significantly different (0.5 ± 0.3; p=0.075).

Regarding, the effect of the different doses of AAV treatment on the OMR function in photopic conditions. The mean response of the uninjected eye and injected eye for each treatment group (n=3 mice tested per group) was not significant (p>0.2 for each group). Thus, the AAV treatments did not

demonstrate a photosensitivity benefit on this test at this time-point.

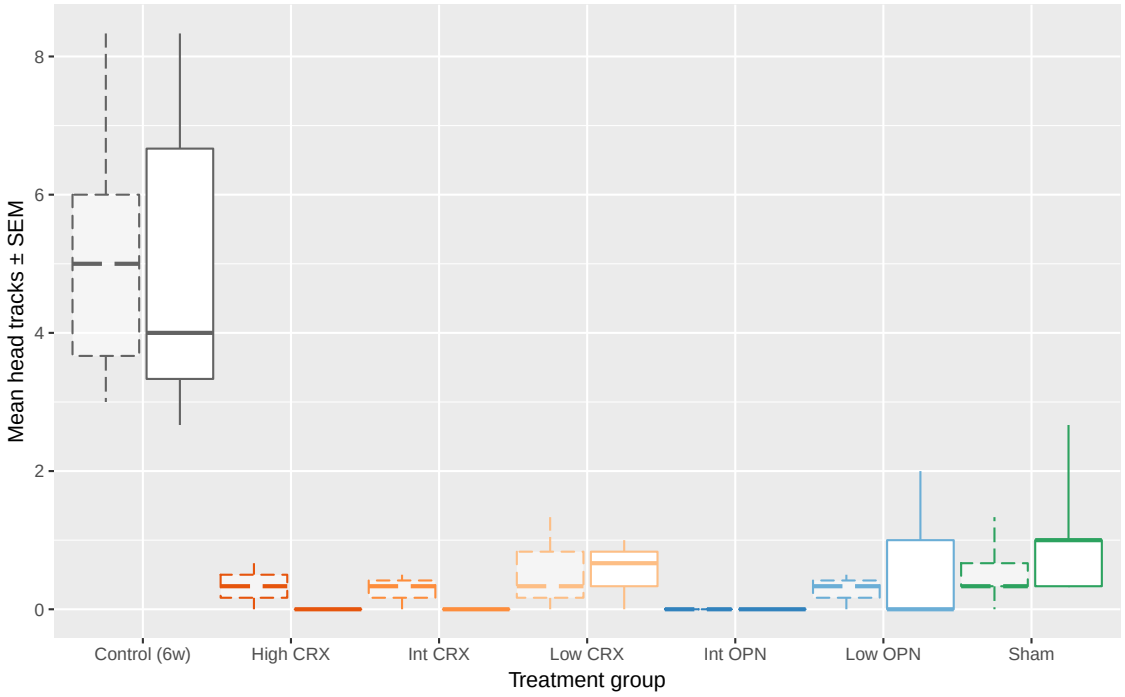


Figure 7.12 | OMR function in photopic conditions. Head tracking behaviour of conscious mice, 14-16 weeks after treatment, tested in photopic conditions (>1000 lumens) using an optomotor response drum with a 0.2 cycles/degree spatial grating. Data from each treatment group (n=3 mice per group) separated into injected eyes (dashed line, transparent) and uninjected eyes (solid line, opaque). Controls (grey; n=6 mice) are untreated Rho$^{-/-}$ mice at 6 weeks of age, separated as untreated left and right eye data. None of the treated eyes showed any rescue effect compared to untreated eyes. Data presented as a boxplot; the line shows the median, the box shows IQR and the whiskers show the highest and lowest values.

7.4.9 Transgene mRNA expression in the retinal transcriptome

A small cohort of mice (n=20) were injected in one eye with AAV treatment and then sacrificed 3 weeks later (mean age PND 43 $\pm$ 1). mRNA was extracted and cDNA reverse transcribed as described in subsubsection 2.3.7.2; cDNA samples were tested using qPCR primers optimised to distinguish between interspecies homology in subsection 5.4.7.

7.4.9.1 Cone opsin mRNA

Primers that were previously able to fully distinguish between species now produced amplicons from both species. Figure 7.13 shows the gene expression profile of *OPN1LW* and *Opn1mw*; the origin of this cone opsin signal could not be clearly distinguished between endogenous and exogenous origin.

After normalisation to the fellow uninjected eye, treatment with AAV.OPN1LW (10^7gc) showed a significant increase (1200% $\pm$ 200%; p=0.011) in cone opsin gene expression compared to sham. Whereas, the PBS sham injected eyes showed no difference (0.72-fold $\pm$ 0.5) compared to the uninjected eye. There was no significant change in AAV.CRX (10^8 gc or 10^7gc) treated retina cone opsin expression compared to sham. The AAV.OPN1LW vector clearly increased the amount of cone opsin transcripts within three weeks of treatment.

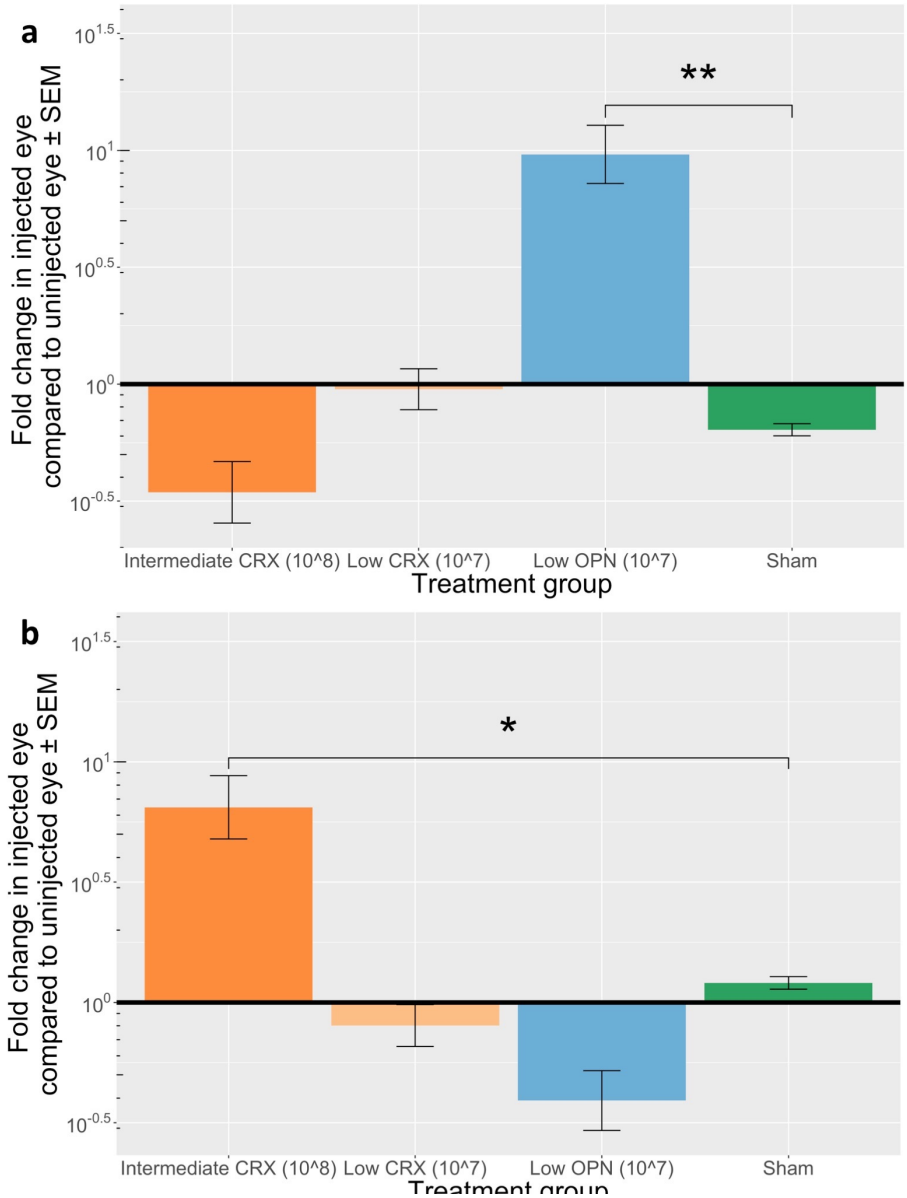


Figure 7.13 | Gene expression in injected eyes. a, Cone opsin gene expression levels normalised to *ActB* reference gene in injected (coloured) and uninjected (grey) neurosensory retinas collected 3 weeks post-injection. The AAV.OPN (10^7gc) injected eyes showed an 11-fold increase in cone opsin gene expression, whereas sham showed no difference between eyes. **b,** Normalised *CRX* gene expression in injected and uninjected eyes showing 10-fold increase in *CRX* expression in AAV.CRX (10^8gc) injected eyes, but no difference in AAV.CRX (10^7gc) injected eyes. n=4 mice in each treatment group. Values displayed as mean ± SEM. * denotes p<0.05

7.4.9.2 CRX and Crx mRNA

After normalisation to the fellow uninjected eye, treatment with AAV.CRX (10^8gc) showed a significant increase (250% ± 130%; p=0.04) in CRX gene expression compared to sham injected eyes. There was no significant change in AAV.CRX

(10^7gc) or AAV.OPN1LW (10^7gc) treated retina *CRX* expression compared to sham. The AAV.CRX vector only increased the amount of *CRX* transcripts three weeks after treatment at doses of 10^8gc or above.

7.4.10 Transgene protein expression on retinal histology

7.4.10.1 CRX expression in RPE cells

Transgenic CRX expression was identified in the dorsal RPE of injected eyes (Figure 7.14). However, this was irregular occurrence and CRX was not expressed in all RPE cells. The staining pattern was localised to the nuclei of the cells as expected for a transcription factor. The RPE of the uninjected contralateral eyes did not demonstrate any instances of CRX expression, thereby making a misidentified endogenous Crx signal less likely. There were no observed instances of RPE cells expressing GFP reporter protein as a result of transgenic CRX expression.

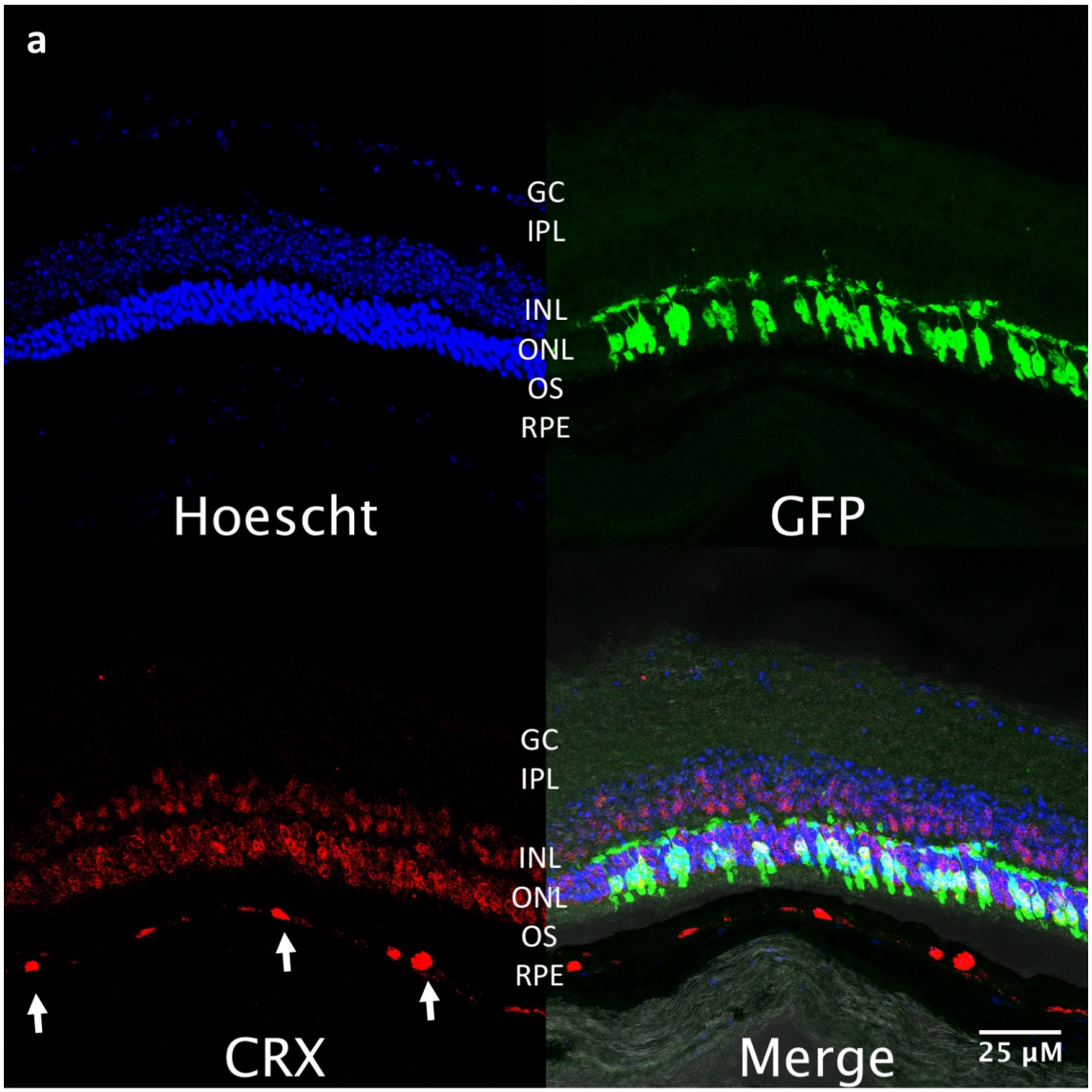


Figure 7.14 | Transgenic CRX expression in RPE. a, 40x lens-objective Z-stack of the dorsal retina of an AAV.CRX (1×10^8gc) treated eye in an $Rho^{-/-\ B6TgOPN1LW\text{-}EGFP+/-}$ mouse sacrificed at PND63 (6 weeks following surgery). Endogenous Opn1-GFP signal combined with exogenous Hoescht stain and Crx antibody (1/500; PA5-32182) and overlaid Nomarski silhouette. White arrows points to transgenic CRX expression in the nuclei of RPE cells. There is no gain of endogenous GFP expression in these transduced RPE cells.

7.4.11 CRX expression in the neurosensory retina

The interspecies homology of the CRX protein is 97%. As explored in subsection 5.4.7, none of the three commercial CRX antibodies tested were able to differentiate between endogenous mouse Crx and exogenous human CRX. Also, endogenous Crx is expressed in the inner nuclear layer as well as the outer nuclear layer [9, 10].

Rho$^{-/-\ B6TgOPN1LW\text{-}EGFP+/-}$ mice treated with AAV.CRX at 1×10^8gc or 1×10^7gc were stained for CRX at PNW9 to PNW10. Figure 7.15 shows that CRX staining was visible in the nuclei of photoreceptors and some of the inner nuclear layer. The staining pattern did not vary between the dorsal and ventral retina. This differs from the previous dorsal gradient which was identified in mice treated with a higher dose (1×10^9gc) of AAV.CRX in Figure 4.5; the injected dorsal retina had more CRX staining. IHC has poor reliability for measuring staining density and no formal analysis was undertaken on these retinal sections to quantify the dorsal gradient in these lower dose mice.

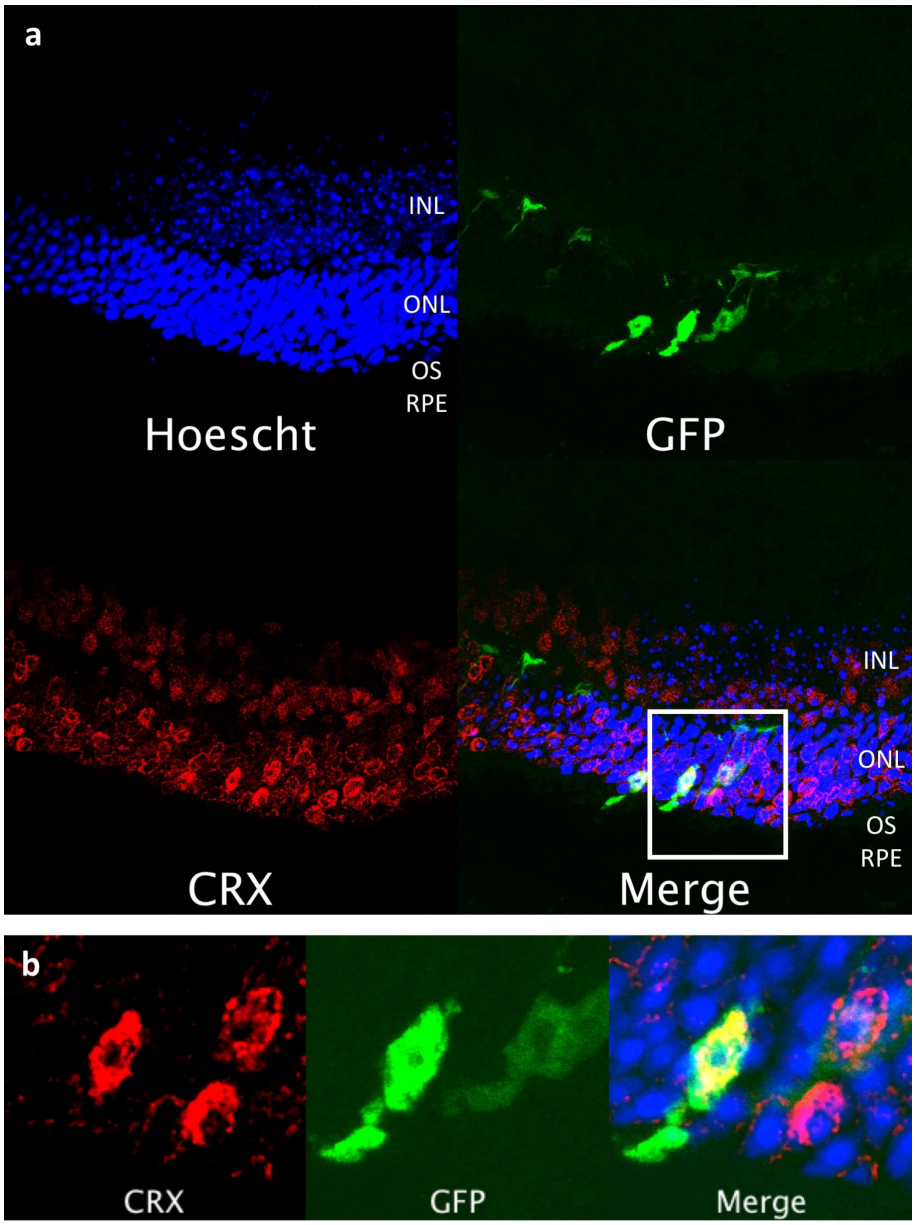


Figure 7.15 | Transgenic CRX expression in photoreceptors. **a,** 63x lens objective Z-stack of the dorsal retina of an AAV.CRX (1×10^8gc) treated eye in a Rho$^{-/-\ B6TgOPN1LW\text{-}EGFP+/-}$ mouse sacrificed at PND71 (7 weeks following surgery). Nuclear-specific Crx staining is seen throughout the outer nuclear layer and, more lightly, in the inner nuclear layer. **b,** Enlarged area of interest showing co-localisation of CRX with endogenous GFP in cone photoreceptors, confined to the nuclei and not extending into the outer segment. CRX staining also occurs in other non-GFP labelled nuclei which are likely rod cells.

CRX staining of treated mice euthanised at PNW14-15 showed few residual photoreceptors; photoreceptor death is almost complete at this late stage of $Rho^{-/-}$ degeneration. Figure 7.17 demonstrates residual cone photoreceptors continue to express GFP despite the loss of outer segments. CRX staining is observed widely throughout the inner nuclear layer. There is no appreciable difference in CRX staining pattern between the injected and uninjected eyes .

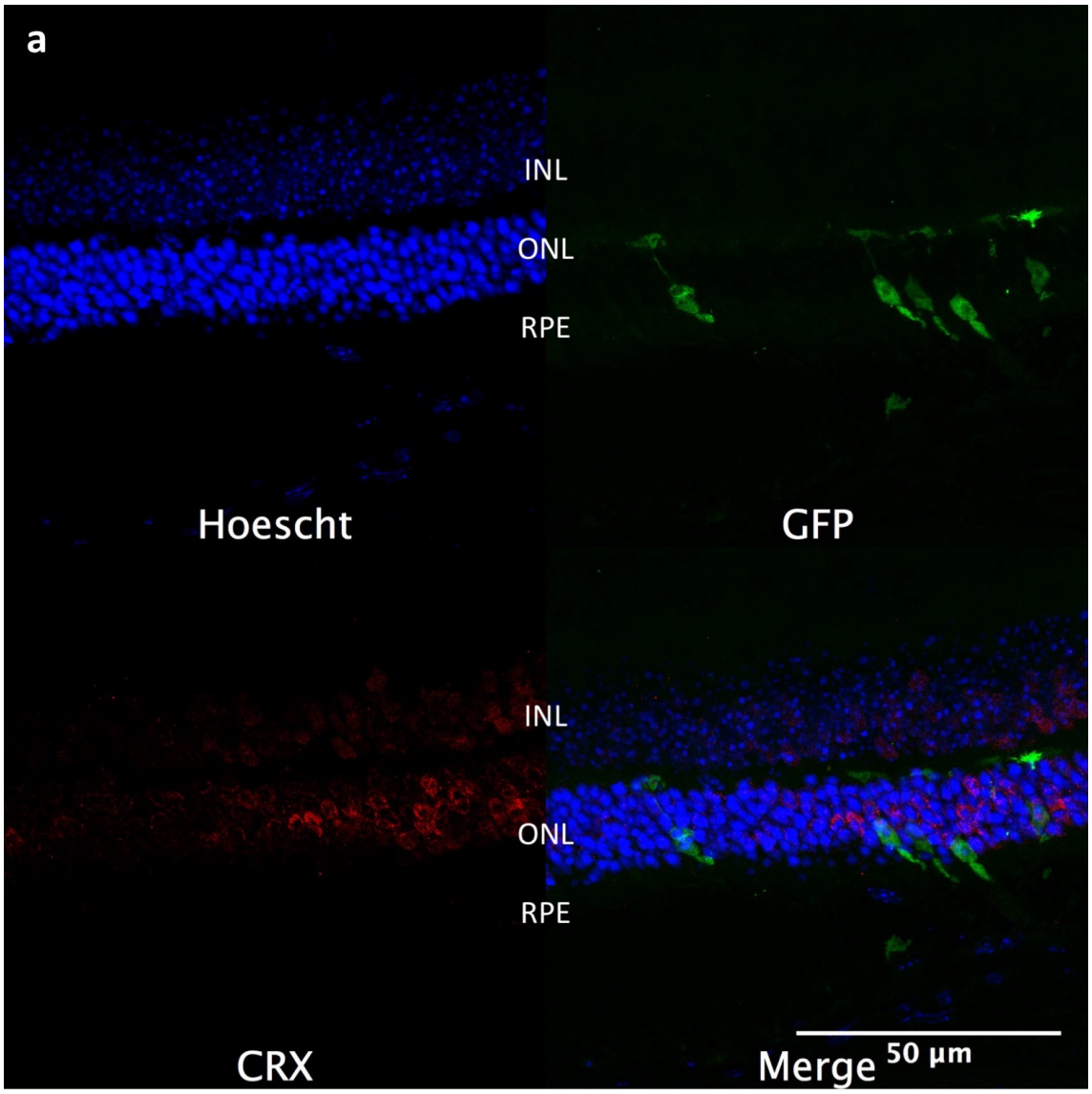


Figure 7.16 | Endogenous CRX expression in photoreceptors. **a,** 63x lens objective Z-stack of the dorsal retina of an untreated eye in an $Rho^{-/-}$ B6TgOPN1LW-EGFP+/- mouse sacrificed at PND69 (7 weeks following surgery). A faint nuclear-specific Crx staining is seen throughout the outer nuclear layer and, more lightly, in the inner nuclear layer. It is appreciably less than the staining observed in AAV.CRX treated eyes.

The presence of residual photoreceptors in PNW15 retinal sections helps understand the rhodopsin transcript identified in Figure 4.9. Residual rod photoreceptors at PNW15 appear as a discontiguous layer of single cells. This incomplete layer is not observable on OCT, but would continue to produce untranslated rhodopsin product measurable on qPCR. Such a phenotype-transcriptome correlation was observed in chapter 4.

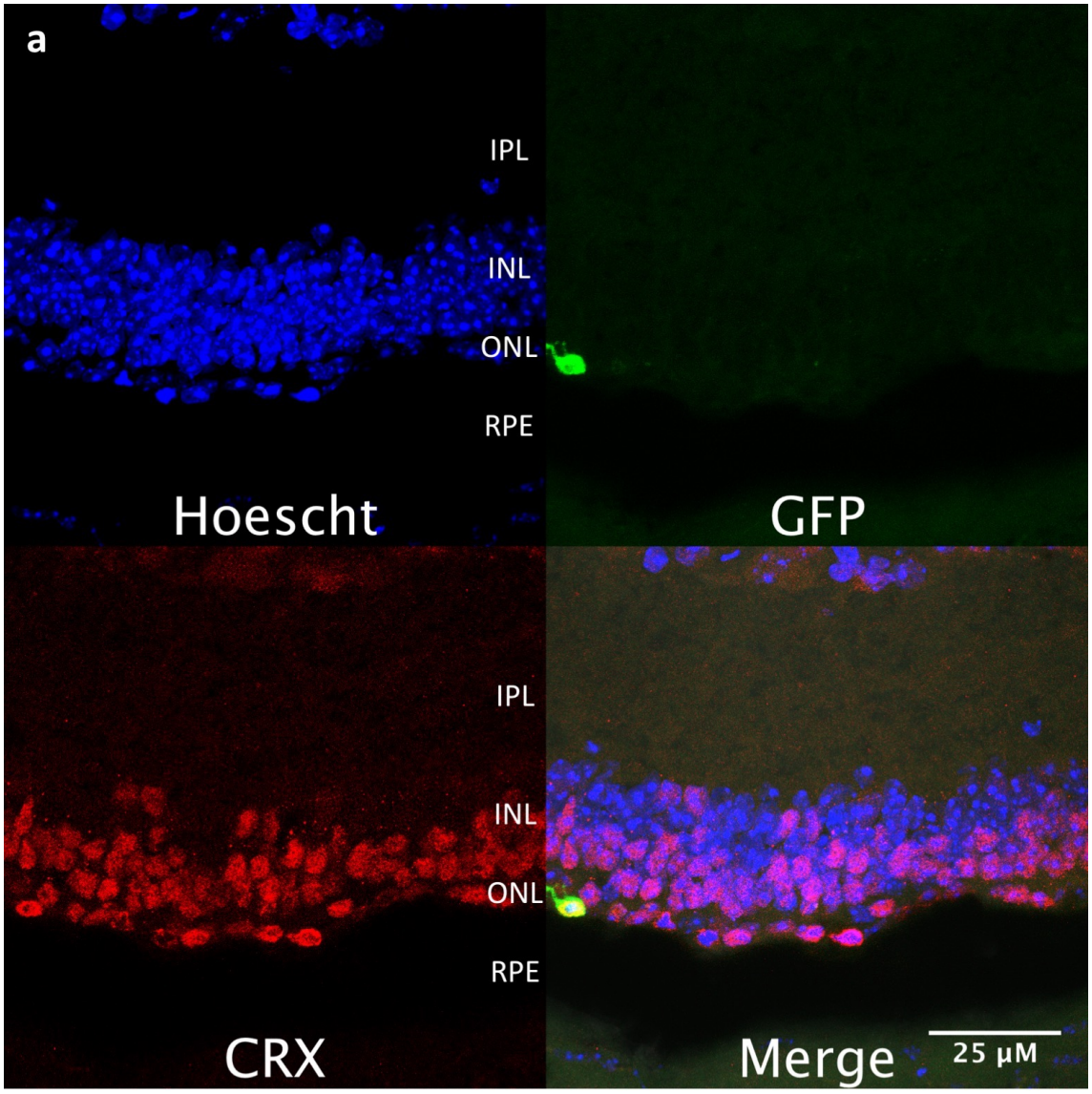


Figure 7.17 | Transgenic CRX expression at PNW14. a, 63x lens objective Z-stack of the dorsal retina of an AAV.CRX (1×10^8gc) treated eye in a $Rho^{-/-\ B6TgOPN1LW\text{-}EGFP+/-}$ mouse sacrificed at PND99 (11 weeks post surgery). Nuclear-specific Crx staining is seen throughout the inner and outer nuclear layers. There are few remaining cones (green) at this age.

7.4.12 OPN1LW expression in the neurosensory retina

Figure 7.18 shows OPN1LW staining performed on retinas collected from mice injected with low dose of AAV.OPN (1×10^7gc) and collected at earlier time-points (PNW9-PNW10). Cone opsin expression in the neurosensory retina of these AAV.OPN treated animals appears normal. At the low dose of AAV.OPN treatment there is no appreciable difference in cone photoreceptor staining between injected and uninjected eyes. There are already isolated examples of mis-localised cone opsin in the cell bodies of cones.

There are multiple instances of OPN1LW signal being detected in the outer retina without co-localising with GFP. In the absence of a rod photoreceptor cytoplasmic stain to show co-localisation — and given that the Opn1.GFP allele only labels a sub-population of cones — this signal cannot be proven to be rod photoreceptor expression of OPN1LW. However, the absence of any scotopic ERG function in Figure 7.8 and Figure 7.9, any rods expressing transgenic OPN1LW do not appear to gain a functional benefit.

A pattern of OPN1LW staining was repeatedly observed in the cytoplasm of RPE cells in the dorsal retina of the injected eye. This RPE staining was not present in uninjected eyes. This is consistent with the more intense RPE staining pattern identified in the pilot study IHC in Figure 4.5.

On IHC, there was no evidence in the eyes injected with low dose AAV.OPN of outer retinal thinning. This is consistent with the OCT measurements in Figure 7.3 showing no low dose toxicity.

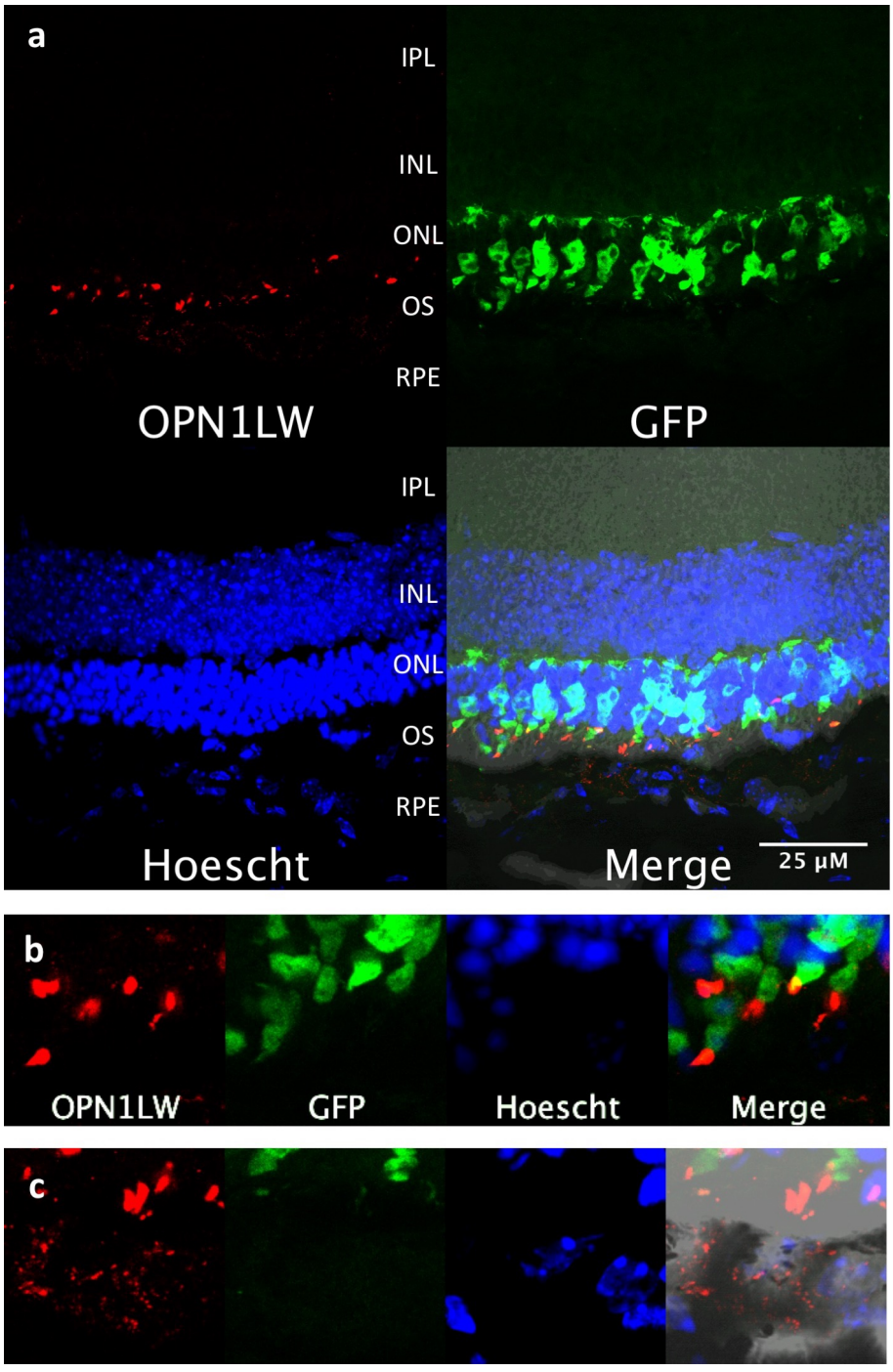


Figure 7.18 | Transgenic OPN1LW expression at PNW10. a, 63x lens objective Z-stack of the dorsal retina of an AAV.OPN (1×10^7gc) treated eye in a Rho$^{-/-\ B6TgOPN1LW\text{-}EGFP+/-}$ mouse sacrificed at PND72 (7 weeks post surgery). **b,** Cone opsin expression is well localised to the outer segments of GFP-labelled cones. **c,** Cone opsin signal is observed in the RPE cytoplasm, potentially due to off target transduction or phagocytosis of photoreceptor outer segments.

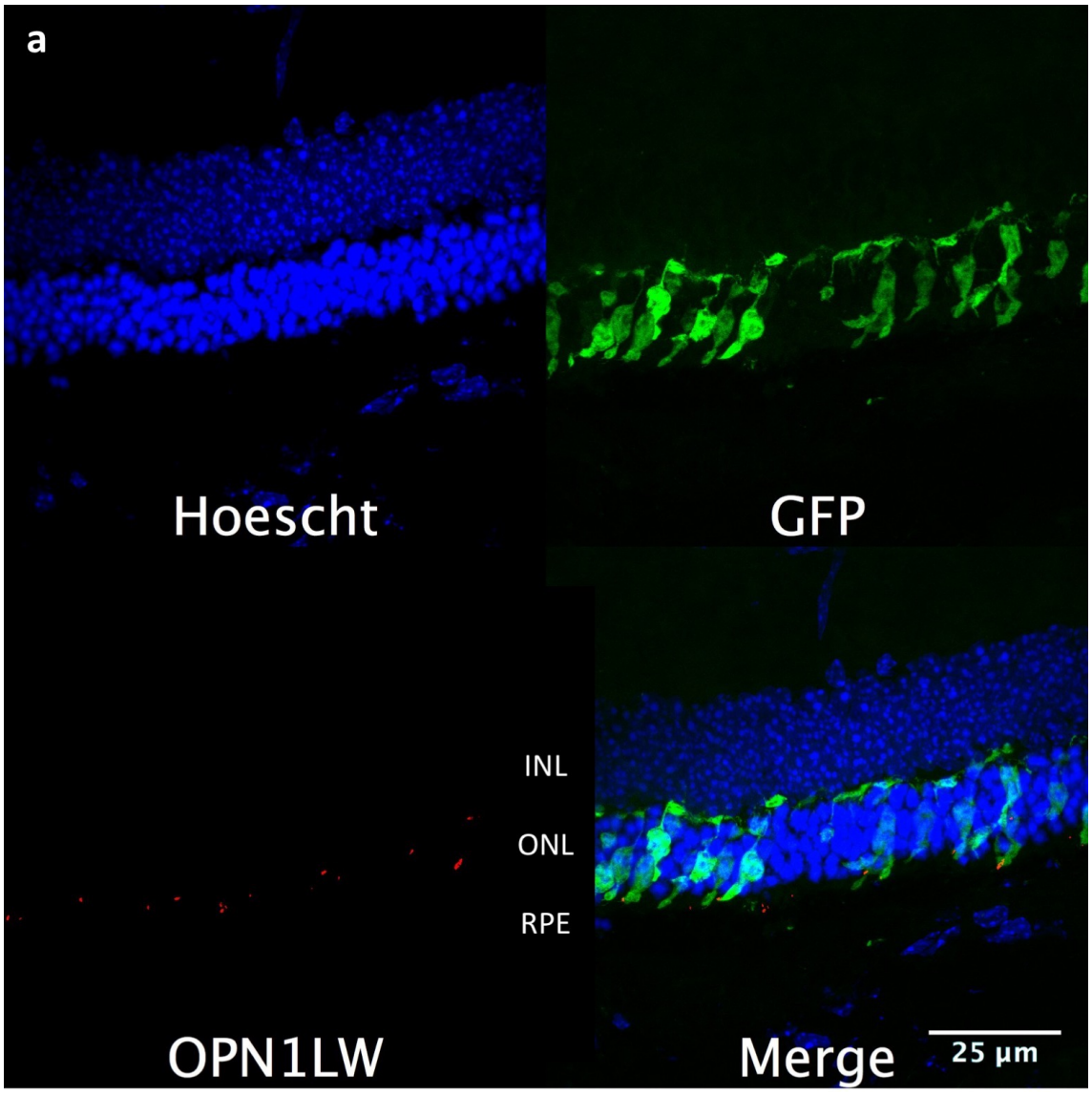


Figure 7.19 | Endogenous cone opsin expression at PNW10. a, 63x lens objective Z-stack of the dorsal retina of an uninjected eye in a $Rho^{-/-\ B6TgOPN1LW\text{-}EGFP+/-}$ mouse sacrificed at PND68 (7 weeks post surgery). There is a faint cone opsin signal localised to the outer segments of the cones that is similar to the cone opsin staining pattern in those mice treated with low dose AAV.OPN virus vector. However, the endogenous pattern is substantially less than that found in mice treated with AAV.OPN (1×10^9gc).

Older mice (PNW14-PNW15) treated with AAV.OPN (1×10^7gc) showed few residual photoreceptors; few remaining cone photoreceptors had formed outer segments. There was less cone opsin staining overall and most cone opsin signal was not correctly localised to the outer segment. This phenomenon of cone opsin mislocalisation is documented in late-stage RP.

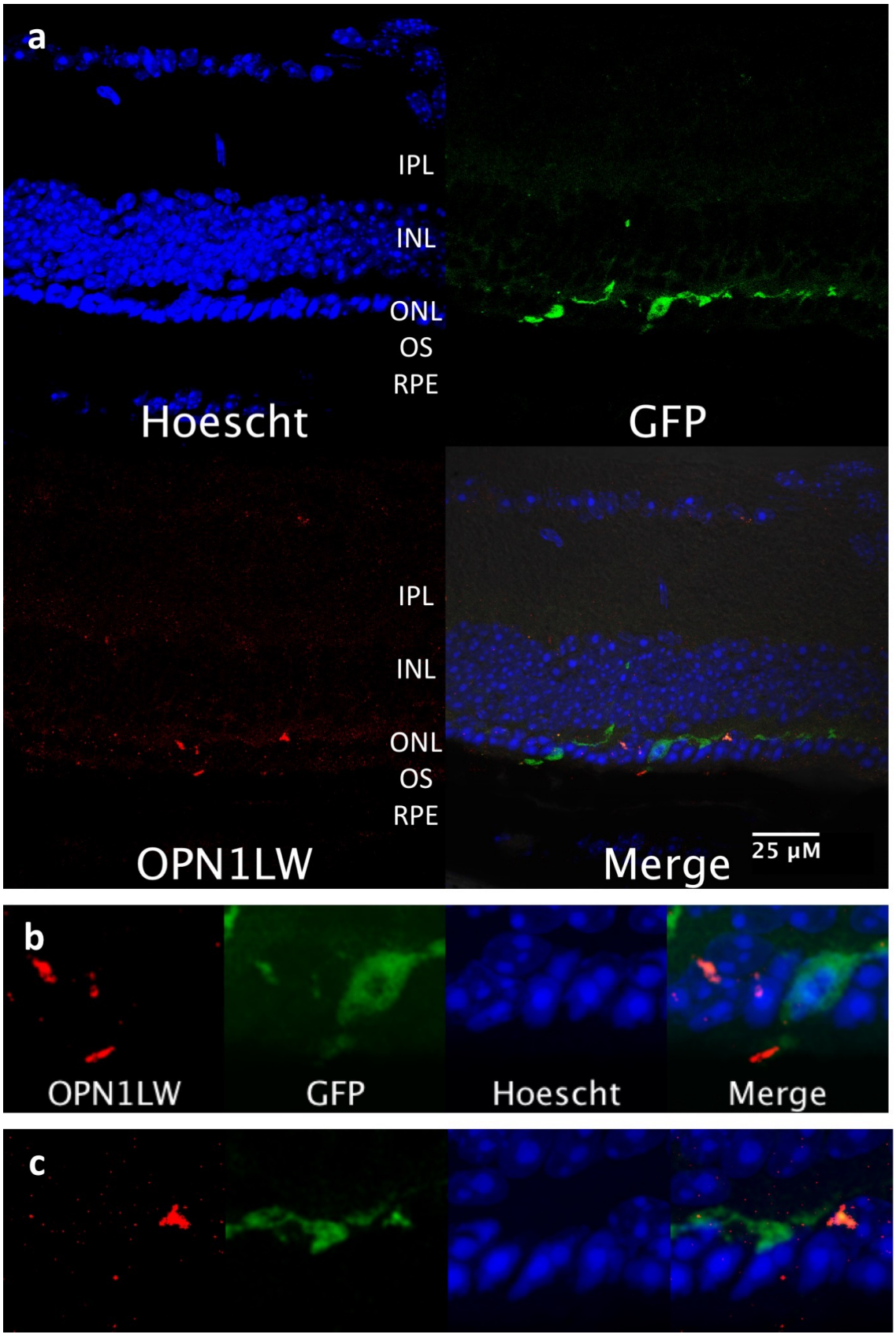


Figure 7.20 | Transgenic OPN1LW expression at PNW15. a, 40x lens objective Z-stack of the dorsal retina of an AAV.OPN (1×10^7gc) treated eye in an Rho$^{-/-\ B6TgOPN1LW\text{-}EGFP+/-}$ mouse sacrificed at PND107 (12 weeks post surgery). The outer nuclear layer is largely absent. **b,** Isolated instances of correctly localised outer segment OPN1LW expression in cones. **c,** Irregular disorganised cone opsin staining in the cytoplasm of cones (green).

7.5 Discussion

The full trial of AAV.OPN and AAV.CRX in Rho$^{-/-\ B6TgOPN1LW\text{-}EGFP+/-}$ achieved the aims and provided a reliable and clear answer to the thesis question. AAV.OPN and AAV.CRX do not improve or prolong cone photosensitivity in a Rho$^{-/-}$ mouse model of RP when delivered by subretinal injection at PND21. Over-expression of down-regulated genes associated with the cone phototransduction appear to provide no benefit in RP.

7.5.1 Surgical success

Subretinal AAV was delivered successfully to 103 mice and the previously developed exclusion criteria was appropriately applied to surgical complications. Treatment was successfully delivered to the full number of mice in the pre-determined power calculations. Mice were monitored longitudinally for changes in phenotype and tissue endpoints were collected and successfully interrogated.

7.5.1.1 Randomisation and heterogenous treatment groups

The decision to use a non-randomised allocation of mice to treatment groups introduced different ERG characteristics to some treatment groups. Larger baseline ERG b-wave amplitude in the later litters was identified as the source of the variation. Yet, the non-randomised process did make the logistical process of anaesthetising and injecting 103 mice much easier.

The sham group received a broad distribution of mice from all litters and remained directly comparable to all treatment groups. The hierarchical mixed-effects model applied during statistical analysis also accommodated much of the baseline variation between treatment groups as intended for this statistical method.

7.5.2 Functional and structural toxicity

At higher doses, both AAV vectors damaged retinal structure and function as first suggested in the small cohorts of the pilot study. This damage is dose-dependent and occurred for both transgenes, except at the lowest doses. Previous work has shown non-native transgene expression (e.g. *LacZ*) could be potentially immunogenic and cause progressive loss of transduced photoreceptors [216]. However, both transgenes share substantial nucleotide and amino acid homology with endogenous murine equivalents.

Alternatively, the over-expression of these genes is simply deleterious to carefully balanced cone homeostasis. Excess protein could accumulate and have harmful effects.

7.5.2.1 Crx-mediated differentiation to photoreceptors

The RPE demonstrated exogenous Crx expression. There were no observed instances of RPE cells expressing GFP reporter protein as a result of transgenic CRX expression. As detailed in Figure 4.5, there was no GFP expression in CRX transduced RPE cells of Nrl-L-EGFP$^{+/-}$:Rho$^{-/-}$ mice. Isolated transgenic CRX expression in the absence of other interacting transcription factors - nuclear receptor subfamily 2 group E member 3 (Nr2e3) and Nrl for rods [246, 131], Rorβ2 and Trβ2 for cone subtypes [7] - does not alter cell differentiation.

Regarding rods, Crx acts in concert with Nrl to bind the Rhodopsin promoter and modulate expression [17]; Nrl also interacts with TATA-binding protein (Tbp) to help modulate Rhodopsin expression [9]. However, Crx has not been shown to affect the expression of Nrl itself [17].

Regarding cones, Crx acts in concert with Rorβ2 to positively regulate S-opsin expression [7]. M-opsin expression is regulated by the combined activity of Trβ2 [7]. This role of Trβ2 is consistent with the observations in mice of a dorsal-ventral retinal gradient of Thyroid hormone during development and a dorsal-ventral gradient in M-cones [13]. Furthermore, Trβ2 exerts a negative effect on S-opsin expression in concert with *Crx* activity[13]. Furthermore,

studies of iPSCs have shown that exogenous RAX, OTX2 and NEUROD co-expression was required to initiate *recoverin*, blue opsin and *PDE6C* gene expression *in vitro* [17].

The inseparable role of other genes in enabling *Crx*-mediated differentiation of photoreceptors suggests that isolated ectopic over-expression of Crx would not affect cell differentiation. The evidence presented in this chapter is consistent with this.

7.5.3 Conclusions

This chapter confirms that the AAV2/8.CAG.CRX.WPRE and AAV2/8.CAG.OPN1LW.WPRE vectors successfully transduce mouse retinas following subretinal injection. The transgene is successfully transcribed to mRNA as early as three weeks following injection— even at lower doses. The high dose injected eyes also demonstrate a staining pattern consistent with transgenic protein expression. At lower doses, it is less clear whether the staining pattern is due to endogenous or transgenic protein because the antibodies do not distinguish between species.

Both AAV vectors cause dose-dependent retinal damage, even at lower doses. This damage is evident in the reduced ERG b-wave amplitudes across a range of stimulus intensities and the retinal thinning on OCT. This initial reduction in retinal function is followed by a continued decline, with no evidence of benefit to retina adjacent to the transduced area. No mice treated at any dose of either vector showed functional or structural improvement.

8

CONCLUSION

8.1 Overview

This thesis was concerned with cone photosensitivity and how that photosensitivity pathway is lost in mouse models of achromatopsia and retinitis pigmentosa. The thesis developed to explore whether over-expression of down-regulated cone genes can improve or restore photosensitivity in RP. The main findings can be summarised in 6 parts:

1. A missense mutation in exon 6 of *Cngb3* in mice - (NM_013927)c.692G>A; p.(R231H) - results in severely diminished cone function. This *cpfl10* mouse is the first example of a spontaneously occurring *Cngb3* achromatopsia model and provides an improved model for pre-clinical development of molecular therapies to restore cone photosensitivity in equivalent human patients. It is also an example of how disruption of a single gene in the cone phototransduction pathway can impair light sensitivity. This observation supported the subsequent examination of cone phototransduction cascade genes in RP mice in the latter half of the thesis.

2. The $B6^{TgOPN1LW\text{-}EGFP}$ mouse model was characterised in detail and

limitations identified. A detailed timeline of the magnitude and timing of intrinsically declining cone photosensitivity function was established. Furthermore, analysis of the transcriptome showed this loss of photosensitivity was not due to declining gene expression in the cone phototransduction cascade. This thesis also reproduced the previously described sampling bias and cell loss in FACS pre-processing of GFP positive cone photoreceptors.

3. Detailed transcriptome analysis of the $Rho^{-/-\ B6TgOPN1LW\text{-}EGFP+/-}$ mouse model identified that, despite not expressing rhodopsin protein, the model still expresses a rhodopsin mRNA transcript at much lower concentrations. This transcript declines over time and correlates well with ONL loss on OCT. It can be used as a surrogate marker of rod photoreceptor loss and raises questions about the mechanism of the rhodopsin gene disruption.

4. A large qPCR gene expression study of the cone phototransduction cascade was undertaken in $Rho^{-/-\ B6TgOPN1LW\text{-}EGFP+/-}$ mice. The *Crx*, *Opn1sw* and *Opn1mw* genes of the mouse cone phototransduction pathway are substantially and significantly down-regulated. The down-regulation of these genes correlates closely with the phenotypic loss of photopic ERG and photopic OMR function.

5. Two AAV vectors were created that successfully expressed human CRX or OPN1LW *in vitro* in HEK293T cells and *in vivo* in the retinas of $Rho^{-/-\ B6TgOPN1LW\text{-}EGFP+/-}$ and Nrl-L-$EGFP^{+/-}$:$Rho^{-/-}$ mice. Over-expression of *CRX* or *OPN1LW* in this way did not improve or prolong the photopic retinal function of mice, nor did it improve cone photoreceptor survival. Also, transgenic CRX expression in RPE cells did not induce GFP expression or evidence of cell type de-differentiation.

6. It is possible that the previously observed down-regulation in *Crx*, *Opn1sw* and *Opn1mw* gene expression were not causative of declining cone

photosensitivity, but instead both derived from a common cause. Loss of cone photosensitivity in RP appears to be underpinned by a common cause outside the phototransduction cascade, such as oxidative stress or metabolic starvation.

These findings provide important insights into cone photoreceptor function and highlight interesting questions for further research.

8.2 *Cpfl10* mouse model

One of the key findings of the current work is that a single missense mutation in the *Cngb3* gene causes complete loss of photopic retinal function in the newly described *cpfl10* mouse model of achromatopsia. There are two possible explanations for how this recessive missense mutation impairs cone phototransduction.

Firstly, the amino acid substitution at a highly conserved residue may cause mis-folded *Cngb3* protein that fails to localise correctly to the membrane of cone outer segments. Altered trafficking of the mis-folded protein has been described in other models of retinal disease [247], but is typically associated with degeneration. Mislocalisation of CNG channels containing missense mutations has been reproduced in photoreceptors cultures [248]. This mislocalisation causes ER stress and reduced cell viability. However, no evidence of retinal degeneration or cell death was observed in the *cpfl10* mouse model. Alternatively, a mis-folded Cngb3 protein may undergo ubiquitin-mediated protein degradation by the 26S proteasome [249]. The resulting absence of Cngb3 would result in incorrect assembly of CNG channels [4].

Alternatively, the mis-folded *Cngb3* protein may still localise correctly to the membrane of the cone outer segments but may fail to integrate correctly into a heterotetramer unit with Cnga3. The Cngb3 subunit plays a modulatory role in the CNG channel [6, 4] and, without it, the channel does not function correctly.

Despite detailed testing of all commercially available anti-Cngb3 antibodies,

no available antibody identified the Cngb3 protein in retinal sections. Thus, it was not possible to distinguish between the two hypotheses outlined above using IHC results. Collaboration with authors in possession of a privately produced anti-Cngb3 antibody could answer this question [36, 159].

The *cpfl10* mouse model is a striking example of the effect of a single gene in the cone phototransduction cascade impairing cone function when altered. There are two examples where re-expression of the dysfunctional *Cngb3* phototransduction enzyme rescued cone function [165, 36]. There are also other examples of where cone photosensitivity is restored after AAV re-expression of a dysfunctional gene in the cone phototransduction cascade [31, 32]. In some instances, the AAV therapy even halted intrinsic loss of cone photoreceptors [34].

The elegant success of these rescue therapies for cone dysfunction held promise for a similar approach to restoring cone phototransduction in RP by over-expressing cone genes. Furthermore, there has been recent success in rescuing retinal photosensitivity by ectopic expression of opsins; human rhodopsin [102], human melanopsin [103] and halorhodopsin [95]. These findings, taken together, supported the subsequent exploration of cone phototransduction AAV therapies in RP.

8.3 B6$^{TgOPN1LW\text{-}EGFP}$ model techniques and limitations

New observations were made about the B6$^{TgOPN1LW\text{-}EGFP}$ mouse model that have not been previously published. Notably, a new *in vivo* cSLO quantification method for monitoring GFP expressing cones was developed and validated. This approach to image acquisition, image sampling and manual counting was validated on a large cohort of B6$^{TgOPN1LW\text{-}EGFP}$ over time. It demonstrated a robust method for wider use and for later application in the AAV *in vivo* experiments.

The B6$^{TgOPN1LW\text{-}EGFP}$ mouse model is known to possess a dominant cone dystrophy with associated loss of cone photosensitivity [128]. Lipinski et al [128] attributed the loss of function to the insertion of the B6$^{TgOPN1LW\text{-}EGFP}$ allele into the region of the North Caroline macular dystrophy (NCMD) and progressive bifocal chorioretinal atrophy (PBCRA) loci. The original paper identified complete loss of cone function on ERG at PND245.

However, NCMD is a congenital stationary condition in humans [250]. This thesis demonstrates both normal cone function at a young age and a progressive loss of cone function in the B6$^{TgOPN1LW\text{-}EGFP}$ mouse over a period of many months. This is a substantial phenotypic difference from the human disease and makes a progressive condition such as PBCRA more likely. Furthermore, the overlapping effects of the Rho$^{-/-}$ and B6$^{TgOPN1LW\text{-}EGFP}$ alleles on declining cone pathway function in young mice are simultaneous confounding factors. The benefits on *in vivo* cone survival measurements carries the complication of confounding functional impairment.

The qPCR data presented in chapter 4 shows that in the B6$^{TgOPN1LW\text{-}EGFP}$ mouse model, there is no down-regulation of phototransduction genes as cone function is lost. None of the genes of the cone phototransduction cascade have been implicated in either PBCRA [251] or NCMD [252] and this finding is consistent. Exploring the expression of equivalent murine transcription factors on qPCR could identify whether they are down-regulated in the B6$^{TgOPN1LW\text{-}EGFP}$ model.

8.4 Rho$^{-/-}$ mouse rhodopsin transcript

The Rho$^{-/-}$ mouse was characterised and a consistent phenotype was described in chapter 4. The phenotype corroborated other published work [62], but also added a detailed description of declining cone photosensitivity in ERG and OMR testing.

Notably, a rhodopsin transcript was identified in Rho$^{-/-}$ mice that the original

authors had not described [132]. As detailed in Figure 4.9, this signal is very unlikely to be a contaminant signal. The presence of transcript raises questions about the proposed mechanism of recessive disease in $Rho^{-/-}$ mice.

Rhodopsin is expressed in different length isoforms [253], but this does not explain the occurrence of multiple transcript amplified using primers spanning the pol2:neo insertion site. Interestingly, an amplicon was produced using the original RT-PCR primers using by Humphries et al [132]. This could be due to the increased sensitivity of qPCR compared to agarose gels, or it could reflect a genetic recombination event arising in the mouse line since its creation. For example, duplication of some or the rhodopsin locus could have arisen in heterozygotes $Rho^{+/-}$ mice, analogous to the historical formation of the human red-green opsin locus on the X-chromosome. This question could be answered by comparing qPCR results from our local colony with samples obtained from $Rho^{-/-}$ colonies elsewhere. Furthermore, copy number qPCR testing could be performed between the colonies to identify any locus duplication.

If the rhodopsin amplicon (spanning the pol2:neo insertion site) is not a product of a genetic recombination event, then it must arise from post-transcriptional splicing of pre-mRNA. Although the pol2:neo cassette sequence was never published [132], perhaps it contains a splice acceptor site that allows post-transcription removal of most of the cassette interrupting exon 2. This mechanism would still produce an identifiable rhodopsin transcript, but could also result in the observed 1000-fold reduction in transcript levels. However, alternative splicing Nucleotide sequencing of the full rhodopsin-neomycin transcript in $Rho^{-/-}$ mice would shed light on any splicing event.

Regardless of mechanism, this unexpected finding does not change the accepted phenotype (congenital rod blindness, progressive ONL loss and declining cone photosensitivity) of the model. However, it does pose questions about the mechanism underlying the RP phenotype. Could efforts to rescue the $Rho^{-/-}$ phenotype by AAV over-expression of rhodopsin could be complicated by

the persistent expression of this transcript? It is known that over-expression gene therapies are not effective in dominant negative or gain-of-function mutations. However, there is no evidence that this unexpected transcript is translated into a mutated rhodopsin protein. The original authors [132] have never identified a rhodopsin signal on WB or IHC in these mice. Even an alternatively spliced rhodopsin transcript, if translated, should be detectable using the N-terminus rhodopsin antibody 4D2 used by Humphries et al [132]. In the absence of mis-folded protein, the disease mechanisms of dominant negative and gain-of-function are not applicable.

Humphries et al [132] do not report ONL thinning in heterozygote $Rho^{+/-}$ mice, yet the representative IHC in figure 2 of the original paper shows shortened outer segments and ONL thinning in heterozygous $Rho^{+/-}$ mice compared to wt litter-mates. No statistical measures of IHC are provided. An alternative mouse model of RP caused by rhodopsin disruption with a neomycin cassette also reported a slow retinal degeneration in $Rho^{+/-}$ heterozygotes [254]. It is hypothesised that this degeneration reflects a mild haploinsufficiency of rhodopsin that is only clinically relevant in homozygous mutants. This is supported by the observation of a mild phenotype in rhodopsin heterozygotes with a non-functioning allele in humans [255].

The historical origin, mRNA sequence and mechanistic implications of this newly identified mutant rhodopsin transcript in $Rho^{-/-}$ mice require further exploration.

8.5 Cone phototransduction cascade gene expression analysis

The qPCR gene expression study identified an interesting pattern of gene down-regulation in cones of Rho textsuperscript-/- mice. The study could have improved by including additional mouse models of RP such as rd1, P23H and $Pde6h^{-/-}$. However, logistical constraints limited this size and diversity of tissue samples.

The analysis of transcription factor expression was limited to *Crx* because of logistical constraints and the central role of this gene in photoreceptor differentiation. However, in hindsight, a detailed analysis of other related photoreceptor transcription factors may have shown a widespread down-regulation of all genes. Alternatively, it may have identified one or two other transcription factors that needed to be co-expressed with a *CRX* AAV vector.

The cone photoreceptor qPCR gene expression study began with a targeted question in mind. In light of high-throughput next generation sequencing technology, future gene expression studies on other retinal cell populations should utilise RNA-seq technologies. The software required to interpret such high volume data is readily available online. Beginning with the whole picture of the cellular transcriptome offered by RNA-seq technology allows a contextual interpretation of individual gene down-regulation.

8.6 AAV over-expression of CRX

The failure of AAV.*CRX* to rescue cone photoreceptor function or survival in these experiments may have arisen from three sources. As discussed in chapter 4, most of the observed down-regulation in *Crx* could have arisen from rod photoreceptor death. This confounding factor could be excluded by isolating a purified cone population using FACS or — given the substantial sampling bias introduced by the $B6^{TgOPN1LW\text{-}EGFP}$ allele FACS — magnetic assisted cell sorting (MACS) isolation of CD-73 positive cells. The answer from this follow-up experiment would clarify whether the observed down-regulation of *Crx* could still be causative, or was simply correlated, with cone photoreceptor function loss.

Secondly, *Crx* acts in concert with *Nr2e3* or *Nrl* to differentiate rods and modulate gene expression [7]. Similarly, *Crx* interacts with Rorβ2 to modulate S-opsin expression and Trβ2 M-opsin in cones [7]. Transgenic expression of isolated *CRX* may have been less beneficial. Expanding the panel of genes in

the qPCR testing protocol to include these additional transcription factors may give more insight. If appropriate, other down-regulated transcription factors could be packaged bistronically alongside *CRX* in a new AAV vector.

Thirdly, the ability of human CRX to bind upstream promoter sequences in murine cone genes is unknown. Human and murine CRX proteins shares 97% homology, including full homology in the active binding region. However, expressed human *CRX* may not interact correctly with the murine genome. The answer to this question could be examined by treating mice expressing reporter proteins (LacZ or GFP) under control of specific murine cone gene promoters (*Opn1mw*, *Opn1sw*, *Crx* etc). An increase in reporter protein expression after transduction with human *CRX* would confirm interaction across species. Performing ChIP using an antibody specific to human CRX could allow the promoter targeting activity of this homolog to be explored; yet no antibody was found that could clearly differentiate between human and mouse protein.

8.7 AAV over-expression of OPN1LW

8.7.1 Compared to previous human opsin work

The failure of AAV.*OPN1LW* to rescue cone photosensitivity in this thesis differs from earlier work showing a functional benefit from ectopic expression of human melanopsin [103] and human rhodopsin [102]. There are a number of differences between these published studies and the work contained in this thesis that may explain the lack of benefit from the AAV.*OPN1LW* vector.

De Silva et al [103] utilised a similar CAG-driven *WPRE*-augmented human transgene construct, packaged in the same AAV8^{Y733F} capsid mutant. This *OPN4* transgene vector was surgically delivered by subretinal delivery into 6- to 8-week old rd1 mice at a final dose of 1.5×10^9gc in 1.5 μL.

Cehajic-Kapetanovic et al [102] treated rd1 mice with two difference constructs. The first was a similar CAG-driven *WPRE*-augmented human transgene construct. The second construct used a *Grm6* ganglion ON-cell

specific promoter. Both of these human *RHO* constructs were packaged in an AAV2 capsid and delivered by intravitreal injection, alongside glycosidic enzymes that increase transduction efficiency. The *RHO* vector was delivered to 8- to 10- week old rd1 mice at a final dose of 1×10^{13} in 3μL.

Regarding the treatment philosophy, both of these papers aimed to restore some function after the loss of photosensitivity, rather than a rescue strategy directed to prolonging photosensitivity. Both papers using the rapidly-degenerating $Pde6b^{rd1}$ mouse model of RP instead of slower-degenerating $Rho^{-/-}$ mice.

Regarding outcome measures, neither paper relied on functional measures as subtle as ERG; ERG requires organised signal transmission through multiple cell types to achieve a recognisable waveform on the recording [256]. Full-field ERG also requires a large enough region of surviving functional cells to generate a large enough wave amplitude to be identified above background noise. The outcome measures explored cellular evidence of photosensitivity and multi-electrode array recordings were tested in both papers. Photosensitivity electrophysiology was also tested using dLGN electrode physiology [102]; dLGN responses do not require organised signal integration from multiple cell types to register a response like ERG. Neither paper examined cell survival in treated mice as the degeneration of rods in rd1 mice is complete by approximately 4 weeks and cones by 10-12 weeks [62].

It is possible that ectopic expression of human *OPN1LW* in the retinas of blind rd1 mice as part of an optogenetic strategy might also achieve some success. The same CAG-driven *OPN1LW* construct created and validated in this thesis could be tested using either subretinal or intravitreal injections. Treatment effect could be measured using a multi-electrode array to demonstrate cellular photosensitivity and non image-forming functional visual tests such as pupillometry and light-avoidance to show useful photosensitivity.

8.7.2 Compared to previous halorhodopsin work

Busskamp et al [95] showed that AAV-mediated expression of bacterial enhanced halorhodopsin (eNpHR) in the cone photoreceptors of Pde6b^{rd1} and Rho$^{-/-}$ mice restored visual function. eNpHR does not require a downstream signalling pathway like human opsins; it uses all-*trans* retinal and directly hyper-polarises the cell in response to light. This direct independent action is most evident in the restoration of cone responses in the Cnga3$^{-/-}$ Rho$^{-/-}$ double-knockout mice; mice that do not have a functioning cone phototransduction cascade.

Possibly, the transgenic OPN1LW depends upon downstream signalling pathways that were not available in degenerating cone photoreceptors. This could involve any enzyme (Pde6h, Gnat2 etc) of the phototransduction cascade described in subsection 1.1.2. Although the qPCR data in chapter 4 did not show any other enzymes that were significantly down-regulated. Also, ectopic expression rhodopsin and melanopsin in the inner retina ganglion cells successfully generated visual impulses without the typical photoreceptor downstream signalling pathways [102, 103].

8.8 Proximate and ultimate causes of cone dysfunction and death

Declining cone photosensitivity and reduced expression of *Crx*, *Opn1sw* and *Opn1mw* genes have been shown in chapter 4 to be closely correlated. The subsequent failure of over-expression *CRX* and *OPN1LW* AAV gene therapy demonstrated that correction of this declining cone gene expression does not rescue the cone phenotype. These transcriptome and phenotype observations are correlated, not causative. This points towards a common cause underlying the correlated observations of reduced cone photosensitivity and reduced cone gene expression. The ultimate cause of cone death in RP is rod death [94]. This rod cell death induces a proximate common cause that is cone-specific.

Oxidative stress [94, 257, 258], metabolic starvation [94, 62] and the role of trophic factors [82, 259] are three important mechanisms.

8.8.1 Ultimate cause: rod death

Primary rod cell death is the ultimate cause of cone photoreceptor dysfunction and death. Rod photoreceptor mutations may be dominant, recessive, X-linked or sporadic; there are over 70 disease genes associated with RP and over 200 different affected genes are known to cause retinal degenerations RetNet [64]. Dominant RP is most commonly caused by mutations in the rhodopsin gene and in North America the p.P23H missense mutation is most common [12, 58]. Autosomal recessive RP is most commonly caused by mutations in CRB1 or USH2A [58]. X-linked RP is most commonly caused by mutations in RPGR [260]. The multitude of potentially affected genes — and the great number of different mutations within each gene — complicate the development of molecular therapies to rescue rods.

In the autosomal dominant Rho^{P23H} mouse model of RP, AAV-mediated re-expression of wild type mouse rhodopsin does sustain phenotype rescue [261]. In the same P23H mouse model, AAV-mediated expression of codon-optimised mouse rhodopsin coupled with a small interfering RNA (siRNA) successfully blocked mutated P23H rhodopsin RNA. This block-and-replace strategy arrested the loss of rod photosensitivity and maintained normal retinal structure on OCT up to 9 months [262]. Other authors have replicated a more modest treatment effect using block-and-replace in the same model [263] and the P347S model of dominant RP [264]. However, allelic heterogeneity still poses a serious problem for efforts to treat autosomal dominant RP by sequence specific reagents. The cost and time required to develop and validate each individual therapy is substantial. There are also technical limitations in the design of guides and DNA sequences depending upon the target sequence.

In the autosomal recessive $Rho^{-/-}$ mouse model of RP, expression of exogenous human rhodopsin restores approximately 40% of wild type rhodopsin

mRNA levels and RHO immunolabelling [265]. There was regeneration of the rod outer segments on microscopy and partial restoration in ERG function. The treatment effect only persisted for approximately 12 weeks after treatment [265].

Gene therapy to rescue rod photoreceptors in X-linked RP has recently entered clinical trials [260]. However, more work remains to develop rod therapies for all RP. The ability to prolong or rescue cone function would be a common treatment with relevance to all patients with RP phenotype, regardless of molecular mechanism.

8.8.2 Proximate causes

Following rod death, there are cone-specific mechanisms that result in the death and dysfunction of cone photoreceptors. Given that up to 90% cone loss does not reduce visual acuity [266], any approach that can preserve even a small proportion of cones could help prevent up to 1.5 million people worldwide from becoming blind [267].

Oxidative stress and metabolic starvation are two mechanisms that contribute to cone cell death in RP; over-expression of trophic factors have also been shown to contribute to cone survival. Treating any such cone-specific common cause may also reverse or prevent the gene expression changes and phototransduction loss observed in chapter 4.

8.8.2.1 Proximate cause: Trophic factors

A neurotrophic factor is a small signalling molecule, typically a peptide, that supports neuronal growth and survival. Neurotrophic factors have been shown to be altered in some animal models of RP. Changes in CNTF [82], nerve growth factor (NGF) and brain derived neurotrophic factor (BDNF) [259] have all been observed in small studies of single rodent models. A comprehensive expression analysis of all retinal trophic factors has not yet been explored in multiple mouse models of RP using a large-scale transcriptomic approach. Similar to the elegant work of Punzo et al [62], Microarray or RNAseq could provide a comprehensive

analysis of trophic factor expression in RP. A common pattern of trophic factor deficiency or excess across multiple models might identify an appropriate to treatment.

Even without such comprehensive transcriptomic or proteomic observations, a focussed approach to CNTF therapies for RP has already shown pre-clinical success. Gene therapy using CNTF transgene prolongs photoreceptor survival and function when delivered by both adenovirus [79] and AAV vectors [53]. Treatment with exogenous CNTF stimulates regrowth of cone outer segments in the S334ter-3 transgenic rat model of RP [80, 81].

CNTF therapy has already been translated to the clinic. In a prospective sham-controlled multicentre trial (NCT00447993 and NCT00447980), 133 late- or early-stage RP patients received an encapsulated cell technology implant that expresses CNTF [268]. This is the same CNTF-releasing implant trialled in achromatopsia patients [56]. Sustained CNTF delivery was safe, but did not improve the primary outcomes of visual acuity or retinal sensitivity at 12 months [268]. High-dose CNTF therapy did reduce retinal sensitivity at 12 months, but this was reversible with removal of the implant. CNTF therapy increased the thickness of the outer retina on OCT [268], which might be explained by the ability of CNTF to stimulate regrowth of outer segments in rodent models of RP [80, 81].

Potentially, the length of the trial was insufficient to reveal any meaningful benefit in such a slowly-progressing retinal degeneration. A longer follow-up time of 5-10 years may yet reveal a treatment effect. The challenge of selecting meaningful surrogate outcome measures for long-running clinical trials in a slowly progressing retinal disease are a broader challenge in AAV gene therapy trials. As an example of over-coming these challenges, the Oxford group demonstrated the utility of microperimetry testing in monitoring choroideremia progression and response to AAV treatment [65].

8.8.2.2 Proximate cause: Oxidative stress

Oxidative stress plays an important role in the death of cone photoreceptors in RP; the primary evidence comes from work on rod derived cone viability factor (RdCVF). RdCVF protein was originally described at Institut de la Vision, Paris and is encoded by the nucleoredoxin-like-1 (Nxnl1) gene. It is a bifunctional protein with a shorter extracellular and a longer intracellular version [75]. RdCVF-L is expressed in both cone and rod photoreceptors, whereas the shorter spliceoform is only produced in rods [83]. The paralogue RdCVF2 is a second bifunctional protein, encoded by the *Nxnl2* gene, that also plays an important trophic factor role in cone survival in RP; RdCVF2 is also expressed widely in the brain [269].

The thioredoxine RdCVF-L is the long spliceoform of the *Nxnl1* gene and plays an important role in redox functions. Thioredoxins contribute to redox homeostasis by reducing oxidised thiol groups in proteins. The thioredoxin system is a substantial disulphide reductase system consisting of NADPH, thioredoxin reductase (TrxR) and thioredoxin (Trx) [270]. RdCVF-L reduces phosphorylation of the microtubule-binding protein TAU and impairs hydrogen peroxide induced oxidative damage to TAU [84].

The shorter RdCVF form is a trophic factor expressed only by rods, not cones [83]. It promotes aerobic glycolysis in cones through its interaction with the basigin-1 and GLUT1 complex on the surface of cones [83]. It has no thiol reductase activity [83].

Subretinal injections of RdCVF protein rescues cone photoreceptors in the P23H rat model of RP [74]. The RdCVF protein injections were performed at 6, 7 and 8 months of age, resulting in improved cone survival at 9 months of age. Similarly, treatment slowed the decline of photopic ERG function from 4 to 9 months. There was no benefit to rod survival or scotopic retinal function, demonstrating that RdCVF protein provides a cone-specific benefit [74].

Further work confirmed that over-expression of RdCVF and RdCVF2 by AAV

vector injections is beneficial [84]. In both the *rd10* mouse model and the *S334ter* rat model, RdCVF transgene expression rescues photopic ERG. The treatment strategy uses a cell-specific promoter to target Mueller cells as a stable cell population for continued expression of RdCVF during ongoing rod cell death [257].

There is good evidence that AAV.RdCVF would be an appropriate therapy to prolong cone photoreceptor survival. The Institut de la Vision in Paris is working towards a clinical trial of AAV.RdCVF therapy [271]; yet, as of December 2017, no trial is currently listed on the European or US clinical trials registries.

NFE2L2 is a transcription factor involved in regulating anti-oxidant pathways; it shows good promise in early experiments on neurons. It promotes neuronal survival in a degenerative environment [86] and gives a cone survival benefit when expressed by AAV in the rd1 mouse model of RP [85].

An AAV vector expressing *NFE2L2* under control of a ubiquitous CAG promoter could be tested in $Rho^{-/-}$ mice using the same techniques applied to the *CRX* and *OPN1LW* vectors above. A detailed examination of cone cell survival using flat mounts and systematic cell counting — alongside the *in vivo* cSLO cone GFP measurements detailed earlier — could monitor any survival benefit from *NFE2L2* treatment. The cumulative effect of multiple antioxidant therapies could be explored by co-administering such a NFE2L2 vector alongside the AAV.RdCVF vector. Because redox homeostasis has multiple components, a cumulative benefit might be observed when expressing multiple antioxidant transgenes (i.e. NFE2L2 and RdCVF) as a combined therapy.

8.8.2.3 Proximate cause: Metabolic starvation

Punzo et al [62] demonstrated that metabolic starvation contributes to cone photoreceptor death. Large-scale microarray analysis of the retinal transcriptome of the $Pde6h^{-/-}$, $Pde6g^{-/-}$, $Rho^{-/-}$ and P23H mouse models of RP was performed. Samples were collected at multiple stages of rod and cone death kinetics; pathway analysis of this large dataset identified substantial

down-regulation of metabolism and transport genes. The pathway with the most hits (12/195 genes) was the insulin/mTOR pathway [62]. Inhibition of the mTOR pathway induced the same opsin mislocalisation in mice. The GLUT1 and HIF-1α receptors were also shown to be up-regulated — a likely a response to glucose starvation.

This starvation was reversed by exogenous supplementation of insulin, thereby normalising the mTOR signalling pathway [62]. Pde6b$^{-/-}$ receiving daily intraperitoneal injections with insulin over a four-week period had increased survival of LacZ labelled cone photoreceptors. Insulin therapy also reduced the mislocalisation of cone opsins and reduced the up-regulation of HIF-1α. The paper shows that metabolic stress in cones is driven by the poor availability of glucose for cellular metabolic functions. An alternative interpretation offered by the authors is possible suppression of autophagy [62].

The role of metabolic starvation in the death of cone photoreceptors is supported by observations of RdCVF. As well as antioxidant functions, RdCVF also stimulates aerobic glycolysis in cones [94]. As detailed earlier, RdCVF deficiency accelerates cone death in RP rodent models [258]. RdCVF supplementation by direct protein injections [74] or AAV-mediated transgene delivery [84] rescues cones. Isolated RdCVF-L replacement therapy does not rescue cone photoreceptors in RP [257]; good evidence that the antioxidant activity of RdCVF is less important than its metabolic activity in preserving cones.

Basigin-1 (BSG1) was identified as the cell surface receptor that binds the RdCVF ligand using far-Western Blot of cone-enriched chicken embryo cultures [94]. This finding was confirmed in a cellular context using an alkaline phosphatase reporter to highlight RdCVF-BSG1 ligand-receptor interaction [94]. SiRNA silencing of BSG1 receptor expression diminished cone cell survival compared to controls [94].

Addition of RdCVF increases glucose uptake of cone photoreceptors in culture, whilst silencing BSG1 with siRNA reduces glucose uptake [94].

Increasing the glucose concentration of culture media also potentiates the effects of RdCVF in a dose-dependent manner [94]. Finally, lactate dehydrogenase inhibition in culture abolished RdCVF-mediated survival; whereas, inhibition of mitochondrial handling of pyruvate did not affect the RdCVF effect [94]. This was final evidence to demonstrate that RdCVF binds to BSG1 to potentiate GLUT1 activity, induce aerobic glycolysis and prolong cone photoreceptor survival.

The GLUT1 receptor is closely related to the GLUT4 receptor involved in the insulin/mTOR pathway also implicated in cone photoreceptor death [62]. The insulin/mTOR [62] and RdCVF-BSG1 papers [94] both converge on the central importance of metabolic starvation in cone photoreceptor death in RP. Both papers identify the high energetic demands of photoreceptor outer segment turnover as early casualties of starving photoreceptors.

The negative impact of metabolic starvation on cone photoreceptor outer segment formation and opsin localisation is confirmed by the data in this thesis. Down-regulation of *Opn1mw* and *Opn1sw* cone opsin transcripts was observed in $Rho^{-/-\ B6TgOPN1LW\text{-}EGFP+/-}$ mice in chapter 4. Mislocalisation of cone opsin proteins in RP was also observed in chapter 7.

It would be interesting to explore the metabolic starvation hypothesis further in a case-control study of human patients with concurrent RP and insulin-dependent diabetes. What effect would insulin treatment have on cone survival in RP patients? Their cone survival could be regularly assessed *in vivo* using adaptive-optics SLO imaging cell counts in the clinic. Their cone pathway function could be followed using a combination of visual acuity, ERG or contrast-sensitivity tests. The parallel development of diabetic eye disease would have to be monitored to avoid confounding. The cohort should be well matched to control confounding factors such as age, gender and causative mutation. It could be an interesting clinical application of insightful laboratory research that has uncovered the role of metabolic starvation in cone photoreceptor death in RP.

8.9 Concluding remarks

Cone opsins might yet be proven effective for optogenetic therapy in late stage retinal degeneration after photoreceptor loss. However, future therapies for improving or prolonging photopic retinal sensitivity in RP appear unlikely to target the cone phototransduction cascade as attempted in this thesis. The further characterisation and treatment of upstream common causes — oxidative stress, metabolic starvation and trophic factor down regulation — appear more promising. Developing these cone-specific therapies remain important until the wider search for effective genetic and molecular therapies for rod rescue in RP is successful.

APPENDICES

A

MANUSCRIPTS AND ABSTRACTS

YALE JOURNAL OF BIOLOGY AND MEDICINE 90 (2017), pp.543-551.

REVIEW YJBM

Gene Therapy for Color Blindness

Mark M. Hassall[a,b,*], Alun R. Barnard[a,b], and Robert E. MacLaren[a,b]

[a]*Nuffield Laboratory of Ophthalmology, Department of Clinical Neurosciences, University of Oxford, Oxford, UK;* [b]*Oxford Eye Hospital, Oxford University Hospitals NHS Foundation Trust, Oxford, UK*

Achromatopsia is a rare congenital cause of vision loss due to isolated cone photoreceptor dysfunction. The most common underlying genetic mutations are autosomal recessive changes in *CNGA3*, *CNGB3*, *GNAT2*, *PDE6H*, *PDE6C*, or *ATF6*. Animal models of *Cnga3*, *Cngb3*, and *Gnat2* have been rescued using AAV gene therapy; showing partial restoration of cone electrophysiology and integration of this new photopic vision in reflexive and behavioral visual tests. Three gene therapy phase I/II trials are currently being conducted in human patients in the USA, the UK, and Germany. This review details the AAV gene therapy treatments of achromatopsia to date. We also present novel data showing rescue of a *Cnga3*$^{-/-}$ mouse model using an rAAV.CBA.CNGA3 vector. We conclude by synthesizing the implications of this animal work for ongoing human trials, particularly, the challenge of restoring integrated cone retinofugal pathways in an adult visual system. The evidence to date suggests that gene therapy for achromatopsia will need to be applied early in childhood to be effective.

INTRODUCTION

Achromatopsia is a rare (1 in 30,000 to 80,000) congenital visual condition characterized by diminished or absent cone photoreceptor function [1]. Patients have severely reduced visual acuity (~20/200), nystagmus and photophobia [2]. Causative autosomal recessive mutations affect genes of the cone phototransduction cascade, *CNGA3, CNGB3, GNAT2, PDE6H, PDE6C,* (Table 1) [3–8] or the transcription factor *ATF6* [9]. A subset of patients have unidentified causative mutations [10]. Patients typically show complete cone function loss, as shown by absent cone-isolating electroretinogram (ERG†) recordings [2]. An incomplete phenotype occurs more rarely, but is not clearly correlated to the underlying mutation [1]. Achromatopsia affects all three classes of photoreceptor and hence, by definition, relates to genes that are expressed in all cone subtypes, as listed above. Conversely, blue monochromatism, tritanopia, and red-green color blindness (deuteranopia and protanopia) are caused by mutations in genes specific to certain subtypes of cone photoreceptors; an important difference to achromatopsia. The blue cone opsin gene is found on chromosome 7 and the red and green opsins are both on the X-chromosome. For instance, Bornholm disease can affect the green or red opsin gene only, or blue cone monochromatism can affect both [11]. Tritanopia (loss of the S-cone opsin) is rare because unlike the X-linked diseases, a recessive variant requires a mutation on both alleles. More commonly tritanopia results from a dominantly inherited S-opsin mutation that leads to progressive loss of the S-cones, similar to the rod loss caused by rhodopsin gene mutations in retinitis pigmentosa.

*To whom all correspondence should be addressed: Dr. Mark M. Hassall, Nuffield Laboratory of Ophthalmology, Level 6, West Wing, John Radcliffe Hospital, Headley Way, Oxford, UK, OX3 9DU, Tel: +44 1865 234768, Email: mark.hassall@merton.ox.ac.uk.

†Abbreviations: ERG, electroretinogram; bp, base pairs; AAV, adeno-associated Virus; gp, genome particle; OMR, optomotor response; CBA, chicken beta actin; IHC, immunohistochemistry; TKO, triple knock out; fMRI, functional magnetic resonance imaging; *CNTF*, Ciliary Neurotrophic Factor.

Keywords: Gene therapy, Achromatopsia, Gene editing, Cone photoreceptors

Copyright © 2017

Table 1. Summary of the genes known to cause achromatopsia.

Gene	Full name	Location	Gene size (kB)	Exons	CDS length (bp)	First report	Percentage of international cases (Kohl, 2004)	Percent of Netherlands cases (Thiadins, 2009)
CNGB3	cyclic nucleotide gated channel beta 3	8q21.3	170	19	2430	(Kohl, 2000)	47	87
CNGA3	cyclic nucleotide gated channel alpha 3	2q11.2	53	9	2085	(Kohl, 1998)	23	5
GNAT2	G protein subunit alpha transducin 2	1p13.3	16.6	9	1065	(Kohl 2002; Aligianis, 2002)	2	0
PDE6C	phosphodiesterase 6C	10q23.33	69	22	2577	(Chang, 2009)	Undiscovered	Not tested
PDE6H	phosphodiesterase 6H	12p12.3	9.6	4	252	(Kohl, 2012)	Undiscovered	Undiscovered
ATF6	Activating Transcription Factor 6	1q23.3	197.8	17	2013	(Kohl, 2015)	Undiscovered	Undiscovered

A well reported achromatopsia population lived on the South Pacific island of Pingelap [12]. A genetic bottleneck following Typhoon Lengkeki in 1775 created a founder effect and over 10 percent of the island population had complete achromatopsia [13]. The story is notably recorded in *The Island of the Colorblind* by the neurologist and author, Oliver Sacks. The causative cyclic nucleotide gated channel beta 3 subunit (*CNGB3*) gene mutation was subsequently genotyped [13]. *CNGA3* was the first achromatopsia gene to be identified [3] and since then five other autosomal (non-X-linked) genes have been discovered [4–9]. The coding sequences of all the genes causing achromatopsia are under 2,600 base pairs (bp), making them all small enough to package in an adeno-associated Virus (AAV) gene therapy vector [14]. Indeed, phase I clinical trials to treat achromatopsia using an AAV vector to deliver *CNGA3* have already started in Germany (NCT02610582), *CNGA3* in the USA and Israel (NCT02935517), *CNGB3* in the USA (NCT02599922), and *CNGB3* in the UK (NCT03001310) (Table 2).

This review will examine the examples of successful AAV rescue in animal models of achromatopsia, the registered human gene therapy trials and the potential barriers still to be overcome; particularly the reactivation of the dormant retinofugal pathway.

PRE-CLINICAL RESCUE OF ANIMAL MODELS

Eight different animal models of achromatopsia have been treated using AAV vectors utilizing either species-specific or cross-species transgenes. There are also two instances of AAV transgene restoring normal spectral sensitivity in dichromatic or monochromatic animal models. After summarizing these preclinical experiments, we also present original data from our own experience with gene therapy for *Cnga3* achromatopsia in mice.

The first successful restoration of color vision using gene therapy in an animal model of achromatopsia delivered *Gnat2* cDNA to the *Gnat*^{cpfl3} mouse. The transgene was packaged in AAV5 under control of a fragment of human red cone opsin gene promoter that expresses in L/M-cones but not S-cones [15]. The vector was delivered by subretinal injection at a 10^{10} genome particle (gp) dose. Restoration of cone function was demonstrated on light adapted (photopic) electroretinography (ERG) and in a optomotor response (OMR) test. This work showed proof of principle for gene therapy to restore cone function in achromatopsia caused by a naturally occurring missense mutation in *Gnat2*.

Two canine models of *Cngb3* achromatopsia (missense in exon 6 or full deletion of *Cngb3*) were subsequently rescued using a AAV5 vector expressing human *CNGB3* [16]. The transgene was expressed with the same fragment of human red-green opsin promoter (PR2.1). The vector was delivered by transvitreal subretinal injection at a 10^{12} gp dose. Treatment improved both photopic electrophysiological response and functional vision in a photopic maze task. This study was the first to rescue a larger, cone-enriched model of achromatopsia and confirmed that human coding sequence could also rescue an animal model with the orthologous

gene defect. Dogs receiving treatment after a year of age however gained little benefit, which was discussed by the researchers as possibly relating to retinal cone pathway remodeling during the period of visual development.

A *Cnga3* knock-out mouse model had been previously developed by targeted deletion of exon 7 [17]. The first gene therapy rescue of this *Cnga3* mouse model also led to an improvement in cone-isolating ERG test steps and showed improved visually-mediated water maze behavior [18]. This study showed that restored cone signaling was integrated into higher cortical function, not just tectally-mediated optomotor responses.

The *Cnga3* knockout mouse model was rescued using a mouse *Cnga3* transgene under control of a 0.5 kB mouse short wavelength opsin promoter. This was packaged in a mutant $AAV5^{Y719F}$ capsid with $6x10^9$ gp injected into the subretinal space of 2-week-old mice [18]. A modest cone ERG rescue was observed, approximately 40 to 50 percent. The magnitude of the ERG rescue is likely to have been diminished because the mouse blue opsin promoter only expresses in S-cones and a subset of M-cones [19].

To explore this promoter question further, the same research group subsequently rescued a different *Cnga3* mouse model (*cpfl5*) using the ubiquitous chicken beta actin (CBA) promoter [20]. This *cpfl5* mouse model of achromatopsia results from a missense mutation in exon 5 of the *Cnga3* gene. Modified CBA.*Cnga3* vector restored cone ERG responses to 80 percent of the wild type levels three weeks after treatment, more than was gained with the first S-cone promoter [18]. This difference in promoter efficacy in restoring normal electrophysiology to all subpopulations of cones may be a significant factor in the human trials currently underway. The *cpfl5* model of *Cnga3* achromatopsia also had a slow cone degeneration; a phenotype that is also seen in human patients. AAV rescue largely prevented cone degeneration and the transgene rescued disrupted cone opsin trafficking [20].

Work by Pang *et al*. (2012) provides independent confirmation that the CBA promoter drives therapeutic levels of transgene expression in cones. This may be relevant to the RPE65 gene therapy clinical trials which also use the CBA promoter, because RPE65 is expressed in cones in some species [21].

Carvalho *et al*. (2011) explored the therapeutic age window for gene therapy in achromatopsia. A mouse model caused by a premature stop codon was rescued with human *CNGB3* transgene packaged in an AAV8 capsid. The use of a cone arrestin promoter fragment resulted in universal expression in all cone subpopulations, an alternative solution to the use of the ubiquitous CBA promoter. The subretinal vector rescued retinal function, as tested by ERG, at a range of ages, but again there were poor visual responses in mice treated at later ages. This confirmed that there is an optimal therapeutic window at a younger age [22]. The limited benefit at later ages may be a result of slow retinal degeneration in this model or amblyopia. Cone outer segment abnormalities have also been noted in achromatopsia animal models and it has been shown that regenerating the outer segments with intravitreal ciliary neurotrophic factor just before achromatopsia gene therapy may improve the responses significantly in older *Cngb3* deficient mice [23].

Interestingly, a clinical trial using *CNTF* delivered by an encapsulated cell-based device aimed to see if achromatopsia in humans could be improved by a similar mechanism on outer segments found no evidence for improved cone function [24]. This trial showed a decline in rod function, which is a critical issue for an achromatopsia patient fully dependent on rod function. These cells do not generally decline in achromatopsia, although there are rare exceptions [25]. The importance of maintaining baseline rod function following achromatopsia gene therapy creates additional challenges compared to typical cone-rod dystrophies in which there is no residual normal population of cells to maintain.

Two serendipitous discoveries of day blindness in unrelated Awassi sheep flocks in Israel yielded two new large-animal models of *Cnga3* achromatopsia. Both models—a premature stop codon [26] and a missense mutation [27]—were rescued using the same human PR2.1-CNGA3 vector described by Komaromy *et al*. (2010). As expected, photopic ERG was restored. Treated animals were also able to use the restored cone function to navigate a maze in photopic conditions. A mouse *Cnga3* transgene also provided a similar rescue effect [26].

All the above studies delivered the vector by subretinal injection. The outer retina is difficult to target efficiently from intravitreal injections and the risk of off-target transduction of inner retinal cells is increased in an intravitreal approach [28]. Regarding other retinal conditions and the comparison of intravitreal vs subretinal delivery; the optimal details of different cell-type promoters, optimized viral capsid serotypes and target cells-types are beyond the scope of this review.

These animal studies have largely explored if the developing visual pathways of young adults benefit from gene therapy and the evidence suggests that the response to treatment gets less as the visual system matures. There is however evidence that plasticity of the mammalian cone visual pathways exists elsewhere. Two related papers explore cone opsin gene therapy in naive visual systems. Human L-opsin gene therapy produces trichromatic vision in Old World dichromatic adult primates. Multifocal-ERG and modified Cambridge color test show new spectral sensitivity in treated monkeys [29]. Secondly, a vector containing rat M-opsin restored M-cone ERG function in a rat model of congenital S-cone

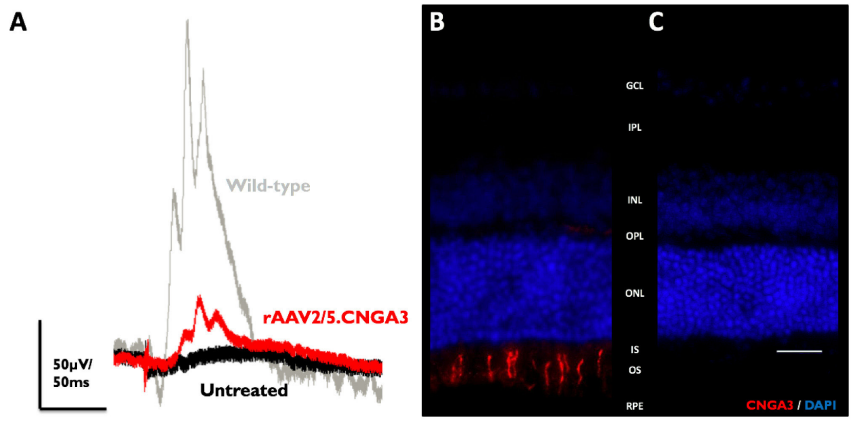


Figure 1. (**A**) Representative photopic ERG traces recorded from CNGA3 (red) treated eye and untreated eye (black trace) of a TKO mouse. The response of an untreated wildtype control is also shown (grey trace). Scale bar is 50µV by 50 ms. (**B**) Immunohistochemical staining for CNGA3 in retinas of TKO mice following injection with rAAV2/5.CBA. CNGA3 but no labelling in an area of distant to the injection in the same eye (**C**). Scale bar 50µM.

monochromatism [30].

These studies in animal models do, however, differ from complete achromatopsia in that both have residual pathways of cone subpopulation function. They therefore presumably have parvo-cellular retinofugal pathways and development of cortical areas such as the blobs in layers 2 and 3 of V1 and the V4 area that mediate color vision [31]. This perhaps proves indirectly that the failure to restore full color vision in the adult achromatopsia models has more to do with re-modelling of the cone visual pathway more than any intrinsic deficiencies in the cone photoreceptors themselves. The implications for human achromatopsia gene therapy are that the treatment will most likely need to be applied in early childhood to be maximally effective.

ORIGINAL DATA ON *CNGA3* RESCUE IN MICE

Mouse models of achromatopsia remain heavily dependent upon rod function and the contribution from the non-image forming melanopsin photoreceptor pathway can also be significant [32]. To isolate any functional vision improvement mediated by cone rescue, we treated a triple knock out (TKO) mouse line that has almost no intrinsic light sensitivity [32]. The mouse is homozygous for targeted mutations in three genes: *Gnat1* (rod-specific alpha transducin), *Opn4* (ganglion cell specific melanopsin) and *Cnga3*. We demonstrated effective cone transduction and rescue of cone ERG following gene therapy with an AAV vector expressing *Cnga3*.

Five to 6-week-old TKO mice received 1µl subretinal injections containing 1 x 10^9 genome particles of rAAV2/5.CBA.CNGA3. The mice received no injection in the fellow eye. Two to 3 months after injection, ERGs were recorded to assess restoration of visual function of transduced retinae *in vivo*. Eyes were removed post-mortem, fixed in 4 percent paraformaldehyde, embedded and sectioned (18 µm) for immunohistochemistry (IHC) to detect and localize CNGA3 protein.

In vivo, treated eyes showed an approximately 20 percent improvement in photopic ERG b-wave amplitude (Figure 1). The restoration of a proportion of visual function in TKO mice shows that *CNGA3* transgene expression acts solely through cone photoreceptors. This is a finding that was not empirically evident from AAV rescue of other achromatopsia models that had other remaining photosensitivity pathways. The functional rescue supported findings by earlier groups that human transgene can successfully rescue mouse models of achromatopsia.

On IHC, the *CNGA3* signal localized to outer segments, with no *CNGA3* signal in the uninjected eyes (Figure 1). This demonstrated effective vector transduction of the cone photoreceptors and correct transport and localization of the transgene. It was interesting to note that Cnga3 staining was not seen in rod photoreceptors, despite use of the ubiquitous CBA promoter. A reason

may be that CNGA3 needs to form a 3:1 tetrameric protein with *CNGB3* to produce a functional cyclic GMP channel [33].

THE HUMAN RETINA IN ACHROMATOPSIA

Achromatopsia fundi are grossly normal. Yet, cone structure and density, as measured with high resolution adaptive-optics SLO, may show subtle changes. Studies of *CNGB3* and *CNGA3* patients show variable foveal appearance on OCT and cone density [34,35]. Notably, patients with *Gnat2* mutations may have almost normal cone density [34,36]. Thus, the causative mutation and cone count may limit the magnitude of any treatment effect and illustrates the overlap between achromatopsia and a slow cone dystrophy. Over half of adult *CNGB3* patients have some degree of foveal hypoplasia. Foveal cone density is less than normal adults, yet cone inner segments remain intact; the cone mosaic pattern is often irregular. Cones also have abnormal reflectance patterns, however, cone density has not been shown to decline with age and is likely a static feature throughout life [35]. This metric is likely not an important influence or barrier to selecting patient age in a trial. The use of intravitreal *CNTF* injections to regenerate cone outer segments as in the animal models may have a role in these patients [23]. One caution is that all these studies on cone mosaics rely on manual quantification by an unreported number of observers. It is unclear if these studies accommodated the inter-observer variability of manual cone mosaic analysis in achromatopsia [37].

Animal models of achromatopsia with cone degeneration show late-stage reduction in rod ERG [20]. However, the scotopic retinal electrophysiology of affected patients is generally normal [38]. Rod photoreceptor electrophysiology is not usually affected in achromatopsia, although there are rare exceptions of *CNGA3* missense changes leading to rod ERG reduction. This is presumed to be due to synaptic changes, since *CNGA3* is not expressed in rods. The canine models of achromatopsia however show normal rod function [16].

In one clinical study, adult patients with congenital achromatopsia viewed photopic and scotopic visual stimuli; functional magnetic resonance imaging (fMRI) recorded the cortical retinotopic representations of foveal function [39]. The study controlled for the effects of achromatopsia nystagmus on vision. Normal controls demonstrated a region of V1 occipital cortex dedicated to the cone-specific fovea. In achromatopsia patients, this same rod-free foveolar representation in the visual cortex was activated by rod-isolating visual tests. Rod visual pathways had monopolized the unused cortical space normally dedicated to cones [39]. Thus, absence of cone visual input during childhood development remodels and re-allocates retinofugal pathways and this fits with psychophysics studies which suggest that achromatopsia patients have faster rates of dark adaptation than normal [40].

ACHROMATOPSIA AND CIRCADIAN RHYTHM

The human circadian rhythm is a roughly 24-hour cycle; the internal body clock. It is endogenously generated, but modulated by external cues, such as light levels. Cones initiate the circadian response to light and melanopsin provides sustained input for ongoing response [41]. Cone photoreceptor electrophysiological response to light also varies by an intrinsic 24-hour cycle [42]. What effect does achromatopsia have on photopic entrainment and the sleep-wake cycle?

No evidence is available for the effect of achromatopsia on circadian rhythm in humans. A small study of patients with red-green color deficiency showed no effect on serum melatonin suppression by light. Melatonin is a signaling molecule secreted in a 24-hr circadian pattern by the pineal gland. It correlates with other markers of circadian rhythm [43]. Yet, mice lacking medium wavelength cones exhibit impaired photopic photo-entrainment and phase shifting [44]. More clinical data from achromatopsia patients is needed to explore circadian disruption.

GENE THERAPY CLINICAL TRIALS FOR ACHROMATOPSIA

As of June 2017, there are four registered clinical trials for gene therapy in achromatopsia, of which three have commenced. All trials use the human transgene driven by cone-specific promoter fragments and packaged in an AAV capsid; details of the vectors and study design are listed in Table 2. All vectors have been previously shown to rescue animal models of achromatopsia. Patients receive delivery of the vector by subretinal injection after vitrectomy. None of the constructs include regulatory elements that increase transgene expression such as WPRE [45] or intron/exon splice sites.

All trials are phase I/II and the primary outcome measure is safety. It is unclear whether the CNG-naive immune system of null mutation achromatopsia patients may react to transgene proteins expressed in the cell membrane. Mutations in *CNGA3* and *CNGB3* account for 70 percent of mutations in human patients; both are channel proteins that insert into the cell membrane. The modest pro-inflammatory stimulus of retinal surgery and viral capsid proteins may potentiate any pro-inflammatory effects of these transmembrane proteins. None of the clinical trials have publicly recorded plans for routine

Table 2. Summary of the publicly registered clinical trials for gene therapy in Achromatopsia.

ClinicalTrials Identifier	Gene	Vector	Capsid	Promoter	Dose	Delivery route	Routine immunosuppression	Locations
NCT03001310	*CNGB3*	AAV2/8-hCARp.hCNGB3	AAV5	Human cone arrestin fragment	Unreported	Vitrectomy + subretinal injection	Unreported	United Kingdom
NCT02610582	*CNGA3*	rAAV.hCNGA3	rAAV8	Potentially, full length red-cone opsin promoter	low dose: ≤ 1x10e10 gp (n=3) intermediate dose: ≤ 5x10e10 vgp (n=3) high dose: ≤ 1x10e11 gp (n=3)	Vit + subretinal injection	Unreported	Tubingham, Germany
NCT02935517	*CNGA3*	rAAV2tYF-PR1.7-hCNGA3 (‘AGTC-402’)	AAV2tYF	PR1.7 (Fragment L-Opsin pr)	Three doses, unspecified	Vit + subretinal injection	Unreported	USA, Israel
NCT02599922	*CNGB3*	rAAV2tYF-PR1.7-hCNGB3	AAV2tYF	PR1.7 (Fragment L-Opsin pr)	Three doses, unspecified	Vit + subretinal injection	Unreported	USA

immunosuppression in treated patients.

Secondary outcomes for the trials include visual acuity, electrophysiology, and color vision function. It is possible that AAV transgene expression may rescue electrophysiology without providing integrated central visual functions like color or acuity. The trials are designed to initially test the safety profile in adult patients, but three of the trials plan to include patients as young as 6 years in later groups. By comparing older and younger patients, the trials will examine differences in integrated functional cone rescue between age groups. If the pattern observed in the animal trials holds true, there may be a difference in benefit due to patient age at time of treatment. Such a difference may arise from reorganization of cortical pathways [39] or foveal hypoplasia [35].

In the one other therapeutic trial registered for achromatopsia (ClinicalTrials.gov number, NCT01648452), six *CNGB3* achromatopsia patients received intraocular implants that released Ciliary Neurotrophic Factor (*CNTF*) [24]. CNTF provides neuroprotection to rod and cone photoreceptors in degenerative retinal disease [46]. Concurrent treatment with intravitreal *CNTF* in a canine model of *CNGB3* achromatopsia potentiated gene therapy rescue. *CNTF* improved ERG rescue in older animals, overcoming a notable inability of gene therapy alone to benefit most dogs over 1 year of age [23]. Limited evidence suggested that *CNTF* pre-treatment de-differentiated the cone photoreceptors by elongating the outer segments to facilitate CNGA3/B3 tetrameric protein assembly. As mentioned above, in the *CNTF* only trial, no functional improvement in cone function occurred. There are no current plans to include *CNTF* pre-treatment in any of the registered human gene therapy trials. This discussion may be reignited if the early trials show difficulty in rescuing cone function in older patients.

CONCLUSION AND OUTLOOK

Animal trials have demonstrated that gene therapy can restore the electrophysiological function of cones. The three most common causative mutations (*Cnga3*, *Cngb3,* and *Gnat2*) have all been rescued, often by multiple groups using different vectors.

There is some evidence that cone density declines with age. This metric is unlikely to affect the therapeutic window. Nonetheless, in a mouse model showing atypical cone degeneration, *Cnga3* re-expression halted cell loss and corrected opsin mislocalization.

The electrophysiological treatment effect is long-lasting; over 180 days in mice and over 3 years in sheep. The effect is maximal in younger animals and more modest in older mice and dogs; making age an important consideration in study design. *CNTF* potentiates cone rescue in animals and is an example of the adjuvant therapies that may be needed to successfully treat older patients.

Optimally, treatment should occur in childhood (under 6 years). Thus, allowing functional cones to direct retinofugal pathway development. In such young patients there would be additional technical challenges to the injection surgery, but a greater potential for integrated functional rescue.

Acknowledgments: Grant support: Rhodes Trust, Fight for Sight, NIHR Oxford Biomedical Research Centre, Royal College of Surgeons of Edinburgh.

Disclosures: The authors have no relevant disclosures relating to achromatopsia.

REFERENCES

1. Michaelides M, Hunt DM, Moore AT. The cone dysfunction syndromes. Br J Ophthalmol. 2004 Feb 1;88(2):291–7.
2. Simunovic MP, Moore AT. The cone dystrophies. Eye . 1998;12 (Pt 3b):553–65.
3. Kohl S, Marx T, Giddings I, Jägle H, Jacobson SG, Apfelstedt-Sylla E, et al. Total colourblindness is caused by mutations in the gene encoding the alpha-subunit of the cone photoreceptor cGMP-gated cation channel. Nat Genet. 1998 Jul 1;19(3):257–9.
4. Kohl S, Baumann B, Broghammer M, Jägle H, Sieving P, Kellner U, et al. Mutations in the CNGB3 gene encoding the beta-subunit of the cone photoreceptor cGMP-gated channel are responsible for achromatopsia (ACHM3) linked to chromosome 8q21. Hum Mol Genet. 2000 Sep 1;9(14):2107–16.
5. Kohl S, Baumann B, Rosenberg T, Kellner U, Lorenz B, Vadalà M, et al. Mutations in the cone photoreceptor G-protein alpha-subunit gene GNAT2 in patients with achromatopsia. Am J Hum Genet. 2002 Aug 1;71(2):422–5.
6. Aligianis IA, Forshew T, Johnson S, Michaelides M, Johnson CA, Trembath RC, et al. Mapping of a novel locus for achromatopsia (ACHM4) to 1p and identification of a germline mutation in the alpha subunit of cone transducin (GNAT2). J Med Genet. 2002 Sep 1;39(9):656–60.
7. Chang B, Grau T, Dangel S, Hurd R, Jurklies B, Sener EC, et al. A homologous genetic basis of the murine cpfl1 mutant and human achromatopsia linked to mutations in the PDE6C gene. Proc Natl Acad Sci U S A. 2009 Nov 17;106(46):19581–6.
8. Kohl S, Coppieters F, Meire F, Schaich S, Roosing S, Brennenstuhl C, et al. A nonsense mutation in PDE6H causes autosomal-recessive incomplete achromatopsia. Am J Hum Genet. 2012 Sep 7;91(3):527–32.
9. Kohl S, Zobor D, Chiang W-C, Weisschuh N, Staller J, Menendez IG, et al. Mutations in the unfolded protein response regulator ATF6 cause the cone dysfunction disorder achromatopsia. Nat Genet. 2015 Jul 1;47(7):757 – +.
10. Mayer AK, Van Cauwenbergh C, Rother C, Baumann B, Reuter P, ACHM Study Group, et al. CNGB3 mutation spectrum including copy number variations in 485 achro-

matopsia patients. Hum Mutat. 2017;38(11):1579-1591.
11. McClements M, Davies WIL, Michaelides M, Young T, Neitz M, MacLaren RE, et al. Variations in Opsin Coding Sequences Cause X-Linked Cone Dysfunction Syndrome with Myopia and Dichromacy. Invest Ophthalmol Vis Sci. 2013 Feb 1;54(2):1361–9.
12. Hussels IE, Morton NE. Pingelap and Mokil Atolls: achromatopsia. Am J Hum Genet. 1972 May;24(3):304–9.
13. Sheffield VC. The vision of Typhoon Lengkieki. Nat Med. 2000 Jul 1;6(7):746–7.
14. Kotterman MA, Schaffer DV. Engineering adeno-associated viruses for clinical gene therapy. Nat Rev Genet. 2014 Jul;15(7):445–51.
15. Alexander JJ, Umino Y, Everhart D, Chang B, Min SH, Li Q, et al. Restoration of cone vision in a mouse model of achromatopsia. Nat Med. 2007 Jun;13(6):685–7.
16. Komáromy AM, Alexander JJ, Rowlan JS, Garcia MM, Chiodo VA, Kaya A, et al. Gene therapy rescues cone function in congenital achromatopsia. Hum Mol Genet. 2010 Apr 8;19(13):2581–93.
17. Biel M, Seeliger M, Pfeifer A, Kohler K, Gerstner A, Ludwig A, et al. Selective loss of cone function in mice lacking the cyclic nucleotide-gated channel CNG3. Proceedings of the National Academy of Sciences. 1999 Jun 22;96(13):7553–7.
18. Michalakis S, Mühlfriedel R, Tanimoto N, Krishnamoorthy V, Koch S, Fischer MD, et al. Restoration of cone vision in the CNGA3-/- mouse model of congenital complete lack of cone photoreceptor function. Mol Ther. 2010 Dec;18(12):2057–63.
19. Akimoto M, Filippova E, Gage PJ, Zhu X, Craft CM, Swaroop A. Transgenic mice expressing Cre-recombinase specifically in M- or S-cone photoreceptors. Invest Ophthalmol Vis Sci. 2004 Jan 1;45(1):42–7.
20. Pang J-J, Deng W-T, Dai X, Lei B, Everhart D, Umino Y, et al. AAV-mediated cone rescue in a naturally occurring mouse model of CNGA3-achromatopsia. PLoS One. 2012 Apr 16;7(4):e35250.
21. MacLaren RE. An analysis of retinal gene therapy clinical trials. Curr Opin Mol Ther. 2009 Oct 1;11(5):540–6.
22. Carvalho LS, Xu J, Pearson RA, Smith AJ, Bainbridge JW, Morris LM, et al. Long-term and age-dependent restoration of visual function in a mouse model of CNGB3-associated achromatopsia following gene therapy. Hum Mol Genet. 2011 Aug 15;20(16):3161–75.
23. Komáromy AM, Rowlan JS, Corr ATP, Reinstein SL, Boye SL, Cooper AE, et al. Transient photoreceptor deconstruction by CNTF enhances rAAV-mediated cone functional rescue in late stage CNGB3-achromatopsia. Mol Ther. 2013 Jun;21(6):1131–41.
24. Zein WM, Jeffrey BG, Wiley HE, Turriff AE, Tumminia SJ, Tao W, et al. CNGB3-Achromatopsia Clinical Trial With CNTF: Diminished Rod Pathway Responses With No Evidence of Improvement in Cone Function. Invest Ophthalmol Vis Sci. 2014 Oct 1;55(10):6301–8.
25. Shaikh RS, Reuter P, Sisk RA, Kausar T, Shahzad M, Maqsood MI, et al. Homozygous missense variant in the human CNGA3 channel causes cone-rod dystrophy. Eur J Hum Genet. 2015 Apr;23(4):473–80.
26. Banin E, Gootwine E, Obolensky A, Ezra-Elia R, Ejzenberg A, Zelinger L, et al. Gene Augmentation Therapy Restores Retinal Function and Visual Behavior in a Sheep Model of CNGA3 Achromatopsia. Mol Ther. 2015 Sep;23(9):1423–33.
27. Gootwine E, Abu-Siam M, Obolensky A, Rosov A, Honig H, Nitzan T, et al. Gene Augmentation Therapy for a Missense Substitution in the cGMP-Binding Domain of Ovine CNGA3 Gene Restores Vision in Day-Blind Sheep. Invest Ophthalmol Vis Sci. 2017 Mar 1;58(3):1577–84.
28. MacLaren RE, Bennett J, Schwartz SD. Gene Therapy and Stem Cell Transplantation in Retinal Disease: The New Frontier. Ophthalmology. 2016 Oct 1;123(10S):S98–106.
29. Mancuso K, Hauswirth WW, Li Q, Connor TB, Kuchenbecker JA, Mauck MC, et al. Gene therapy for red-green colour blindness in adult primates. Nature. 2009 Jan 1;461(7265):784–U34.
30. Zhang Z, Pang J, Xia F, Guo Q, Li L, An J, et al. AAV-mediated Gene Therapy Restores Cone Function In A Rat With An M-cone Opsin Deficiency, A Model For Blue Cone Monochromacy. Invest Ophthalmol Vis Sci. 2011 Apr 22;52(14):1403–1403.
31. Zeki S, Bartels A. The clinical and functional measurement of cortical (in)activity in the visual brain, with special reference to the two subdivisions (V4 and V4 alpha) of the human colour centre. Philos Trans R Soc Lond B Biol Sci. 1999 Jul 29;354(1387):1371–82.
32. Hattar S, Lucas RJ, Mrosovsky N, Thompson S, Douglas RH, Hankins MW, et al. Melanopsin and rod-cone photoreceptive systems account for all major accessory visual functions in mice. Nature. 2003 Jan 1;424(6944):76–81.
33. Peng C, Rich ED, Varnum MD. Subunit configuration of heteromeric cone cyclic nucleotide-gated channels. Neuron. 2004 May 13;42(3):401–10.
34. Dubis AM, Cooper RF, Aboshiha J, Langlo CS, Sundaram V, Liu B, et al. Genotype-dependent variability in residual cone structure in achromatopsia: toward developing metrics for assessing cone health. Invest Ophthalmol Vis Sci. 2014 Oct 2;55(11):7303–11.
35. Langlo CS, Patterson EJ, Higgins BP, Summerfelt P, Razeen MM, Erker LR, et al. Residual Foveal Cone Structure in CNGB3-associated Achromatopsia. Invest Ophthalmol Vis Sci. 2016 Aug 1;57(10):3984–95.
36. Ueno S, Nakanishi A, Kominami T, Ito Y, Hayashi T, Yoshitake K, et al. In vivo imaging of a cone mosaic in a patient with achromatopsia associated with a GNAT2 variant. Jpn J Ophthalmol. 2017 Jan;61(1):92–8.
37. Abozaid MA, Langlo CS, Dubis AM, Michaelides M, Tarima S, Carroll J. Reliability and Repeatability of Cone Density Measurements in Patients with Congenital Achromatopsia. Adv Exp Med Biol. 2016;854(Chapter 37):277–83.
38. Zobor D, Werner A, Stanzial F, Benedicenti F, Rudolph G, Kellner U, et al. The clinical phenotype of CNGA3-related achromatopsia: Pretreatment characterization in preparation of a gene replacement therapy trial. Invest Ophthalmol Vis Sci. 2017 Feb 1;58(2):821–32.
39. Baseler HA, Brewer AA, Sharpe LT, Morland AB, Jägle H, Wandell BA. Reorganization of human cortical maps caused by inherited photoreceptor abnormalities. Nat Neurosci. 2002 Apr 1;5(4):364–70.

40. Aboshiha J, Luong V, Cowing J, Dubis AM, Bainbridge JW, Ali RR, et al. Dark-Adaptation Functions in Molecularly Confirmed Achromatopsia and the Implications for Assessment in Retinal Therapy Trials. Invest Ophthalmol Vis Sci. 2014 Oct 1;55(10):6340–9.
41. Dollet A, Albrecht U, Cooper HM, Dkhissi-Benyahya O. Cones are required for normal temporal responses to light of phase shifts and clock gene expression. Chronobiol Int. 2010 Jun;27(4):768–81.
42. Cameron MA, Barnard AR, Hut RA, Bonnefont X, van der Horst GTJ, Hankins MW, et al. Electroretinography of wild-type and Cry mutant mice reveals circadian tuning of photopic and mesopic retinal responses. J Biol Rhythms. 2008 Dec;23(6):489–501.
43. Ruberg FL, Skene DJ, Hanifin JP, Rollag MD, English J, Arendt J, et al. Melatonin regulation in humans with color vision deficiencies. J Clin Endocrinol Metab. 1996 Aug;81(8):2980–5.
44. Dkhissi-Benyahya O, Gronfier C, De Vanssay W, Flamant F, Cooper HM. Modeling the role of mid-wavelength cones in circadian responses to light. Neuron. 2007 Mar 1;53(5):677–87.
45. Patrício MI, Barnard AR, Orlans HO, McClements ME, MacLaren RE. Inclusion of the Woodchuck Hepatitis Virus Posttranscriptional Regulatory Element Enhances AAV2-Driven Transduction of Mouse and Human Retina. Mol Ther Nucleic Acids. 2017 Mar 17;6:198–208.
46. Lipinski DM, Barnard AR, Singh MS, Martin C, Lee EJ, Davies WIL, et al. CNTF Gene Therapy Confers Lifelong Neuroprotection in a Mouse Model of Human Retinitis Pigmentosa. Mol Ther. 2015 Aug 1;23(8):1308–19.

Abstract

Submitted Nov 2017 **Hassall M M**, McClements M, Barnard A R, Aslam S A MacLaren R E. E-abstract. Assessment of adjunctive gene therapy to dormant cones in end-stage retinitis pigmentosa. ARVO conference 2018

Purpose: It is well known that residual 'dormant' cone photoreceptors remain in patients with Retinitis Pigmentosa (RP), long after cone photosensitivity is extinguished. It has also been shown by others that behavioural light responses may be restored by expressing Halorhodopsin (a bacterial chloride channel) in these cells. We sought to determine if a human protein normally present in cones might achieve the same aim. We therefore sought first to determine which genes encoding proteins in the phototransduction cascade were down regulated in dormant cones of the rhodopsin knockout mouse retina and second to see if over-expressing these genes might restore some light responses.

Methods: Opn1 and Crx were found to be significantly downregulated compared with other genes Plasmid vectors containing either CRX or OPN1LW cDNA under control of the ubiquitous CAG promoter were used to produce AAV2/8.CAG.CRX.WPRE.pA (AAV.CRX) or AAV2/8.CAG.OPN1LW.WPRE.pA (AAV.OPN). Rho-/- mice that expressed GFP in cones (n=105) received subretinal injections in one eye at PND21; the fellow eye was left as an uninjected control. Treated eyes received 1.5L of either AAV.CRX (1x109, 1x108 or 1x107 gc), AAV.OPN (1x108 or 1x107gc) or PBS sham. Mice were repeatedly assessed over the subsequent four months using optical coherence tomography (OCT), scanning laser ophthalmoscope (SLO), electroretinography (ERG) and optomotor response (OMR). Eyes were collected at multiple timepoints (PND42, PND63, PND105 and PND135) for qPCR, IHC or WB. qPCR primers were optimised to differentiate between human and murine targets; antibodies did not distinguish between interspecies homology.

Results: The AAV.CRX vector expressed transgene mRNA in injected eyes

at PND42 and demonstrated CRX staining in the nuclei of photoreceptors and the inner retina; expression appeared dose-dependent. The AAV.OPN vector expressed transgene mRNA in injected eyes at PND42 and OPN1LW in the outer segments and RPE cells. Neither AAV construct improved cone-pathway ERG photosensitivity 3 weeks after treatment ($p<0.001$), despite transgene expression. Neither AAV treatment significantly prolonged ERG photosensitivity beyond PND84 ($p<0.001$), at which time cone function is extinguished in the untreated eye. OMR function in photopic conditions at PND98 was also not improved by either treatment ($p<0.05$). IHC and repeated In vivo SLO measurements of cone signal GFP over time did not show any benefit to cone survival. The higher doses of both vectors were associated with retinal damage and loss of the outer retina.

Conclusions: CRX and OPN1LW were found to be downregulated in the cone photoreceptors in end-stage Rho-/- mice. Re-expression of these genes did not however lead to improved cone function on ERG or OMR, nor prolonged cone survival. The positive responses to Halorhodopsin may therefore represent the fact that a channel protein does not need second messenger systems, which may also be compromised in cones in end-stage RP.

Abstract

Hassall M M, Barnard A R, Charbel Issa P, Aslam S A MacLaren R E. An improved mouse model of complete achromatopsia for development of Cngb3 gene therapies. EuRetina conference 2017

Purpose: We identified a colony of inbred mice with complete achromatopsia and hypothesised that a novel genetic mutation was responsible. A local colony of inbred mice (129S6/SvEvTac origin), that had been bred in isolation for over a decade, were found to have completely absent light-adapted electroretinogram (ERG) responses. We investigated the inheritance and genetic basis of this phenotype of cone photoreceptor function loss (cpfl).

Methods: We performed dark- and light-adapted electroretinography (ERG) to assess retinal function. An affected 129S6/SvEvTac colony animal was outcrossed to a wild-type C57BL/6J mouse to produce first filial generation hybrid offspring (F1). The F1 animals were intercrossed to investigate inheritance in the F2 generation. Chi-squared test with Yates's continuity correction was used for statistical analysis of phenotypic outcomes. Genomic DNA was extracted from several mice and fluorescent dideoxynucleotide sequencing was performed on particular genes known to cause a similar cpfl phenotype and/or identified as causing achromatopsia in humans (Gnat2, Cnga3, Cngb3, Pde6c Hcn1, Syne2). The eyes of a subset of animals underwent histological sectioning and cone arrestin immunostaining.

Results: All founder colony animals tested lacked cone pathway function by ERG testing (n= 9), although rod pathway based ERG responses remained unaffected. None of the C57BL/6 outcross F1 progeny displayed a deficit in cone ERG function (n = 15). However, several animals in the F2 generation showed the original cpfl phenotype, indicating a recessive inheritance pattern. Targeted re-sequencing revealed that the colony did not carry any of the spontaneous mutations previous found in other inbred lines. Instead a novel missense

mutation was identified in exon 6 of the Cngb3 gene, which causes an amino acid substitution at a highly conserved residue. Genotyping of the F2 generation found that, out of 59 animals tested: 15 were wildtype, 29 were heterozygous and 15 were homozygous for the novel Cngb3 mutation. These numbers were not significantly different from the expected genotypic ratio ($X = 0.9745$, $df = 2$, $p = 0.6143$). All mice homozygous for the mutation demonstrated the achromatopsia phenotype. Ocular imaging (cSLO and OCT) showed no obvious retinal degeneration or other anatomical problems. Histological sectioning and IHC for Cone Arrestin showed normal retinal architecture and cone cell morphology.

Conclusions: The existing mouse model of Cngb3 achromatopsia is a knock-out with partial cone function. Our model demonstrates a novel missense mutation and complete achromatopsia. This absolute absence of cone function makes this mouse an optimal model for future pre-clinical development of therapies. It will also be an important resource to further explore the reason for the functional difference between complete and incomplete achromatopsia.

Abstract

Barnard AR, **Hassall M M**, Charbel-Issa P, Aslam S A MacLaren RE. A missense change in Cngb3 causes achromatopsia in a naturally occurring mouse model. Oxford Ophthalmological Congress, UK, June 2017

The full copy of this abstract is no longer available on the Oxford Ophthalmological Congress website. However, a copy of the poster presented at the conference is available below:

A missense change in *Cngb3* causes achromatopsia in a naturally occurring mouse model.

Alun R. Barnard[1,2], Mark M. Hassall[1], Peter Charbel Issa[1,2], Robert E. MacLaren[1,2,3].

1. Nuffield Laboratory of Ophthalmology, Nuffield Department of Clinical Neurosciences, University of Oxford, Oxford, UK.
2. Oxford Eye Hospital, Oxford University Hospitals NHS Foundation Trust, Oxford, UK.
3. Moorfields Eye Hospital, NHS Foundation Trust, London, UK.

Background & Purpose

A local colony of inbred mice (129S6/SvEvTac origin), previously bred in isolation for over a decade, were found to have completely absent light-adapted electroretinogram (ERG) responses. We investigated the inheritance and genetic basis of this cone photoreceptor function loss (cpfl) phenotype.

Methods

We performed electroretinogram (ERG) testing using an Espion E3 system. An affected 129S6/SvEvTac colony animal was outcrossed to a wild-type C57BL/6J mouse to produce first filial generation hybrid offspring (129SB6F1). The 129SB6F1 animals were intercrossed to investigate inheritance in the F2 generation. Targeted re-sequencing was performed on genes known to cause a cpfl phenotype and/or identified as causing achromatopsia in humans (Gnat2, Cnga3, Cngb3, Pde6c, Hcn1, Syne2). Selected eyes underwent histological sectioning and cone arrestin immunostaining.



Figure 1. The inbred strain originates from a pigmented, agouti 129S6/SvEvTac colony (A). ERG testing was performed using an Espion E3 with colourdome light stimulator (B). The clinical system is modified to improve mouse testing.

Results

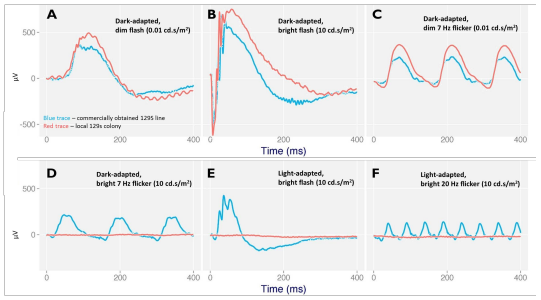


Figure 2: Electroretinogram (ERG) recording and the cone photoreceptor function loss (cpfl) phenotype of the inbred line. Dark-adapted dim flash (A), dark-adapted, bright flash (B) and dark-adapted, dim 7 Hz flicker (C) ERG responses are present and appear normal in the inbred line. These responses are derived primarily from rod photoreceptor pathways in the retina or from a combination of rod and cone pathway activation. ERG responses to dark-adapted, bright 7 Hz flicker (D), light-adapted, bright flash (E) and light-adapted, bright 20 Hz flicker (F) are completely absent in the locally inbred line. These later responses are normally driven by retinal cone pathway activation. In all graphs the blue trace represents a commercially obtained control mouse and the red trace represents an individual from the local inbred colony.

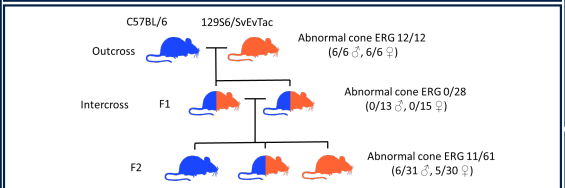


Figure 3: Selected breeding of the inbred colony (outcross-intercross) suggests a recessive, monogenic inheritance pattern to the cpfl phenotype. When a selected, affected animal is crossed with an unrelated wildtype (outcross), no offspring (F1) tested show the original phenotype. When to unaffected F1 mice are bred (intercross) approximately a quarter of the resultant offspring (F2) that are tested show the original cpfl phenotype.

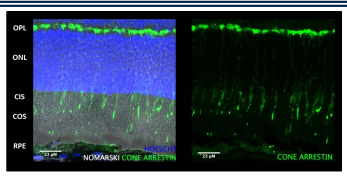


Figure 4: Despite the absence of cone-pathway retinal function, cones are present and have normal morphology in the inbred line. The eye from a selected affected animal has been processed to identify cone photoreceptors by cone arrestin immunostaining (green). The image on the left shows the transmitted light channel (Nomarski) and a blue nuclear counterstain (Hoescht). For clarity, the image on the right shows the green arrestin immunostaining only.

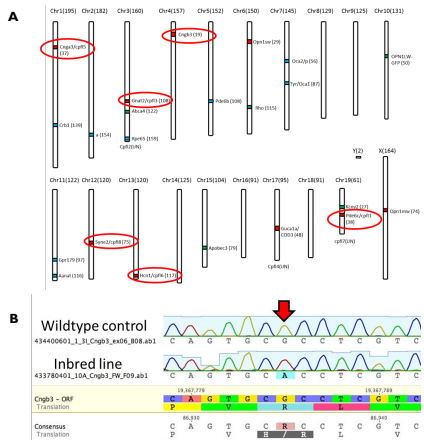


Figure 5: The mutation causing the cpfl phenotype was identified through targeted resequencing. A number of genes that cause a similar phenotype in existing mouse models lines or cause achromatopsia in humans were selected for targeted resequencing in affected mice. These genes are shown in their approximate chromosomal locations in A. Coding exons and flanking intronic sequence was amplified and Sanger sequenced. A number of single nucleotide polymorphisms and/or synonymous mutations were found in the inbred line when compared to reference sequence, however, the mutations causing a similar phenotype in other inbred lines were not found. Instead, a novel missense mutation in the *Cngb3* gene was identified (B).

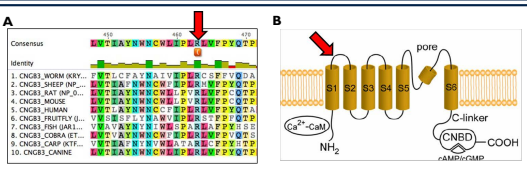


Figure 6: The identified mutation leads to a substitution of a residue that is perfectly conserved across species and resides in a region that influences cation channel opening. Together with CNGA3, CNGB3 forms the cation channel that is essential for cone phototransduction. The identified mutation changes an arginine residue to a histidine. Although a conservative change, the amino acid sequence alignment across several species (A) shows that this particular residue is invariable an arginine. The residue is located within the S1 domain (B, modified from Podda & Grassi, 2014), which regulates channel opening and influences agonist efficacy.

Significance

We have identified a novel missense mutation in the *Cngb3* gene, which results recessive inheritance of cone pathway function loss in mice. In humans, *CNGB3* achromatopsia due to missense changes presumably result in production of a non-functional protein in cones, rather than a complete absence. Hence, this naturally occurring achromatopsia mouse model may closely represent this aspect of the human disease and may be a informative model to assess the potential effects of *CNGB3* gene therapy.

Nuffield Department of Clinical Neurosciences
FMRIB NLO DCN NDA
THE RHODES SCHOLARSHIPS
The Royal College of Surgeons of Edinburgh

Abstract

Hassall M M, McClements ME, Barnard AR, Aslam SA and MacLaren RE. Gene therapy for cone photoreceptor rescue in a mouse model of retinitis pigmentosa, Oxford Ophthalmological Congress, UK, June 2017 *(Presentation and Poster)*

Introduction: We hypothesised that there is a loss of cone photosensitivity that precedes cone cell death, resulting in a subpopulation of 'dormant' cone photoreceptors that could be reactivated through molecular therapies. We aimed to correlate changes in cone-specific gene expression on qPCR with phenotypical changes in cone function in a mouse model of RP, thereby identifying candidates for subsequent gene therapy trials.

Methods: The Rhodopsin knockout (Rho-/-) mouse model of RP was examined using Optical Coherence Tomography (OCT), Scanning Laser Ophthalmoscopy (SLO) and Electroretinography (ERG). The neural retina from Rho-/- mice and wild type controls were collected across five time-points. Each retinal transcriptome was extracted and converted to cDNA. Primers for qPCR were designed to eight genes involved in the mouse cone phototransduction cascade: Opn1mws, Opn1sws, Arr3, Crx, Pde6h, Cnga3, Cngb3 and Gnat2.

Results: In the WT mice, regression analysis showed cone-specific gene expression levels were significantly higher in all genes except Cngb3. Furthermore, the rate of decline in cone gene expression between Rho-/- and WT mice was significantly faster in all genes but Cngb3. The magnitude of overall difference and temporal change was greatest in Opn1sws and Crx genes.

Discussion: The results of the gene expression analyses correlated with the phenotypic observations. The magnitude of gene expression change suggested that Crx and cone opsins are appropriate candidates for future gene therapy attempts to restore photosensitivity in dormant cone cells in RP.

Abstract

Hassall M M, A new mouse model of achromatopsia that more closely resembles the human condition, Oxford-Bristol-Cardiff-Southampton Ophthalmology meeting, Southampton, UK, June 2017

Presentation arranged without abstract submission; invited presentation via Professor Robert MacLaren.

Abstract

Hassall M M, McClements ME, Barnard AR, Aslam SA and MacLaren RE. Crx and Cone Opsins are candidates for gene therapy in a mouse model of Retinitis Pigmentosa, ARVO, Baltimore, USA, May 2017

Purpose: It has been observed that residual cone photoreceptors remain in human patients with retinitis pigmentosa (RP) long after cone photosensitivity is extinguished. We hypothesised that there is a loss of cone photosensitivity that precedes cone cell death, resulting in a subpopulation of 'dormant' cone photoreceptors that could be reactivated through molecular therapies. We aimed to correlate changes in cone-specific gene expression on qPCR with phenotypical changes in cone function in a mouse model of RP, thereby identifying candidates for subsequent gene therapy trials.

Methods: The Rhodopsin knockout (Rho -/-) mouse model of RP was examined using Optical Coherence Tomography (OCT), Scanning Laser Ophthalmoscopy (SLO) and Electroretinography (ERG). Five time-points for qPCR were then chosen correlating to: 1) early rod degeneration; 2) the peak of rod cell death on OCT; 3) the beginning of cone cell death on SLO; 4) the loss of cone photosensitivity on ERG and 5) an advanced stage of degeneration. The neural retina from Rho-/- mice and wild type controls were collected across these five time-points (n=5 per time point). Each retinal transcriptome was extracted and converted to cDNA. Primers for qPCR were designed to eight genes involved in the mouse cone phototransduction cascade: Opn1mws, Opn1sws, Arr3, Crx, Pde6h, Cnga3, Cngb3 and Gnat2. All primer sets were optimised to achieve 90-100% efficiencies and all target gene values were normalised to Bactin.

Results: In the WT mouse, cone-specific gene expression levels were stable across all time points except for a gradual decline in Pde6h and a small decline in Opn1sws expression between 17 and 25 weeks of age. Crx revealed a steep

increase in expression levels between 6 and 17 weeks with a further increase between 17 and 25 weeks. By contrast, in Rho -/- mice all genes assessed decreased in expression over time ($p<0.05$). The biggest overall decline was observed between 6 and 12 weeks and was particularly apparent in Pde6h (though this was equivalent to that observed in WT), Opn1sws and Crx.

Conclusions: The results of the gene expression analyses correlated with the phenotypic observations and suggested that Crx and cone opsins are appropriate candidates for future gene therapy attempts to restore photosensitivity in dormant cone cells in RP.

Abstract

Barnard A R, **Hassall M M**, Charbel-Issa P and MacLaren RE. A spontaneously occurring mouse model of complete achromatopsia due to a missense mutation in Cngb3. ARVO, Baltimore, USA

Purpose: A local colony of inbred mice (129S6/SvEvTac origin), that had been bred in isolation for over a decade, were found to have completely absent light-adapted electroretinogram (ERG) responses. We investigated the inheritance and genetic basis of this phenotype of cone photoreceptor function loss (cpfl).

Methods: We performed ERG testing using a modified Espion E3 system. An affected 129S6/SvEvTac colony animal was outcrossed to a wild-type C57BL/6J mouse to produce first filial generation hybrid offspring (129SB6F1). The 129SB6F1 animals were intercrossed to investigate inheritance in the F2 generation. Genomic DNA was extracted from several mice and targeted re-sequencing was performed on particular genes known to cause a similar cpfl phenotype and/or identified as causing achromatopsia in humans (Gnat2, Cnga3, Cngb3, Pde6c Hcn1, Syne2). The eyes of a subset of animals underwent histological sectioning and cone arrestin immunostaining.

Results: All 129S6/SvEvTac colony animals tested lacked cone pathway function by ERG testing (n= 12), although rod pathway based ERG responses remained unaffected. None of the C57BL/6 outcross F1 progeny (129SB6F1) displayed a deficit in cone ERG function (n = 28). However, several animals in the F2 generation showed the original cpfl phenotype, indicating a recessive inheritance pattern. Targeted re-sequencing revealed that the colony did not carry any of the spontaneous mutations previous found in other inbred lines. Instead a novel missense mutation was identified in exon 6 of the Cngb3 gene, which causes an amino acid substitution at a highly conserved residue. Genotyping of the F2 generation found that, out of 59 animals tested: 15 were

wildtype, 29 were heterozygous and 15 were homozygous for the novel Cngb3 mutation. These numbers were not significantly different from the expected 1:2:1 genotypic ratio (X = 0.9745, df = 2, p = 0.6143). Animals that had normal cone ERG response were invariably either wildtype or heterozygous for the Cngb3 mutation, whereas all F2 animals that showed the cpfl phenotype were homozygous for the Cngb3 mutation. Histological analysis showed an absence of gross retinal degeneration and the presence of cone photoreceptors with normal cell morphology in the original colony and all subsequent crosses.

Conclusions: We identified the spontaneous occurrence of cone pathway function loss in an isolated line of inbred mice. Taken together, our result indicate that this is caused by a novel mutation in the Cngb3 gene, with a fully recessive inheritance pattern. Interestingly, the Cngb3 knock-out mouse model still retains partial cone function, whereas our novel missense mutation leads to a complete abolition of cone function. Understanding the basis of this difference may prove crucial in the future development of therapies for achromatopsia.

Abstract

Hassall M M, Barnard AR, Charbel-Issa P and MacLaren RE. An improved mouse model of achromatopsia for pre-clinical development of gene therapies. FLOREtina conference, Italy, 2017

Introduction We identified a colony of inbred mice with complete achromatopsia and hypothesised that a novel genetic mutation was responsible. Test crossing, electrophysiological testing and candidate gene sequencing were used to investigate the inheritance pattern and genetic cause of the phenotype. A recessive missense mutation was identified in Cngb3 causing complete loss of cone function.

Methods We performed dark- and light-adapted electroretinography (ERG) to assess retinal function. Genomic DNA was extracted from tail tissue of mice and genotyped using commercial fluorescent dideoxynucleotide sequencing. Chi-squared test with Yates's continuity correction was used for statistical analysis of phenotypic and genotypic outcomes.

Results Affected mice had absent light-adapted ERG response. DNA sequencing of genes important for cone phototransduction and function revealed a missense mutation in exon 6 of the Cngb3 gene, which causes an amino acid substitution at a highly conserved residue. 100% of affected mice (n = 16) were homozygous for the mutation ($X2 = 28.15$, $p < 0.0001$). Mice that were heterozygous for the mutation did not exhibit achromatopsia.

Ocular imaging (cSLO and OCT) showed no obvious retinal degeneration or other anatomical problems. Histological sectioning and IHC for Cone Arrestin showed normal retinal architecture and cone cell morphology.

Conclusions The only existing mouse model of Cngb3 achromatopsia is a knock-out with partial cone function. Our model demonstrates a novel missense mutation and complete achromatopsia. This absolute absence of cone function makes this mouse an optimal model for future pre-clinical development of

therapies.

Abstract

Hassall M M, Barnard A, Charbel-Issa P and MacLaren R, The 129S6/SvEvTac mouse strain exhibits achromatopsia and abnormal cone morphology unrelated to Cnga3, Oxford Ophthalmological Congress, UK, 2016.

Introduction: We observed that a colony of inbred mice (129S6/SvEvTac) had poor visual responses after light-adaption and hypothesised that a new genetic mutation was present. Vision was assessed by electroretinogram (ERG) recording. Cross-breeding was used to investigate the inheritance pattern and genetic basis of the achromatopsia.

Methods: We performed dark- and light-adapted electroretinogram (ERG) testing on anesthetized animals (ketamine xylazine) using a modified Espion E3 system. Animals of both sexes were tested from the 129S6/SvEvTac colony, progeny of a C57B/6 outcross and progeny from an outcross with a Cnga3 knock-out mouse.

Results: All 129S6/SvEvTac colony animals that were tested lacked cone pathway function by ERG testing (n = 12). The C57BL/6 outcross F1 progeny all displayed normal cone function (n = 21). All F1 progeny from the Cnga3 complementation test showed intact cone ERG function (n = 10). Immunohistochemistry shows dysmorphic cone photoreceptors.

Discussion: We have identified a spontaneous occurrence of achromatopsia. Rod pathway function remains normal. It is likely an autosomal recessive inheritance pattern, but we have excluded any involvement of Cnga3, a gene that is commonly mutated in human achromatopsia. We have also demonstrated abnormal cone morphology. 129SB6F1 intercrossing is currently underway to confirm the inheritance pattern of the phenotype and allow the underlying mutation to be mapped and identified. Identification of new candidate genes and mouse models is important, as the genetic basis of some forms of human achromatopsia remains unknown.

Abstract

Hassall M, Barnard AR, Issa PC, Maclaren R. Identification of a potential new mouse model of chromatopsia through spontaneous occurrence of cone pathway function loss. Invest Ophthalmol Vis Sci. 2016;57(12):644–644.

Purpose: We noticed that a particular colony of inbred mice (of 129S6/SvEvTac origin) had poor light-adapted visual responses and hypothesised that a novel genetic mutation was responsible. Retinal function was assessed by electroretinogram (ERG) recording. Test crossing was used to investigate the inheritance pattern and genetic basis of the phenotype.

Methods: We performed dark- and light-adapted electroretinogram (ERG) testing on anesthetized animals (ketamine xylazine) using a modified Espion E3 system. 129S6/SvEvTac colony animals of both sexes were tested, at ages of post-natal day (PD) 28 to 56. An affected 129S6/SvEvTac colony animal was outcrossed to a commercially obtained, wild-type C57BL/6J mouse. All first filial generation hybrid offspring (129SB6F1) from this out-cross (n=15) underwent ERG testing at PD 36 to 64. An affected 129S6/SvEvTac animal was outcrossed with a homozygous targeted knock-out for a common achromatopsia causing gene (Cnga3-/-). All offspring of this complementation test cross (n=10) underwent ERG testing at PD 46 to 75. Chi squared test with Yates's continuity correction was used for statistical analysis of phenotypic outcomes..

Results: All 129S6/SvEvTac colony animals that were tested lacked cone pathway function by ERG testing (n = 9), although dark-adapted, rod-pathway based ERG responses remained intact. None of the C57BL/6 outcross F1 progeny (129SB6F1) displayed a deficit in cone ERG function (n = 15), demonstrating the phenotype is likely to be recessive ($X2 = 26.1$, $p < 0.005$). 129SB6F1 offspring are currently being intercrossed. All F1 progeny from the Cnga3 complementation test showed intact cone ERG function (n = 10), demonstrating Cnga3 is not likely the affected gene ($X2 = 16.2$, $p < 0.005$).

Conclusions: We have identified the spontaneous occurrence of cone pathway function loss in a line of inbred mice. Our results so far are consistent with an autosomal recessive inheritance pattern but we have excluded any involvement of Cnga3, a gene that is commonly mutated in human achromatopsia. 129SB6F1 intercrossing is currently underway to confirm the inheritance pattern of the phenotype and allow the underlying mutation to be mapped and identified. Identification of new candidate genes and mouse models is important, as the genetic basis of some forms of achromatopsia remains unknown.

B

REAGENTS

Table B.1 | List of all reagents.

Reagent	Catalogue code	Company	Headquarters
100bp gel ladder	Hyperladder 100	Bioline	
1kB gel ladder	12100	Norgen	
1M Tris(hydroxymethyl)aminomethane	1031156X	VWR	
2-Propanol	20842.300	VWR	
Ampicillin sodium salt	A9518-25G	Sigma	
Antisedan (Atipamezole)	134787-2	Zoetis	
B-Mercaptoethanol	M3148-25ML	Sigma	
Buffer ALT (Cat# 1014756)	1014756	Qiagen	Hilden, Germany
Buffer AW1 (Cat# 1014790)	1014790	Qiagen	Hilden, Germany
Buffer AW2 (Cat# 1014592)	1014592	Qiagen	Hilden, Germany
Chloramphenicol eye drops (0.5%)	76836	Bausch & Lomb	
cOmplete mini EDTA-free protease inhibitor cocktail tablets	4693159001	VWR	
Dry ice	UN1845 PGIII	Air Liquide UK	
Dulbecco's Modified Eagle's Medium - high glucose	D6546-500ML	Sigma	
Ethanol (100%)	20821.321	VWR	
Ethidium Bromide	E1510-10mL	Sigma	
Fetal Bovine Serum	10500-064	Gibco	
Formaldehyde (PFA) 16% w/v	28906	Thermo-Fisher	
Gel loading dye 6x	B7024S	New England Biolabs	
Glycerol			
High-Res standard Agarose	AGD1	AGTC bioproducts	
Hypromellose 0.3%	D01673	Martindale Pharma	
Hypromellose 1%		Martindale Pharma	
Immomix Red	BIO-25022	Bioline	
iTaq SYBR green mix	172-5120	Bio-Rad	
KOD Hot Start Master Mix	71842-3	Nonagon	
L-Glutamine 200nM	G7513	Sigma	
Luria broth powder	12795-027	Invitrogen	
MB H2O	W4502	Sigma	
Methanol	20847.307	VWR	
O.C.T compound	361603E	VWR	
Odyssey blocking buffer (TBS)	927-50000	LI-COR	
OptiPrep density gradient medium	D1556-250ML	Sigma	
Penicillin-Streptomycin	P4333-100ML	Sigma	
Phenylepinephrine eye drops (2.5%)	76854	Bausch & Lomb	
Phosphate Buffered Solution tablets	18912-014	Gibco	
Polyethylenimine (PEI) transfection reagent	23966-2	Polysciences	
ProLong Diamond Antifade Mountant	P36961	Life technologies	
Protein ladder	15H24	Geneflow	
Protein loading buffer	EC-887	National Diagnostics	
Proteinase K (Cat# 1045166)	1045166	Qiagen	Hilden, Germany
Proxymetacaine HCl minims		Bausch & Lomb	
RIPA lysis buffer	20-188	Temecula	
RNAlater	AM7204	Thermo-Fisher	
Rompun (Xylazine)	81548358	Bayer	
S.O.C. Medium (NZY+ medium)	15544-03	Invitrogen	
Select agar powder	30391-023	Invitrogen	
Shrimp Alkaline Phosphatase	M0371S	New England Biolabs	
Sodium Chloride, reagent grade	S9625	Sigma	
Sodium Hydroxide	S8045	Sigma	
Sucrose powder	S9378-500G	Sigma	
T4 DNA Ligase	M0202S	New England Biolabs	
T4 DNA Ligase	B0202S	New England Biolabs	
Trans-Blot Turbo 5x Transfer Buffer	36-22-42	Bio-Rad	
TransIT-LT1 transfection reagent	MIR2300	Mirus	
Tris-Buffered Saline (TBS) 10x buffer	170-6435	Bio-Rad	
Tris/Glycine/SDS 10x running buffer	EC-870	Nat Diagnostics	
Triton X-100	9002-93-1	Sigma	
Tropicamide eye drops (1%)	76852	Bausch & Lomb	
Tween 20	P1373-500ML	Sigma-Aldrich	
Tween-20	P1379-500ml	Sigma	
Vetalar (Ketamine)	E12222044PBE	Boehringer Ingelheim	
Virkon 1%	330003	VWR	
Viscotears	44011T	Alcon	
XL10-Gold Ultracompetent Cells	200315	Agilent Technologies	

C

KITS

Table C.1 | List of all commercial kits.

Kit	Catalogue code	Company	Headquarters
Endofree plasmid Mega-prep kit	12381	Qiagen	Hilden, Germany
Gel extraction kit	28704	Qiagen	Hilden, Germany
Genelute plasmid mini prep kit	PLN350-1KT	Sigma-Aldrich	St Louis, MO, USA
PCR purification kit	28106	Qiagen	Hilden, Germany
Purelink HiPure Precipitator Module	K2100-22	Invitrogen	Waltham, MA
QIAamp DNA Mini Kit	51304	Qiagen	Hilden, Germany
RNase-Free DNase Set	79254	Qiagen	Hilden, Germany
RNeasy mini-kit	74104	Qiagen	Hilden, Germany
Superscript III Reverse Transcriptase kit	18080-051	Invitrogen	Waltham, MA

D

HARDWARE

Table D.1 | List of all hardware.

Generic name	Model	Catalogue code	Company	Headquarters
Agarose gel imaging console	U:Genius	SYUG/1343	Syngene	Boston, MA, USA
Agarose gel powerpack	PowerPac basic	041BR69803	Bio-Rad	
Agarose gel UV dissection light	NA	FG-05	Geneflow	
Autoclave	Touchclave	0086 & 0037	LTE Scientific	
Bench top micro-centrifuge	Microstar 17	521-1646	VWR	
Bench top microscope	EZ24	10447197	Leica	
Bench-top Heater-stirrer		UC152	Stuart	
Bench-top stirrer		UC151	Stuart	
Benchtop nano-centrifuge	NA	C1301B-230V	Unknown	
Bevelled subretinal needle	Nanofil 35G	NF35BV	World Precision Instruments	
Biological safety cabinet	Mars class 2		Scanlaf	
Cell culture imaging system	Retiga 2000R	Fast1394	Q-imaging	
Colordome Electroretinography machine			Diagnosys LLC	
Cryotome LSE			Thermo Scientific	
Culture plate incubator		BD53	Binder	
Custom optomotor drum	Customised	Customised	Customised	
Electrode lens moulded pliers	customised	customised	customised	
Freezer (-20°C)				
Freezer (-80°C)		U570-86G	New Brunswick Scientific	
Head torch			CLUlite	
Heat block		FBD02DD	Techni	
Heated mouse recovery box			Mediheat	
ImmaPen		H-4000	Vector Labs	
Incubator-shaker	Excella E24	M1352-0002	New Brunswick Scientific	
Lamp (1000 lumens) on mechanical arm				
Medium-red optical filter plastic		027	Lee Filters	
Megafuge	Heraeus 16R	41508322	Thermo Scientific	
Non-toothed forceps		SC71	Surgitrac	
Operating microscope		OpMi-1	Zeiss	
PCR thermocycler	T100 thermal cycler	621BR08630	Bio-Rad	
Pellet Pestle Motor			Kontes	
pH meter	FiveEasy plus	01-911-302	Mettler Toledo	
Pipette 1000μL		P1000	Gilson	
Pipette 200μL		P200	Gilson	
Pipette 20μL		P20	Gilson	
Pipette 2μL		P2N	Gilson	
qPCR plate spinner		MPS1000	Labnet	
qPCR thermocycler plate-reader	CFX Connect Optics Module	788BR2016	Bio-Rad	
Scales		CS200	Ohaus	
Serological electronic pipette	Pipetboy	939939	PBS Integra	
Spectrophotometer	Nanodrop	ND1000	Thermo scientific	
Subretinal syringe		Nanofil	World Precision Instruments	
Tissue culture CO2 incubator	R		Galaxy	
Tissue culture microscope		AE31E	Motic	
Toothed forceps		SC49	Surgitrac	
Ultracentrifuge	Optima XE-90	CXE13016	Beckman Coulter	
Ultracentrifuge rotor	Type 70Ti	13E 1007	Beckman Coulter	
Vacuum engine for megaprep		MZ 2C NT	Vacuubrand	
Vannas scissors		SC81	Surgitrac	
Vortex mixer	rotamixer	NA	IATI	
Water heater circulation unit	T-pump	TP702	Gaymar	
Water-heated mouse plate		EZ-210	World Precision Instruments	
Waterbath		FB60305	Fisherbrand	
Webcam (for OMR)	C920	C920	Logitech	
Western Blot imaging machine	Odyssey	2800	Li-Cor	
Western Blot protein transfer unit	Trans-Blot Turbo transfer	690BR013715	Bio-Rad	
Western Blot vacuum incubation unit	Snap i.d. 2.0 system	S003710	SNAP2BASE	

E

SOFTWARE

Table E.1 | List of all software

Software	Version	Company	Headquarters/URL
Espion ERG	6.0	Diagnosys	Westford, MA, USA
Excel for Mac	15.33	Microsoft	Redmond, WA, USA
Word for Mac	15.33	Microsoft	Redmond, WA, USA
Eye Explorer		Heidelberg	Heidelberg, Germany
Geneious	7.0	Biomatters	Auckland, New Zealand
Image studio	5.2.5	Licor	Lincoln, NE, USA
ImageJ	1.48v	NA (open source)	imagej.nih.gov/ij/
R language	3.4	CRAN	https://cran.r-project.org/bin/macosx/
Rstudio for Mac	1.0.136	Rstudio	Boston, MA, USA
Stepper motor control	1.0	PC Control	
Papers 3 for Mac	3.4	Digital Science & Research Solutions Inc	London, UK
qPCR CFX manager	3.1	BioRad	Hercules, CA, USA
Evernote	6.11	Evernote	Redwood City, CA, USA
Powerpoint for Mac	15.33	Microsoft	Redmond, WA, USA
Photo booth	8.0	Apple	Silicon Valley, CA, USA
Logitech camera settings	3.31	Logitech	Silicon Valley, CA, USA
LaTeX type-setting software	3	LaTeX 3 project	Mainz, Germany
TexPad	1.7	Valetta Ventures LLP	Kent, UK

F

ANTIBODIES & STAINS

Table F.1 | List of all stains and blocking serums

Reagent	Catalogue code	Company	Headquarters
Hoescht nuclear stain	62249	Thermo-scientific	
Normal donkey serum	D9663-10ML	Sigma	
Normal goat serum	G9023-10ML	Sigma	

Table F.2 | List of all primary antibodies

Primary antibody name	Catalogue	Target protein	Source animal	Immunogen	Clonal	Supplier
CRX (CORD)	ab54635	CRX	Mouse	Peptides 1-96 of human	Monoclonal	Abcam
CRX Antibody (Q17)	sc-81958	CRX	Mouse	Recomb human CRX	Monoclonal	SantaCruz
CORD2 Antibody	PA5-32182	CRX	Rabbit	Human CORD2 aa1-168	Polyclonal	Life Tech
OPN1MW (AA21-50; N-terminus)	ABIN651110	OPN1LWS	Rabbit	Human OPN1MW (aa21-50)	Polyclonal	Abgent
OPN1MW (C-Term) antibody	ABIN2788202	OPN1LWS	Rabbit	Human OPN1MW (aa313-350)	Polyclonal	Aviva systems
Red-Green antibody	PA1-9517	OPN1LWS	Chicken	Mouse Opsin 1 - Synthetic	Polyclonal	ThermoFisher
Red-Green opsin antibody		OPN1LWS	Rabbit	Recombinant human red/green opsin	Polyclonal	Merck-Millipose
Cngb3 antibody (AA160-210)	ABIN571515	Cngb3	Rabbit	Mouse Cngb3 AA160-210	Polyclonal	Antibodies online
Cngb3 antibody (N-terminal)	CPBT 31596RH	CNGB3	Rabbit	Human CNGB3 N-terminus	Polyclonal	Creative diagnostics
Cngb3 antibody	orb156415	CNGB3	Rabbit	synthetic human CNGB3	Polyclonal	Biobyt
Anti-cone arrestin	AB15282	Cone arrestin	Rabbit	Synthetic rodent cone arrestin	Polyclonal	Millipore
Anti-GAPDH	TA802519	GAPDH	Mouse	Human GAPDH transcript variant 1	Monoclonal	OriGene

Table F.3 | List of secondary IHC and WB antibodies

Secondary antibody name	Wavelength (nm)	Host	Target	Catalogue	Company	Headquarters
Donkey anti-Rabbit IgG (H+L) secondary Alexa Fluor 568nm	568	Donkey	Rabbit	A10042	Fisher-Scientific	
Goat anti-Chicken IgY (H+L) secondary Alexa Fluor 568nm	568	Goat	Chicken	A11041	Fisher-Scientific	
IRDye 800CW Donkey anti-rabbit	800	Donkey	Rabbit	926-32213	Licor	
IRDye 800CW Donkey anti-mouse	800	Donkey	Mouse	925-32212	Licor	
IRDye 800CW Donkey anti-chicken	800	Donkey	Chicken	926-32218	Licor	
IRDye® 680RD Donkey anti-Mouse IgG (H + L)	680	Donkey	Mouse	925-68072	Licor	

Table F.4 | List of recombinant proteins for positive controls

Recombinant protein	Catalogue	Company	Headquarters
Recombinant human CORD2 protein	ab158201	Abcam	
Opsin 1 (Cone pigments), Long-Wave-Sensitive	ABIN1330344	Abnova	

G

SOLUTIONS

Table G.1 | List of all prepared solutions.

Solution	Components
Complete DMEM	High glucose DMEM 10% fetal bovine serum 1% penicillin-stretomycin (100 units/ml and 100 μg/ml, respectively) 2mM L-glutamine
Lysis buffer	1M Tris(hydroxymethyl)aminomethane 150 mM NaCl *Autoclave*
PBS-MK 5x	5x PBS tablets 5 mM magnesium chloride 12.5mM potassium chloride *Autoclave 5x PBS* *Then add 0.22μm filtered solutions of $MgCl_2$ and KCl*

H

CONE PHOTORECEPTOR QPCR PRIMERS

Table H.1 | List of manually designed qPCR primer pairs and efficiencies obtained during optimisation steps.

Primer pair	Best	Second
cGFP FW2 (431)	1.1	0.864
cGFP FW3 (136)	0.803	0.726
cGFP FW4 (457)	0.939	0.909
Cnga3 fw 1	1.267	0.983
Cngb3 fw 1	0.963	0.907
Cngb3 fw 2	1.08	0.881
Cone Arrestin fw 1	1.139	1.012
Cone Arrestin fw 2	0.807	0.803
Cone pde6h fw 1	0.994	0.939
Crx FW1 (27)	0.98	0.814
Crx FW2 (129)	0.803	0.681
Crx FW3 (10)	1.07	0.965
Crx FW4 (203)	0.998	0.908
Gapdh fw 1	0.92	0.819
Gapdh fw 2	0.826	0.723
Gnat2 fw 1	0.918	0.889
Opn1mw FW3 (81)	0.921	0.857
Opn1mw FW4 (339)	0.953	0.873
Opn1mws FW1 (68)	0.99	0.821
Opn1mws FW2 (594)	0.884	
Opn1sws fw 1	1.138	0.999
Opn1sws fw 2	0.865	0.856
Rho FW1 (227)	1.011	0.808
Rho FW2 (618)	0.916	0.765
Rho FW3 (542)	1.05	0.82
Rho FW4 (666)	0.728	0.476

List of References

1. R W Young. “Cell differentiation in the retina of the mouse”. en. In: *Anat. Rec.* 212.2 (June 1985), pp. 199–205.

2. Dan Larhammar, Karin Nordström, and Tomas A Larsson. “Evolution of vertebrate rod and cone phototransduction genes”. en. In: *Philos. Trans. R. Soc. Lond. B Biol. Sci.* 364.1531 (Oct. 2009), pp. 2867–2880.

3. Yasushi Imamoto and Yoshinori Shichida. “Cone visual pigments”. en. In: *Biochim. Biophys. Acta* 1837.5 (May 2014), pp. 664–673.

4. Changhong Peng, Elizabeth D Rich, and Michael D Varnum. “Subunit configuration of heteromeric cone cyclic nucleotide-gated channels”. en. In: *Neuron* 42.3 (May 2004), pp. 401–410.

5. U Benjamin Kaupp and Reinhard Seifert. “Cyclic nucleotide-gated ion channels”. en. In: *Physiol. Rev.* 82.3 (July 2002), pp. 769–824.

6. Haining Zhong et al. “The heteromeric cyclic nucleotide-gated channel adopts a 3A:1B stoichiometry”. en. In: *Nature* 420.6912 (Nov. 2002), pp. 193–198.

7. Anne K Hennig, Guang-Hua Peng, and Shiming Chen. “Regulation of photoreceptor gene expression by Crx-associated transcription factor network”. en. In: *Brain Res.* 1192 (Feb. 2008), pp. 114–133.

8. C L Freund et al. “Cone-rod dystrophy due to mutations in a novel photoreceptor-specific homeobox gene (CRX) essential for maintenance of the photoreceptor”. en. In: *Cell* 91.4 (Nov. 1997), pp. 543–553.

9. Y Liu et al. “Isolation and characterization of a zebrafish homologue of the cone rod homeobox gene”. en. In: *Invest. Ophthalmol. Vis. Sci.* 42.2 (Feb. 2001), pp. 481–487.

10. L C Bibb et al. “Temporal and spatial expression patterns of the CRX transcription factor and its downstream targets. Critical differences during human and mouse eye development”. en. In: *Hum. Mol. Genet.* 10.15 (July 2001), pp. 1571–1579.

11. Akiko Furukawa et al. “The mouse Crx 5’-upstream transgene sequence directs cell-specific and developmentally regulated expression in retinal photoreceptor cells”. en. In: *J. Neurosci.* 22.5 (Mar. 2002), pp. 1640–1647.

12. M M Sohocki et al. “Prevalence of mutations causing retinitis pigmentosa and other inherited retinopathies”. en. In: *Hum. Mutat.* 17.1 (2001), pp. 42–51.

13. Irene Campi et al. “Retinal Photoreceptor Functions Are Compromised in Patients With Resistance to Thyroid Hormone Syndrome (RTHβ)”. en. In: *J. Clin. Endocrinol. Metab.* 102.7 (July 2017), pp. 2620–2627.

14. Guang-Hua Peng and Shiming Chen. “Chromatin immunoprecipitation identifies photoreceptor transcription factor targets in mouse models of retinal degeneration: new findings and challenges”. en. In: *Vis. Neurosci.* 22.5 (Sept. 2005), pp. 575–586.

15. Philip A Ruzycki et al. “Graded gene expression changes determine phenotype severity in mouse models of CRX-associated retinopathies”. en. In: *Genome Biol.* 16.1 (Sept. 2015), p. 171.

16. Catherine Jomary, Stephen E Jones, and Andrew J Lotery. “Generation of light-sensitive photoreceptor phenotypes by genetic modification of human adult ocular stem cells with Crx”. en. In: *Invest. Ophthalmol. Vis. Sci.* 51.2 (Feb. 2010), pp. 1181–1189.

17. Yuko Seko et al. “Derivation of human differential photoreceptor cells from adult human dermal fibroblasts by defined combinations of CRX, RAX, OTX2 and NEUROD”. en. In: *Genes Cells* 19.3 (Mar. 2014), pp. 198–208.

18. M Michaelides, D M Hunt, and A T Moore. “The cone dysfunction syndromes”. en. In: *Br. J. Ophthalmol.* 88.2 (Feb. 2004), pp. 291–297.

19. Alberta A H J Thiadens et al. “Genetic etiology and clinical consequences of complete and incomplete achromatopsia”. en. In: *Ophthalmology* 116.10 (Oct. 2009), 1984–9.e1.

20. S Kohl et al. “Total colourblindness is caused by mutations in the gene encoding the alpha-subunit of the cone photoreceptor cGMP-gated cation channel”. en. In: *Nat. Genet.* 19.3 (July 1998), pp. 257–259.

21. S Kohl et al. “Mutations in the CNGB3 gene encoding the beta-subunit of the cone photoreceptor cGMP-gated channel are responsible for achromatopsia (ACHM3) linked to chromosome 8q21”. en. In: *Hum. Mol. Genet.* 9.14 (Sept. 2000), pp. 2107–2116.

22. Susanne Kohl et al. “Mutations in the cone photoreceptor G-protein alpha-subunit gene GNAT2 in patients with achromatopsia”. en. In: *Am. J. Hum. Genet.* 71.2 (Aug. 2002), pp. 422–425.

23. I A Aligianis et al. “Mapping of a novel locus for achromatopsia (ACHM4) to 1p and identification of a germline mutation in the alpha subunit of cone transducin (GNAT2)”. en. In: *J. Med. Genet.* 39.9 (Sept. 2002), pp. 656–660.

24. Susanne Kohl et al. “A nonsense mutation in PDE6H causes autosomal-recessive incomplete achromatopsia”. en. In: *Am. J. Hum. Genet.* 91.3 (Sept. 2012), pp. 527–532.

25. Bo Chang et al. “A homologous genetic basis of the murine cpfl1 mutant and human achromatopsia linked to mutations in the PDE6C gene”. en. In: *Proc. Natl. Acad. Sci. U. S. A.* 106.46 (Nov. 2009), pp. 19581–19586.

26. Susanne Kohl et al. “Mutations in the unfolded protein response regulator ATF6 cause the cone dysfunction disorder achromatopsia”. en. In: *Nat. Genet.* 47.7 (July 2015), pp. 757–765.

27. Susanne Kohl et al. “CNGB3 mutations account for 50% of all cases with autosomal recessive achromatopsia”. en. In: *Eur. J. Hum. Genet.* 13.3 (Mar. 2005), pp. 302–308.

28. Mark M Hassall, Alun R Barnard, and Robert E MacLaren. “Gene Therapy for Color Blindness”. en. In: *Yale J. Biol. Med.* 90.4 (Dec. 2017), pp. 543–551.

29. I E Hussels and N E Morton. “Pingelap and Mokil Atolls: achromatopsia”. en. In: *Am. J. Hum. Genet.* 24.3 (May 1972), pp. 304–309.

30. V C Sheffield. “The vision of typhoon lengkieki”. en. In: *Nat. Med.* 6.7 (July 2000), pp. 746–747.

31. John J Alexander et al. “Restoration of cone vision in a mouse model of achromatopsia”. en. In: *Nat. Med.* 13.6 (June 2007), pp. 685–687.

32. András M Komáromy et al. “Gene therapy rescues cone function in congenital achromatopsia”. en. In: *Hum. Mol. Genet.* 19.13 (July 2010), pp. 2581–2593.

33. N L Hawes et al. “A Point Mutation in the Cnga3 Gene Causes Cone Photoreceptor Function Loss (cpfl5) in Mice”. In: vol. 47. The Association for Research in Vision and Ophthalmology, May 2006, pp. 4579–4579.

34. Stylianos Michalakis et al. “Restoration of cone vision in the CNGA3-/- mouse model of congenital complete lack of cone photoreceptor function”. en. In: *Mol. Ther.* 18.12 (Dec. 2010), pp. 2057–2063.

35. Ji-Jing Pang et al. “AAV-mediated cone rescue in a naturally occurring mouse model of CNGA3-achromatopsia”. en. In: *PLoS One* 7.4 (Apr. 2012), e35250.

36. Livia S Carvalho et al. “Long-term and age-dependent restoration of visual function in a mouse model of CNGB3-associated achromatopsia following gene therapy”. en. In: *Hum. Mol. Genet.* 20.16 (Aug. 2011), pp. 3161–3175.

37. Eyal Banin et al. “Gene Augmentation Therapy Restores Retinal Function and Visual Behavior in a Sheep Model of CNGA3 Achromatopsia”. en. In: *Mol. Ther.* 23.9 (Sept. 2015), pp. 1423–1433.

38. Elisha Gootwine et al. “Gene Augmentation Therapy for a Missense Substitution in the cGMP-Binding Domain of Ovine CNGA3 Gene Restores Vision in Day-Blind Sheep”. en. In: *Invest. Ophthalmol. Vis. Sci.* 58.3 (Mar. 2017), pp. 1577–1584.

39. Katherine Mancuso et al. “Gene therapy for red-green colour blindness in adult primates”. en. In: *Nature* 461.7265 (Oct. 2009), pp. 784–787.

40. Zuoming Zhang et al. “AAV-mediated Gene Therapy Restores Cone Function In A Rat With An M-cone Opsin Deficiency, A Model For Blue Cone Monochromacy”. In: *Invest. Ophthalmol. Vis. Sci.* 52.14 (Apr. 2011), pp. 1403–1403.

41. Adam M Dubis et al. “Genotype-dependent variability in residual cone structure in achromatopsia: toward developing metrics for assessing cone health”. en. In: *Invest. Ophthalmol. Vis. Sci.* 55.11 (Oct. 2014), pp. 7303–7311.

42. Christopher S Langlo et al. “Residual Foveal Cone Structure in CNGB3-Associated Achromatopsia”. en. In: *Invest. Ophthalmol. Vis. Sci.* 57.10 (Aug. 2016), pp. 3984–3995.

43. Shinji Ueno et al. “In vivo imaging of a cone mosaic in a patient with achromatopsia associated with a GNAT2 variant”. en. In: *Jpn. J. Ophthalmol.* 61.1 (Jan. 2017), pp. 92–98.

44. Paul Yang et al. “Retinal morphology of patients with achromatopsia during early childhood: implications for gene therapy”. en. In: *JAMA Ophthalmol.* 132.7 (July 2014), pp. 823–831.

45. Mortada A Abozaid et al. “Reliability and Repeatability of Cone Density Measurements in Patients with Congenital Achromatopsia”. en. In: *Adv. Exp. Med. Biol.* 854.Chapter 37 (2016), pp. 277–283.

46. Joseph L Fleiss. “Measuring nominal scale agreement among many raters”. In: *Psychol. Bull.* 76.5 (1971), p. 378.

47. William A Scott. “Reliability of Content Analysis:The Case of Nominal Scale Coding”. In: *Public Opin. Q.* 19.3 (Jan. 1955), pp. 321–325.

48. J M Bland and D G Altman. “Statistical methods for assessing agreement between two methods of clinical measurement”. en. In: *Lancet* 1.8476 (Feb. 1986), pp. 307–310.

49. Heidi A Baseler et al. “Reorganization of human cortical maps caused by inherited photoreceptor abnormalities”. en. In: *Nat. Neurosci.* 5.4 (Apr. 2002), pp. 364–370.

50. Ethan A Rossi et al. “Visual function and cortical organization in carriers of blue cone monochromacy”. en. In: *PLoS One* 8.2 (Feb. 2013), e57956.

51. Maria I Patrıcio et al. “Inclusion of the Woodchuck Hepatitis Virus Posttranscriptional Regulatory Element Enhances AAV2-Driven Transduction of Mouse and Human Retina”. en. In: *Mol. Ther. Nucleic Acids* 6 (Mar. 2017), pp. 198–208.

52. Wadih M Zein et al. “CNGB3-Achromatopsia Clinical Trial With CNTF: Diminished Rod Pathway Responses With No Evidence of Improvement in Cone Function”. In: *Invest. Ophthalmol. Vis. Sci.* 55.10 (Oct. 2014), pp. 6301–6308.

53. Daniel M Lipinski et al. “CNTF Gene Therapy Confers Lifelong Neuroprotection in a Mouse Model of Human Retinitis Pigmentosa”. en. In: *Mol. Ther.* 23.8 (Aug. 2015), pp. 1308–1319.

54. András M Komáromy et al. “Transient photoreceptor deconstruction by CNTF enhances rAAV-mediated cone functional rescue in late stage CNGB3-achromatopsia”. en. In: *Mol. Ther.* 21.6 (June 2013), pp. 1131–1141.

55. Elisha Gootwine et al. “Safety and Efficacy Evaluation of rAAV2tYF-PR1.7-hCNGA3 Vector Delivered by Subretinal Injection in CNGA3 Mutant Achromatopsia Sheep”. en. In: *Hum Gene Ther Clin Dev* 28.2 (June 2017), pp. 96–107.

56. Wadih M Zein et al. “CNGB3-achromatopsia clinical trial with CNTF: diminished rod pathway responses with no evidence of improvement in cone function”. en. In: *Invest. Ophthalmol. Vis. Sci.* 55.10 (Sept. 2014), pp. 6301–6308.

57. Dario Marangoni et al. “Intravitreal Ciliary Neurotrophic Factor Transiently Improves Cone-Mediated Function in a CNGB3-/- Mouse Model of Achromatopsia”. en. In: *Invest. Ophthalmol. Vis. Sci.* 56.11 (Oct. 2015), pp. 6810–6822.

58. Stephen P Daiger, Sara J Bowne, and Lori S Sullivan. “Perspective on genes and mutations causing retinitis pigmentosa”. en. In: *Arch. Ophthalmol.* 125.2 (Feb. 2007), pp. 151–158.

59. Marianne Haim. “Epidemiology of retinitis pigmentosa in Denmark”. en. In: *Acta Ophthalmol. Scand. Suppl.* 233 (2002), pp. 1–34.

60. Y Murakami et al. “Necrotic cone photoreceptor cell death in retinitis pigmentosa”. en. In: *Cell Death Dis.* 6 (Dec. 2015), e2038.

61. Peter A Campochiaro and Tahreem A Mir. “The mechanism of cone cell death in Retinitis Pigmentosa”. en. In: *Prog. Retin. Eye Res.* 62 (Jan. 2018), pp. 24–37.

62. Claudio Punzo, Karl Kornacker, and Constance L Cepko. “Stimulation of the insulin/mTOR pathway delays cone death in a mouse model of retinitis pigmentosa”. en. In: *Nat. Neurosci.* 12.1 (Jan. 2009), pp. 44–52.

63. Connie Cepko and Claudio Punzo. “Cell metabolism: Sugar for sight”. en. In: *Nature* 522.7557 (June 2015), pp. 428–429.

64. S P Daiger et al. “Data services and software for identifying genes and mutations causing retinal degeneration”. In: *Invest. Ophthalmol. Vis. Sci.* 39 (1998), S295.

65. Robert E MacLaren et al. “Retinal gene therapy in patients with choroideremia: initial findings from a phase 1/2 clinical trial”. en. In: *Lancet* 383.9923 (Mar. 2014), pp. 1129–1137.

66. William W Hauswirth et al. “Treatment of leber congenital amaurosis due to RPE65 mutations by ocular subretinal injection of adeno-associated virus gene vector: short-term results of a phase I trial”. en. In: *Hum. Gene Ther.* 19.10 (Oct. 2008), pp. 979–990.

67. James W B Bainbridge et al. “Effect of gene therapy on visual function in Leber’s congenital amaurosis”. en. In: *N. Engl. J. Med.* 358.21 (May 2008), pp. 2231–2239.

68. Alice T Chuang, Curtis E Margo, and Paul B Greenberg. “Retinal implants: a systematic review”. en. In: *Br. J. Ophthalmol.* 98.7 (July 2014), pp. 852–856.

69. Zong-Yi Li and Ann H Milam. “Apoptosis in Retinitis Pigmentosa”. en. In: *Degenerative Diseases of the Retina*. Boston, MA: Springer, Boston, MA, 1995, pp. 1–8.

70. Keiichi Komeima et al. “Antioxidants reduce cone cell death in a model of retinitis pigmentosa”. en. In: *Proc. Natl. Acad. Sci. U. S. A.* 103.30 (July 2006), pp. 11300–11305.

71. Shinichi Usui et al. “Increased expression of catalase and superoxide dismutase 2 reduces cone cell death in retinitis pigmentosa”. en. In: *Mol. Ther.* 17.5 (May 2009), pp. 778–786.

72. Shinichi Usui et al. “NADPH oxidase plays a central role in cone cell death in retinitis pigmentosa”. en. In: *J. Neurochem.* 110.3 (Aug. 2009), pp. 1028–1037.

73. S Mohand-Said et al. “Normal retina releases a diffusible factor stimulating cone survival in the retinal degeneration mouse”. en. In: *Proc. Natl. Acad. Sci. U. S. A.* 95.14 (July 1998), pp. 8357–8362.

74. Ying Yang et al. “Functional cone rescue by RdCVF protein in a dominant model of retinitis pigmentosa”. en. In: *Mol. Ther.* 17.5 (May 2009), pp. 787–795.

75. Thierry Léveillard et al. “Identification and characterization of rod-derived cone viability factor”. en. In: *Nat. Genet.* 36.7 (July 2004), pp. 755–759.

76. Nisha Gupta, Kimberly E Brown, and Ann H Milam. “Activated microglia in human retinitis pigmentosa, late-onset retinal degeneration, and age-related macular degeneration”. en. In: *Exp. Eye Res.* 76.4 (Apr. 2003), pp. 463–471.

77. Harris Ripps. “Cell death in retinitis pigmentosa: gap junctions and the ’bystander’ effect”. en. In: *Exp. Eye Res.* 74.3 (Mar. 2002), pp. 327–336.

78. Rong Wen et al. “CNTF and retina”. en. In: *Prog. Retin. Eye Res.* 31.2 (Mar. 2012), pp. 136–151.

79. M Cayouette and C Gravel. “Adenovirus-mediated gene transfer of ciliary neurotrophic factor can prevent photoreceptor degeneration in the retinal degeneration (rd) mouse”. en. In: *Hum. Gene Ther.* 8.4 (Mar. 1997), pp. 423–430.

80. Yiwen Li et al. “CNTF induces regeneration of cone outer segments in a rat model of retinal degeneration”. en. In: *PLoS One* 5.3 (Mar. 2010), e9495.

81. Rong Wen et al. “Regeneration of cone outer segments induced by CNTF”. en. In: *Adv. Exp. Med. Biol.* 723 (2012), pp. 93–99.

82. Karin Roesch, Michael B Stadler, and Constance L Cepko. “Gene expression changes within Müller glial cells in retinitis pigmentosa”. en. In: *Mol. Vis.* 18 (May 2012), pp. 1197–1214.

83. Xin Mei et al. “The Thioredoxin Encoded by the Rod-Derived Cone Viability Factor Gene Protects Cone Photoreceptors Against Oxidative Stress”. en. In: *Antioxid. Redox Signal.* 24.16 (June 2016), pp. 909–923.

84. José-Alain Sahel et al. “Functional rescue of cone photoreceptors in retinitis pigmentosa”. en. In: *Graefes Arch. Clin. Exp. Ophthalmol.* 251.7 (July 2013), pp. 1669–1677.

85. David M Wu et al. “Overexpression of human Nrf2 rescues cone photoreceptors and retinal pigment epithelial cells from degeneration in the rd1 mouse”. In: *Investigative Ophthalmology and Visual Science*. B0158. 2017.

86. Wenjun Xiong et al. “NRF2 promotes neuronal survival in neurodegeneration and acute nerve damage”. en. In: *J. Clin. Invest.* 125.4 (Apr. 2015), pp. 1433–1445.

87. Young-Sam Keum. “Regulation of Nrf2-Mediated Phase II Detoxification and Anti-oxidant Genes”. en. In: *Biomol. Ther.* 20.2 (Mar. 2012), pp. 144–151.

88. Thomas W Kensler, Nobunao Wakabayashi, and Shyam Biswal. “Cell survival responses to environmental stresses via the Keap1-Nrf2-ARE pathway”. en. In: *Annu. Rev. Pharmacol. Toxicol.* 47 (2007), pp. 89–116.

89. Bin Lin, Richard H Masland, and Enrica Strettoi. “Remodeling of cone photoreceptor cells after rod degeneration in rd mice”. en. In: *Exp. Eye Res.* 88.3 (Mar. 2009), pp. 589–599.

90. S K John et al. “Loss of cone molecular markers in rhodopsin-mutant human retinas with retinitis pigmentosa”. en. In: *Mol. Vis.* 6 (Nov. 2000), pp. 204–215.

91. Michael Adamian et al. “Rod and cone opsin mislocalization in an autopsy eye from a carrier of X-linked retinitis pigmentosa with a Gly436Asp mutation in the RPGR gene”. en. In: *Am. J. Ophthalmol.* 142.3 (Sept. 2006), pp. 515–518.

92. Baerbel Rohrer et al. “Cone opsin mislocalization in Rpe65-/- mice: a defect that can be corrected by 11-cis retinal”. en. In: *Invest. Ophthalmol. Vis. Sci.* 46.10 (Oct. 2005), pp. 3876–3882.

93. Marijana Samardzija et al. “In conditions of limited chromophore supply rods entrap 11-cis-retinal leading to loss of cone function and cell death”. en. In: *Hum. Mol. Genet.* 18.7 (Apr. 2009), pp. 1266–1275.

94. Najate Aıt-Ali et al. “Rod-derived cone viability factor promotes cone survival by stimulating aerobic glycolysis”. en. In: *Cell* 161.4 (May 2015), pp. 817–832.

95. Volker Busskamp et al. “Genetic reactivation of cone photoreceptors restores visual responses in retinitis pigmentosa”. en. In: *Science* 329.5990 (July 2010), pp. 413–417.

96. Shannon E Boye et al. “A comprehensive review of retinal gene therapy”. en. In: *Mol. Ther.* 21.3 (Mar. 2013), pp. 509–519.

97. Matthew P Simunovic et al. “Structural and Functional Recovery Following Limited Iatrogenic Macular Detachment for Retinal Gene Therapy”. en. In: *JAMA Ophthalmol.* 135.3 (Mar. 2017), pp. 234–241.

98. A W Taylor. “Ocular immune privilege”. en. In: *Eye* 23.10 (Oct. 2009), pp. 1885–1889.

99. Thomas L Edwards et al. “Visual Acuity after Retinal Gene Therapy for Choroideremia”. en. In: *N. Engl. J. Med.* 374.20 (May 2016), pp. 1996–1998.

100. Jasleen K Jolly et al. “A Qualitative and Quantitative Assessment of Fundus Autofluorescence Patterns in Patients With Choroideremia”. en. In: *Invest. Ophthalmol. Vis. Sci.* 57.10 (Aug. 2016), pp. 4498–4503.

101. Viviana Gradinaru, Kimberly R Thompson, and Karl Deisseroth. “eNpHR: a Natronomonas halorhodopsin enhanced for optogenetic applications”. en. In: *Brain Cell Biol.* 36.1-4 (Aug. 2008), pp. 129–139.

102. Jasmina Cehajic-Kapetanovic et al. “Restoration of Vision with Ectopic Expression of Human Rod Opsin”. en. In: *Curr. Biol.* 25.16 (Aug. 2015), pp. 2111–2122.

103. Samantha R De Silva et al. “Long-term restoration of visual function in end-stage retinal degeneration using subretinal human melanopsin gene therapy”. en. In: *Proc. Natl. Acad. Sci. U. S. A.* (Oct. 2017).

104. D R Pepperberg et al. “Visual pigment and photoreceptor sensitivity in the isolated skate retina”. en. In: *J. Gen. Physiol.* 71.4 (Apr. 1978), pp. 369–396.

105. K O Donner and T Reuter. “Dark-adaptation processes in the rhodopsin rods of the frog’s retina”. en. In: *Vision Res.* 7.1 (Jan. 1967), pp. 17–41.

106. D A Baylor, T D Lamb, and K W Yau. “The membrane current of single rod outer segments”. en. In: *J. Physiol.* 288 (Mar. 1979), pp. 589–611.

107. P A Hargrave and J H McDowell. “Rhodopsin and phototransduction: a model system for G protein-linked receptors”. en. In: *FASEB J.* 6.6 (Mar. 1992), pp. 2323–2331.

108. C S Leibrock, T Reuter, and T D Lamb. “Molecular basis of dark adaptation in rod photoreceptors”. en. In: *Eye* 12 (Pt 3b) (1998), pp. 511–520.

109. Xuemei Zhu et al. “GRK1-dependent phosphorylation of S and M opsins and their binding to cone arrestin during cone phototransduction in the mouse retina”. en. In: *J. Neurosci.* 23.14 (July 2003), pp. 6152–6160.

110. E R Weiss et al. “Species-specific differences in expression of G-protein-coupled receptor kinase (GRK) 7 and GRK1 in mammalian cone photoreceptor cells: implications for cone cell phototransduction”. en. In: *J. Neurosci.* 21.23 (Dec. 2001), pp. 9175–9184.

111. Bo Chang et al. “Cone photoreceptor function loss-3, a novel mouse model of achromatopsia due to a mutation in Gnat2”. en. In: *Invest. Ophthalmol. Vis. Sci.* 47.11 (Nov. 2006), pp. 5017–5021.

112. N L Hawes et al. “A New Mouse Model of Cone Photoreceptor Fuction Loss (cpfl7)”. In: vol. 48. The Association for Research in Vision and Ophthalmology, May 2007, E–abstract 1350.

113. B Chang et al. “A new mouse model of cone photoreceptor function loss (cpfl1)”. In: *Investigative Ophthalmology & Visual Science*. Vol. 42. 2001, S527–S527.

114. Bo Chang, J Wang, and B FitzMaurice. “A new mouse model of cone photoreceptor function loss (cpfl9) with cone photoreceptor degeneration”. In: *Invest Ophthalmol Vis Sci*. 319 Retinal Genetics. 2016, 222: ARVO E–abstract B0250.

115. N L Hawes et al. “A new mouse model of cone photoreceptor function loss (cpfl4)”. In: vol. 45. The Association for Research in Vision and Ophthalmology, May 2004, E–abstract: 3590.

116. Jungyeon Won et al. “Mouse model resources for vision research”. en. In: *J. Ophthalmol.* 2011 (2011), p. 391384.

117. N L Hawes et al. “A New Mouse Model of Cone Photoreceptor Function Loss (Cpfl2)”. In: *Invest. Ophthalmol. Vis. Sci.* Vol. 44. The Association for Research in Vision and Ophthalmology, May 2003, E–Abstr 4531.

118. M Dominik Fischer et al. “Structural and functional phenotyping in the cone-specific photoreceptor function loss 1 (cpfl1) mouse mutant - a model of cone dystrophies”. en. In: *Adv. Exp. Med. Biol.* 664 (2010), pp. 593–599.

119. Dennis M Maddox et al. “A Mutation in Syne2 Causes Early Retinal Defects in Photoreceptors, Secondary Neurons, and Müller Glia”. en. In: *Invest. Ophthalmol. Vis. Sci.* 56.6 (June 2015), pp. 3776–3787.

120. M Biel et al. “Selective loss of cone function in mice lacking the cyclic nucleotide-gated channel CNG3”. en. In: *Proc. Natl. Acad. Sci. U. S. A.* 96.13 (June 1999), pp. 7553–7557.

121. C J Jeon, E Strettoi, and R H Masland. “The major cell populations of the mouse retina”. en. In: *J. Neurosci.* 18.21 (Nov. 1998), pp. 8936–8946.

122. C A Curcio et al. “Human photoreceptor topography”. en. In: *J. Comp. Neurol.* 292.4 (Feb. 1990), pp. 497–523.

123. Fernando Allan de Farias Rocha et al. “Spectral Sensitivity Measured with Electroretinogram Using a Constant Response Method”. en. In: *PLoS One* 11.1 (Jan. 2016), e0147318.

124. G H Jacobs and J Neitz. “Inheritance of color vision in a New World monkey (Saimiri sciureus)”. en. In: *Proc. Natl. Acad. Sci. U. S. A.* 84.8 (Apr. 1987), pp. 2545–2549.

125. M L Applebury et al. “The murine cone photoreceptor: a single cone type expresses both S and M opsins with retinal spatial patterning”. en. In: *Neuron* 27.3 (Sept. 2000), pp. 513–523.

126. Y Wang et al. “A locus control region adjacent to the human red and green visual pigment genes”. en. In: *Neuron* 9.3 (Sept. 1992), pp. 429–440.

127. Y Fei and T E Hughes. “Transgenic expression of the jellyfish green fluorescent protein in the cone photoreceptors of the mouse”. en. In: *Vis. Neurosci.* 18.4 (July 2001), pp. 615–623.

128. Daniel M Lipinski et al. “Characterization of a dominant cone degeneration in a green fluorescent protein-reporter mouse with disruption of Loci associated with human dominant retinal dystrophy”. en. In: *Invest. Ophthalmol. Vis. Sci.* 52.9 (Aug. 2011), pp. 6617–6623.

129. S Hattar et al. “Melanopsin and rod-cone photoreceptive systems account for all major accessory visual functions in mice”. en. In: *Nature* 424.6944 (July 2003), pp. 76–81.

130. Annette E Allen et al. “Visual responses in mice lacking critical components of all known retinal phototransduction cascades”. en. In: *PLoS One* 5.11 (Nov. 2010), e15063.

131. Masayuki Akimoto et al. “Targeting of GFP to newborn rods by Nrl promoter and temporal expression profiling of flow-sorted photoreceptors”. en. In: *Proc. Natl. Acad. Sci. U. S. A.* 103.10 (Mar. 2006), pp. 3890–3895.

132. M M Humphries et al. “Retinopathy induced in mice by targeted disruption of the rhodopsin gene”. en. In: *Nat. Genet.* 15.2 (Feb. 1997), pp. 216–219.

133. Constance L Cepko. “Emerging gene therapies for retinal degenerations”. en. In: *J. Neurosci.* 32.19 (May 2012), pp. 6415–6420.

134. Matthew Kearse et al. “Geneious Basic: an integrated and extendable desktop software platform for the organization and analysis of sequence data”. en. In: *Bioinformatics* 28.12 (June 2012), pp. 1647–1649.

135. Andreas Untergasser et al. “Primer3–new capabilities and interfaces”. en. In: *Nucleic Acids Res.* 40.15 (Aug. 2012), e115.

136. Hilda Petrs-Silva et al. “High-efficiency transduction of the mouse retina by tyrosine-mutant AAV serotype vectors”. en. In: *Mol. Ther.* 17.3 (Mar. 2009), pp. 463–471.

137. Chengwen Li and R Jude Samulski. “Serotype-specific replicating AAV helper constructs increase recombinant AAV type 2 vector production”. en. In: *Virology* 335.1 (Apr. 2005), pp. 10–21.

138. R Core Team. *R: A Language and Environment for Statistical Computing*. Vienna, Austria, 2017.

139. RStudio Team. *RStudio: Integrated Development Environment for R*. Boston, MA, 2015.

140. Hadley Wickham. *ggplot2: Elegant Graphics for Data Analysis*. 2009.

141. Hadley Wickham. *tidyverse: Easily Install and Load 'Tidyverse' Packages*. 2017.

142. Jose Pinheiro et al. *nlme: Linear and Nonlinear Mixed Effects Models*. 2017.

143. J C Pinheiro and D M Bates. "Linear Mixed-Effects Models: Basic Concepts and Examples". en. In: *Mixed-Effects Models in S and S-PLUS*. Statistics and Computing. Springer, New York, NY, 2000, pp. 3–56.

144. G E P Box and D R Cox. "An Analysis of Transformations". In: *J. R. Stat. Soc. Series B Stat. Methodol.* 26.2 (1964), pp. 211–252.

145. Donald C Hood and David G Birch. "Human cone receptor activity: The leading edge of the a–wave and models of receptor activity". In: *Vis. Neurosci.* 10.5 (Sept. 1993), pp. 857–871.

146. T C Chou and P Talalay. "Quantitative analysis of dose-effect relationships: the combined effects of multiple drugs or enzyme inhibitors". en. In: *Adv. Enzyme Regul.* 22 (1984), pp. 27–55.

147. K I Naka and WAH Rushton. "Spotentials from luminosity units in the retina of fish (Cyprinidae)". In: *J. Physiol.* (1966).

148. Sander Greenland et al. "Statistical tests, P values, confidence intervals, and power: a guide to misinterpretations". en. In: *Eur. J. Epidemiol.* 31.4 (Apr. 2016), pp. 337–350.

149. Regina Nuzzo. "Scientific method: statistical errors". In: *Nature* 506 (Feb. 2014), pp. 150–152.

150. Debarshi Mustafi, Andreas H Engel, and Krzysztof Palczewski. "Structure of cone photoreceptors". en. In: *Prog. Retin. Eye Res.* 28.4 (July 2009), pp. 289–302.

151. J L Schnapf, T W Kraft, and D A Baylor. "Spectral sensitivity of human cone photoreceptors". en. In: *Nature* 325.6103 (1987), pp. 439–441.

152. Meredith H Remmer et al. “Achromatopsia: a review”. en. In: *Curr. Opin. Ophthalmol.* 26.5 (July 2015), pp. 333–340.

153. Tanya Tolmachova et al. “Functional expression of Rab escort protein 1 following AAV2-mediated gene delivery in the retina of choroideremia mice and human cells ex vivo”. en. In: *J. Mol. Med.* 91.7 (July 2013), pp. 825–837.

154. B Chang et al. “A New Mouse Model of Cone Photoreceptor Function Loss (cpfl6) Associated With the Targeted Hcn1 Gene Mutation”. In: vol. 47. The Association for Research in Vision and Ophthalmology, May 2006, E–Abstract 2294–2294.

155. Christian Schön et al. “Loss of HCN1 enhances disease progression in mouse models of CNG channel-linked retinitis pigmentosa and achromatopsia”. en. In: *Hum. Mol. Genet.* 25.6 (Mar. 2016), pp. 1165–1175.

156. W Humphrey, A Dalke, and K Schulten. “VMD: visual molecular dynamics”. en. In: *J. Mol. Graph.* 14.1 (Feb. 1996), pp. 33–8, 27–8.

157. Minghui Li et al. “Structure of a eukaryotic cyclic-nucleotide-gated channel”. en. In: *Nature* 542.7639 (Feb. 2017), pp. 60–65.

158. Alberta A H J Thiadens et al. “Comprehensive analysis of the achromatopsia genes CNGA3 and CNGB3 in progressive cone dystrophy”. en. In: *Ophthalmology* 117.4 (Apr. 2010), 825–30.e1.

159. Xi-Qin Ding et al. “Impaired cone function and cone degeneration resulting from CNGB3 deficiency: down-regulation of CNGA3 biosynthesis as a potential mechanism”. en. In: *Hum. Mol. Genet.* 18.24 (Dec. 2009), pp. 4770–4780.

160. Alexander V Matveev et al. “Native cone photoreceptor cyclic nucleotidegated channel is a heterotetrameric complex comprising both CNGA3 and CNGB3: a study using the conedominant retina of Nrl/ mice”. In: *J. Neurochem.* 106.5 (Sept. 2008), pp. 2042–2055.

161. Anja Kathrin Mayer et al. “CNGB3 mutation spectrum including copy number variations in 485 achromatopsia patients”. In: *Hum. Mutat.* (Aug. 2017).

162. Yongwook Choi and Agnes P Chan. “PROVEAN web server: a tool to predict the functional effect of amino acid substitutions and indels”. en. In: *Bioinformatics* 31.16 (Aug. 2015), pp. 2745–2747.

163. Ivan A Adzhubei et al. “A method and server for predicting damaging missense mutations”. en. In: *Nat. Methods* 7.4 (Apr. 2010), pp. 248–249.

164. Arjun Raj et al. “Variability in gene expression underlies incomplete penetrance”. en. In: *Nature* 463.7283 (Feb. 2010), pp. 913–918.

165. Guo-Jie Ye et al. “Safety and Biodistribution Evaluation in CNGB3-Deficient Mice of rAAV2tYF-PR1.7-hCNGB3, a Recombinant AAV Vector for Treatment of Achromatopsia”. en. In: *Hum Gene Ther Clin Dev* 27.1 (Mar. 2016), pp. 27–36.

166. Jia-Ju Bao et al. “Reexpression of the tumor suppressor gene ARHI induces apoptosis in ovarian and breast cancer cells through a caspase-independent calpain-dependent pathway”. en. In: *Cancer Res.* 62.24 (Dec. 2002), pp. 7264–7272.

167. Joeli A Brinkman and Dorraya El-Ashry. “ER re-expression and re-sensitization to endocrine therapies in ER-negative breast cancers”. en. In: *J. Mammary Gland Biol. Neoplasia* 14.1 (Mar. 2009), pp. 67–78.

168. S W Lee et al. “Down-regulation of a member of the S100 gene family in mammary carcinoma cells and reexpression by azadeoxycytidine treatment”. en. In: *Proc. Natl. Acad. Sci. U. S. A.* 89.6 (Mar. 1992), pp. 2504–2508.

169. Prasun J Mishra and Glenn Merlino. “MicroRNA reexpression as differentiation therapy in cancer”. en. In: *J. Clin. Invest.* 119.8 (Aug. 2009), pp. 2119–2123.

170. Gurman S Pall and Andrew J Hamilton. “Improved northern blot method for enhanced detection of small RNA”. en. In: *Nat. Protoc.* 3.6 (2008), pp. 1077–1084.

171. Y J Ma et al. “RNase Protection Assay”. en. In: *Methods* 10.3 (Dec. 1996), pp. 273–278.

172. Anders Ståhlberg et al. “Properties of the reverse transcription reaction in mRNA quantification”. en. In: *Clin. Chem.* 50.3 (Mar. 2004), pp. 509–515.

173. Anna Git et al. “Systematic comparison of microarray profiling, real-time PCR, and next-generation sequencing technologies for measuring differential microRNA expression”. en. In: *RNA* 16.5 (May 2010), pp. 991–1006.

174. M Taniguchi et al. “Quantitative assessment of DNA microarrays–comparison with Northern blot analyses”. en. In: *Genomics* 71.1 (Jan. 2001), pp. 34–39.

175. V Bolón-Canedo et al. “A review of microarray datasets and applied feature selection methods”. In: *Inf. Sci.* 282 (Oct. 2014), pp. 111–135.

176. Shanrong Zhao et al. “Comparison of RNA-Seq and microarray in transcriptome profiling of activated T cells”. en. In: *PLoS One* 9.1 (Jan. 2014), e78644.

177. K Allanach et al. “Comparing microarray versus RT-PCR assessment of renal allograft biopsies: similar performance despite different dynamic ranges”. en. In: *Am. J. Transplant* 8.5 (May 2008), pp. 1006–1015.

178. K J Livak and T D Schmittgen. “Analysis of relative gene expression data using real-time quantitative PCR and the 2(-Delta Delta C(T)) Method”. en. In: *Methods* 25.4 (Dec. 2001), pp. 402–408.

179. Zhong Wang, Mark Gerstein, and Michael Snyder. “RNA-Seq: a revolutionary tool for transcriptomics”. en. In: *Nat. Rev. Genet.* 10.1 (Jan. 2009), pp. 57–63.

180. Zong Hong Zhang et al. “A comparative study of techniques for differential expression analysis on RNA-Seq data”. en. In: *PLoS One* 9.8 (Aug. 2014), e103207.

181. Manuel Garber et al. “Computational methods for transcriptome annotation and quantification using RNA-seq”. en. In: *Nat. Methods* 8.6 (June 2011), pp. 469–477.

182. David Svec et al. “How good is a PCR efficiency estimate: Recommendations for precise and robust qPCR efficiency assessments”. en. In: *Biomol Detect Quantif* 3 (Mar. 2015), pp. 9–16.

183. Yann Karlen et al. “Statistical significance of quantitative PCR”. en. In: *BMC Bioinformatics* 8.1 (Apr. 2007), p. 131.

184. Stephen A Bustin et al. “The MIQE guidelines: minimum information for publication of quantitative real-time PCR experiments”. en. In: *Clin. Chem.* 55.4 (Apr. 2009), pp. 611–622.

185. Emi Arikawa et al. “Cross-platform comparison of SYBR Green real-time PCR with TaqMan PCR, microarrays and other gene expression measurement technologies evaluated in the MicroArray Quality Control (MAQC) study”. en. In: *BMC Genomics* 9 (July 2008), p. 328.

186. Hiroshi Maeda et al. “Quantitative real-time PCR using TaqMan and SYBR Green for Actinobacillus actinomycetemcomitans, Porphyromonas gingivalis, Prevotella intermedia, tetQ gene and total bacteria”. en. In: *FEMS Immunol. Med. Microbiol.* 39.1 (Oct. 2003), pp. 81–86.

187. T D Schmittgen et al. “Quantitative reverse transcription-polymerase chain reaction to study mRNA decay: comparison of endpoint and real-time methods”. en. In: *Anal. Biochem.* 285.2 (Oct. 2000), pp. 194–204.

188. J Huggett et al. “Real-time RT-PCR normalisation; strategies and considerations”. en. In: *Genes Immun.* 6.4 (June 2005), pp. 279–284.

189. Vlasta Korenkova et al. “The focus on sample quality: Influence of colon tissue collection on reliability of qPCR data”. en. In: *Sci. Rep.* 6 (July 2016), p. 29023.

190. Liang Shan et al. “A novel PCR assay for quantification of HIV-1 RNA”. en. In: *J. Virol.* 87.11 (June 2013), pp. 6521–6525.

191. Simone Fleige and Michael W Pfaffl. “RNA integrity and the effect on the real-time qRT-PCR performance”. en. In: *Mol. Aspects Med.* 27.2-3 (Apr. 2006), pp. 126–139.

192. Sandrine Imbeaud et al. “Towards standardization of RNA quality assessment using user-independent classifiers of microcapillary electrophoresis traces”. en. In: *Nucleic Acids Res.* 33.6 (Mar. 2005), e56.

193. Herbert Auer et al. “Chipping away at the chip bias: RNA degradation in microarray analysis”. en. In: *Nat. Genet.* 35.4 (Dec. 2003), pp. 292–293.

194. M A Grotzer et al. “Biological stability of RNA isolated from RNAlater-treated brain tumor and neuroblastoma xenografts”. en. In: *Med. Pediatr. Oncol.* 34.6 (June 2000), pp. 438–442.

195. Jo Vandesompele et al. “Accurate normalization of real-time quantitative RT-PCR data by geometric averaging of multiple internal control genes”. en. In: *Genome Biol.* 3.7 (June 2002), RESEARCH0034.

196. Ncbi Gene. *Gapdh glyceraldehyde-3-phosphate dehydrogenase [Mus musculus (house mouse)] - Gene - NCBI*. `https://www.ncbi.nlm.nih.gov/gene/14433`. Accessed: 2017-10-26.

197. Ncbi Gene. *Actb actin, beta [Mus musculus (house mouse)] - Gene - NCBI*. `https://www.ncbi.nlm.nih.gov/gene/11461`. Accessed: 2017-10-26.

198. Benjamin Hofner, Matthias Schmid, and Lutz Edler. “Reproducible research in statistics: A review and guidelines for the Biometrical Journal”. en. In: *Biom. J.* 58.2 (Mar. 2016), pp. 416–427.

199. Nicole A Vasilevsky et al. “On the reproducibility of science: unique identification of research resources in the biomedical literature”. en. In: *PeerJ* 1 (Sept. 2013), e148.

200. Shareen A Iqbal et al. “Reproducible Research Practices and Transparency across the Biomedical Literature”. en. In: *PLoS Biol.* 14.1 (Jan. 2016), e1002333.

201. Peter Charbel Issa et al. “Optimization of in vivo confocal autofluorescence imaging of the ocular fundus in mice and its application to models of human retinal degeneration”. en. In: *Invest. Ophthalmol. Vis. Sci.* 53.2 (Feb. 2012), pp. 1066–1075.

202. R Heim and R Y Tsien. “Engineering green fluorescent protein for improved brightness, longer wavelengths and fluorescence resonance energy transfer”. en. In: *Curr. Biol.* 6.2 (Feb. 1996), pp. 178–182.

203. Ulrich F O Luhmann et al. “The drusenlike phenotype in aging Ccl2-knockout mice is caused by an accelerated accumulation of swollen autofluorescent subretinal macrophages”. en. In: *Invest. Ophthalmol. Vis. Sci.* 50.12 (Dec. 2009), pp. 5934–5943.

204. L J Fisher. “Development of synaptic arrays in the inner plexiform layer of neonatal mouse retina”. en. In: *J. Comp. Neurol.* 187.2 (Sept. 1979), pp. 359–372.

205. Christopher Baum et al. “Mutagenesis and oncogenesis by chromosomal insertion of gene transfer vectors”. en. In: *Hum. Gene Ther.* 17.3 (Mar. 2006), pp. 253–263.

206. N Somia and I M Verma. “Gene therapy: trials and tribulations”. en. In: *Nat. Rev. Genet.* 1.2 (Nov. 2000), pp. 91–99.

207. R M Blaese et al. “T lymphocyte-directed gene therapy for ADA- SCID: initial trial results after 4 years”. en. In: *Science* 270.5235 (Oct. 1995), pp. 475–480.

208. Masahiro Yamashita and Michael Emerman. “Retroviral infection of non-dividing cells: old and new perspectives”. en. In: *Virology* 344.1 (Jan. 2006), pp. 88–93.

209. D St Louis and I M Verma. “An alternative approach to somatic cell gene therapy”. en. In: *Proc. Natl. Acad. Sci. U. S. A.* 85.9 (May 1988), pp. 3150–3154.

210. Joseph Zabner et al. “Safety and efficacy of repetitive adenovirus–mediated transfer of CFTR cDNA to airway epithelia of primates and cotton rats”. en. In: *Nat. Genet.* 6.1 (Jan. 1994), pp. 75–83.

211. J Zabner et al. “Adenovirus-mediated gene transfer transiently corrects the chloride transport defect in nasal epithelia of patients with cystic fibrosis”. en. In: *Cell* 75.2 (Oct. 1993), pp. 207–216.

212. C Jomary et al. “Adenovirus-mediated gene transfer to murine retinal cells in vitro and in vivo”. en. In: *FEBS Lett.* 347.2-3 (June 1994), pp. 117–122.

213. A Puppo et al. “Retinal transduction profiles by high-capacity viral vectors”. en. In: *Gene Ther.* 21.10 (Oct. 2014), pp. 855–865.

214. Y Yang et al. “Cellular immunity to viral antigens limits E1-deleted adenoviruses for gene therapy”. en. In: *Proc. Natl. Acad. Sci. U. S. A.* 91.10 (May 1994), pp. 4407–4411.

215. E Marshall. “Gene therapy death prompts review of adenovirus vector”. en. In: *Science* 286.5448 (Dec. 1999), pp. 2244–2245.

216. R R Ali et al. “Gene transfer into the mouse retina mediated by an adeno-associated viral vector”. en. In: *Hum. Mol. Genet.* 5.5 (May 1996), pp. 591–594.

217. Douglas M McCarty, Samuel M Young Jr, and R Jude Samulski. “Integration of adeno-associated virus (AAV) and recombinant AAV vectors”. en. In: *Annu. Rev. Genet.* 38 (2004), pp. 819–845.

218. Felix F Reichel et al. “AAV8 Can Induce Innate and Adaptive Immune Response in the Primate Eye”. en. In: *Mol. Ther.* (Aug. 2017).

219. James W B Bainbridge et al. “Long-term effect of gene therapy on Leber’s congenital amaurosis”. en. In: *N. Engl. J. Med.* 372.20 (May 2015), pp. 1887–1897.

220. Jean Bennett et al. “Safety and durability of effect of contralateral-eye administration of AAV2 gene therapy in patients with childhood-onset blindness caused by RPE65 mutations: a follow-on phase 1 trial”. en. In: *Lancet* 388.10045 (Aug. 2016), pp. 661–672.

221. Philip M Smallwood et al. “Genetically engineered mice with an additional class of cone photoreceptors: implications for the evolution of color vision”. en. In: *Proc. Natl. Acad. Sci. U. S. A.* 100.20 (Sept. 2003), pp. 11706–11711.

222. Wei Wang et al. “Two-Step Reactivation of Dormant Cones in Retinitis Pigmentosa”. en. In: *Cell Rep.* 15.2 (Apr. 2016), pp. 372–385.

223. J Miyazaki et al. “Expression vector system based on the chicken beta-actin promoter directs efficient production of interleukin-5”. en. In: *Gene* 79.2 (July 1989), pp. 269–277.

224. Youn-Bok Lee et al. “Optimizing regulatable gene expression using adenoviral vectors”. en. In: *Exp. Physiol.* 90.1 (Jan. 2005), pp. 33–37.

225. S Ylä-Herttuala - Molecular Therapy and 2012. “Endgame: glybera finally recommended for approval as the first gene therapy drug in the European union”. In: *cell.com* (2012).

226. Katsuya Inagaki et al. “Robust systemic transduction with AAV9 vectors in mice: efficient global cardiac gene transfer superior to that of AAV8”. en. In: *Mol. Ther.* 14.1 (July 2006), pp. 45–53.

227. Regine Mühlfriedel et al. “AAV-Mediated Gene Supplementation Therapy in Achromatopsia Type 2: Preclinical Data on Therapeutic Time Window and Long-Term Effects”. en. In: *Front. Neurosci.* 11 (May 2017), p. 292.

228. Mariacarmela Allocca et al. “Novel adeno-associated virus serotypes efficiently transduce murine photoreceptors”. en. In: *J. Virol.* 81.20 (Oct. 2007), pp. 11372–11380.

229. Luk H Vandenberghe et al. “Dosage thresholds for AAV2 and AAV8 photoreceptor gene therapy in monkey”. en. In: *Sci. Transl. Med.* 3.88 (June 2011), 88ra54.

230. H Mizuguchi et al. “IRES-dependent second gene expression is significantly lower than cap-dependent first gene expression in a bicistronic vector”. en. In: *Mol. Ther.* 1.4 (Apr. 2000), pp. 376–382.

231. Evy Lobbestael et al. “Immunohistochemical detection of transgene expression in the brain using small epitope tags”. en. In: *BMC Biotechnol.* 10 (Feb. 2010), p. 16.

232. Kp Suresh. “An overview of randomization techniques: An unbiased assessment of outcome in clinical research”. en. In: *J. Hum. Reprod. Sci.* 4.1 (Jan. 2011), pp. 8–11.

233. Gillian A Lancaster, Susanna Dodd, and Paula R Williamson. “Design and analysis of pilot studies: recommendations for good practice”. en. In: *J. Eval. Clin. Pract.* 10.2 (May 2004), pp. 307–312.

234. Christine N Kay et al. “Targeting photoreceptors via intravitreal delivery using novel, capsid-mutated AAV vectors”. en. In: *PLoS One* 8.4 (Apr. 2013), e62097.

235. Deniz Dalkara et al. “Inner limiting membrane barriers to AAV-mediated retinal transduction from the vitreous”. en. In: *Mol. Ther.* 17.12 (Dec. 2009), pp. 2096–2102.

236. Christiana J Johnson et al. “Technical brief: subretinal injection and electroporation into adult mouse eyes”. en. In: *Mol. Vis.* 14 (Dec. 2008), pp. 2211–2226.

237. Ji-Jing Pang et al. “Gene therapy restores vision-dependent behavior as well as retinal structure and function in a mouse model of RPE65 Leber congenital amaurosis”. en. In: *Mol. Ther.* 13.3 (Mar. 2006), pp. 565–572.

238. Atul A Gawande et al. “An Apgar score for surgery”. en. In: *J. Am. Coll. Surg.* 204.2 (Feb. 2007), pp. 201–208.

239. Saumil Sethna and Silvia C Finnemann. “Analysis of photoreceptor rod outer segment phagocytosis by RPE cells in situ”. en. In: *Methods Mol. Biol.* 935 (2013), pp. 245–254.

240. Kenneth F Schulz et al. “CONSORT 2010 statement: updated guidelines for reporting parallel group randomised trials”. en. In: *BMJ* 340 (Mar. 2010), p. c332.

241. Carol Kilkenny et al. “Improving bioscience research reporting: the ARRIVE guidelines for reporting animal research”. en. In: *PLoS Biol.* 8.6 (June 2010), e1000412.

242. Joseph Dettori. “The random allocation process: two things you need to know”. en. In: *Evid. Based Spine Care J.* 1.3 (Dec. 2010), pp. 7–9.

243. C Roberts and D Torgerson. “Randomisation methods in controlled trials”. en. In: *BMJ* 317.7168 (Nov. 1998), p. 1301.

244. Jennifer A Hirst et al. “The need for randomization in animal trials: an overview of systematic reviews”. en. In: *PLoS One* 9.6 (June 2014), e98856.

245. J Cohen. “A power primer”. en. In: *Psychol. Bull.* 112.1 (July 1992), pp. 155–159.

246. Neena B Haider et al. “Nr2e3-directed transcriptional regulation of genes involved in photoreceptor development and cell-type specific phototransduction”. en. In: *Exp. Eye Res.* 89.3 (Sept. 2009), pp. 365–372.

247. Vidyullatha Vasireddy et al. “Rescue of photoreceptor degeneration by curcumin in transgenic rats with P23H rhodopsin mutation”. en. In: *PLoS One* 6.6 (June 2011), e21193.

248. Deborah L Duricka, R Lane Brown, and Michael D Varnum. “Defective trafficking of cone photoreceptor CNG channels induces the unfolded protein response and ER-stress-associated cell death”. en. In: *Biochem. J* 441.2 (Jan. 2012), pp. 685–696.

249. Stewart H Lecker, Alfred L Goldberg, and William E Mitch. “Protein degradation by the ubiquitin-proteasome pathway in normal and disease states”. en. In: *J. Am. Soc. Nephrol.* 17.7 (July 2006), pp. 1807–1819.

250. K W Small et al. “North Carolina macular dystrophy is assigned to chromosome 6”. en. In: *Genomics* 13.3 (July 1992), pp. 681–685.

251. R E Kelsell et al. “Localization of the gene for progressive bifocal chorioretinal atrophy (PBCRA) to chromosome 6q”. en. In: *Hum. Mol. Genet.* 4.9 (Sept. 1995), pp. 1653–1656.

252. Kent W Small et al. “North Carolina Macular Dystrophy Is Caused by Dysregulation of the Retinal Transcription Factor PRDM13”. en. In: *Ophthalmology* 123.1 (Jan. 2016), pp. 9–18.

253. NCBI. *Rho rhodopsin [Mus musculus (house mouse)] - Gene - NCBI*. `https://www.ncbi.nlm.nih.gov/gene/212541`. Accessed: 2017-11-22.

254. J Lem et al. “Morphological, physiological, and biochemical changes in rhodopsin knockout mice”. en. In: *Proc. Natl. Acad. Sci. U. S. A.* 96.2 (Jan. 1999), pp. 736–741.

255. P J Rosenfeld et al. “A null mutation in the rhodopsin gene causes rod photoreceptor dysfunction and autosomal recessive retinitis pigmentosa”. en. In: *Nat. Genet.* 1.3 (June 1992), pp. 209–213.

256. Lawrence H Pinto et al. “Interpretation of the mouse electroretinogram”. en. In: *Doc. Ophthalmol.* 115.3 (Nov. 2007), pp. 127–136.

257. Leah C Byrne et al. “AAV-mediated Delivery of Rod-derived Cone Viability Factor in a Mouse Model of Retinal Degeneration”. In: *Invest. Ophthalmol. Vis. Sci.* 52.14 (Apr. 2011), pp. 1395–1395.

258. T Cronin et al. “The disruption of the rod-derived cone viability gene leads to photoreceptor dysfunction and susceptibility to oxidative stress”. en. In: *Cell Death Differ.* 17.7 (July 2010), pp. 1199–1210.

259. Tiziana Amendola, Marco Fiore, and Luigi Aloe. “Postnatal changes in nerve growth factor and brain derived neurotrophic factor levels in the retina, visual cortex, and geniculate nucleus in rats with retinitis pigmentosa”. en. In: *Neurosci. Lett.* 345.1 (July 2003), pp. 37–40.

260. M Dominik Fischer et al. “Codon-Optimized RPGR Improves Stability and Efficacy of AAV8 Gene Therapy in Two Mouse Models of X-Linked Retinitis Pigmentosa”. en. In: *Mol. Ther.* 25.8 (Aug. 2017), pp. 1854–1865.

261. Haoyu Mao et al. “AAV delivery of wild-type rhodopsin preserves retinal function in a mouse model of autosomal dominant retinitis pigmentosa”. en. In: *Hum. Gene Ther.* 22.5 (May 2011), pp. 567–575.

262. Haoyu Mao et al. “Long-term rescue of retinal structure and function by rhodopsin RNA replacement with a single adeno-associated viral vector in P23H RHO transgenic mice”. en. In: *Hum. Gene Ther.* 23.4 (Apr. 2012), pp. 356–366.

263. Mary O’Reilly et al. “RNA interference-mediated suppression and replacement of human rhodopsin in vivo”. en. In: *Am. J. Hum. Genet.* 81.1 (July 2007), pp. 127–135.

264. Sophia Millington-Ward et al. “Suppression and replacement gene therapy for autosomal dominant disease in a murine model of dominant retinitis pigmentosa”. en. In: *Mol. Ther.* 19.4 (Apr. 2011), pp. 642–649.

265. Arpad Palfi et al. “Adeno-associated virus-mediated rhodopsin replacement provides therapeutic benefit in mice with a targeted disruption of the rhodopsin gene”. en. In: *Hum. Gene Ther.* 21.3 (Mar. 2010), pp. 311–323.

266. A M Geller and P A Sieving. “Assessment of foveal cone photoreceptors in Stargardt’s macular dystrophy using a small dot detection task”. en. In: *Vision Res.* 33.11 (July 1993), pp. 1509–1524.

267. A F Wright. “A searchlight through the fog”. In: *Nature genetics* 17 (Oct. 1997), pp. 132–134.

268. David G Birch et al. “Randomized trial of ciliary neurotrophic factor delivered by encapsulated cell intraocular implants for retinitis pigmentosa”. en. In: *Am. J. Ophthalmol.* 156.2 (Aug. 2013), 283–292.e1.

269. Frédéric Chalmel et al. “Rod-derived Cone Viability Factor-2 is a novel bifunctional-thioredoxin-like protein with therapeutic potential”. en. In: *BMC Mol. Biol.* 8 (Aug. 2007), p. 74.

270. Jun Lu and Arne Holmgren. “The thioredoxin antioxidant system”. en. In: *Free Radic. Biol. Med.* 66 (Jan. 2014), pp. 75–87.

271. Ben Shaberman. *ARVO 2015 Highlight: New Research Boosts Prospects for Saving Vision with RdCVF - Eye on the Cure*. `http://www.blindness.org/blog/index.php/arvo-2015-highlight-new-research-boosts-prospects-for-saving-vision-with-rdcvf/`. Accessed: 2018-1-2. May 2015.